



## City Research Online

### City, University of London Institutional Repository

---

**Citation:** Mitroglou, N. (2006). Multihole injectors for direct-injection gasoline engines. (Unpublished Doctoral thesis, City University London)

This is the accepted version of the paper.

This version of the publication may differ from the final published version.

---

**Permanent repository link:** <https://openaccess.city.ac.uk/id/eprint/8487/>

**Link to published version:**

**Copyright:** City Research Online aims to make research outputs of City, University of London available to a wider audience. Copyright and Moral Rights remain with the author(s) and/or copyright holders. URLs from City Research Online may be freely distributed and linked to.

**Reuse:** Copies of full items can be used for personal research or study, educational, or not-for-profit purposes without prior permission or charge. Provided that the authors, title and full bibliographic details are credited, a hyperlink and/or URL is given for the original metadata page and the content is not changed in any way.

**School of Engineering and Mathematical Sciences**

# **Multihole Injectors for Direct-Injection Gasoline Engines**

**Dipl.(Eng) Nicholas Mitroglou**

**This thesis is submitted for the fulfilment of the requirements for the  
Degree of Doctor of Philosophy**

**August 2006**

Αφιερωμένο στην οικογένειά μου.

Σας ευχαριστώ πολύ για την υπομονή, την κατανόηση και τη συμπαράσταση που δείξατε όλο αυτό το διάστημα.

## *Table of Contents*

<i>List of Tables</i>	6
<i>List of Figures</i>	8
<i>Acknowledgements</i>	15
<i>Declaration</i>	16
<i>Abstract</i>	17
<i>Nomenclature</i>	18
<i>Chapter 1 Introduction</i>	21
1.1 HISTORY OF THE SPARK IGNITION ENGINE	21
1.2 CLIMATE CHANGE AND ENGINES	24
1.2.1 Air pollution	24
1.2.2 Cars and carbon dioxide (CO <sub>2</sub> )	27
1.3 DIRECT-INJECTION GASOLINE ENGINES	32
1.3.1 Direct-injection concepts	34
1.3.2 Fuel injection equipment (FIE)	39
1.4 THESIS OUTLINE	46
<i>Chapter 2 Literature Review</i>	47
2.1 INTRODUCTION	47
2.2 INTERNAL NOZZLE FLOW (LARGE-SCALE/REAL-SIZE)	48
2.3 HIGH-PRESSURE FUEL SPRAY CHARACTERISATION	53
2.4 MIXTURE PREPARATION CHARACTERISATION	63
2.5 MISCELLANEOUS ENGINE EXPERIMENTS	74
2.6 SUMMARY OF LITERATURE REVIEW	83
<i>Chapter 3 Internal Nozzle Flow</i>	85
3.1 INVESTIGATED LARGE-SCALE TRANSPARENT NOZZLE	85
3.2 ENLARGED INJECTOR TEST-RIG	88
3.3 HIGH-SPEED DIGITAL VIDEO TECHNIQUE	91
3.3.1 Experimental Setup	91
3.3.2 Image Processing	94
3.4 EXPERIMENTAL RESULTS	96

<b>3.4.1 Internal nozzle flow patterns</b>	<b>96</b>
<b>3.4.2 Incipient cavitation</b>	<b>99</b>
<b>3.4.3 Developed cavitation</b>	<b>105</b>
<b>3.5 SUMMARY</b>	<b>115</b>
<b><i>Chapter 4 Spray Characterisation</i></b>	<b>117</b>
<b>4.1 INVESTIGATED MULTI-HOLE NOZZLE CONFIGURATIONS</b>	<b>118</b>
<b>4.2 HIGH-PRESSURE\TEMPERATURE CHAMBER TEST RIG</b>	<b>124</b>
<b>4.2.1 Experimental set-up</b>	<b>125</b>
<b>4.2.2 Control and monitoring of experiments</b>	<b>127</b>
<b>4.3 MIE-SCATTERING VISUALISATION</b>	<b>128</b>
<b>4.4 PHASE-DOPPLER ANEMOMETRY</b>	<b>132</b>
<b>4.5 EXPERIMENTAL RESULTS</b>	<b>139</b>
<b>4.5.1 Mie scattering visualisation</b>	<b>140</b>
<b>4.5.2 Phase – Doppler anemometry</b>	<b>166</b>
<b>4.6 SUMMARY</b>	<b>184</b>
<b><i>Chapter 5 Mixture Distribution</i></b>	<b>187</b>
<b>5.1 OPTICAL ENGINE TEST RIG</b>	<b>189</b>
<b>5.1.1 Research engine</b>	<b>189</b>
<b>5.1.2 Optical engine experimental set-up</b>	<b>191</b>
<b>5.1.3 Engine management</b>	<b>193</b>
<b>5.2 LASER INDUCED FLUORESCENCE TECHNIQUE</b>	<b>195</b>
<b>5.2.1 Principles of the LIF technique</b>	<b>196</b>
<b>5.2.2 Choice of dopant</b>	<b>198</b>
<b>5.2.3 LIF optical arrangement</b>	<b>199</b>
<b>5.2.4 Calibration of images</b>	<b>202</b>
<b>5.3 EXPERIMENTAL RESULTS</b>	<b>212</b>
<b>5.3.1 Homogeneous stoichiometric engine operation</b>	<b>214</b>
<b>5.3.2 Stratified lean-in-fuel engine operation</b>	<b>233</b>
<b>5.4 SUMMARY</b>	<b>246</b>
<b><i>Chapter 6 Conclusions &amp; Recommendations</i></b>	<b>249</b>
<b>6.1 INTERNAL NOZZLE FLOW</b>	<b>250</b>
<b>6.1.1 Internal nozzle flow patterns</b>	<b>250</b>
<b>6.1.2 Incipient cavitation</b>	<b>251</b>

6.1.3 Developed cavitation	252
6.2 SPRAY CHARACTERISATION	253
6.2.1 Spray visualisation	254
6.2.2 Phase-Doppler anemometry	255
6.3 MIXTURE DISTRIBUTION	256
6.3.1 Homogeneous stoichiometric engine operation	257
6.3.2 Stratified overall lean engine operation	258
6.4 RECOMMENDATIONS FOR FUTURE WORK	259
6.4.1 Internal nozzle flow investigations	260
6.4.2 Spray investigations	260
6.4.3 Engine investigations	261
<i>Chapter 7 References</i>	262

## *List of Tables*

Table 1-1: European Union emission standards for newly registered vehicles.	26
Table 1-2: Average specific CO <sub>2</sub> emissions of new passenger cars per fuel type for ACEA and the European Union (Source ACEA, EU).	30
Table 1-3: Trends in composition of new cars registered on the market for ACEA and the EU (Source ACEA,EU).	30
Table 2-1: Literature relative to internal nozzle flow of high-pressure injectors.	48
Table 2-1: Literature relative to internal nozzle flow of high-pressure injectors (continued).	49
Table 2-1: Literature relative to internal nozzle flow of high-pressure injectors (continued).	50
Table 2-1: Literature relative to internal nozzle flow of high-pressure injectors (continued).	51
Table 2-1: Literature relative to internal nozzle flow of high-pressure injectors (continued).	52
Table 2-1: Literature relative to internal nozzle flow of high-pressure injectors (continued).	53
Table 2-2: Literature relative to spray characterisation of high-pressure injectors.	53
Table 2-2: Literature relative to spray characterisation of high-pressure injectors (continued).	54
Table 2-2: Literature relative to spray characterisation of high-pressure injectors (continued).	55
Table 2-2: Literature relative to spray characterisation of high-pressure injectors (continued).	56
Table 2-2: Literature relative to spray characterisation of high-pressure injectors (continued).	57
Table 2-2: Literature relative to spray characterisation of high-pressure injectors (continued).	58
Table 2-2: Literature relative to spray characterisation of high-pressure injectors (continued).	59
Table 2-2: Literature relative to spray characterisation of high-pressure injectors (continued).	60
Table 2-2: Literature relative to spray characterisation of high-pressure injectors (continued).	61
Table 2-2: Literature relative to spray characterisation of high-pressure injectors (continued).	62
Table 2-2: Literature relative to spray characterisation of high-pressure injectors (continued).	63
Table 2-3: Literature relative to mixture preparation characterisation.	63
Table 2-3: Literature relative to mixture preparation characterisation (continued).	64
Table 2-3: Literature relative to mixture preparation characterisation (continued).	65
Table 2-3: Literature relative to mixture preparation characterisation (continued).	66
Table 2-3: Literature relative to mixture preparation characterisation (continued).	67
Table 2-3: Literature relative to mixture preparation characterisation (continued).	68
Table 2-3: Literature relative to mixture preparation characterisation (continued).	69
Table 2-3: Literature relative to mixture preparation characterisation (continued).	70

Table 2-3: Literature relative to mixture preparation characterisation (continued).	71
Table 2-3: Literature relative to mixture preparation characterisation (continued).	72
Table 2-3: Literature relative to mixture preparation characterisation (continued).	73
Table 2-3: Literature relative to mixture preparation characterisation (continued).	74
Table 2-4: Literature of miscellaneous engine experiments.	74
Table 2-4: Literature of miscellaneous engine experiments (continued).	75
Table 2-4: Literature of miscellaneous engine experiments (continued).	76
Table 2-4: Literature of miscellaneous engine experiments (continued).	78
Table 2-4: Literature of miscellaneous engine experiments (continued).	79
Table 2-4: Literature of miscellaneous engine experiments (continued)	80
Table 2-4: Literature of miscellaneous engine experiments (continued).	81
Table 2-4: Literature of miscellaneous engine experiments (continued).	82
Table 3-1: Flow conditions inside the large-scale multi-hole nozzle for needle lifts 0.51-1.53mm.	100
Table 3-2: Flow conditions inside the large-scale 3-D multi-hole model nozzle at full needle lift.	101
Table 4-1: Still imaging test conditions for three different multi-hole nozzles.	141
Table 4-2: Still imaging test conditions for two different multi-hole nozzles simulating engine-operating conditions.	142
Table 4-3: High-speed imaging test conditions.	143
Table 4-4: Overall spray cone angle for two multi-hole nozzles.	159
Table 4-5: Test conditions for the 6-hole symmetric nozzle.	167
Table 4-6: Test conditions for the 6-hole – Asymmetric nozzle.	167
Table 4-7: Test conditions for the 12-hole symmetric nozzle.	167
Table 4-8: Double injection test cases for the 6-hole – Asymmetric and the 12-hole symmetric nozzles.	168
Table 5-1: Experimental cases for the in-cylinder LIF investigation at 1500rpm engine speed. – SCV90 stands for swirl control valve fully open (no swirl), SCV60 for 60degrees opening (medium swirl) and SCV0 for fully closed (high swirl).	216
Table 5-2: Experimental cases for the in-cylinder LIF investigation at 3000rpm engine speed. – SCV90 stands for swirl control valve fully open (no swirl), SCV60 for 60degrees opening (medium swirl) and SCV0 for fully closed (high swirl).	217
Table 5-3: Experimental cases for the in-cylinder LIF investigation at 1500rpm engine speed. – SCV90 stands for swirl control valve fully open (no swirl), SCV0 for fully closed (high swirl) and AFR 35 / 45 stands for two different AFR values.	235
Table 5-4: Experimental cases for the in-cylinder LIF investigation at 3000rpm engine speed. – SCV90 stands for swirl control valve fully open (no swirl), SCV0 for fully closed (high swirl) and AFR 35 / 45 stands for two different AFR values.	236

## *List of Figures*

Figure 1.1: Award winning atmospheric gas engine (about 1866/7)	22
Figure 1.2: Nicolaus August Otto with a. his first four-stroke cycle engine (1876), and b. the Otto working diagram (9 <sup>th</sup> May, 1876).	22
Figure 1.3: European Driving Cycle pattern for emission tests.	26
Figure 1.4: (a). CO, uHC and NO <sub>x</sub> concentrations' dependence on air/fuel mixture quality for fuel gasoline and (b). Cut-out of an oxygen sensor (lambda sensor).	27
Figure 1.5: (a). Carbon dioxide (CO <sub>2</sub> ) emissions in the EU-15 (Source, EEA 2000). (b). Energy related CO <sub>2</sub> emissions in the EU-25, projected in Mt till the year of 2030 (Source, EEA 2005).	29
Figure 1.6: Mercedes 300SL. The first vehicle equipped with a direct-injection gasoline engine.	34
Figure 1.7: (a). Conventional port-fuel-injection system and (b). direct-injection fuel system.	35
Figure 1.8: Direct-injection combustion systems.	36
Figure 1.9: Typical direct-injection, spark-ignition engine system layout [8].	39
Figure 1.10: (a). Schematic of the air-assisted, outward opening injector. (b). Separation of fuel metering and direct injection events (Injection Sequencing) and (c). Premixed charge spray under atmospheric conditions. [11]	41
Figure 1.11: (a). Model of an outward opening nozzle injector. (b), (c). Side and bottom images of the hollow cone spray under atmospheric chamber pressure produced by an outward opening nozzle.	42
Figure 1.12: (a). Swirl pressure atomiser nozzle cut-out. (b). Spray generated under atmospheric ambient pressure and (c). under 12bar chamber pressure.	43
Figure 1.13: (a). Schematic and (b). spray image of the slit injector generated fan spray.	44
Figure 1.14: (a). Multi-hole nozzle cut-out. (b). Possible nozzle configurations. (c). Spray of a 6-hole injector and (d). Hole blockage from carbon deposits.	45
Figure 3.1: Geometry of the 6-hole fully symmetric injection nozzle.	86
Figure 3.2: Three-dimensional models of the large-scale 6-hole nozzle. (a). Isometric view of Perspex nozzle. (b). Prospective cut-out. (c), (d). Front and side view, respectively and (e). Bottom view.	86
Figure 3.3: From real-size to large-scale injector.	87
Figure 3.4: Enlarged transparent and metal needle parts.	88
Figure 3.5: Schematic of the large-scale injector test rig.	89
Figure 3.6: Schematic of HSDV imaging in large-scale 3-D model nozzle.	92
Figure 3.7: Schematic of imaging areas and viewpoints for the side camera (HSDV Camera 1).	93
Figure 3.8: Schematic of the imaging areas as viewed from the bottom camera (HSDV Camera 2).	94
Figure 3.9: Image sequence demonstrating primary inlet flow to the injection hole.	97

Figure 3.10: Image sequence demonstrating flow splitting in-between two injection holes.	98
Figure 3.11: Image sequence demonstrating the low-scale flow at the sac volume.	99
Figure 3.12: <i>Top row</i> : Image sequence of “needle string” development. <i>Bottom row</i> : combined side and bottom view images of a “needle string” taken simultaneously.	102
Figure 3.13: Side view cavitation visualisation at CN=0.73. <i>Top row</i> : image sequence of bubble cloud at upper hole corner. <i>Bottom row</i> : interaction between needle string and hole cavitation.	103
Figure 3.14: Demonstration of cavitation regime occupying the hole inlet from upper to side entrance walls at CN=0.9 and full valve lift.	103
Figure 3.15: Image sequence demonstrating cavitation at the side entrance walls at CN=0.9 and full valve lift.	104
Figure 3.16: Image sequence of canopy shaped cavitation film development at CN=0.9 and full valve lift.	104
Figure 3.17: Cavitation regimes inside the 3-D large-scale model nozzle	106
Figure 3.18: Image sequence with developing cavitation string.	107
Figure 3.19: Image sequence with in-hole cavitation string creation mechanism at CN=1.	108
Figure 3.20: Interaction between cavitation string and in-hole cavitation structures at CN=1.	109
Figure 3.21: Alternation of pre-film to film stage cavitation at CN=2.	111
Figure 3.22: Effect of needle lift on cavitation structures (CN=1.5, Re~46,500, ~49,000).	111
Figure 3.23: Representation of recirculation zone inside the gaseous pocket of film cavitation at CN=2.5 and full valve lift.	112
Figure 3.24: Flow structure inside the gaseous pocket of film cavitation at CN=2.5 and full valve lift.	113
Figure 3.25: Representative image of film stage cavitation at CN=3 and full valve lift.	114
Figure 3.26: Effect of needle lift on cavitation structures at CN=3.2.	115
Figure 3.27: <i>Top row</i> : Full needle lift (2.04mm) at CN=3.2. <i>Bottom row</i> : One quarter of full needle lift (0.51mm) at CN=5.2.	115
Figure 4.1: Tested multi-hole nozzle configurations. (a). Symmetric 6-hole, (b). Asymmetric 6-hole, (c). 5-hole plus one central hole and (d). 12-hole nozzle with 2 missing peripheral holes and a central hole.	119
Figure 4.2: Multi-hole injector triggering signal and typical needle lift diagram.	121
Figure 4.3: Direct comparison of volumetric capacity of all tested multi-hole injectors at 120bar injection pressure.	122
Figure 4.4: Iso-surface of vapour fraction for (a). 6- and (b). 12-hole nozzles [113].	123
Figure 4.5: Volumetric capacity of (a). 6-hole symmetric injector and (b). 12-hole injector with a central hole and two blocked side holes.	124
Figure 4.6: Schematic of the high-pressure\temperature constant volume chamber (HPVT CVC) test rig and the high-pressure injection system.	126
Figure 4.7: User-interface of the <i>Chamber Control</i> software.	128

Figure 4.8: Schematic of the Mie scattering visualisation set-up.	129
Figure 4.9: (a). Spray regions of interest and imaging planes. (b). Definition of spray quantitative parameters and (c). Spray image used to compare test cases.	131
Figure 4.10: Imaging areas and spatial resolution of selected frame rates for HSDV.	132
Figure 4.11: Schematic of the measurements principle of PDA (Source: Dantec Dynamics).	133
Figure 4.12: Scattered light from a spherical particle (Source: Dantec Dynamics).	134
Figure 4.13: Doppler Velocity measurement principle.	135
Figure 4.14: Particle diameter measurement principle.	136
Figure 4.15: Schematic of the Dantec 2D PDA system.	137
Figure 4.16: Top view of the PDA optics set-up.	138
Figure 4.17: Start of injection identification for the 5+1 central holes nozzle at (a). 80bar and (b). 120bar injection pressures.	144
Figure 4.18: Effect of injection pressure on SOI time for a 10 (12-2) + 1 central holes nozzle. (a). 80 and (b). 120bar.	145
Figure 4.19: Predicted pressure distribution inside the injection nozzle, showing the pressure-drop taking place at the needle seat area [38].	145
Figure 4.20: Sequential images of the initial spray development of 5+1 central holes injector.	146
Figure 4.21: First stages of fully developed spray for the 5+1 central holes nozzle (length scale is in mm).	147
Figure 4.22: Example of air-entrainment in a 5+1 central holes injector spray.	148
Figure 4.23: Comparison of the individual jet cone angle for (a). 6- and (b). 12-hole nozzles. <i>Top row</i> is atmospheric and <i>bottom row</i> is higher chamber pressure.	149
Figure 4.24: Comparison of images of central jet shape of a 5+1 central holes injector taken at identical conditions but on two different imaging planes.	150
Figure 4.25: Spray tip penetration lengths of central and side jets as calculated from Mie images at (a). 80bar and (b). 120bar injection pressures.	151
Figure 4.26: Effect of injection pressure on spray atomisation.	152
Figure 4.27: Time-dependent comparison of a 10 (12-2) + 1 central holes spray injected at injection pressures of (a). 80 and (b). 120bar.	153
Figure 4.28: Time-dependent comparison of a 6-hole spray injected at injection pressures of (a). 120 and (b). 200bar.	154
Figure 4.29: Effect of injection pressure on (a). side and (b). central jet tip penetration lengths for 5+1 central holes (top row) and 10 (12-2) + 1 central holes (bottom row) nozzles.	155
Figure 4.30: Effect of injection pressure on spray tip penetration lengths for (a). 6-hole symmetric and (b). 6-hole asymmetric injectors.	155
Figure 4.31: Effect of chamber pressure on a 6-hole nozzle spray. (a). 1bar and (b). 12bar.	156
Figure 4.32: Effect of chamber pressure on a 10 (12-2) + 1 central hole nozzle spray. (a). 1bar and (b). 6bar.	157

Figure 4.33: Effect of chamber pressure on spray tip penetration length at 120bar injection pressure for (a). 6-hole asymmetric and (b). 10 (12-2) + 1 central holes nozzles.	157
Figure 4.34: Effect of chamber pressure on spray tip penetration length at 200bar injection pressure for the 6-hole symmetric nozzle.	158
Figure 4.35: Comparison of overall spray cone angle between (a). 1bar and (b). 8bar chamber pressures, for an injection pressure of 80bar.	159
Figure 4.36: Schematic representation of the processing procedure.	160
Figure 4.37: Temperature effect on droplet vaporisation for the 10 (12-2) + 1 central holes nozzle at two times after SOI ( <i>top row</i> : 0.4ms and <i>bottom row</i> : 0.9ms ASOI) expressed as probability density function for temperatures (a). 50° to 90° and (b). 50° to 120°.	161
Figure 4.38: Temperature effect on droplet vaporisation for the 6-hole asymmetric nozzle at two times after SOI ( <i>top row</i> : 0.4ms and <i>bottom row</i> : 0.9ms ASOI) expressed as probability density function for temperatures (a). 50° to 90° and (b). 50° to 120°.	162
Figure 4.39: Definitions of injection duration and “Dwell time” in double injection.	163
Figure 4.40: Double injection with symmetric duration pulses of 1ms injection duration and 0.3ms dwell time. Time sequence of high-speed images acquired during the dwell time period.	164
Figure 4.41: Time-dependent comparison of different injection durations at 120bar injection pressure.	165
Figure 4.42: PDA measurements grid and resultant velocity vector definition.	169
Figure 4.43: Effect of injection pressure on droplet velocities at 10mm from the nozzle exit for the 10(12-2) + 1 central holes nozzle. Spatial representation at 0.9ms ASOI of (a). 80b and (b). 120b. (c). Temporal velocity profiles for 1.5ms injection duration at 1bar chamber pressure at the centre point of the jet ( $r=10\text{mm}$ ).	170
Figure 4.44: Effect of injection pressure on droplet velocities at 10mm from nozzle exit for the 6-hole symmetric nozzle. Spatial representation at 0.9ms ASOI of (a). 120b and (b). 200b. (c). Temporal velocity profiles for 1.5ms injection duration at 1bar chamber pressure at the centre point of the jet ( $r=7\text{mm}$ ).	170
Figure 4.45: Effect of chamber pressure: (a). 10 (12-2) + 1 central holes nozzle at 10mm from nozzle exit at 80bar injection pressure and (b). 6-hole symmetric nozzle at 30mm from nozzle exit at 200bar injection pressure at the centre points of the jets ( $r_a=10$ and $r_b=7\text{mm}$ ).	171
Figure 4.46: Effect of injection duration at 80bar injection pressure and 1bar chamber pressure in (a). 6-hole asymmetric and (b). 10 (12-2) + 1 central holes nozzles.	172
Figure 4.47: Effect of injection pressure on the minimum injection duration of 0.7ms	172
Figure 4.48: Effect of ambient chamber temperature on droplet velocities for a 6-hole asymmetric nozzle at 80bar injection pressure at 10mm from the nozzle exit.	173
Figure 4.49: Double injection triggering and needle response time.	174
Figure 4.50: Effect of injection pressure on double injection for a 6-hole asymmetric nozzle injecting at 1bar chamber pressure; values measured at 2.5mm from the nozzle exit.	175
Figure 4.51: Effect of dwell time on double injection for a 6-hole asymmetric nozzle. Values measured at 2.5mm from the nozzle exit at 80bar injection pressure.	175
Figure 4.52: Double injection droplet velocities from a 6-hole nozzle at 80bar injection pressure and at 10mm from nozzle exit	176

Figure 4.53: Effect of L/D ratio on droplet velocities for 80bar injection pressure, 1bar chamber pressure at (a). 2.5mm and (b). 10mm from the nozzle exit.	177
Figure 4.54: Effect of L/D ratio on droplet size distribution for 80bar injection and 1bar chamber pressures at 0.9ms ASOI at (a). 2.5mm and (b). 10mm from the nozzle exit.	178
Figure 4.55: Spatial representation of ambient chamber temperature effect on droplet size distribution for a 6-hole asymmetric injector at 10mm from the nozzle exit at 0.9ms ASOI. (a). 50°C, (b). 90°C, (c). 115°C and (d). AMD and SMD values.	178
Figure 4.56: Effect of chamber pressure for a 6-hole injector at 30mm from the nozzle exit injecting at 200bar.	179
Figure 4.57: Effect of chamber pressure for a 10 (12-2) + 1 central holes injector at 10mm from the nozzle exit at 80bar injection pressure. (a). Spatial profile and (b). Normalised size distribution graph for the entire injection duration and the total jet cross-section.	180
Figure 4.58: Effect of injection duration for a 10(12-2) + 1 central holes injector at 10mm from the nozzle exit at 80bar injection pressure. (a). Spatial sizing profile and (b). Normalised size distribution graph for the entire injection duration and the total jet cross-section.	181
Figure 4.59: Effect of injection pressure for a 10 (12-2) + 1 central holes injector at atmospheric chamber pressure. <i>Top row</i> : Spatial sizing profiles at 0.9ms ASOI at (a). 2.5mm and (b). 10mm from the nozzle exit. <i>Bottom row</i> : Normalised size distribution graphs for the entire injection duration and the total jet cross-section at (a) 2.5mm and (b) 10mm from the nozzle exit.	182
Figure 4.60: Effect of injection pressure for a six-hole injector at atmospheric chamber pressure. (a). Spatial sizing profile at 10mm from the nozzle exit at 0.9ms ASOI and (b). Normalised size distribution graph for the entire injection duration and the total jet cross-section.	183
Figure 4.61: Effect of dwell time for a 6-hole asymmetric nozzle at 80bar injection pressure, at 2.5mm from the nozzle exit. (a). Dwell time of 0.3ms and (b). Dwell time of 1ms.	184
Figure 5.1: Schematic representation of the key elements of the 5-valve, twin-spark ignition optical engine.	190
Figure 5.2: Schematic diagram of the Swirl Control Valve operation.	191
Figure 5.3: Schematic representation of the inlet pre-mixing chamber.	192
Figure 5.4: Screen shot of the engine control software.	194
Figure 5.5: Screen shot of the engine monitoring and data acquisition software.	195
Figure 5.6: Electron energy transfer diagram.	197
Figure 5.7: Schematic of LIF optical set up.	201
Figure 5.8: Schematic representation of the laser sheet position relative to the spark plugs.	201
Figure 5.9: Graphical representation of image calibration.	204
Figure 5.10: Calibration results. (a). [115]	211
Figure 5.11: Fuel liquid concentration at 25°C ASOI for the 12-hole nozzle at injection timings of (a). 30°, (b). 50° and (c). 70°C.	218
Figure 5.12: Fuel liquid concentration at 25°C ASOI for the 6-hole nozzle at injection timings of (a). 70°, (b). 90° and (c). 120°C.	219
Figure 5.13: Two-dimensional deviation of air/fuel ratio (AFR) distribution at 340°C (20° before compression TDC) of the 12-hole injector at injection timings of (a). 30°, (b). 50° and (c).	

70°CA.	219
Figure 5.14: Two-dimensional deviation of air/fuel ratio (AFR) distribution at 340°CA (20° before compression TDC) of the 6-hole injector at injection timings of (a). 70°, (b). 90° and (c). 120°CA.	220
Figure 5.15: Fuel liquid concentration at 30°CA ASOI for the 12- (top row) and the 6-hole (bottom row) nozzles at injection timings of (a). 50°, (b). 70° and (c). 90°CA.	221
Figure 5.16: Two-dimensional deviation of air/fuel ratio (AFR) distribution at 340°CA (20° before compression TDC) of the 12-hole injector at injection timings of (a). 50°, (b). 70° and (c). 90°CA.	222
Figure 5.17: Two-dimensional deviation of air/fuel ratio (AFR) distribution at 340°CA (20° before compression TDC) of the 6-hole injector at injection timings of (a). 70°, (b). 90° and (c). 120°CA.	222
Figure 5.18: Two-dimensional deviation of air/fuel ratio (AFR) distribution at 340°CA (20° before compression TDC) of the 12-hole injector at double-injection strategy. The timing of the first injection in the sequence is set at 50°CA (top row), at 70°CA (middle row) and at 90°CA (bottom row). The second injection timing is placed at (a). 30°CA after the start of the first injection event, (b). 180°CA, or bottom dead centre and (c). 220°CA, timing at which inlet valves have closed.	224
Figure 5.19: Two-dimensional deviation of air/fuel ratio (AFR) distribution at 340°CA (20° before compression TDC) of the 12-hole injector at triple-injection strategy. The timing of the first injection in the sequence is set at 50°CA, the second at 70°CA and the third injection timing is placed at (a). 90°CA and (b). 220°CA, timing at which inlet valves have closed.	225
Figure 5.20: Two-dimensional deviation of air/fuel ratio (AFR) distribution at 340°CA (20° before compression TDC) of the 6-hole injector at double-injection strategy. The timing of the first injection in the sequence is set at 70°CA (top row), at 90°CA (middle row) and at 120°CA (bottom row). The second injection timing is placed at (a). 30°CA after the start of the first injection event, (b). 180°CA, or bottom dead centre and (c). 220°CA, timing at which inlet valves have closed.	226
Figure 5.21: Two-dimensional deviation of air/fuel ratio (AFR) distribution at 340°CA (20° before compression TDC) of the 6-hole injector at triple-injection strategy. The timing of the first injection in the sequence is set at 70°CA (top row), at 90°CA (middle row) and at 120°CA (bottom row). The second at 20°CA after the start of the first pulse and the third injection timing is placed at (a). 20°CA after the start of the second pulse, (b). 180°CA or bottom dead centre and (c). 220°CA, timing at which inlet valves have closed.	227
Figure 5.22: Two-dimensional deviation of air/fuel ratio (AFR) distribution at 340°CA (20° before compression TDC) of the 12-hole injector at double-injection strategy. The timing of the first injection in the sequence is set at 70°CA, the second injection timing is placed at (a). 30°CA after the start of the first injection event and (b). 213°CA, timing at which inlet valves have closed.	228
Figure 5.23: Two-dimensional deviation of air/fuel ratio (AFR) distribution at 340°CA (20° before compression TDC) of the 12-hole injector at triple-injection strategy. Injection timings of (a). 50-90-120°CA, (b). 70-110-140°CA and (c). 90-130-160°CA.	228
Figure 5.24: Two-dimensional deviation of air/fuel ratio (AFR) distribution at 340°CA (20° before compression TDC) of the 6-hole injector at double-injection strategy. Injection timings of (a). 70-213°CA, (b). 90-213°CA and (c). 120-213°CA.	229
Figure 5.25: Comparison of three different in-cylinder swirl levels for the 12-hole nozzle operating at single- (top row) and double-injection (bottom row) conditions. (a). No swirl (SCV 90°), (b). Medium swirl (SCV 60°) and (c). Maximum swirl (SCV 0°) at 50°CA injection timing.	230
Figure 5.26: Comparison of two different in-cylinder swirl levels for the 6-hole nozzle operating at single- (top row) and double-injection (bottom row) conditions. (a). No swirl (SCV 90°) and (b).	

Maximum swirl (SCV 0°) at 120°CA injection timing.	231
Figure 5.27: Two-dimensional deviation of air/fuel ratio (AFR) distribution at 340°CA (20° before compression TDC) of the 12-hole injector injecting at 70°CA at (a). 60, (b). 80 and (c). 120bar injection pressure.	232
Figure 5.28: Two-dimensional deviation of air/fuel ratio (AFR) distribution at 340°CA (20° before compression TDC) of the 12-hole injector at 1,500rpm (top row) and 3,000rpm (bottom row) engine speed. Injection timing is kept constant at 50°CA and injection pressure is set to (a). 80 and (b). 120bar.	233
Figure 5.29: Schematic representation of the stratification concept for the five-valve twin-spark direct-injection gasoline engine.	234
Figure 5.30: Two-dimensional AFR distribution for the 12-hole injector at injection timing of (a). 240°CA, (b).270°CA and (c). 300°CA at 80bar injection pressure and 1,500rpm.	237
Figure 5.31: Two-dimensional AFR distribution for the 6-hole injector at injection timing of (a). 270°CA and (b). 300°CA at 80bar injection pressure and 1,500rpm.	237
Figure 5.32: Two-dimensional AFR distribution for the 12-hole (top row) and the 6-hole (bottom row) injectors at injection timings of (a). 240°CA, (b).260°CA and (c). 300°CA at 80bar injection pressure and 3,000rpm.	239
Figure 5.33: Two-dimensional AFR distribution for the 12-hole injector at double-injection strategy. Injection timings of (a). 240-255°CA, (b).270-285°CA and (c). 290-306°CA at 80bar injection pressure and 1,500rpm.	240
Figure 5.34: Two-dimensional AFR distribution for the 6-hole injector at double-injection strategy. Injection timings of (a). 270-285°CA and (b). 290-306°CA at 80bar injection pressure and 1,500rpm.	240
Figure 5.35: Two-dimensional AFR distribution for the 6-hole injector at triple-injection strategy. Injection timings of (a). 240-252-263°CA, (b).250-262-273°CA and (c). 270-282-293°CA at 80bar injection pressure and 1,500rpm.	241
Figure 5.36: Two-dimensional AFR distribution for the 12-hole injector at double-injection strategy. Injection timings of (a). 250-275°CA, (b).260-285°CA and (c). 280-305°CA at 80bar injection pressure and 3,000rpm.	242
Figure 5.37: Two-dimensional AFR distribution for the 12-hole injector at triple-injection strategy. Injection timings of (a). 220-240-260°CA and (b).240-260-279°CA at 80bar injection pressure and 3,000rpm.	242
Figure 5.38: Two-dimensional AFR distribution for the 6-hole injector at double-injection strategy. Injection timings of (a). 250-285°CA, (b).260-285°CA and (c). 270-295°CA at 80bar injection pressure and 3,000rpm.	243
Figure 5.39: Two-dimensional AFR distribution for the 6-hole injector at triple-injection strategy. Injection timings of (a). 220-243-257°CA, (b).240-253-287°CA and (c). 250-273-297°CA at 80bar injection pressure and 3,000rpm.	243
Figure 5.40: Two-dimensional AFR distribution for the 6-hole injector at low (1,500rpm – top row) and high (3,000rpm – bottom row) engine speed. Injection pressure of (a). 80bar and (b). 120bar at two different injection timings.	244
Figure 5.41: Two-dimensional AFR distribution for the 6-hole injector at low (1,500rpm – top row) and high (3,000rpm – bottom row) engine speed. Injection at 270°CA at 80bar for (a). SCV open (no swirl) and (b). SCV closed (high swirl).	245

## *Acknowledgements*

Firstly, I would like to thank Professor C. Arcoumanis as my supervisor, for his continuous professional and human support during the time towards completion of my PhD. Furthermore I am very grateful that he not only found the funding and provided the freedom, but also supported many opportunities for me to pursue my research work. Of course these opportunities would have never been given to me without my professors in Aristotle University of Thessaloniki, Prof. Z. Samaras and Prof. N. Kyriakis, who encouraged me to join Prof. C. Arcoumanis research group, as one of the top research groups in Europe.

I would like also to thank Dr. J.M. Nouri who is my second supervisor and supported me along the way in all possible ways, but especially with his tremendous knowledge on PDA measurements, and in experiments in general, a part of which he managed to pass on to me. Jamshid thank you very much for all the motivation, courage and knowledge you have given me during all these years.

In addition, I would like to thank Dr. M. Gavaises for his valuable ideas and suggestions; his continuous pressing for more “accurate” measurements made me explore and learn new, very useful, experimental techniques. Moreover, I thank Dr. R.D. Lockett, Dr. Y. Yan and Dr. K.S. Jeong for their useful theoretical and practical support in various stages of this work.

A special thank you goes to Mr. J. Ford and Mr. T. Flemming for their technical support. Many parts of this work would have been impossible without the help of these two wizards of electronics and machining, respectively. In addition, I thank Mr. Gunawardana, Mr. J. Kenny and Mr. I. Wright for their technical and administrative support.

A very big and warm thank you goes to my friends and colleagues in the City University research group and London, in general; Rudi, Simo, Elias, Talal, Dia, Manos, Dimitris, Maria, Kenji, Nick, Kevin, Diego, Andrea, Luca, Ashvin, Hamid, Kibo, Sara, Essam, Penny, Sia, Vasia, Matina and Christos thank you for being around and for helping me in various ways!

Additionally, I would like to acknowledge the financial support of the Yamaha Motor Corporation Japan. All the employees of YMC responsible for the DI project made true all our requests in terms of instrumentation and component support. I express my gratitude to Yamashita-san, Motoyama-san, Kometani-san and all the other members of the DI project in Iwata! Furthermore, I would like to acknowledge BMW for their financial support in the first stages of this work.

Last, but not least, I would like to thank my family and all my friends in Greece who managed to deal with my crazy behaviour for all these years! Υπόσχομαι να είμαι ήρεμος από εδώ και στο εξής!

## *Declaration*

I hereby declare that the presented work in this thesis is my own or was developed in a joint effort with other members of the research group as it is stated and referenced in the text accordingly!

I grant powers of discretion to the University Librarian to allow this thesis to be copied in whole or in part without further reference to me. This permission covers only single copies made for study purposes, subject to normal conditions of acknowledgement.

London, \_\_\_\_\_

\_\_\_\_\_  
(Nicholas Mitroglou)

## *Abstract*

High-pressure multi-hole nozzles, carrying a Diesel-derived technology, are believed to be promising Fuel Injection Equipment (FIE) for Direct-Injection (DI) Spark-Ignition (SI) gasoline engines. Having explored thoroughly swirl pressure atomisers and their spray behaviour, multi-hole nozzles represent the second-generation injectors. Thus, complete investigation of multi-hole nozzle flow, spray characteristics and their engine performance is a vital part of development of future DI gasoline engines. The internal nozzle flow of an enlarged transparent multi-hole injector was investigated for different flow rates and needle lifts under steady state flow conditions. High-resolution CCD camera and high speed digital video systems were employed to visualize the nozzle flow patterns and cavitation development. The images identified the onset of cavitation in multi-hole gasoline nozzles and revealed the transition from pre-film to film stage cavitation. Cavitation strings were also visualized inside the injection hole that could extend to the needle face. However, these structures are highly unstable and directly affected by needle lift and cavitation number, although it appeared to be independent of the  $Re$ , in a behaviour similar to that of multi-hole diesel injectors. The sprays from various high-pressure multi-hole nozzle designs injected into a high-pressure/temperature constant-volume chamber have been visualised and quantified in terms of droplet velocity and diameter with a two-component phase-Doppler Anemometry (PDA) system at injection pressures up to 200bar and chamber pressures varying from atmospheric to 12bar. The overall spray angles relative to the axis of the injector were found to be almost independent of injection and chamber pressure, a significant advantage relative to swirl pressure atomisers. Within the measured range, the effect of injection pressure on droplet size was rather small while the increase in chamber pressure from atmospheric to 12bar resulted in much smaller droplet velocities, by up to fourfold, and larger droplet sizes by up to 40%. The effect of chamber temperature on multi-hole sprays confirmed the expected trends that dictate smaller droplet size distributions as temperature rises from 50 to 90 and 120°C. Additionally, multiple-injection proved to have similar dependencies to the single injection with certain operating limits. Laser-induced fluorescence has been mainly used to characterise the two-dimensional fuel vapour concentration inside the cylinder of a multi-valve twin-spark ignition engine equipped with high-pressure multi-hole injectors. The effects of injection timing, in-cylinder charge motion and injector tip layout have been quantified. The flexibility in nozzle design of the multi-hole injectors has proven to be a powerful tool in terms of matching overall spray cone angle and number of holes to specific engine configurations. Injection timing was found to control spray impingement on the piston and cylinder wall, thus contributing to quick and efficient fuel evaporation. Multiple-injection performed well under certain operating conditions and proved to be a powerful tool in the hands of engine manufacturers. It was confirmed that in-cylinder charge motion plays a major role in engine's stable operation by assisting in the transportation of the air-fuel mixture towards the ignition locations (i.e. spark-plugs) in the way of a uniformly distributed charge or by preserving stratification of the charge depending on operating mode of the engine.

## *Nomenclature*

### Abbreviations

<b>1-D</b>	One dimensional
<b>2-D</b>	Two dimensional
<b>3-D</b>	Three dimensional
<b>ASOI</b>	After Start of Injection
<b>AFR</b>	Air/fuel ratio
<b>ACEA</b>	Association des Constructeurs Europeens d'Automobiles
<b>AMD</b>	Arithmetic mean diameter
<b>AITDC</b>	After induction top-dead-centre
<b>BSFC</b>	Break specific fuel consumption
<b>BMEP</b>	Break mean effective pressure
<b>BTDC</b>	Before top-dead-centre
<b>BDC</b>	Bottom-dead-centre
<b>CCD</b>	Charge cooling device
<b>CFD</b>	Computational fluid dynamics
<b>CI</b>	Compression-ignition
<b>CIDI</b>	Compression-ignition direct-injection
<b>CA</b>	Crank angle
<b>CO/CO<sub>2</sub></b>	Carbon monoxide/dioxide
<b>CH<sub>4</sub></b>	Methane
<b>COV</b>	Coefficient of variance
<b>CN</b>	Cavitation Number
<b>DI</b>	Direct-injection
<b>DISI</b>	Direct-injection spark-ignition
<b>DAQ</b>	Data acquisition
<b>DT</b>	Dwell time
<b>EU</b>	European Union
<b>EEA</b>	European Environment Agency
<b>EGR</b>	Exhaust gas recirculation
<b>ECU</b>	Electronic control unit
<b>EOI</b>	End of injection
<b>EVC</b>	Exhaust valve closing time
<b>EVO</b>	Exhaust valve opening time
<b>FIE</b>	Fuel injection equipment
<b>GHG</b>	Green-house gases
<b>uHC</b>	Unburned Hydrocarbons
<b>HFC</b>	Hydrofluorcarbons
<b>HSDV</b>	High-speed digital video
<b>IVC</b>	Inlet valve closing
<b>IVO</b>	Inlet valve opening
<b>LDA</b>	Laser Doppler Anemometry
<b>LDV</b>	Laser Doppler Velocimetry
<b>LIF</b>	Laser induced fluorescence

<b>LIEF</b>	Laser induced Exciplex fluorescence
<b>LSD</b>	Laser sheet drop-sizing
<b>l-h-s</b>	Left-hand-side
<b>NO<sub>x</sub></b>	Nitrogen oxides
<b>N<sub>2</sub>O</b>	Nitrous oxide
<b>PFI</b>	Port-fuel injection
<b>PDA</b>	Phase Doppler Anemometry
<b>pdf</b>	Probability density function
<b>PM</b>	Particulate Matter
<b>PFC</b>	Perfluorocarbons
<b>PIV</b>	Particle Image Velocimetry
<b>r-h-s</b>	Right-hand-side
<b>RMS</b>	Root mean square
<b>RPM</b>	Revolutions per minute
<b>SMD</b>	Sauter mean diameter
<b>SI</b>	Spark-ignition
<b>SOI</b>	Start of injection
<b>SCV</b>	Swirl control valve
<b>TWC</b>	Three-way catalyst
<b>TCCS</b>	Texaco controlled combustion system
<b>TDC</b>	Top-dead-centre
<b>TTL</b>	Transistor-Transistor Logic
<b>VCO</b>	Valve Covering Orifice
<b>YAG</b>	Yttrium Aluminium Garnet

### Roman Symbols

<b>D</b>	Injection hole diameter / Droplet diameter
<b>h</b>	Plank's constant
<b>I</b>	Light intensity
<b>L</b>	Injection hole length
<b>m</b>	Mass
<b>n</b>	Polytropic coefficient
<b>p</b>	Pressure
<b>p<sub>back</sub>, p<sub>b</sub></b>	Chamber pressure
<b>p<sub>inj</sub></b>	Injection pressure
<b>Re</b>	Reynolds number
<b>T</b>	Temperature
<b>U, V</b>	Velocity
<b>M</b>	Molecular weight
<b>R</b>	Universal gas constant
<b>r</b>	Radius of curvature at injection hole inlet

**Greek Symbols**

$\lambda$	Lamda ratio
$\phi$	Equivalence ratio
$\rho$	Density

# *Chapter 1*

## *Introduction*

Internal combustion engines have been the dominant powerplant for automobiles for over a century. Since the early 20<sup>th</sup> century, compression and spark ignition engines using oil-based fuels have seen tremendous technological advances. Advantages and disadvantages of both combustion concepts have set the operating field of diesel and gasoline engines. Currently, the continuously increasing number of newly registered, fuel-powered, automobiles has triggered the public concern for environmental pollution. Diesel-powered vehicles have been continuously characterised as environmental friendly solutions, due to their lower exhaust gas emissions compared to their gasoline-fuelled counterparts. As a result, diesel market share rises continuously as it starts occupying a traditionally gasoline engine dominant field; vehicles for personal use. Engine manufacturers worldwide have already started exploring ways of reducing exhaust gas emissions of gasoline engines. This has led to the re-examination of the spark ignition engine as a trustworthy solution for personal use vehicles.

### **1.1 HISTORY OF THE SPARK IGNITION ENGINE**

*Paris, 1867: Against all odds, the prototype engine of Nicolaus August Otto and Eugen Langen is awarded the gold metal in the Paris World's Fair, as the first and most efficient gas engine ever produced (Figure 1.1).* Nevertheless, the first serious attempt, as far as the invention of the internal combustion engine is concerned, is dated back to 1858 by the Belgian-born engineer Jean Joseph Etienne Lenoir, who invented and patented (1860) a double-acting electric spark-ignition internal combustion engine fuelled by coal gas. In 1863 Lenoir improved his design by using petroleum and a primitive carburettor. In the meantime, specifically in 1862, a French civil engineer named Alphonse Beau de Rochas patented, but never built, a four-stroke engine! It was these inventions that inspired a German salesman, Nicolaus August Otto, to start experiments for the invention of a gas engine; he and his

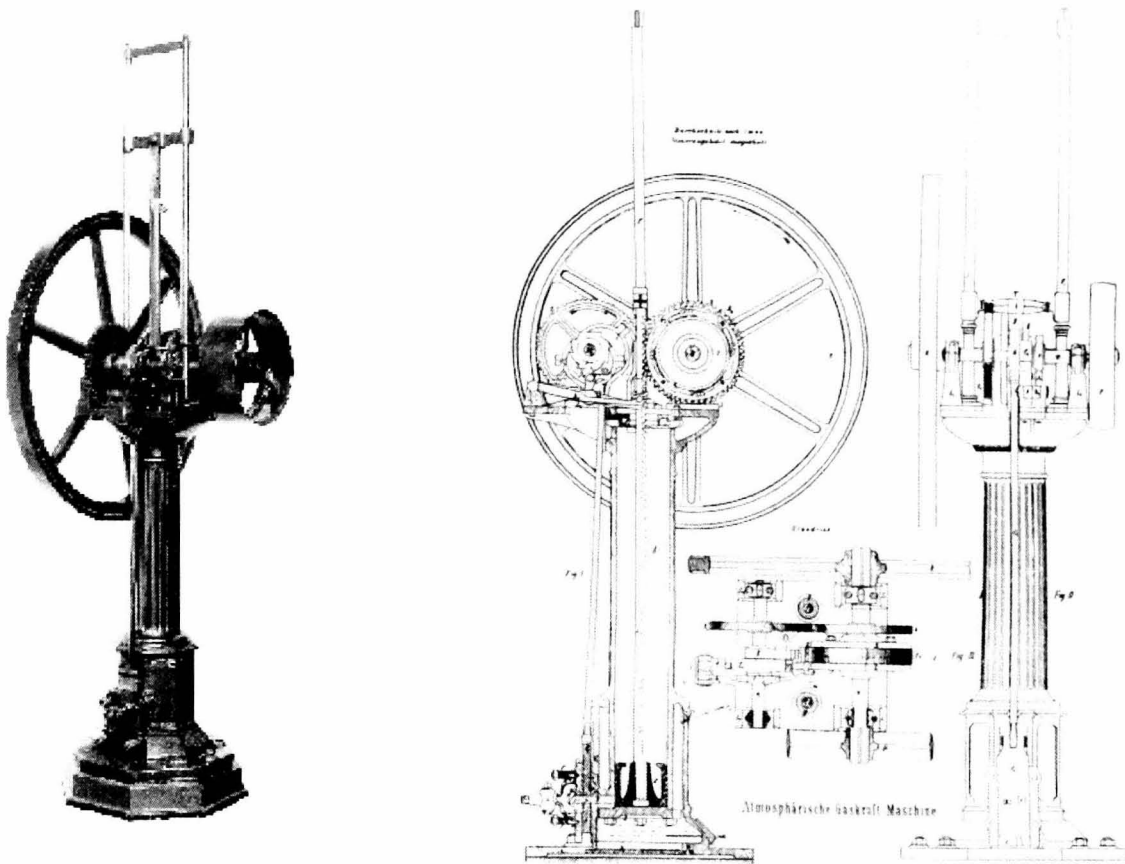


**Figure 1.1: Award winning atmospheric gas engine (about 1866/7)**

counterpart, Eugen Langen, a German industrialist, patented a two-stroke engine that run on gas in 1861. After further improving this engine (Figure 1.1), they won the gold medal in Paris World Fair in 1867. However, they had a strong competitor, Etienne Lenoir, whose design completely overshadowed the Otto-Langen engine. After tirelessly running tests though, the German duo was awarded the gold medal for the most efficient gas engine ever produced. Following their success, Otto continued working for the development of his prototype. His efforts were finally rewarded when in May 1876 he built, and later patented, the first four-stroke piston cycle internal combustion engine. This was the first practical alternative to the steam engine and since then it is called the “Otto Cycle Engine” (Figure 1.2).

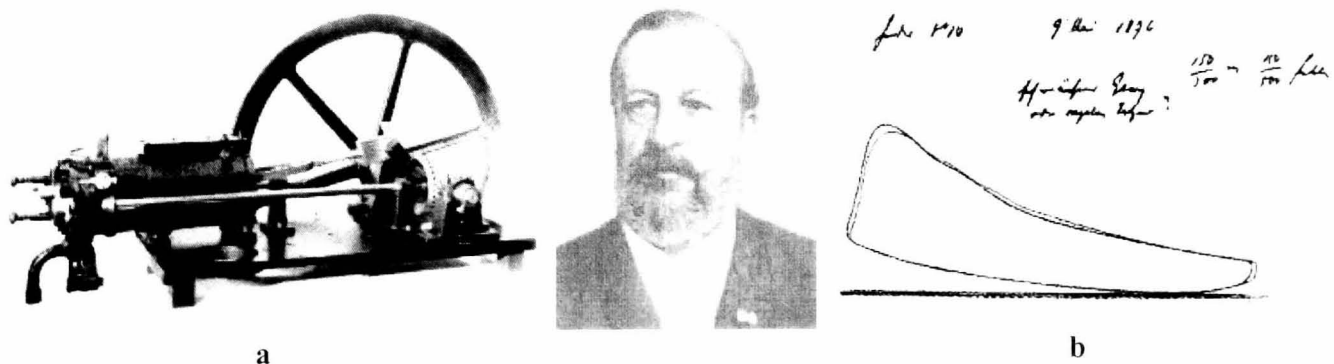


**Figure 1.2: Nicolaus August Otto with a. his first four-stroke cycle engine (1876), and b. the Otto working diagram (9<sup>th</sup> May, 1876).**

Otto continued to develop his four-stroke engine after 1876 and he considered his work finished after his invention of the first magneto-ignition system for low voltage ignition in 1884. In the ten following years more than 30,000 engines of this type were sold. He died in January 1891, but his contribution to society was especially important because it was his four-stroke design that was universally adopted for liquid fuelled automobiles. Although Otto never thought of placing his engine in a vehicle featuring more than two wheels, two other German inventors of his time, Karl Benz and Gottlieb Daimler, shared Otto's vision and, by taking one step further the Otto cycle engine, have conceived the start of the automobile industry as it is known today. In 1885, Gottlieb Daimler and Wilhelm Maybach improved Otto's design and they patented what is generally recognised as the precursor of the modern gas engine. It was a small, lightweight engine featuring a vertical cylinder and the first ever gasoline-injected carburettor. Despite this record-breaking patent, it was a competitor of Gottlieb Daimler, Karl Benz, who patented the first three-wheeler gas-fuelled car in early 1886. Karl Benz, therefore, was the first inventor to integrate an internal combustion engine with a chassis, designing both together. A few months later, in March of the same year, Daimler converted a stagecoach in a way to hold his engine as an answer to Benz's progress. Daimler's conversion entitles him to be considered the father of the world's first four-wheeled automobile. A few years later, in 1889, Gottlieb Daimler and his design engineer, Wilhelm Maybach, were the first to build a four-wheel automobile from scratch, without adapting other purpose vehicles. Twelve years later, in 1901, Maybach designed the first Mercedes automobile for the Daimler Automobile Company (Daimler Motoren Gesellschaft), which remains more than 100 years later one of the most prestigious automakers worldwide.

Since the early days of the twentieth century, and the first Mercedes automobile, the Otto cycle engine has seen record-breaking technological improvements due mainly to the continuously increasing public interest in this specific method of transport. Starting from the first V-shaped engine of Daimler-Maybach, more cylinders were added later to the vertical single-cylinder engine. Having four cylinders in a row as the classic in-line approach, oversized engines featuring 6 and 8 cylinders appeared in a quest for more power output. Sharing the same drive, numerous manufacturers improved the idea of the first gasoline-injected carburettor by introducing sophisticated mechanical innovations for monitoring the engine's airflow and

increasing the cross-sectional flow area using double, or even more, throttle valves for the same engine. The appearance of the small-sized turbochargers and their coupling with internal combustion engines in the late 70's and early 80's, introduced the need for more accurate fuel/air monitoring and metering devices. These devices were supplied by the electronics sector and they simply moved the fully mechanically-controlled engine, one step further towards the higher-accuracy electronic control mechanisms. This new technology allowed the introduction of the first fuel injection systems, replacing the old-fashioned carburettor with accurate and fast acting fuel injectors.

Throughout all these years, the main concern of engine manufacturers has been how to increase the power output of a vehicle's powerplant. This trend lasted almost a century. In the late years of the twentieth century the majority of the automobile industry shifted its direction and started considering ways to improve the relatively low efficiency of gasoline engines, compared to Diesel engines. In many cases some of the known advantages of the gasoline engine had to be sacrificed for the sake of lower fuel consumption and exhaust emissions. The reason for this change in philosophy lies in the perceived uncontrollable use of technological developments, which directly affect the environment that we live in. In other words, the consequences of the industrial revolution and the advances that it brought to the service of people have poisoned the earth's atmosphere to a degree that is now directly compromising human health and threatens earth's ecobalance.

## **1.2 CLIMATE CHANGE AND ENGINES**

### **1.2.1 Air pollution**

An internal combustion engine converts fuel's chemical energy in to mechanical energy, according to the Diesel or Otto operating cycle, through combustion of an air/fuel mixture. Based on the principles of the Otto cycle, conventional port-injected, spark-ignited (SI), gasoline-fuelled engines require extensive throttling and a certain air/fuel ratio (AFR) in order to achieve stable and efficient combustion of the air/fuel mixture. The current development status of these types of engine can offer a maximum fuel efficiency of 40%. The incomplete and inefficient combustion directly leads to undesirable by-products. Exhaust gases of imperfect combustion of gasoline,

such as carbon monoxide (CO), oxides of nitrogen (NO<sub>x</sub>) and unburned hydrocarbons (uHC), are classified as pollutants. These gaseous pollutants reduce the air quality and exhibit negative links to human health. In particular, carbon monoxide (CO) reduces the blood's oxygen carrying capacity, which in turn reduces the availability of oxygen to key organs of the human body. Therefore, extreme levels of exposure could be fatal. At lower concentrations CO may pose a health risk, especially to those suffering from heart diseases. The second pollutant, nitrogen oxides (NO<sub>x</sub>), represents the sum of nitrogen monoxide (NO) and nitrogen dioxide (NO<sub>2</sub>). The first component is the dominant between the two in the exhaust gases. Once released, it reacts in the atmosphere to form additional nitrogen dioxide (NO<sub>2</sub>), which can have adverse effects on health, particularly among people with respiratory illness. High levels of exposure have been linked to hospital admissions due to respiratory problems, while long-term exposure may affect lung functions and increase the response to allergens in sensitive people. NO<sub>x</sub> also contributes to smog formation, and acid rain, while it can damage vegetation and contributes to ground level ozone formation. Unburned hydrocarbons (uHC) also participate in the ozone formation mechanism at ground levels and can increase the risk of damaging the human respiratory system. Additionally, some uHC with aromatic content are carcinogenic.

In an attempt to improve the European air quality, members of the European Union have developed measures and certain actions that lead to reduced emissions from the above pollutants. The first decisive step happened in the late 1980's in the form of the EURO legislation imposed by the European Union to all its member states. In particular, the European Environment Agency established a way of controlling the emissions of newly produced vehicles, by setting the maximum legal values of the three gaseous pollutants as they are produced from the car's gasoline engine when it follows a well-defined driving test cycle (Figure 1.3). The maximum acceptable values are expressed in g/km, and are given in Table 1-1.

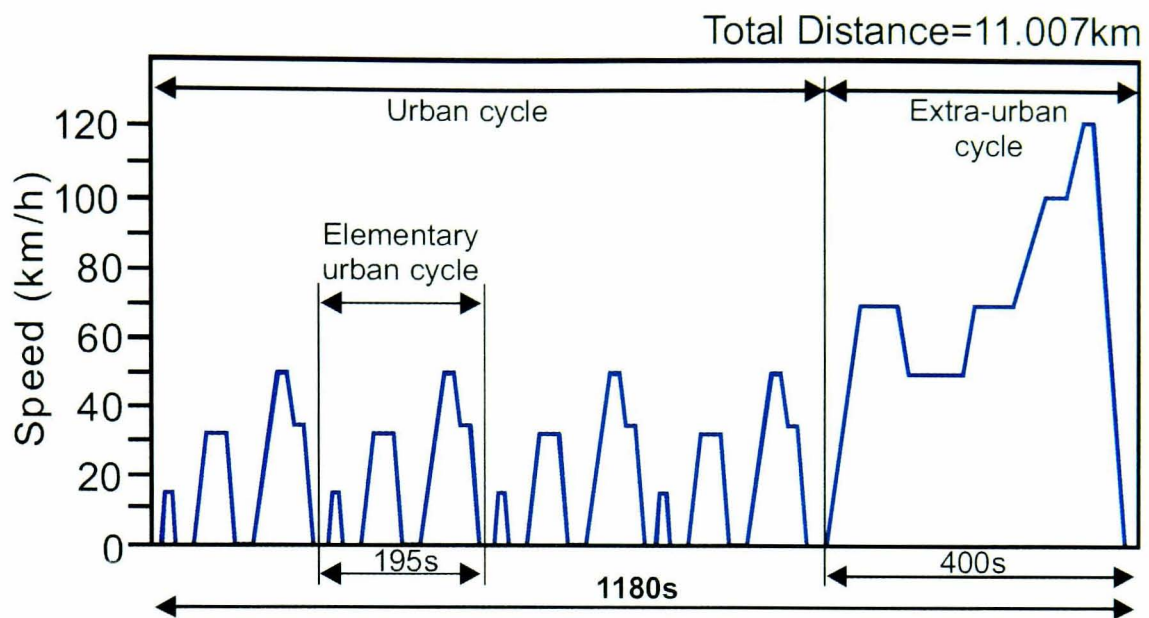


Figure 1.3: European Driving Cycle pattern for emission tests.

	No. of seats	Fuel	Limit Values (g/km)				Implementation Date
			CO	HC	NO <sub>x</sub>	HC+NO <sub>x</sub>	
Euro I	up to 9	petrol	2.72	-	-	0.97	1993
Euro II	up to 9	petrol	2.2	-	-	0.7	1996
Euro III	up to 9	petrol	2.3	0.2	0.15	-	2000
Euro IV	up to 9	petrol	1	0.1	0.08	-	2005

Table 1-1: European Union emission standards for newly registered vehicles.

The intention of the EU legislation can be clearly seen in the above table. From Euro I standard through Euro IV the aim is to reduce gradually the production of all three major pollutants emitted from gasoline engines. The automotive industry responded to this challenge by introducing new technologies in internal combustion engine control. Based on fundamental chemistry principles, the composition of combustion products of an air/gasoline mixture strongly depends on the amount of air present in the combustion chamber, relative to the fuel quantity (equivalence ratio). However, the Otto operating cycle dictates throttled engine operation, therefore there is not excess air present in the engine's combustion chamber. On the contrary, it requires precise control of the inducted air for combustion to be as close to complete as possible; stoichiometric engine combustion thus ensures misfire-free operation. Under homogeneous mixture conditions, pollutants emissions vary according to Figure 1.4a. For this reason, the automotive industry developed control mechanisms to monitor and maintain the air/fuel ratio (AFR) during engine operation at the desired value that provides exhaust gases of known composition. This task has successfully been carried out since the 70's by an oxygen sensor installed in the exhaust manifold (Figure 1.4b). At the same time, an exhaust after-treatment system was installed downstream of the

oxygen sensor, in the exhaust pipe. This was a ceramic monolith soaked in catalytic substances that enhanced further chemical reactions of the three major pollutants and ensured their successful transformation into carbon dioxide ( $\text{CO}_2$ ), water ( $\text{H}_2\text{O}$ ) and nitrogen ( $\text{N}_2$ ). This device is known as a Three-Way Catalytic converter (TWC) and it first appeared in production vehicles in the early years of 1990. The results of these technological improvements in exhaust-gas after-treatment are extremely satisfying and all production cars have been equipped with the above-mentioned “clean” system ever since.

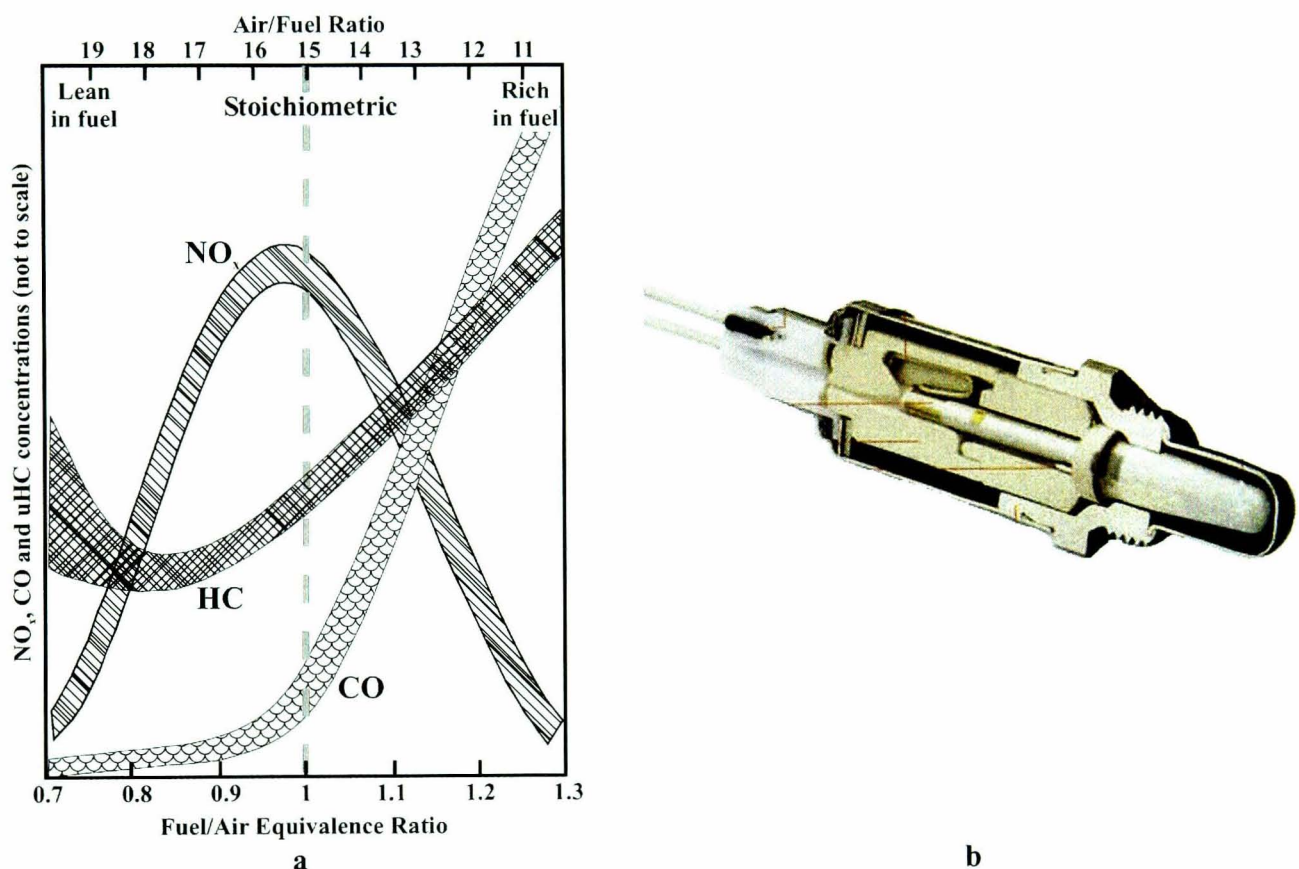
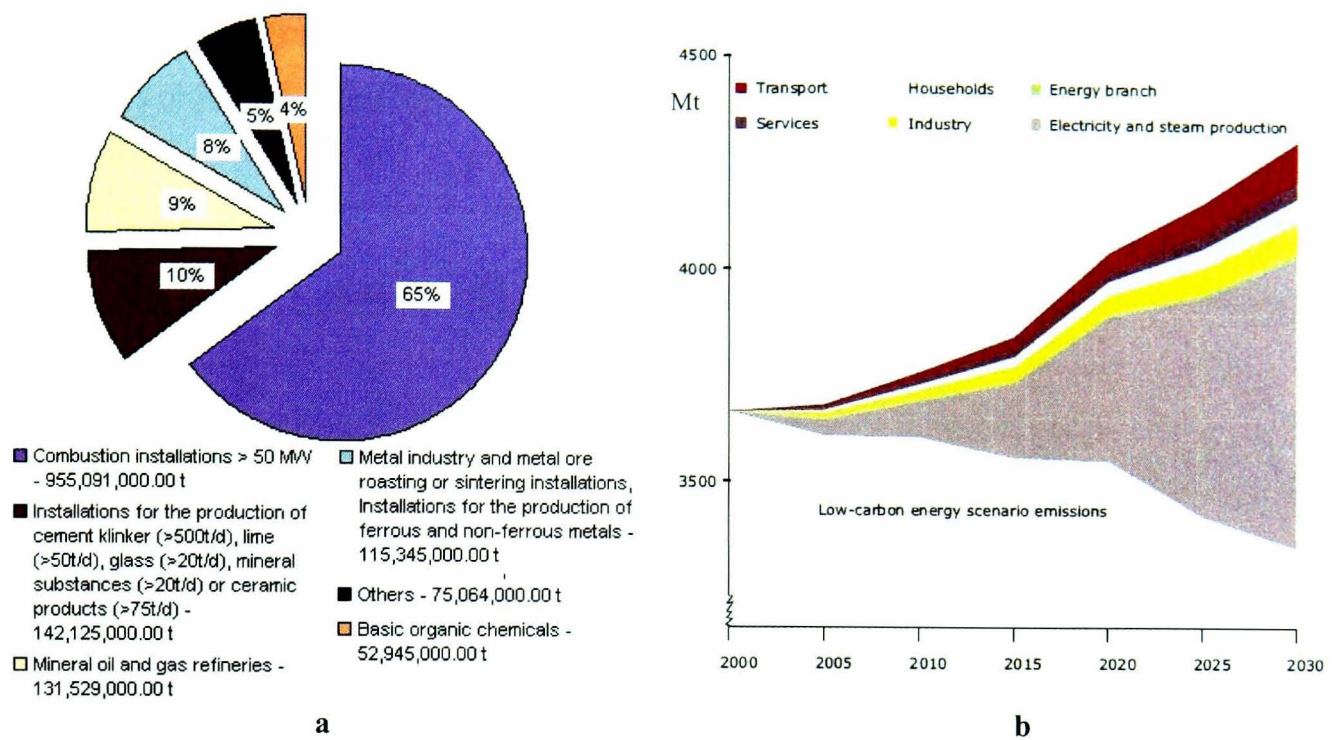


Figure 1.4: (a). CO, uHC and  $\text{NO}_x$  concentrations' dependence on air/fuel mixture quality for fuel gasoline and (b). Cut-out of an oxygen sensor (lambda sensor).

### 1.2.2 Cars and carbon dioxide ( $\text{CO}_2$ )

Following this successful reduction in pollutants emissions from internal combustion engines, and combustion processes in general, air quality is believed to be better than a decade ago and healthier for humans. Despite this fact, in the past hundred years, the sea level has risen, at least partially as a result of the warming of seawater and the melting of glaciers. The coverage of the earth's surface with ice and snow has shrunk and precipitation patterns have changed. Recently, central and northern Europe received more rain than in the past. In contrast, south and southeastern Europe has become drier. All these facts are closely linked to the observed increase in mean earth

temperature. Globally, the temperature increase over the past hundred years was about 1°C. Mean temperature is likely to increase by 1.4-5.8°C between 1990 and 2100 [1]. This phenomenon is called “climate change”, often referred to as “global warming”, and it is considered to be one of the greatest environmental threats facing the world today. Climate change impacts could be catastrophic for human life and for our planet’s future. The principle behind this environmental threat is very similar to the greenhouse operation; there is a gaseous layer in the atmosphere, which blocks the sun’s radiation of escaping back to the stratosphere after being reflected from the earth’s surface. As a result, it stays trapped in the planet’s inner atmosphere and “contributes” to this rise in mean global temperature. These gases that impede the sun’s radiation from escaping, are called greenhouse gases (GHGs). Human activities have increased the concentration of these gases in the atmosphere and there is new stronger evidence that most of the observed warming over the past fifty years is attributed to emissions of GHGs from these activities, in particular to emissions of carbon dioxide (CO<sub>2</sub>). This is by far the most important greenhouse gas. It is the direct product of combustion and of the highly industrialised European economic system, as well as the economies of other industrialised countries, as our industrial activities rely on a carbon-intensive energy system. Substantial amounts of fossil fuels are burned, both in power and heat production and in sectors using energy, therefore “contributing” to CO<sub>2</sub> production. Other important direct anthropogenic GHGs include methane (CH<sub>4</sub>) from agriculture and waste management, nitrous oxide (N<sub>2</sub>O) from agriculture and industry and industrial halogenated gases. Tropospheric ozone is also a greenhouse gas; it is formed in the atmosphere from carbon monoxide, nitrogen oxides and non-methane volatile organic compounds emitted by human activity (industry, road transport, households, energy industries). As a first step towards the ultimate objective of stabilising greenhouse gases concentrations, all major industrialised nations attended a World conference held in Kyoto, Japan in 1997. Most of the participants agreed and signed the Kyoto Protocol, which obliges the joining parties in adopting binding targets for emissions of six GHGs, including carbon dioxide (CO<sub>2</sub>), methane (CH<sub>4</sub>), nitrous oxide (N<sub>2</sub>O), hydrofluorcarbons (HFCs), perfluorcarbons (PFCs) and sulphur hexafluoride. The Kyoto Protocol was formally inacted on 16<sup>th</sup> of February 2005.



**Figure 1.5: (a). Carbon dioxide (CO<sub>2</sub>) emissions in the EU-15 (Source, EEA 2000). (b). Energy related CO<sub>2</sub> emissions in the EU-25, projected in Mt till the year of 2030 (Source, EEA 2005).**

Figure 1.5a shows the current status of CO<sub>2</sub> emissions in fifteen EU member countries. It is clear that the major sources of CO<sub>2</sub> are combustion installations. Figure 1.5b projects only the energy related CO<sub>2</sub> emissions in the EU of 25 member states for the next 25 years. In this graph, carbon dioxide emissions from transport appear to be the second biggest source, of the complete energy related emissions, after electricity and steam production. Based on the data collected from the European Environment Agency, carbon dioxide from passenger cars accounts for half of all CO<sub>2</sub> emissions in the transport sector, and almost 12% of total CO<sub>2</sub> emissions in the EU-25. According to the Kyoto Protocol, a global reduction of 8% in the emissions of CO<sub>2</sub> has been agreed to, relative to 1990 levels by 2008-2012 the latest. Following this directive, the European Union plans to adopt a Low-Carbon energy system in its territory that will be followed from all its member states. This will inevitably affect internal combustion engines and cars' power units in general. As an example, the average CO<sub>2</sub> emissions from current passenger car fleets in Europe are 186g/km (amount of CO<sub>2</sub> emitted during the New European Driving Cycle, Figure 1.3). The European Union's target is to reduce this value to 120g/km by 2008-2010 the latest. Furthermore, the EU in conjunction with ACEA (Association des Constructeurs Europeens d'Automobiles – European Automobile Manufacturers) has set the target of 140g/km CO<sub>2</sub> by 2008; a number that will be reached by the automotive industry using technological

developments, being the intermediate milestone towards the 2010 (a two year delay is possible) objective of 120g/km CO<sub>2</sub>.

ACEA	CO <sub>2</sub> (g/km)								Change 95-02 (%)
	1995	1996	1997	1998	1999	2000	2001	2002	
Gasoline	188	186	183	182	180	177	172	171	-9%
Diesel	176	174	172	167	161	159	153	152	-13.6%
<b>All fuels</b>	<b>185</b>	<b>183</b>	<b>180</b>	<b>178</b>	<b>174</b>	<b>169</b>	<b>165</b>	<b>163</b>	<b>-12.1%</b>

**Table 1-2: Average specific CO<sub>2</sub> emissions of new passenger cars per fuel type for ACEA and the European Union (Source ACEA, EU).**

ACEA	Percentage of newly registered cars (%)								Change 95-02 (%)
	1995	1996	1997	1998	1999	2000	2001	2002	
Gasoline	73.4	72.9	73.1	70.3	65.8	60.9	52.8	56.3	-17.1
Diesel	24.0	24.3	24.3	27.0	31.0	35.8	39.4	43.6	19.6

**Table 1-3: Trends in composition of new cars registered on the market for ACEA and the EU (Source ACEA,EU).**

A quick overview of Tables 1-2 and 1-3 illustrates immediately the trend in internal combustion engines, and fuel preferences, in general, in the EU. For vehicles manufactured by the European automotive companies (ACEA), the emitted CO<sub>2</sub> has decreased since 1995, a decrease of 12.1% until 2002. A very interesting trend is also observed throughout these years, specifically since 1995, and it concerns the market share of diesel-powered vehicles versus their gasoline counterparts. There is a significant increase of 19.6% as far as newly registered diesel-powered vehicles are concerned. In the year 2002 gasoline-fuelled engines usage has decreased to 56.3%, vis-à-vis the rise of 43.6% of the diesel engines. The reason behind this trend lies in the continuously developing diesel engine technology, which has transformed the already robust diesel-powered vehicle into a cleaner and more competitive means of transport. For the European automotive industry it is a great challenge to manage and produce engines for passenger cars featuring low CO<sub>2</sub> emissions. As mentioned before, the traditional operating cycle of a gasoline engine requires a very strict and accurate control of the air/fuel ratio of the mixture to be burnt. This fact limits the bottom-line of CO<sub>2</sub> emissions unless there is a sudden change in combustion technology. Automotive industries are not alone in this race in reducing carbon dioxide emissions. There is relative legislation imposing changes in fuel quality. All petroleum companies are forced to improve fuel quality and therefore contribute to the increased expenses required for a low-carbon energy system.

Analysis of the European Environment Agency has shown that the transport sector will be one of the most difficult areas in which to reduce CO<sub>2</sub> emissions in the short to medium term. This is because of the rapid increase in passenger and freight demand projected over the next 25 years and the difficulty in replacing oil as the fuel on which the transport sector is almost totally dependent. The impact of these two factors is that the transport sector is the only one showing continuously growing CO<sub>2</sub> emissions over the next 25 years. However, in the medium to long term, there are a number of engine technologies and fuels that could substantially reduce carbon emissions from road transport. These include for engines:

- Improvements to internal combustion engines, including advanced fuel injection systems and downsizing;
  - Hybrid vehicles, which have an internal combustion engine used in combination with an electric motor;
  - Fuel cell vehicles, which have a dedicated electric motor;
- and for fuels:
- Hydrogen for fuel cells from one of a wide range of possible sources;
  - Biofuels, including alcohols made out of starch crops and diesel made from oilseeds as well as advanced fuels based on the gasification of biomass.

These new technologies and fuel alternatives feature certain advantages and disadvantages in regard to vehicle's emissions, speed and driveability, refuelling infrastructure and to the cost of motoring. Starting from the most radical ones, alternative fuels like hydrogen and biofuels would be the first to evaluate. Hydrogen-fueled vehicles promise reduced or eliminated tailpipe emissions. However, fuel-cycle emissions vary greatly according to production method. Speed and drivability of hydrogen-powered vehicles is mainly dependant on the engine capabilities and design. On the other hand, existing refuelling infrastructure does not fulfil the requirements for hydrogen storage. Therefore major new infrastructure is needed, and coupled with the probability of increased motoring costs of these vehicles, the timescale for widespread deployment is rather long and placed post the year 2030! The second alternative fuel examined is biofuels, which promises reduced tailpipe emissions. Its fuel-cycle shows reduced CO<sub>2</sub> emissions, but a probable increase in N<sub>2</sub>O and PM emissions. These engines do not show increased speed and driveability, compared to today's gasoline-fuelled ones, and may require increased motoring costs. Finally, the need for significant new refuelling infrastructure makes this solution seem

slightly better than hydrogen with a short to medium (2006-2030) adoption timescale. As far as engine technology is concerned, fuel cell cars seem very promising mainly because of virtually eliminated tailpipe emissions and improved driveability. However, the probability of major new refuelling infrastructure and the uncertain motoring costs, shift their introduction to the market for later than 2030. The last two, most attractive solutions, come from existing know-how in internal combustion engines and electronics. By using gasoline as the main fuel, refuelling infrastructure costs are immediately eliminated and changes in speed and driveability will not be radically different to how vehicles behave today. Additionally, technologically advanced internal combustion engines and hybrids promise reduced CO<sub>2</sub> and regulated pollutants emissions and lower fuel consumption, a fact that equalises the slight increase in motoring costs, and a short to immediate timescale for widespread deployment. In more detail, a hybrid vehicle features a dual-fuel power plant; it is equipped with a conventional port-fuel-injected (PFI) gasoline engine, which is mechanically linked to a second electric engine (motor), powered by a battery rack. Effectively, it is a bi-fuel vehicle, using mainly electric power stored in its batteries and gasoline when engine-loading conditions are increased. As a result, the overall fuel consumption is reduced significantly. Its gasoline-only counterparts are vehicles equipped with internal combustion engines featuring technologically advanced and highly sophisticated fuel-injection systems. Such engines are called “direct-injection (DI) gasoline engines” or “direct-injection spark-ignition (DISI) engines” and they could potentially demonstrate a reduction in fuel consumption of 20%, relative to conventional PFI engines.

### **1.3 DIRECT-INJECTION GASOLINE ENGINES**

In order to understand what the term “technologically advanced” internal combustion engine means, one must closely examine the target of this new technology that has always reduced fuel consumption with obvious benefits on the objective of reduced carbon dioxide (CO<sub>2</sub>) emissions. It is known, in the scientific community, that the fuel economy of the compression-ignition direct-injection (CIDI) diesel engine is superior to that of the port-fuel-injected (PFI) spark-ignition engine, mainly due to the use of a significantly higher compression ratio, coupled with unthrottled operation. Nevertheless the spark-ignited (SI) internal combustion engine still represents the

most flexible and cost effective solution for a mass-produced power train. Over the past two decades attempts have been made to develop an internal combustion engine for automotive applications that combines the best features of the SI and the diesel engines. The objective has been to combine the specific power of the gasoline engine with the efficiency of the diesel engine at part-load. Based on the diesel operating cycle, research has indicated that a promising candidate achieving this goal is a direct-injection, four-stroke, spark-ignition engine that does not throttle the inlet mixture to control the load. In this engine, a fuel spray plume is injected directly into the cylinder, generating a fuel/air mixture with an ignitable composition at the spark-gap at the time of ignition. In a similar manner to that of the diesel engine, the power output is controlled by varying the amount of fuel injected into the cylinder. The induction air is not significantly throttled, thus minimising the pumping losses of the cycle.

From a historical perspective, interest in these significant benefits has promoted a number of important investigations of the potential of direct-injection, spark-ignition (DISI) gasoline engines. Several detailed combustion strategies were proposed and implemented, including the Texaco Controlled Combustion System (TCCS), MAN-FM of Maschinenfabrik Augsburg-Nurnberg and the Ford programmed combustion system (PROCO). All these fuel economy oriented systems never reached series production, not because of their performance, but mainly due to technological problems in injection system design at those times. However, the first ever-produced car that featured a direct-injection gasoline engine is dated back to the mid-fifties (Figure 1.6). This car took advantage of the already developed direct-injection technology by BOSCH and BMW for aircraft engines in the 1930's. Using a mechanical fuel pump and BOSCH fuel-injectors placed on the engine block, the creator, clearly, did not look for fuel efficiency; on the contrary it was the fastest sports car of its times.

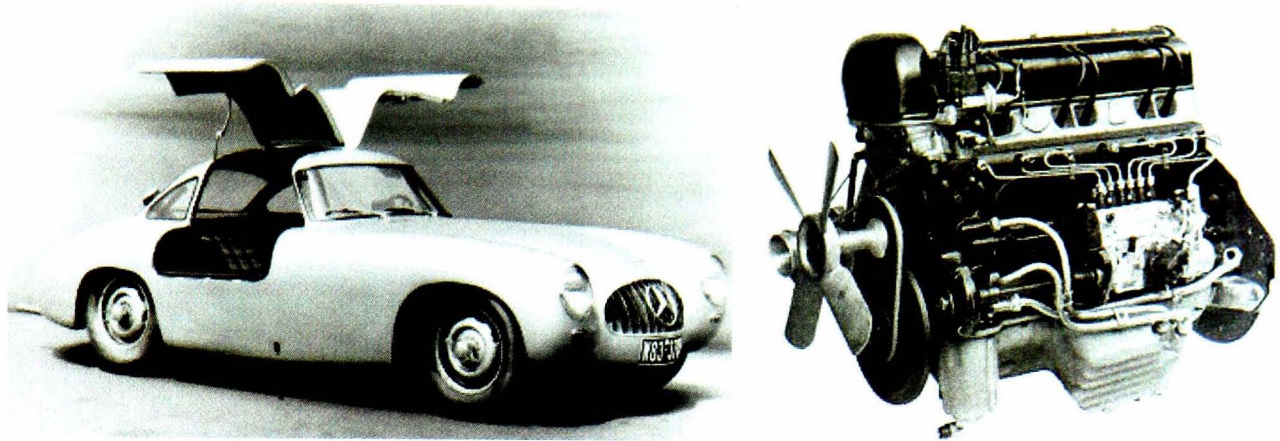


**Figure 1.6: Mercedes 300SL. The first vehicle equipped with a direct-injection gasoline engine.**

Featuring a six cylinder engine, it produced 215PS enabling the vehicle to reach a top-speed of 260km/h. As stated before, the objective of this engine was high power output, therefore its increased fuel consumption figures of 12-19ltr/100km was the main reason that led the officials to stop its production, three years after its first introduction in the market.

### 1.3.1 Direct-injection concepts

In an attempt to evaluate the key potential benefits that direct-injection technology could offer and the major differences, relative to conventional PFI technology, should be pointed out. As illustrated schematically in Figure 1.7, the major difference is the mixture preparation strategy. In the PFI approach, fuel is injected into the intake port of each cylinder and the majority of current automotive PFI engines utilises a closed-valve injection, a technique that enhances vaporisation of the injected fuel while the intake valve is closed. Although better atomisation results can be achieved, relative to open-valve injection, there is a time lag between the injection event and the final induction of the formed air/fuel mixture into the cylinder. The unavoidable fuel film that is created in the intake port walls causes a fuel delivery delay and introduces a certain metering error of the amount of fuel actually used in the next engine cycle. Under these conditions, light fuel enrichment is needed in order to ensure that the desired air/fuel ratio (AFR) is maintained throughout any operating conditions. All the aforementioned facts result in increased fuel consumption and subsequently in increased CO<sub>2</sub> emissions. Another obstacle to more fuel-efficient PFI engines is the throttling requirement for basic engine's load control. Thermodynamic losses associated to throttling are such, that the thermal efficiency degradation at low levels of the engine load will always limit final fuel consumption figures.

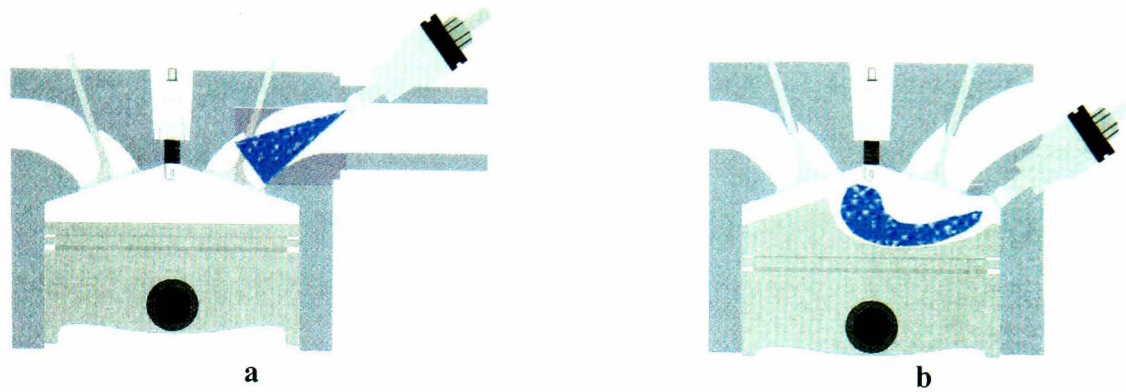


**Figure 1.7: (a). Conventional port-fuel-injection system and (b). direct-injection fuel system.**

On the other hand, direct-injection technology (Figure 1.7b) features injection of well-atomised fuel directly into the cylinder, resulting in a very accurate way of controlling the amount of fuel actually used in each engine cylinder, during any operating conditions. The basic concept is the formation of a stable, ignitable air/fuel mixture cloud around the vicinity of the spark plug. The size of the stoichiometric mixture cloud increases with increasing load, thus fuel consuming engine throttling is not necessary to control the load. In order to make full use of the potential for fuel economy improvement, a stratified operation of the engine should be possible at part engine loads. This is translated to high overall air/fuel ratios ( $AFR > 30$ ), which means less than half the amount of fuel required for stoichiometric operation ( $AFR \sim 15$ ) should be injected in the cylinder. The vaporised fuel should then form a stable and ignitable mixture cloud around the spark-plug vicinity, which means local AFR could be around 15, or slightly richer in fuel ( $13 > AFR > 16$ ), while the rest of the cylinder is occupied by air. As engine load increases, engine operation tends to become more homogeneous, as the mixture cloud occupies more volume in the cylinder, because of the increased fuel quantity injected. Ultimately, at full engine load, operation mode switches to stoichiometric homogeneous, where the appropriate amount of fuel for an  $AFR \sim 15$  is injected and the best possible air/fuel mixing is required for a homogeneous charge to cover the entire cylinder volume.

The most important theoretical advantage of the DI engine, based on previously presented operating modes, relative to its PFI counterpart, is improved fuel economy, which could potentially reach figures of 25%. This is also due to the improved volumetric efficiency that these engines exhibit. Injection of fuel into the cylinder while the intake valve is opened (early injection – injection during induction), results in lower charge temperatures, which effectively means lower in-cylinder pressures

and therefore more fresh air is dragged in, to charge the whole cylinder volume. Additionally, DI engines feature improved transient response, mainly due to more precise air/fuel ratio control, and extended exhaust gas recirculation (EGR) tolerance limit. Despite all these advantages, DI engine technology is not trouble-free. Certain advances of port-fuel-injected engines that are imposed by their operating principles should now be investigated and re-established for the case of direct-injection spark-ignition engines. Fuel atomisation times are too long due to the “absence” of warm intake port walls that injection into the cylinder commands. Fuel should be very well atomised, so that full vaporisation of the fuel is ensured, during the limited time between injection and ignition. Additionally, liquid fuel film found on cylinder walls increases liner wear considerably. The previously mentioned problems of a DI gasoline engine lead to a challenging attempt of creating a fuel injection system which is able of preparing and stabilising the mixture cloud by means of precisely controlled fuel injection and in-cylinder air motion. Developing such an injection system is a rather complicated task mainly because of its desired potential to create homogeneous, as well as, stratified mixture using the same components. In detail, homogeneity is achieved by early injection of the fuel during the induction stroke. The time given to the injected fuel to be fully atomised is adequate and in conjunction with an intake generated large-scale turbulence, complete homogenisation of the mixture can be accomplished. On the other hand, stratification is achieved by late injection of the fuel during compression stroke and just before ignition timing. Compared to stoichiometric and homogeneous engine operation, stratified mode requires complete injection and atomisation of the fuel within milliseconds. High injection pressures and accurate electronic control of the injector solenoid is more likely to secure this behaviour.

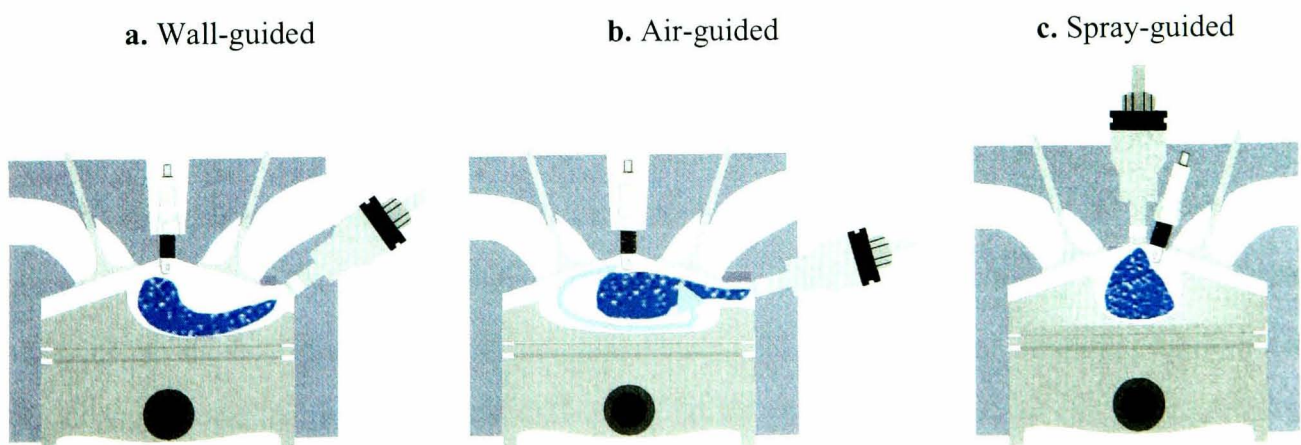


**Figure 1.8: Direct-injection combustion systems.**

Over the past years, numerous feasible design configurations for spark-ignition gasoline direct-injection engines have been developed. The distinction among the different concepts is the method used to guide the mixture cloud towards the spark-plug; thus, they are classified as wall-, air- or spray-guided combustion systems (Figure 1.8), employing central or side fuel injection depending on the charge motion used to stabilise the mixture plume created by the high-pressure injector [2, 3]. The first production DI engine of our times entered the market in 1990. It came from Mitsubishi Motors, the Japanese automobile company. The engine featured a wall-guided approach (Figure 1.8a) having the injector installed in the periphery of the cylinder, at a certain distance from the spark plug that was centrally located (wide-spacing concept) [4, 5]. In such systems the fuel spray is directed towards a specially designed piston-bowl cavity, which is responsible of transferring the fuel plume towards the spark-plug gap. The injector is commonly placed underneath the intake port and between the intake valves; position, which provides improved entrainment of intake air into the fuel spray and sufficient injector-tip cooling. By principal, systems using spray impingement on solid surfaces exhibit reduced sensitivity to spray-shape variations. On the other hand, fuel impingement forms a liquid fuel film, mainly on the piston crown, which potentially results in pool-burning, main source of unburned hydrocarbons (uHC). In an attempt to eliminate the undesirable effects of wall impingement, engine researchers presented the air-guided system (Figure 1.8b), a variation of the wide-spacing approach. This system utilises the in-cylinder charge motion to direct the fuel plume towards the spark-plug gap, eliminating any intentional fuel-wall interaction. In this way, all the aforementioned advantages of the wall-guided system are retained combined with improved uHC emissions, due to reduced wall wetting. On the contrary, strong airflow (swirl or tumble) requirements necessitate special combustion chamber designs and the introduction of port-airflow control mechanisms for swirl and tumble flow generation. Over the last five years, a new trend in DI combustion concepts has appeared. In order to minimise the use of complex piston cavity designs and intake flow control mechanisms, researchers started experimenting on closed-spacing approaches [6]. In Figure 1.8c, a schematic representation of the spray-guided system shows that positioning of the fuel injector very close to the spark plug almost eliminates wall wetting and complex in-cylinder flow requirements. More specifically, the spark plug is located at the outer edge of spray periphery and the fuel plume is close to the ignition source regardless of flow

conditions and combustion chamber geometry. The need for piston cavities and good airflow control is diminished, therefore, making the system more attractive due to reduced modifications relative to existing port-fuel-injected engine design. The quality of final mixture preparation relies mainly on the spray characteristics, such as atomisation level and velocity profiles. Additionally, there are increased requirements in spray structural stability, as unpredicted spatial variations of the spray structure could result in ignition fouling from impingement of fuel on the spark-plug electrodes. Another challenge facing the scientific community today is the rate of formation of injector deposits, which becomes a large-scale problem when the injector is placed very close to the ignition source. Finally, in modern engine design, the close-spacing approach could introduce packaging problems due to increased valve sizes in pent-roof shaped combustion chamber designs.

Since the first vehicle equipped with a direct-injection gasoline engine entered the market, many European and Japanese automotive manufacturers have adopted the wall-guided concept. However, the industry is now expecting the development of the air- and spray-guided systems or a combination of the two, as these systems show increased adoptability to existing, conventional engine designs using flat pistons. Lately, the previously well-defined boundaries, among the different combustion concepts in DI engine technology, have faded out. Systems like spray/wall-guided have appeared [7], featuring flat piston designs, central injection and twin-spark technologies, which look promising mainly due to minimum modification requirements. However, the major component of a fuel injection system that is responsible for preparing an ignitable fuel/air mixture cloud is the high-pressure injector. The progress in direct-injection gasoline engines depends entirely on new injector technologies and the appropriate exploitation of the in-cylinder airflow. The latter is of great importance and is effectively reflected on the selected injection timing for achieving homogeneous, as well as, stratified engine operation. In other words, the development of a successful combustion system depends upon the optimised design of the fuel injection system, the proper matching of the system components and the careful development of injection timing maps, for the best possible exploitation of the in-cylinder airflow and the advantages it offers towards effective transportation of the desired fuel vapour clouds to the spark-plug positions.

### 1.3.2 Fuel injection equipment (FIE)

In recent years significant progress has been made in the development of advanced computer controlled fuel injection systems that have enabled the expansion of research and development of the direct-injection, spark-ignition (DISI) engine. The vital components of a DISI fuel system layout can be seen in Figure 1.9. In detail, a low-pressure fuel pump is responsible for delivering fuel to the high-pressure pump, which in turn, provides pressurised fuel up to 200bar to the common rail. A pressure sensor and regulator are installed on the common rail and regulate the fuel injection pressure, according to any operating condition. Injection pressure and duration are controlled electronically from the electronic control unit (ECU), which is the main signal processor of an engine management system. Signals related to engine's operation, such as, intake air mass and temperature, throttle valve position, manifold pressure and oxygen ( $O_2$ ) concentration in the exhaust gases are all directed to the ECU. Following certain evaluation of these data, the ECU then drives various actuators, and controls fuel injection pressure and duration, exhaust gas recirculation (EGR) rate and spark plug ignition energy.

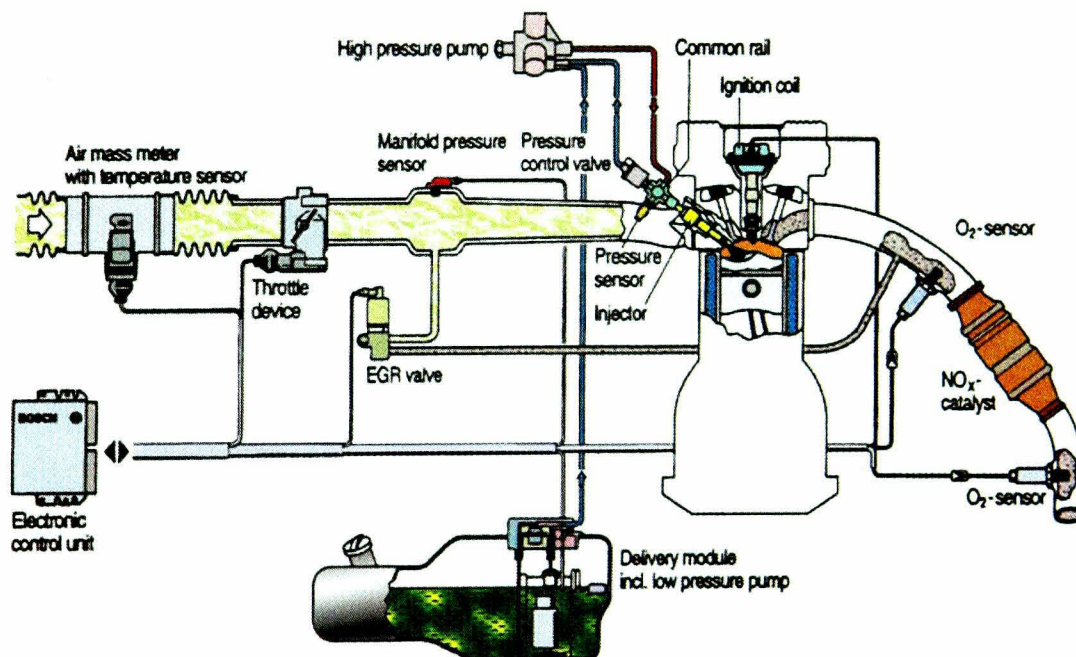


Figure 1.9: Typical direct-injection, spark-ignition engine system layout [8].

The task of the injection system is to provide a suitable mixture preparation for both, homogeneous and stratified, operating modes of a DI engine. In general, for efficient mixture preparation, the objective is a well-homogenised fine fuel spray with a fuel-jet geometry adapted to fast mixing of the spray with the required amount of air. A high-pressure injection system should provide the potential for late injection within the engine cycle with combustion chamber pressures up to 20bar or even more, in the

case of a turbocharged DISI engine, in order to enable unthrottled operation in the entire load range. Immediately it becomes obvious that a high-pressure injector should be able to provide a compact and repeatable spray structure. Additionally, injection pressures in excess of 50bar should be considered as a lower limit to Fuel Injection Equipment (FIE) candidates, in order to meet the requirements for stratified engine operation by late fuel injection during the compression stroke. The above-mentioned fact introduces the problem of spray-tip penetration velocity, which should be of the same value than the in-cylinder flow velocity, to enable a certain convective transport of mixture [9, 10]. In addition to that, a single high-pressure injector should be able to generate a well-atomised spray for stratification at engine part-load and a wide spread spray, to ensure good homogeneity at full engine loads. On the other hand, correct positioning of the high-pressure injector in the combustion chamber is critical for its thermal stability and efficiency. Also, good dynamic control of the injector is required for avoiding unwanted secondary fuel injection. The latter has main implications on an engine's stable operation and exhaust gas emissions. Immediately, it becomes obvious that there are certain critical requirements that a high-pressure gasoline injector should meet, in contrast to PFI applications specific equipment. Specifically, significantly enhanced atomisation levels are required for efficient mixing. Emphasis on spray penetration control is critical for avoiding fuel/wall interaction. There should also be careful internal nozzle design so that secondary fuel injections, created by needle bouncing, are avoided, and sufficient combustion sealing is provided. Additionally, such an injector should perform according to its standards under increased body and tip temperatures and it should present increased resistance to deposit formations. Ultimately, nozzle tip design should provide the flexibility in producing off-axis sprays in various inclined axes to meet different combustion system requirements.

The first FIE for DI engines derived from Diesel technology. Since then, important development steps and the evaluation of the aforementioned requirements have led to more gasoline-specific injection strategies. Currently, there is a wide range of injector types producing sprays with different spatial and temporal characteristics. They are classified into single- and dual-fluid (air-assisted) injectors, according to the media they inject, and to inward and outward opening, according to the opening direction of their pintle. Well-known inward opening, single-fluid injectors are the swirl pressure

atomiser, the multi-hole (BOSCH) and the close cap slit injector (DENSO-TOYOTA). As outward opening nozzles, one could find the relatively new piezo injector of SIEMENS and all the dual-fluid injectors (air-assisted), as the one of Orbital. The latter type of injector is a system very close to conventional port-fuel-injection requirements. It comprises of a fuel metering injector, very similar to low-pressure PFI injectors, and an air injector that delivers metered air/fuel mixture into the combustion chamber (Figure 1.10a). A pressurised air-stream is utilised to atomise the injected fuel, which is injected at relatively low pressures of 8-10bar, through shear action. Effectively, the difference of this system, compared to single-fluid injectors, is the separation of the fuel metering event and the direct injection event (Figure 1.10b). Fuel is injected first and after the pressurised air is introduced into the small injection chamber, the mixture is injected directly into the cylinder.

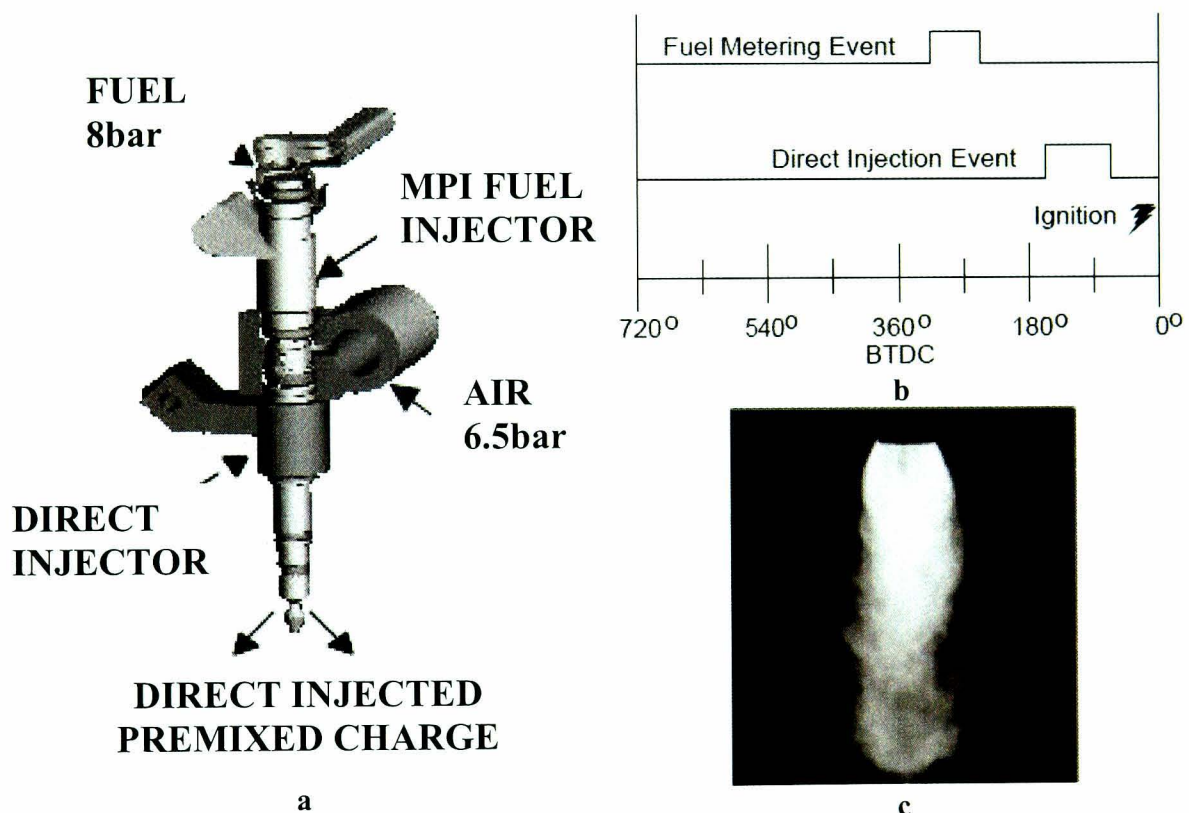


**Figure 1.10: (a). Schematic of the air-assisted, outward opening injector. (b). Separation of fuel metering and direct injection events (Injection Sequencing) and (c). Premixed charge spray under atmospheric conditions. [11]**

This mechanism allows the direct injection event to be tailored to the combustion characteristics rather than being limited from high-pressure injection systems requirements. Atomisation principals of air-assisted injection make this system ideal for spray-guided combustion concepts due to reduced spray penetration length (Figure 1.10c), reduced fuel concentration gradients under stratified operation and wider ignitable windows [11-13]. On the other hand, the poor pressure differential introduces limitations in injection timings, as the air pressure has to be higher than

that of the cylinder for injection to occur.

Single-fluid injectors, featuring an outward opening pintle, as the air-assisted injection system, have appeared recently in the market. Siemens Automotive has been strong supporter of this technology, and they have also released an outward opening injector (Figure 1.11), known as piezo injector, because of the high-class electromagnetic actuator (PIEZO) operating the pintle and promising extremely small needle opening and closing delays. These types of injectors produce hollow-cone sprays with the cone-angle mainly being controlled through the needle-seat angle (Figure 1.11b,c).

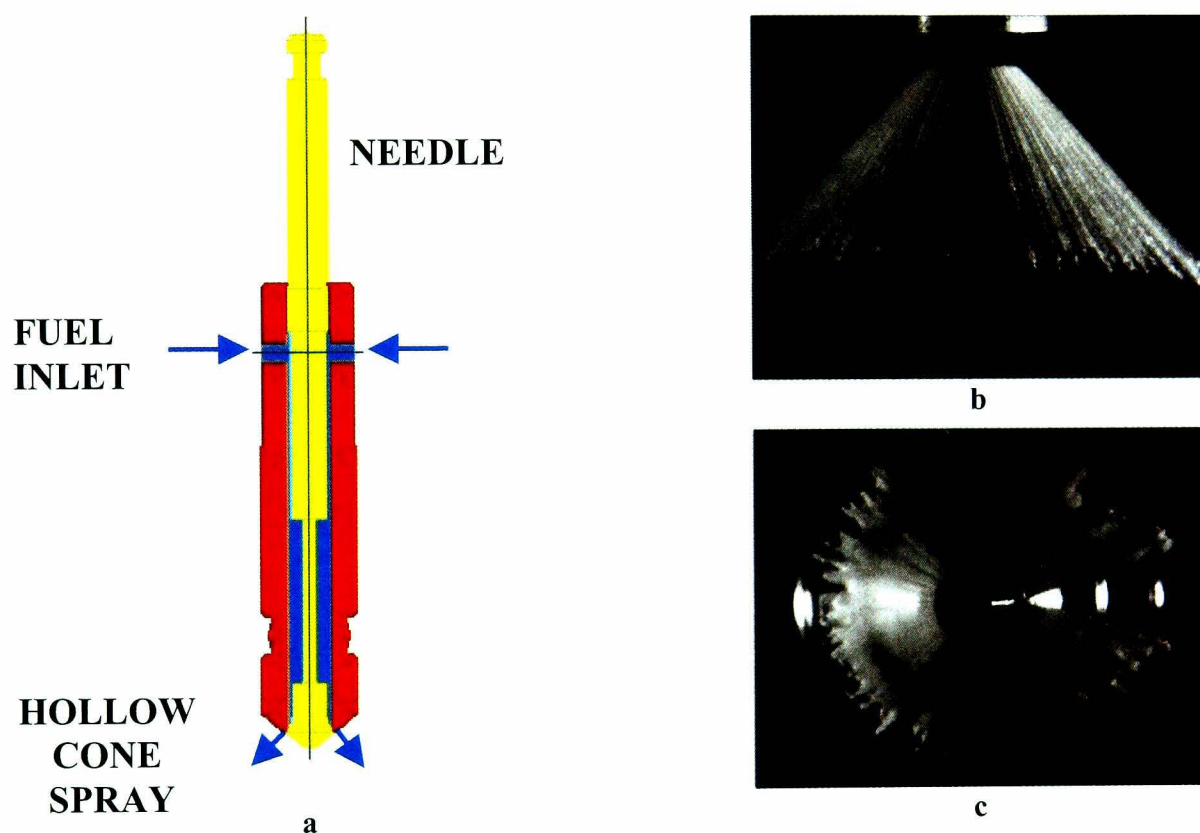


**Figure 1.11: (a). Model of an outward opening nozzle injector. (b), (c). Side and bottom images of the hollow cone spray under atmospheric chamber pressure produced by an outward opening nozzle.**

The immediate advantage of this design is the prevention of the initial sac-spray generated by the fuel liquid trapped into the sac volume (in-nozzle volume between the needle-seat and the nozzle exit) of most inwardly opening DISI injectors. Additionally, initial liquid sheet thickness is directly controlled by the pintle stroke rather than injection pressure and in-nozzle swirling flow patterns present in inwardly opening injectors. Thus, outward opening injectors offer design flexibility, structural stability in a way that ambient pressure affects only the spray penetration length, good atomisation and enhanced robustness against carbon deposition. Nevertheless, a

problem that remains to be solved is the pulse-to-pulse repeatability in spray shape [14-17]. A problem that becomes larger when this injector is to be used in spray-guided concepts, as it has been developed.

The inward opening single-fluid injectors represent the majority in present fuel-injection equipment. A well-known and thoroughly investigated type is the swirl pressure atomiser (Figure 1.12). Pressurised liquid fuel enters a conical swirl chamber through one or more tangential slots of a cylindrical or rectangular cross-section. The fluid emerges a single discharge hole of relatively large diameter (0.5-0.9mm) as an annular cylindrical sheet that spreads radially outwards to form a hollow-cone spray, due to the fluid's high tangential velocity, an air-core, coincident to the injector centreline, is formed soon after the first fluid emerges at the nozzle exit.

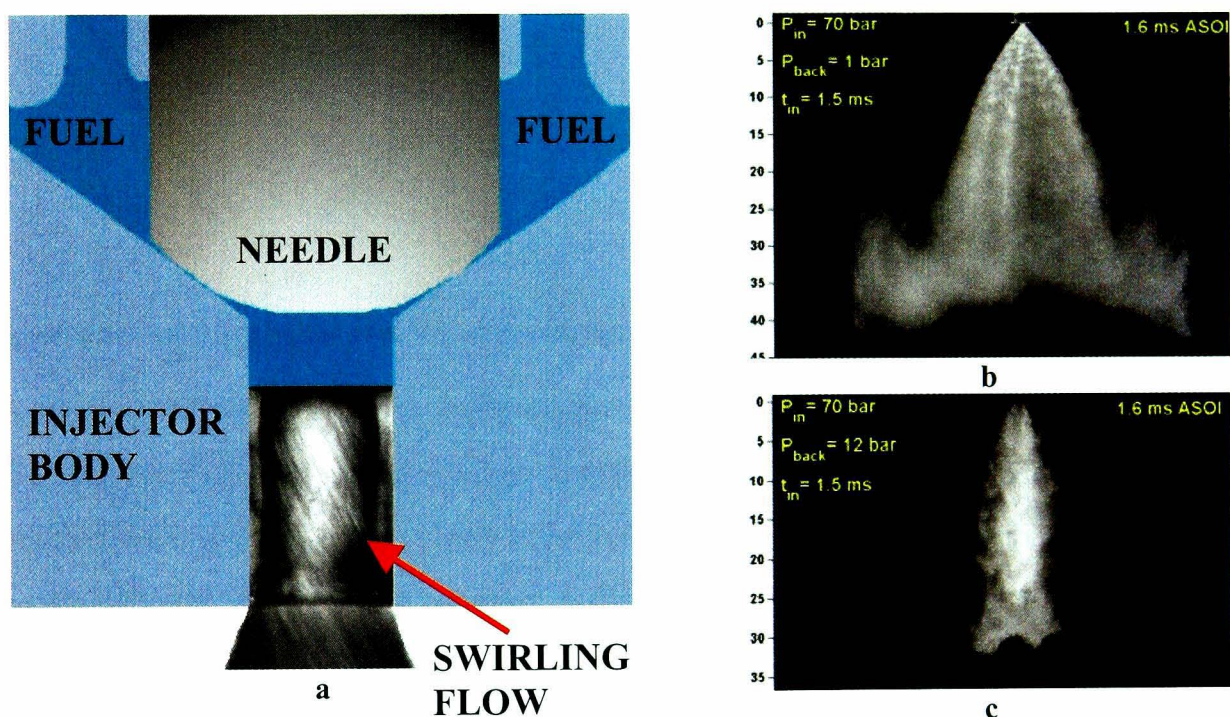


**Figure 1.12: (a). Swirl pressure atomiser nozzle cut-out. (b). Spray generated under atmospheric ambient pressure and (c). under 12bar chamber pressure.**

The development of the spray of the swirl pressure atomiser can be divided into discrete stages [18-25]. The first is the initial atomisation process that occurs at or near the injector exit. This is mainly dependent on the injector design factors such as nozzle geometry, needle opening characteristics and fuel pressure. The second stage of spray development is the atomisation that occurs during the spray penetration process, which is dominated by the interaction of the fuel droplets with the surrounding air flow-field. A known disadvantage of swirl pressure atomisers is the pre-spray, as the first fuel to exit the nozzle is fuel trapped in the sac volume and exits the hole with very low injection pressure. This results in very poor atomisation and a

significant amount of fuel enters the cylinder as large liquid droplets. During the second stage of spray development, the spray cone-angle is an important parameter, governing the fuel-air interaction, and is nominally determined by the injector design; however, in the actual application the spray cone-angle of a swirl injector varies with the in-cylinder air-density (in-cylinder pressure). This spray structure dependency on chamber ambient conditions and its cycle-to-cycle repeatability proved unable to satisfy the requirements of steady combustion for a spray-guided layout during stratified engine operation. However, the majority of wall-guided combustion systems in production are equipped with swirl pressure atomisers due to reduced sensitivity of these concepts to spray shape variations.

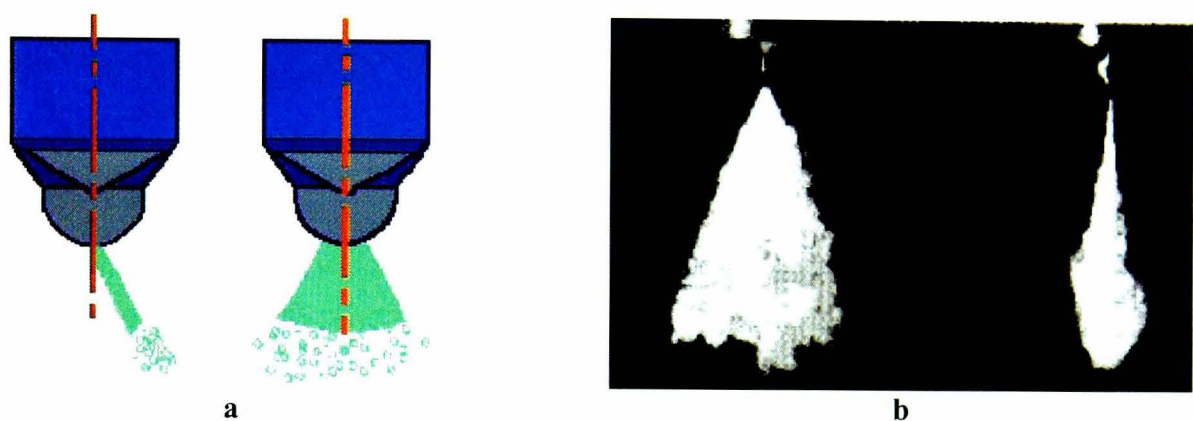


**Figure 1.13: (a). Schematic and (b). spray image of the slit injector generated fan spray.**

As spray-guided combustion systems evolve and look more promising, compared to their wall-/air-guided counterparts, automotive companies started developing new injectors that would satisfy these requirements. The Toyota Motor Corporation has specifically developed a slit injector, which is a single-hole atomiser featuring a thin slit of 0.1-0.2mm producing a two-dimensional triangular fan shaped spray structure (Figure 1.13) [26-32]. It combines high penetration rates of small-angled sprays with adequate air utilisation of dispersed wide-angle sprays. Thus, good stratification in wide-spacing concepts and satisfactory spray stability for spray-guided systems can be achieved. Another major automotive supplier, BOSCH, has chosen a well-known nozzle design (Figure 1.14a) that has been the main FIE for diesel engines. Multi-hole nozzles have been used and developed for many years in DI diesel engines and therefore extensive design and manufacturing know-how exists. These injectors offer increased flexibility in nozzle design (Figure 1.14b) and spray shape requirements. Discharge holes can be placed almost anywhere on the nozzle, allowing designers to flexibly vary the number of individual jets (hole number), the direction of each jet and the individual jet and overall spray cone angle. Multi-hole injectors with five (5) up to twelve (12) holes can be found. Holes are commonly placed on a periphery of a circle,

providing also the extra possibility of including centrally located holes in every design. Typical diameters are in the range of 0.07-0.14mm. Certain studies have shown that the ratio of hole-length over hole-diameter ( $L/D$ ) affect, to a large degree, the characteristics of generated sprays [7, 9, 33-40]. Individual fuel jet plumes could have a cone angle of  $5-14^\circ$ , value that undoubtedly affects air entrainment, atomisation quality and penetration length. Furthermore, the remarkable global spray

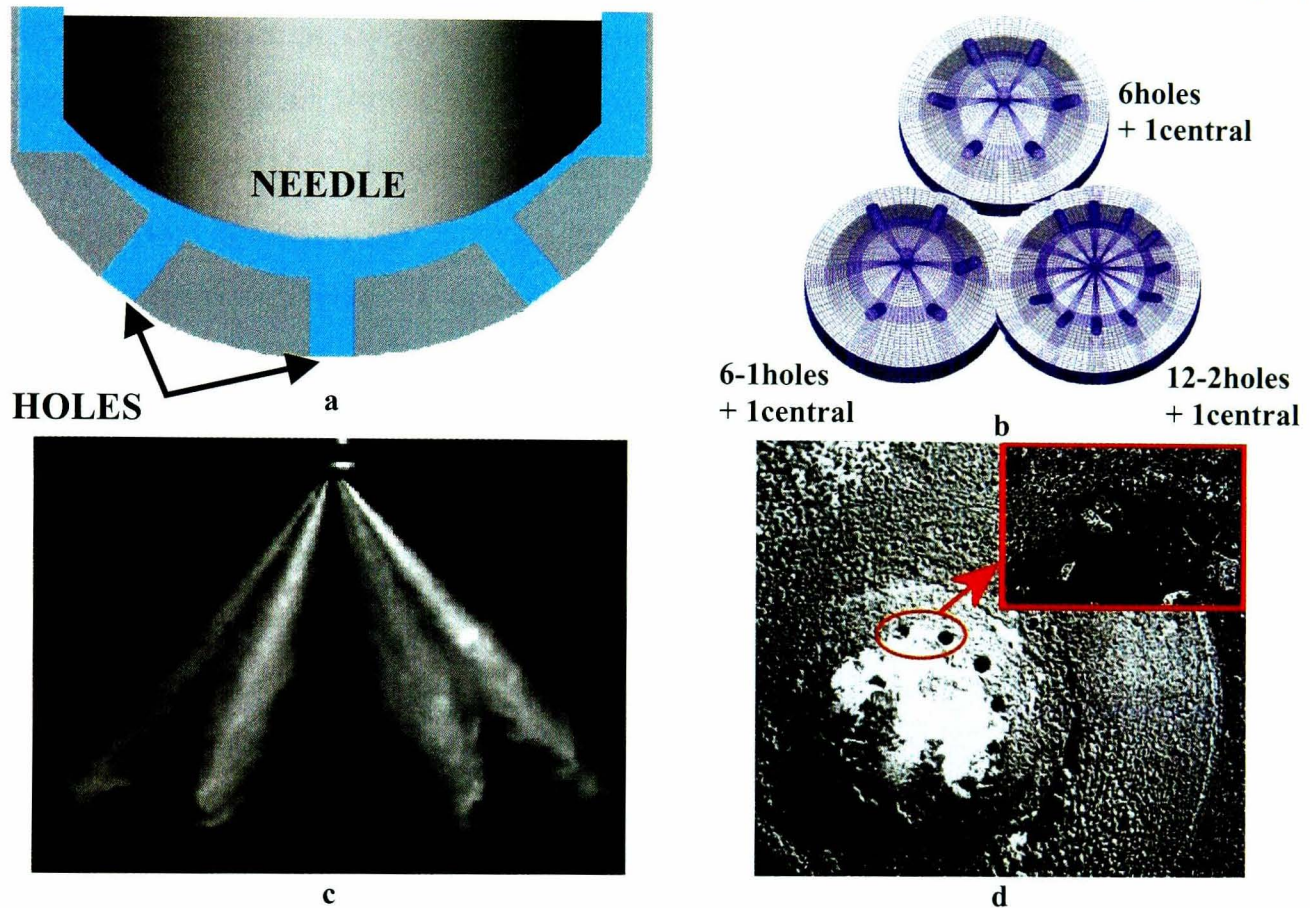


**Figure 1.14:** (a). Multi-hole nozzle cut-out. (b). Possible nozzle configurations. (c). Spray of a 6-hole injector and (d). Hole blockage from carbon deposits.

stability of multi-hole injectors can turn them into priority candidates for future spray-guided combustion layouts. Ambient in-cylinder conditions do not seem to affect the spray shape, but the penetration length. However, there are certain remaining issues that injector manufacturing companies should solve in conjunction to their automotive counterparts. Increased injection pressure that enhances atomisation generally leads to over-penetrating individual fuel sprays which, in turn, lead to extensive wall wetting. Additionally, multi-hole injectors present the highest risk of all nozzles in terms of contamination. This is due to increased tip temperatures that enhance cocking<sup>1</sup> and, as a result, holes could end up being partially blocked with carbon (Figure 1.14d). It is

<sup>1</sup> Inside the cylinder of a direct-injection spark-ignition engine there are high temperatures (higher than the ones encountered normally in conventional port-fuelled engines) during combustion due to the stratified combustion. As a result, the injector nozzle is heated considerably and acts as a secondary ignition source causing imperfect combustion of the fuel surrounding it. The latter results in soot formation that remains on the nozzle and most of the times it blocks the injection holes.

therefore essential that the injector position in the combustion chamber is optimised not only for mixture preparation but also to limit the average injector tip temperature.

## 1.4 THESIS OUTLINE

The present thesis consists of seven chapters including the introductory Chapter 1, where the basic principles of direct-injection spark-ignition gasoline engine is outlined and a brief history of the development of the spark-ignition engine is given. Moreover, a brief introduction to the problem of global warming is given and the reasons that triggered the ongoing research towards environmental friendly engines are described followed by a summarised description of the various fuel injection equipment candidates for direct-injection gasoline engines. Chapter 2 reviews relevant publications in the area of measurement techniques, experimental internal injector nozzle flow, spray characterisation and engine investigations along with miscellaneous publications dealing with miscellaneous investigations on direct-injection spark-ignition engine emissions and combustion stability. Chapter 3 through Chapter 5 present the main investigation phases of this work. More specifically, Chapter 3 presents the experimental techniques, the equipment used and the major findings in terms of the fluid flow through enlarged transparent multi-hole nozzles. Chapter 4 presents the spray characteristics for different high-pressure gasoline multi-hole nozzle designs. Furthermore, the techniques used are analysed along with the experimental setup for each investigation. Finally, Chapter 5 presents the potential of gasoline multi-hole injectors in creating homogeneous as well as stratified lean mixture distributions inside a single-cylinder direct-injection twin-spark gasoline engine. The technique used to quantify the 2-D mixture distributions and the engine setup are also analysed. Chapter 6 concludes the thesis with the summary of the major findings, whereby Chapter 3 through Chapter 5 have their own brief summaries. Recommendations for further work in the area of experimental research in multi-hole gasoline injectors are also given in Chapter 6. A list of the relevant publications, which were reviewed and referenced in this thesis, is given in the bibliography in Chapter 7.

## *Chapter 2*

### *Literature Review*

#### **2.1 INTRODUCTION**

The following literature survey provides an overview of research and a summary of the most important findings relevant to the present investigation. The overview focuses on a number of areas: large scale nozzle investigations, characterisation of direct injection sprays, interaction of spray structure with in-cylinder flow, mixture formation, and distribution. A tabular format has been used within which the major findings are listed in addition to the experimental configuration and the applied techniques. This is followed by a discussion of the state of development in DISI engines and identification of relevant gaps, which led to the experimental programme described in Chapters 3-5. The selected format which intends to summarise the main publications on the subject of this thesis, allows easier scanning and classification of the relevant research programmes as well as preparation for a more critical analysis of the research performed on internal nozzle flow in high-pressure injectors, in-cylinder flow-fuel spray interaction, mixture preparation and distribution in DISI gasoline engines.

## 2.2 INTERNAL NOZZLE FLOW (LARGE-SCALE/REAL-SIZE)

Authors	Experimental Set-up	Techniques	Major Findings
Roth, H., Giannadakis, E., Gavaises, M., Arcoumanis, C., Yanagihara, H. Sakata, I. (2005) [41]	Diesel common rail injection test rig with real-size multi-hole injector fitted featuring a transparent hole. Single and multiple injections into liquid by employment of a small transparent chamber filled with liquid and attached to the nozzle.	<ul style="list-style-type: none"> <li>• Computational Fluid Dynamics analysis of in-hole cavitation development</li> <li>• Backlit CCD Imaging of cavitation structures</li> </ul>	<ul style="list-style-type: none"> <li>• With increasing chamber pressure the start of cavitation is retarded. Additionally, swirling cavitation patterns are more confined and remaining post-injection vapour bubbles collapse much faster.</li> <li>• Increase of injection pressure forces cavitation to accelerate with slightly pronounced swirling motion.</li> <li>• At low chamber pressures the existence of pilot injection advances the cavitation inception of the main injection. With increasing interval time between pilot and main injections such influence fades out due to the collapse of the remaining bubbles in that time, before main injection is triggered.</li> <li>• Both, pilot and main injections, exhibited the same stages of cavitation development.</li> <li>• At higher chamber pressures no cavitation can be seen in pilot injection for small injection quantities. Moreover it seems to enhance the collapse of remaining cavitation bubbles after pilot injection has ended.</li> <li>• Injection duration and pressure do not play a great role in the dynamic formation of the varying cavitation patterns. Injection pressure only seems to accelerate the already developed cavitation structures.</li> <li>• Cavitation inside the nozzle exhibited a strong swirling motion around the hole axis. This motion was accompanied by development of string cavitation structures.</li> </ul>
Nouri, J.M., Abo-Serie, E., Marchi, A., Mitroglou, N. Arcoumanis, C. (2005) [14]	Steady state flow test rig with large scale model injector (outward opening gasoline direct injector)	<ul style="list-style-type: none"> <li>• Imaging of internal nozzle flow patterns and cavitation structures with CCD and high-speed video cameras</li> <li>• Laser Doppler Velocimetry</li> </ul>	<ul style="list-style-type: none"> <li>• Four jet-like flows were identified internally and upstream the valve seat due to the design configuration of the needle.</li> <li>• In the mixing chamber of the four jet-like flows just upstream the valve seat, four pairs of counter-rotating vortices were identified with highly unstable patterns</li> <li>• The aforementioned instability can be seen downstream the valve seat on the spray itself</li> <li>• Existence of cavitation confirmed; it is initiated on the valve seat.</li> </ul>

**Table 2-1: Literature relative to internal nozzle flow of high-pressure injectors.**

Scholz, J., Roetmann, K. Beushausen, V. (2003) [42]	Steady state flow test rig with large scale model injector (slit nozzle injector – 3 different design configurations)	<ul style="list-style-type: none"> <li>• Particle Image Velocimetry of in-nozzle flow patterns</li> <li>• Double pulsed backlit photography of free liquid films near the nozzle exit</li> </ul>	<ul style="list-style-type: none"> <li>• The development of turbulent boundary layers stabilises the liquid film, as long as the turbulence intensity is not too strong.</li> <li>• Energy transfer or/and velocity equalisation between core flow and liquid film surface at the nozzle exit plays an important role in the promotion of liquid film disturbances, which lead to rough liquid film surface and detachment of big droplets.</li> </ul>
Roth, H., Gavaises, M. Arcoumanis, C. (2002) [43]	Steady-state and quasi transient flow test rig with large-scale model injector (transparent 6-hole conical mini-sac and VCO type nozzle)	<ul style="list-style-type: none"> <li>• Refractive Index Matching</li> <li>• Laser Doppler Velocimetry measurements in mini-sac nozzle</li> <li>• Imaging of cavitation structures in both nozzle types with high-speed digital video</li> </ul>	<ul style="list-style-type: none"> <li>• Vortex flow inside nozzle tip volume is prerequisite for string cavitation</li> <li>• Cavitation strings in the nozzle tip volume can induce hole cavitation</li> <li>• Strong helical flow and ‘needle strings’ inside injection hole of VCO nozzle identified</li> <li>• Cavitation initiation at side corners of hole inlet possible</li> <li>• Higher needle lift results in more stable cavitation flow structures for both nozzle types</li> <li>• No appreciable liquid movement identified in lower nozzle tip volume</li> <li>• Non-cavitating flow conditions result in reduced recirculation zones close to the injection hole entrance for higher needle lifts</li> <li>• Turbulence levels increase in lower part of injection hole with increasing cavitation numbers at moderate flow rates</li> <li>• At moderate as well as increased flow rates the normalised RMS are higher at low needle lifts compared to those at high needle lifts due to bottleneck effect</li> <li>• Increasing cavitation and Reynolds numbers result in higher turbulent kinetic energy in the injection hole bulk flow although this increase is less apparent further downstream</li> <li>• Close to the hole exit the averaged TKE decreases asymptotically to the turbulence level of the non-cavitating flow due to cavitation bubble break-up</li> </ul>

**Table 2-1: Literature relative to internal nozzle flow of high-pressure injectors (continued).**

<p>Arcoumanis, C., Gavaises, M., Flora, H. Roth, H. (2001) [44]</p>	<p>Closed loop common-rail injection test rig with optical accessible real-size mini-sac injection nozzle; large-scale steady-flow test rig with mini-sac model nozzle</p>	<ul style="list-style-type: none"> <li>• Imaging of cavitation structures inside real-size injection hole with high magnification CCD camera</li> <li>• Imaging of cavitation in sac and injection hole of large-scale nozzle with CCD camera</li> </ul>	<ul style="list-style-type: none"> <li>• Higher cavitation numbers are required to initiate hole cavitation in the real-size nozzle relative to the enlarged nozzle</li> <li>• Thickness of cavitation film does not seem to scale with hole size</li> <li>• Cavitating two-phase flow extends to hole exit for sufficient high cavitation and Reynolds numbers</li> <li>• String cavitation more apparent at higher needle lifts inside real-size nozzle</li> <li>• Strings interact with hole cavitation and create cavitation bubble clouds in both real-size and enlarged nozzle holes</li> </ul>
<p>Soteriou, C., Andrews, R., Smith, M., Torres, N. Sankhalpara, S. (2000) [45]</p>	<p>Steady-state flow test rig with transparent 20x scaled up models of plain orifices employing either variable throttling of the injection hole exit or the hole inlet; injection into atmosphere</p>	<ul style="list-style-type: none"> <li>• Refractive Index Matching</li> <li>• Laser light sheet illumination and still imaging of non-cavitating flow (seeded with hollow glass spheres)</li> <li>• Laser Doppler Velocimetry measurements close to hole exit</li> <li>• Spray visualisation and determination of spray angle</li> </ul>	<ul style="list-style-type: none"> <li>• Flow through throttled model orifices and emerging jets/sprays are significantly different compared to those produced by conventional sac or VCO type nozzles</li> <li>• Fan-shaped jets, horseshoe-shaped jets and quasi-normal sprays were observed for decreasing degrees of exit throttling; cavitation is suppressed for most of the investigated conditions</li> <li>• In the case of hole entry throttling, hollow non-circular, non-circular, two-jet and rotated non-circular sprays were identified with progressive opening of the hole; cavitation occurred at reduced levels compared to normal nozzles and produced bushy opaque sprays in some cases</li> <li>• Overall, inlet throttling causes spray angles to be significantly wider than with normal orifices, but not as large as with exit throttling</li> <li>• Entry throttling causes the flow velocity to drop appreciable inside the orifice, while exit throttling seems to have a smaller effect on the velocity; thus, for the same degree of throttling, partially open entry throttled holes produce lower spray velocities than partially open exit throttled holes</li> </ul>

**Table 2-1: Literature relative to internal nozzle flow of high-pressure injectors (continued).**

<p>Afzal, H., Arcoumanis, C., Gavaises, M. Kampanis, N. (1999) [46]</p>	<p>Steady-state flow test rig with enlarged model injector (transparent 6-hole conical mini-sac and VCO type nozzle)</p>	<ul style="list-style-type: none"> <li>• Refractive Index Matching</li> <li>• Flow rate and pressure measurements</li> <li>• Imaging of cavitation structures</li> <li>• CFD calculations for non-cavitating conditions</li> </ul>	<ul style="list-style-type: none"> <li>• Initiation and development of cavitation structures inside the injection holes and nozzle volumes were visualised and this revealed different patterns in terms of spatial and temporal development of the cavitation bubbles as a function of needle lift and needle eccentricity</li> <li>• Discharge coefficient decreases asymptotically to its minimum value for increasing cavitation numbers</li> <li>• Over a wide range of nozzle operating conditions significant transient pressure variations (5-10% of the mean) have been recorded for the difference between upstream and downstream pressure</li> <li>• From the various images obtained, comprehensive sketches were drawn summarising the most important observations of the cavitating flow structures in the two nozzles</li> <li>• CFD calculations of velocity flow field, pressure and turbulent kinetic energy distribution for varying needle lift and nozzle geometries</li> </ul>
<p>Arcoumanis, C., Gavaises, M., Nouri, J.M., Abdul-Wahab, E. Horrocks, R.W. (1998) [47]</p>	<p>Steady-state flow test rig with enlarged model injector (transparent 6-hole conical mini-sac type nozzle)</p>	<ul style="list-style-type: none"> <li>• Refractive Index Matching</li> <li>• Laser Doppler Velocimetry</li> <li>• Flow rate measurements</li> <li>• Imaging of cavitation structures with CCD and high-speed cameras</li> <li>• CFD calculations for non-cavitating conditions</li> </ul>	<ul style="list-style-type: none"> <li>• Flow rate shows asymptotic behaviour for needle lifts higher than a value that is still “far” below full lift</li> <li>• Even for symmetric nozzle conditions the individual hole flow rates can vary noticeably due to small differences in hole size, wall roughness and hole inlet shape</li> <li>• CFD calculations of velocity flow field, pressure and turbulent kinetic energy distribution for varying needle lift and nozzle geometries as a parametric study</li> <li>• CFD calculations confirmed that manufacturing tolerances in the geometry of the nozzle from its nominal geometric characteristics result in unequal flow distribution between the injection holes</li> <li>• LDV results from measurements of local mean velocities and RMS values were used to validate CFD calculations; predictions are generally in good agreement with experimental values, but do not capture well the recirculation zone at the hole inlet</li> <li>• Initiation and development of cavitation structures inside the injection hole were visualised and this revealed different patterns in terms of spatial and temporal development of the cavitation bubbles as a function of needle lift and needle eccentricity</li> </ul>

**Table 2-1: Literature relative to internal nozzle flow of high-pressure injectors (continued).**

Yule, A.J., Dalli, A.M. Yeong, K.B. (1998) [48]	Large-scale axisymmetric models of VCO nozzle orifice (sharp and rounded orifice inlet edge) under transient flow conditions due to fast valve (needle) movement; various working fluids were utilised	<ul style="list-style-type: none"> <li>• High-speed video imaging of developing orifice flow</li> <li>• Valve opening rate determination from image data</li> <li>• Pressure measurements and calculation of discharge coefficient</li> </ul>	<ul style="list-style-type: none"> <li>• Interesting aspects of internal flow development occurred during first third of injection duration</li> <li>• Recirculation zone at the orifice inlet contains cavitation bubbles above a certain pressure drop</li> <li>• Movement of the pulsing recirculation zone near the orifice wall towards the orifice exit is believed to cause hydraulic flip above a certain Reynolds number even without occurrence of cavitation</li> <li>• Atomisation occurred more rapidly for the orifice with sharp inlet edge compared to the rounded one under the same pressure conditions</li> </ul>
Arcoumanis, C. Gavaises, M. (1998) [49]	Review of experimental and computational work on Diesel injector cavitation	<ul style="list-style-type: none"> <li>•</li> </ul>	<ul style="list-style-type: none"> <li>• The experimental results of the reviewed literature demonstrate the complexity of the problem, but also give valuable information about aspects of the phenomenon of cavitation</li> <li>• Concerning the computational efforts it was evident that numerous attempts have been made to simulate the flow inside the nozzle holes of Diesel injectors, but it is still necessary to develop a method which can accurately predict most of the characteristics of cavitation</li> </ul>
Soteriou, C.C.E., Smith, M. Andrews, R.J. (1993) [50]	Steady-state flow rig with large-scale model nozzles transient injection test rig with various real-size nozzles; injection into liquid and into gas	<ul style="list-style-type: none"> <li>• Still imaging of cavitation in transparent large-scale and simplified real-size nozzles</li> <li>• Still imaging of spray from real-size and model nozzles</li> <li>• Detailed pressure measurements and calculation of nozzle discharge coefficients</li> </ul>	<ul style="list-style-type: none"> <li>• Investigation of large-scale nozzle flow and spray characteristics considered to be a valuable tool when cavitation and Reynolds number are matched simultaneously to those found in real-size flows</li> <li>• Overall, results from investigations in large-scale and real-size nozzles in good agreement</li> <li>• Cavitation in injection holes to be found the predominant mechanism causing spray atomisation</li> <li>• Cavitation encourages separation in the boundary layer of the nozzle hole flow</li> <li>• Higher turbulence levels in nozzle flow can prevent occurrence of hydraulic flip phenomenon</li> <li>• Hydraulic flip is believed to cause unequal sprays from VCO nozzles</li> <li>• VCO nozzles with eccentric needle produce hollow cone sprays</li> <li>• Discharge coefficient only depends on cavitation number and not on Reynolds number</li> <li>• Cavitation characteristics do not change beyond a specific cavitation or Reynolds number and above a certain pressure</li> </ul>

**Table 2-1: Literature relative to internal nozzle flow of high-pressure injectors (continued).**

Arcoumanis, C., Nouri, J.M. Andrews, R.J. (1992) [51]	Steady-state flow test rig with enlarged model injector (transparent single-hole nozzle)	<ul style="list-style-type: none"> <li>• Refractive Index Matching</li> <li>• Laser Doppler Velocimetry</li> </ul>	<ul style="list-style-type: none"> <li>• Simulating Diesel fuel with a mixture of hydrocarbons having the same refractive index as the acrylic model nozzle proved to be a useful tool in characterising the internal flow in Diesel injectors</li> <li>• Three-dimensional components of mean velocities and RMS values measured for <math>Re = 18800</math></li> <li>• The measured flow field provided insight into the dependence of the injector flow on nozzle geometry, needle lift and injection pressure</li> <li>• The results are useful for validating multi-dimensional CFD models</li> </ul>
---	--	--	--

**Table 2-1: Literature relative to internal nozzle flow of high-pressure injectors (continued).**

### 2.3 HIGH-PRESSURE FUEL SPRAY CHARACTERISATION

Authors	Experimental Set-up	Techniques	Major Findings
Mitroglou, N., Nouri, J.M. Arcoumanis, C. (2006) [38]	High pressure gasoline fuel injection test rig fitted on a constant volume chamber – six hole multi-hole injector	<ul style="list-style-type: none"> <li>• Mie imaging</li> <li>• Phase Doppler Anemometry</li> </ul>	<ul style="list-style-type: none"> <li>• The overall angle of each spray from the injector axis was found to be <math>40^\circ</math> and almost independent of the injection pressure (120, 200bar).</li> <li>• The effect of chamber pressure was to reduce the spray tip penetration of each of the six spray plumes due to increased drag.</li> <li>• Temporal velocity profiles revealed that droplet velocities increased sharply at the start of injection to a maximum value, then remained unchanged during the main part of injection, before decreasing rapidly towards the end of injection.</li> <li>• The spatial velocity profiles were jet-like at all axial locations with the maximum values on the spray axis.</li> <li>• The Sauter mean diameters in the main spray at 10mm distance from the nozzle exit were of the order of 19 and <math>14\mu\text{m}</math> at injection pressure of 120 and 200bar respectively under atmospheric chamber pressure.</li> <li>• The effect of injection pressure on the droplet size was small while the increase in chamber pressure resulted in smaller droplet velocities by up to fourfold and larger droplet sizes by up to 40%</li> </ul>

**Table 2-2: Literature relative to spray characterisation of high-pressure injectors.**

<p>Yan, Y., Gashi, S., Nouri, J.M., Lockett, R.D. Arcoumanis, C. (2005) [15]</p>	<p>Single cylinder direct injection engine – (transparent quartz liner and piston window – outward opening piezo activated hollow cone high-pressure injector)</p>	<ul style="list-style-type: none"> <li>• Planar Laser Induced Fluorescence</li> <li>• Mie imaging</li> <li>• Laser Doppler Velocimetry</li> </ul>	<ul style="list-style-type: none"> <li>• Quantification of in-cylinder airflow by LDV measurements showed one order of magnitude difference between induction and compression strokes. At the spark-plug position an RMS value of 7Vp during induction became 0.7Vp at the same position during compression stroke.</li> <li>• Spray fuel droplets presented a maximum value of 73m/s at 16mm below the injector tip when injecting late during compression stroke.</li> <li>• Hollow cone spray tends to bend inwards at elevated chamber pressures.</li> </ul>
<p>Pontoppidan, M, Gaviani, G., Rotondi, R. DeMaio, A. (2005) [10]</p>	<p>Virtual high pressure gasoline fuel injection test rig – Real engine test bed</p>	<ul style="list-style-type: none"> <li>• Computational fluid dynamics</li> <li>• Basic engine operational parameters acquisition</li> </ul>	<ul style="list-style-type: none"> <li>• In an attempt to reduce the spray momentum of a high-pressure gasoline injector, simulation tools pointed out an optimised nozzle design that combines characteristics of multi-hole nozzles and principles from the colliding flow theory. The colliding jets injector is a multi-hole injector having its jets very closely spaced that eventually a few millimetres downstream the hole exit they collide, enhancing in this way atomisation and reducing spray momentum.</li> <li>• The penetration depth decrease capability is proportional to the jet collision angle. Angles greater than 25° show a substantial decrease in penetration length.</li> <li>• In a direct comparison of the colliding jet injector with the standard multi-hole injector a penetration reduction of 35% at 100bar injection pressure and 49% at 220bar injection pressure can be observed for the CJ-injector. Moreover, the same injector shows a diameter decrease (<math>D_{32}</math>) of 19% at 100bar injection pressure at an axial location of 45mm below hole exit relative to its multi-hole counterpart.</li> </ul>
<p>Moon, S., Choi, J., Abo-Serie, E. Bae, C. (2005) [29]</p>	<p>High pressure gasoline fuel injection test rig – heated injector body holder – injection inside a wind tunnel – single cylinder optical engine test bed – swirl and slit type injectors</p>	<ul style="list-style-type: none"> <li>• Mie and shadowgraphy imaging</li> <li>• Phase Doppler Anemometry</li> </ul>	<ul style="list-style-type: none"> <li>• Increasing injector body temperature results in a decrease in spray penetration. At the same time the spray width of the slit type injector increases and a reduction in both AMD and SMD values is evident.</li> <li>• The above-mentioned characteristic of the slit injector is responsible for achieving fast combustion when in homogeneous mode with increasing injector body temperature.</li> <li>• On the other hand, in stratified mode operation there is an optimum injector temperature at which the best operating behaviour is evident.</li> </ul>

**Table 2-2: Literature relative to spray characterisation of high-pressure injectors (continued).**

<p>Nauwerck, A., Pfeil, J., Velji, A., Spicher, U. Richter, B. (2005) [52]</p>	<p>High pressure gasoline fuel injection test rig with high pressure/temperature constant volume chamber – multihole injector (12holes, 90° cone angle)</p>	<ul style="list-style-type: none"> <li>• Spray imaging</li> <li>• Particle Image Velocimetry</li> <li>• Phase Doppler Anemometry</li> </ul>	<ul style="list-style-type: none"> <li>• Frictional effects predominate the initial stages of the spray, so both spray width and length are reduced.</li> <li>• At later stages during the injection event inertia of the fuel mass caused a widening of the jet, while its length remained nearly constant. This effect increases with increasing injection pressure as more fuel mass is injected.</li> <li>• Dependencies of injection pressure and ambient pressure on the extension of the entrainment flow and air velocities have been determined. An increase of maximal velocities in the entrainment flow with higher injection pressure was detected.</li> <li>• High velocity gradients were detected inside the spray, as spray droplet velocities do not increase in the same dimension as injection pressure does. The smallest droplet diameters were detected with the highest fuel pressure and presented the highest measured velocities.</li> </ul>
<p>Pontoppidan, M., Gaviani, G., Bella, G. De Maio, A. (2004) [53]</p>	<p>Constant volume high pressure chamber – Firing engine</p>	<ul style="list-style-type: none"> <li>• Spray imaging</li> <li>• Particle image velocimetry</li> <li>• Phase Doppler anemometry</li> <li>• Computational fluid dynamics</li> <li>• Basic engine data acquisition</li> </ul>	<ul style="list-style-type: none"> <li>• The main objective of the particular study was to isolate the fundamental injector atomizer parameters to optimise within the frame of physical phenomenon of mixture preparation in a high-speed spray guided wide spacing racing engine operating at homogeneous stoichiometric mode.</li> <li>• The data collected form visualisation measurements, PIV and PDA on various sprays produced by a swirl, a closed cap slit, a multi-hole, and a colliding jet multi-hole injector were used as inputs to the CFD optimisation code.</li> <li>• A 4 hole multi-hole injector with the holes located in a linear array with a maximum angular separation of the outer jet axis of 80° was found to give the best results which were also validated during the firing engine tests.</li> <li>• Although the colliding multi-hole injector had the potential to give the best performance results, as it promotes a secondary break up, it did not give any improvement compared to the multi-hole injector due to the very limited free path space available in the racing engine around the intake TDC.</li> <li>• The work done showed that it is possible to obtain a potential 2% high-end performance gain with DI-technology compared to PFI-technology.</li> </ul>

**Table 2-2: Literature relative to spray characterisation of high-pressure injectors (continued).**

Abe, M, Okamoto, Y, Kadomukai, Y., Tanabe, Y. Ishikawa, T. (2004) [54]	High pressure gasoline fuel injection test rig with constant volume chamber	<ul style="list-style-type: none"> <li>• Mie imaging</li> </ul>	<ul style="list-style-type: none"> <li>• Two new nozzles with new spray pattern were developed for meeting the needs of the wide spacing and the close spacing spray guided DISI configurations.</li> <li>• An L-cut orifice nozzle that produces a horseshoe spray pattern was used to create a rich and lean concentration region. The spray shape and the fuel distribution was found to be controllable by configuring the L-cut step walls.</li> <li>• The rich portion within the horseshoe spray fuel distribution is created from the vertical side edge of the L-step while the lean portion is created by the obstruction of the L-step wall</li> </ul>
Wigley, G., Goodwin, M., Pitcher, G. Blondel, D. (2004) [55]	Constant volume chamber – swirl pressure atomiser	<ul style="list-style-type: none"> <li>• Laser Doppler Anemometry</li> <li>• Phase Doppler Anemometry</li> <li>• Imaging of near-nozzle spray</li> </ul>	<ul style="list-style-type: none"> <li>• Simultaneous application of three measurement techniques proved to be very helpful in essential quantification of spatial and temporal development of the injected liquid sheet and its break-up, as well as quantification of the velocity of sheet disintegration products and velocity and size of the droplet field.</li> </ul>
Choi, J., Lee, S. Bae, C. (2004) [56]	High pressure gasoline fuel injection test rig fitted on a wind tunnel for testing various in-cylinder flow conditions employing a swirl pressure atomiser	<ul style="list-style-type: none"> <li>• Mie imaging</li> <li>• Shadowgraphy</li> <li>• Phase Doppler Anemometry</li> </ul>	<ul style="list-style-type: none"> <li>• High-pressure swirl injection characteristics of a GDI injector in a cross-flow up to 15m/s were investigated to study the interaction between flow field and spray.</li> <li>• The sac spray penetration (pre spray) depth varied with injection pressure but the main spray penetration depth and spray width were not affected by injection pressure or cross-flow velocity.</li> <li>• Fuel vaporisation rate was found to be proportional to cross-flow velocity.</li> <li>• Liquid and vapour fuel were distinguished by Mie scattered images and shadowgraphy.</li> <li>• The PDA velocity measurements showed the existence of vortices with different motion at various cross-flow velocities.</li> <li>• Acceleration of the fuel droplet vaporisation by increasing cross-flow velocity was confirmed by PDA.</li> </ul>
Seibel, C., Gartung, K., Arndt, S. Weigand, B. (2003) [16]	High pressure gasoline injection test rig – Constant volume chamber with max pressure/temperature capabilities of 20b/400°C respectively – annular orifice injector	<ul style="list-style-type: none"> <li>• Particle Image Velocimetry</li> <li>• Tomographic imaging approach</li> <li>• Computational fluid dynamics</li> </ul>	<ul style="list-style-type: none"> <li>• Spray induced air flow strongly influences the spray propagation.</li> <li>• The amount of entrained air into the spray region essentially affects the vaporisation rate.</li> <li>• The variation of injection timing showed the effects of spray surface, relative velocity and air density on air entrainment.</li> <li>• Late injection timings, as simulated by ambient conditions simulation in the CVC, presented the highest air entrainment of all conditions tested.</li> </ul>

**Table 2-2: Literature relative to spray characterisation of high-pressure injectors (continued).**

Abo-Serie, E., Gavaises, M. Arcoumanis, C. (2003) [57]	High pressure/ temperature constant volume chamber accommodating a heated plate in an attempt to simulate the piston surface – Six hole multi-hole injector	<ul style="list-style-type: none"> <li>• Mie imaging</li> <li>• Phase Doppler Anemometry</li> </ul>	<ul style="list-style-type: none"> <li>• Spray images for both a free spray and an impinging spray on a hot surface showed that the spray from a multi-hole injector maintains a constant angle independent of injection (70, 100bar) or chamber pressure (1,3,7bar).</li> <li>• PDA results for the free spray revealed that the mean velocity of the droplets across the spray exhibits a maximum value at the spray centreline where the droplet diameter is minimum.</li> <li>• The droplet mean diameter after the impingement was found to be strongly dependent on the plate inclination angle.</li> <li>• Increasing the surface temperature of the plate resulted to a slight increase in the droplet mean velocity after the impingement and a decrease in their Sauter mean diameter.</li> </ul>
Dewel, I., Kunzelmann, T., Schorr, J., Schulz, C. Wolfrum, J. (2003) [58]	Ethanol pressure atomiser coupled with an air co flow produce a spray flame. – monodisperse droplet generator	<ul style="list-style-type: none"> <li>• Dropsizing imaging based on the ratio of laser induced fluorescence and Mie scattering</li> </ul>	<ul style="list-style-type: none"> <li>• LIF/Mie dropsizing is well studied in non-evaporating sprays but systematic errors occur due to tracer enrichment and depletion of tracers during evaporation. By comparison of results obtained with tracers with different volatilities these systematic errors were specified in an ethanol spray flame with maximum SMD of 150µm.</li> <li>• Tracers with negligible vapour pressure give LIF signals that represent the initial liquid volume. They allow to assess the spray evaporation with a simple evaporation model.</li> <li>• It was found that the evaporation is slow compared with the transport inside of the droplet, which allows complete tracer enrichment.</li> </ul>
Wigley, G., Goodwin, M., Pitcher, G. Blondell, D. (2003) [25]	High pressure gasoline injection fuel test rig – swirl pressure atomiser	<ul style="list-style-type: none"> <li>• Laser Doppler Anemometry</li> <li>• Phase Doppler Anemometry</li> <li>• Spray Imaging</li> </ul>	<ul style="list-style-type: none"> <li>• All measurements were done in a max distance of 5mm from the nozzle exit where the spray is optically dense and partially atomised</li> <li>• Big droplets can be found in the axis of the hollow cone swirl spray, where low pressure region exists</li> <li>• Full agreement of LDA/PDA measured velocities can be found at the fully developed spray core and the recirculation zone created at the low pressure region</li> <li>• Droplet dynamics at the spray periphery are determined by a strong velocity-size correlation, in a way that large droplets maintain their velocity, while smaller ones are influenced by air entrainment</li> </ul>

**Table 2-2: Literature relative to spray characterisation of high-pressure injectors (continued).**

Ineichen, B. (2003) [59]	High pressure/temperature combustion cell – single-hole diesel injector	<ul style="list-style-type: none"> <li>• 2D laser-speckles based imaging technique</li> <li>• Particle Image Velocimetry</li> </ul>	<ul style="list-style-type: none"> <li>• Speckles light reflection, refraction and scattering behaviour of droplets can be used to characterise sprays micro- and macroscopically.</li> <li>• The developed technique leads to two-dimensional temporal and spatial detection of droplet size, shape and velocity.</li> <li>• Technique showed very good repeatability.</li> </ul>
Goodwin, M. Wigley, G. (2003) [60]	High pressure gasoline fuel injection test rig – swirl pressure atomiser and rotary slit valve	<ul style="list-style-type: none"> <li>• High magnification spray imaging</li> </ul>	<ul style="list-style-type: none"> <li>• In the case of the swirl pressure atomiser four separate regions were identified at an injection pressure of 10bar: <ul style="list-style-type: none"> <li>➢ Continuous sheet</li> <li>➢ Perforated sheet</li> <li>➢ Filaments</li> <li>➢ Droplets</li> </ul> <p>These regions reduce in size and retreat towards the nozzle as injection pressure increases whilst the surface structure increased in complexity.</p> </li> <li>• The rotary valve nozzle was configured to produce a straight flat liquid sheet of 30x0.15mm. Short injection durations did not allow full sheet development at low pressures, therefore liquid sheet breakup lengths were observed at pressures exceeding 20bar. The results showed clear evidence that aerodynamic forces dominate the breakup process at pressures higher than 20bar.</li> </ul>
Hung, D.L.S., Chmiel, D.M. Markle, L.E. (2003) [61]	High pressure gasoline fuel atmospheric injection test rig – Single cylinder optically accessed engine – swirl pressure atomiser	<ul style="list-style-type: none"> <li>• Spray Imaging for determining cycle-to-cycle variations</li> </ul>	<ul style="list-style-type: none"> <li>• The apparent spray characteristics are largely dependent on the measurement technique used to evaluate them. Whether intrusive or in-situ, or based on diffraction, interferometry, or imaging the reported spray is a function of how it is measured!</li> <li>• Mie-scattering images can be particularly deceiving as the small particles in sprays have similar diameters to the wavelength of light source used, so they scatter light disproportionately to their diameter or mass.</li> <li>• The demonstrated image analysis technique enhances visualisation of the variation of multiple spray characteristics simultaneously; therefore it creates a useful tool for injector design and application development.</li> </ul>

**Table 2-2: Literature relative to spray characterisation of high-pressure injectors (continued).**

<p>Stegemann, J., Seebode, J., Baltes, J., Baumgarten, C. Merker, G.P. (2002) [62]</p>	<p>High pressure diesel fuel piezo-electrically controlled common rail injection test rig – Rapid compression machine ensures engine like chamber conditions – multi-hole diesel injector</p>	<ul style="list-style-type: none"> <li>• Ultra high speed spray imaging</li> <li>• Accurate control of all injector operating parameters (needle lift, needle speed)</li> </ul>	<ul style="list-style-type: none"> <li>• Results indicate a significant influence throttle effects at the needle seat on the spray characteristics.</li> <li>• Effects generated by pressure drop at the needle seat have a much bigger influence than a variation of injection pressure. Throttle effects at the needle seat show a distinct influence on the spray angle.</li> <li>• Pressure drop due to partial needle lifts generate cavitation phenomena that move into the sac hole and influence the flow inside the injection holes. As a result spray breakup and dispersion are influenced.</li> </ul>
<p>Pontoppidan, M., Gaviani, G., Bella, G. De Maio, A. (2002) [28]</p>	<p>High pressure gasoline fuel injection test rig – constant volume chamber – firing engine test bed – swirl pressure atomiser and fan spray injectors featuring piezo-activation electronics tested</p>	<ul style="list-style-type: none"> <li>• Phase Doppler Anemometry</li> <li>• Particle Image Velocimetry</li> <li>• High speed/laser sheet imaging</li> <li>• Computational fluid dynamics</li> </ul>	<ul style="list-style-type: none"> <li>• <b>Constant volume chamber</b> <ul style="list-style-type: none"> <li>➤ As fuel rail pressure increases, both, swirl and fan sprays, show a reduction in their overall spray cone angle of 30%</li> <li>➤ Fan sprays presented more repeatable spray patterns than swirl hollow cone sprays.</li> <li>➤ Both nozzles showed a reduction in AMD by a factor of 9-10 when rail pressure increased. This increase also resulted in an increase in penetration lengths of 2.5</li> </ul> </li> <li>• <b>Firing engine</b> <ul style="list-style-type: none"> <li>➤ For cylinder bores smaller than 60mm liner wetting is increased and it is an issue. On the contrary, things are better for two-stroke engines due to high in-cylinder turbulence.</li> <li>➤ Increasing injection pressure at 300bar a torque stability improvement was noticed.</li> <li>➤ Overall, firing engine results confirmed the aforementioned constant volume chamber findings.</li> </ul> </li> </ul>
<p>Nouri, J.M Whitelaw, J.H (2001) [22]</p>	<p>High pressure gasoline fuel injection test rig fitted on a constant volume chamber using a swirl pressure atomiser</p>	<ul style="list-style-type: none"> <li>• Mie imaging</li> <li>• Phase Doppler Anemometry</li> </ul>	<ul style="list-style-type: none"> <li>• The photographic investigation of a prototype swirl injector indicated delay times of 0.225 and 0.2ms due to the opening and closing of the needle of the injector.</li> <li>• The shape of the sprays was nearly independent of injection pressure at all chamber pressures.</li> <li>• The effect of chamber pressure was considerable with large reduction in droplet mean velocity by up to 50%, spray cone angle by 35%, suppression of the droplet velocity fluctuations by 40% , and an increase in the droplet arithmetic Sauter mean diameters by up to 20% with an increase in the chamber pressure from 1 to 12 bars.</li> </ul>

**Table 2-2: Literature relative to spray characterisation of high-pressure injectors (continued).**

Arndt, S., Gartung, K. Brueggemann, D. (2001) [33]	High pressure gasoline fuel injection test rig fitted on a constant volume chamber to evaluate sprays from swirl atomisers, multi-hole and annular orifice injectors	<ul style="list-style-type: none"> <li>• Particle Image Velocimetry</li> <li>• High speed imaging</li> <li>• Strain gage sensor</li> </ul>	<ul style="list-style-type: none"> <li>• Recirculating air flow is a characteristic of high pressure injection and it is caused by local pressure gradients and air displacement that is present in all high pressure fuel jets.</li> <li>• This spray induced air flow is essential for the vapour phase. It affects air entrainment, rate of evaporation and spatial distribution of fuel vapour.</li> <li>• Basic characteristics of the three types of injectors used are as follows: <ul style="list-style-type: none"> <li>➤ <b>Swirl pressure atomiser.</b> It is characterised by strong air entrainment, good atomisation but its spray structure is very sensitive to chamber pressure changes.</li> <li>➤ <b>Mutli-hole injector</b> Its strong advantage is the robust spray pattern under any chamber pressure conditions and its robust spatial vapour distribution.</li> <li>➤ <b>Annular orifice injector</b> This new generation injector features a hollow cone structured spray regardless any chamber pressure changes. It also characterised by a recirculating air flow inside the cone region.</li> </ul> </li> </ul>
Wigley, G., Heath, J., Pitcher, G. Whybrew, A. (2001) [63]	Atmospheric fuel injection test rig – mono-dispersed droplet generator	<ul style="list-style-type: none"> <li>• Laser Doppler Anemometry</li> <li>• Phase Doppler Anemometry</li> <li>• Backlit Imaging</li> </ul>	<ul style="list-style-type: none"> <li>• In partially atomised sprays when measuring in the periphery of the spray there is poor agreement between LDA and PDA. The reason is the existence of large liquid elements of irregular shape, which PDA will reject while LDA will validate.</li> <li>• In poly-dispersed sprays there is much better agreement with some disagreement in the initial and final transient states of opening and closing of the needle, where fuel ligaments can be found.</li> <li>• Overall, the systematic approach of establishing an LDA/PDA measurement technique that allows measurements to be made over a wide droplet size range has proved to be robust and confident.</li> <li>• Simultaneously applied backlit imaging techniques are required for correct interpretation of the data collected.</li> </ul>
Arndt, S., Gartung, K., Pauer, T., Staudt, M. Renz, U. (2000) [64]	High-pressure/temperature constant volume chamber – Diesel and gasoline sprays tested	<ul style="list-style-type: none"> <li>• Laser Doppler Anemometry</li> <li>• Phase Doppler Anemometry</li> <li>• Comp. Fluid Dynamics to simulate the fuel spray development</li> </ul>	<ul style="list-style-type: none"> <li>• Combination of liquid and vapour phase measurements concluded that high pressure spray evolution is characterised by small scale turbulence.</li> <li>• Momentum exchange between spray and surrounding air directly influences fuel evaporation, in both Diesel and gasoline high-pressure sprays.</li> </ul>

Table 2-2: Literature relative to spray characterisation of high-pressure injectors (continued).

Arndt, S., Gartung, K., Pauer, T., Zeh, D., Brueggemann, D., Egermann, J., Ipp, W., Wagner, V. Leipertz, A. (2000) [65]	High-pressure/temperature constant volume chamber – Diesel and gasoline sprays tested	<ul style="list-style-type: none"> <li>• Laser Induced Exciplex Fluorescence</li> <li>• Raman Spectroscopy</li> <li>• Computational Fluid Dynamics on fuel evaporation</li> </ul>	<ul style="list-style-type: none"> <li>• Fuel vapour phase follows the path of fuel liquid phase, using nearly the same volume</li> <li>• High ambient pressure and temperature improve evaporation.</li> <li>• High injection pressures also improve vaporisation by effective air-entrainment in the spray boundaries.</li> </ul>
Boyaval, S. Dumouchel, C. (2000) [66]	High-pressure gasoline injection fuel test rig – Four pressure swirl atomisers with different design considerations	<ul style="list-style-type: none"> <li>• Light forward-diffraction technique</li> </ul>	<ul style="list-style-type: none"> <li>• Spray produced during the opening stage of the needle could be improved by increasing injection pressure.</li> <li>• Reduction of injector shape parameters (internal nozzle geometry) is found to improve atomisation and enhance the production of small droplets. Furthermore, it was found to reduce liquid spray penetration lengths.</li> <li>• Reduction of injector shape parameters is found also to increase pre-spray droplet sizes and transient stage duration.</li> <li>• Development of high-pressure swirl atomisers can be seen as a compromise between atomisation quality and pre-spray properties.</li> </ul>
Allen, J. Hargrave, G. (2000) [67]	High pressure gasoline injection test rig incorporating optically accessed 3D nozzles of swirl atomisers	<ul style="list-style-type: none"> <li>• Particle Image Velocimetry</li> <li>• Laser Doppler Anemometry</li> </ul>	<ul style="list-style-type: none"> <li>• Quantification of fluid flow velocities and structures inside real sized nozzles is valuable in developing future injectors</li> <li>• In the near nozzle exit area velocities in excess of 260m/s were measured, at injection pressure of 90bar, due to reduction of available flow area because of cavitation development</li> <li>• Processing of PIV images and their conversion to velocity maps proved to be time consuming. Since knowledge of these values are important in the development of GDI injectors, alternative techniques for quantifying fluid velocities need to be established.</li> </ul>
Lee, C.H. Reitz, R.D. (2000) [68]	Liquid drop generator and a gas nozzle arranged in a cross-flow pattern inside a constant volume chamber	<ul style="list-style-type: none"> <li>• High magnification ultra-short duration pulsed imaging</li> </ul>	<ul style="list-style-type: none"> <li>• Drop-breakup mechanism depends on the value of Weber number in each breakup regime.</li> <li>• Three breakup regimes appear as Weber number increases: <ul style="list-style-type: none"> <li>➤ Bag breakup</li> <li>➤ Stretching/thinning breakup</li> <li>➤ Catastrophic breakup</li> </ul> </li> <li>• Breakup of drops in all breakup regimes does not depend on Reynolds number.</li> </ul>

**Table 2-2: Literature relative to spray characterisation of high-pressure injectors (continued).**

Jeong, K.S, Jermy, M.C Greenhalgh, D.A (2000) [69]	High pressure gasoline fuel injection test rig fitted on a constant volume chamber using a swirl pressure atomiser	<ul style="list-style-type: none"> <li>• Laser Sheet Dropsizing</li> <li>• Laser Induced Exciplex Fluorescence</li> </ul>	<ul style="list-style-type: none"> <li>• The developed exciplex system demonstrated its potential in the LSD technique when applied to both, cold and hot high pressure gasoline fuel sprays.</li> </ul>
Araneo, L., Coghe, A., Brunello, G. Donde, R. (2000) [70]	High pressure/temperature constant volume chamber with a heated injector body assembly and a piston accumulator high pressure injection system employing a swirl injector	<ul style="list-style-type: none"> <li>• Mie imaging</li> <li>• Laser Doppler Velocimetry</li> <li>• Phase Doppler Anemometry</li> </ul>	<ul style="list-style-type: none"> <li>• Increase of the nozzle temperature and consequently fuel temperature caused an increase of the spray tip penetration velocity and a decrease of the Mean Droplet Diameter (AMD) – effect is mostly important at low ambient pressures.</li> <li>• A strong enlargement of the spray angle at the nozzle exit was noticed when fuel temperature is above the boiling point at chamber pressure conditions. At certain distance from nozzle exit, a contraction of the spray cone occurs and the hollow cone structure disappears.</li> <li>• The same effect of elevated fuel temperature was noticed even at higher chamber pressures.</li> </ul>
Nouri, J.M., Brehm, C. Whitelaw, J.H. (1999) [23]	High pressure gasoline fuel injection test rig – swirl pressure atomiser – variable injection pressure (30-100bar) and duration (3-9ms)	<ul style="list-style-type: none"> <li>• Spray Imaging</li> <li>• Phase Doppler Anemometry</li> </ul>	<ul style="list-style-type: none"> <li>• Qualitative and quantitative measurements were performed in a prototype swirl injector. It was found that the shape of the spray is almost independent of the injection pressure (30,70 and 100bars). Although spray penetration was found to increase by increasing injection pressure.</li> <li>• The maximum droplet velocities were found to increase from 50m/s to 70m/s by increasing the injection pressure from 30 to 70bar respectively while the arithmetic as well as the Sauter mean diameters (30 and 60<math>\mu</math>m respectively) were found to be nearly independent of the injection pressure.</li> </ul>
Abo-Serie, E., Arcoumanis, C., Gavaises, M., Argueyrolles, B. Galzin, F. (1999) [20]	High pressure gasoline fuel injection test rig with a constant volume chamber – swirl pressure atomiser	<ul style="list-style-type: none"> <li>• Spray Imaging</li> </ul>	<ul style="list-style-type: none"> <li>• The spray development generated by a high pressure swirl injector was analysed and four stages were identified. The first two correspond to the period prior to the liquid film formation, in the nozzle hole, while the other two to the period of film development. <ul style="list-style-type: none"> <li>➤ A very early asymmetric purely atomised bulk of liquid located at the centre of the injection hole</li> <li>➤ An asymmetric non-hollow spray</li> <li>➤ A swirl developing hollow-cone spray with a multi layer structure</li> <li>➤ A fully developed and well-atomised hollow cone spray with cone angle nearly independent of injection press.</li> </ul> </li> <li>• High magn/tion images revealed 2 modes of droplet formation, through ligaments in the direction of injection and through wave crest stripping in the radial direction.</li> </ul>

Table 2-2: Literature relative to spray characterisation of high-pressure injectors (continued).

Ipp, W., Wagner, V., Kraemer, H., Wensing, M., Leipertz, A., Arndt, S. Jain, A.K. (1999) [21]	High pressure gasoline fuel injection test rig with constant volume chamber – swirl pressure atomisers	<ul style="list-style-type: none"> <li>• Mie imaging</li> <li>• Laser Induced Exciplex Fluorescence</li> </ul>	<ul style="list-style-type: none"> <li>• There is strong influence of the ambient conditions and of the fuel rail pressure on the spray formation (cone angle, tip penetration, radial and angular distribution curves).</li> <li>• The fuel vapour phase follows the fuel liquid phase throughout the injection process and even more than 2ms after end of injection.</li> <li>• Higher injector body and fuel temperature caused a more compact distribution of both liquid and vapour fuel accompanied by a visible reduction of large droplets.</li> </ul>
Wigley, G., Hargrave, G.K. Heath, J. (1998) [19]	High pressure gasoline fuel injection test rig – air assisted and swirl pressure atomisers tested by injecting into a plenum	<ul style="list-style-type: none"> <li>• Planar imaging</li> <li>• Laser Doppler Anemometry</li> <li>• Phase Doppler Anemometry</li> </ul>	<ul style="list-style-type: none"> <li>• A new generation of LDA/PDA transmitter systems has been designed and constructed. Simultaneous 2D LDA and PDA measurements have been presented to characterise the atomisation of gasoline by high pressure automotive fuel injectors.</li> <li>• In the near nozzle area where atomisation is incomplete it is found that 2D PDA measurements underestimate the fluid flow velocity and that laser light sheet imaging could lead to false impression of the atomisation processes.</li> </ul>

**Table 2-2: Literature relative to spray characterisation of high-pressure injectors (continued).**

## 2.4 MIXTURE PREPARATION CHARACTERISATION

<b>Authors</b>	<b>Experimental Set-up</b>	<b>Techniques</b>	<b>Major Findings</b>
Fansler, T. Drake, M. (2005) [71]	Optical research DI engine with double configuration: spray-guided with central injection and wall-guided employing central spark plug – machined to accommodate endoscope probes	<ul style="list-style-type: none"> <li>• Mie high speed video</li> <li>• Spark emission spectroscopy</li> <li>• High speed spectrally resolved imaging</li> <li>• High speed refractive index matching imaging</li> </ul>	<ul style="list-style-type: none"> <li>• This paper has reviewed a suite of optical diagnostic techniques that are designed to address specific issues in developing stratified charge spark ignition direct injection gasoline engines.</li> <li>• The average air/fuel ratio at the spark gap must be rich in order to avoid misfires and partial burns associated with the large cycle-to-cycle variations in AFR.</li> <li>• Pool fires supported by thin liquid films on the piston are the dominant source of soot emissions from the wall guided engine under warmed-up, part load conditions.</li> <li>• In the early development stages of the wall guided concept it was thought that the optimum fuel /air ratio at the spark plug would be stoichiometric or slightly lean to minimise rich combustion that was the primary source of soot formation and that fuel films on the piston were a major if not dominant source of hydrocarbon emissions.</li> </ul>

**Table 2-3: Literature relative to mixture preparation characterisation.**

<p>Mitroglou, N., Arcoumanis, C., Mori, K. Motoyama, Y. (2005) [7]</p>	<p>Single cylinder optical DI engine – multi-valve, central injected, twin-spark configuration – variable swirl control valve installed – multi-hole nozzles (6hole asymmetric, 12hole symmetric, both 90° cone angle)</p>	<ul style="list-style-type: none"> <li>• Laser Induced Fluorescence</li> </ul>	<ul style="list-style-type: none"> <li>• Laser induced fluorescence was employed to reveal fuel concentration and local air/fuel ratio measurements in a fully optical single cylinder DI engine with central injection, twin spark-plug and variable in-cylinder swirl levels, along a central plane of the cylinder with a 6.5mm offset relative to the spark-plugs plane.</li> <li>• The twin-spark combustion concept is offering advantages in HC and smoke emissions relative to its side-injection, wall-guided counterpart. Additionally, the resulted reduced injector tip temperature minimises the problem of cocking in multi-hole injectors.</li> <li>• Multi-hole sprays are characterised by increased spray tip penetration, relative to swirl or hollow cone sprays. This feature presents some fuel impingement on the piston. On the other hand, increased penetration momentum makes the spray insensitive to in-cylinder airflow leading to simpler engine management systems.</li> <li>• Injection timing controls wall impingement resulting in quick and efficient evaporation for homogeneous operation. It also helps in creating stratification by correct timing of piston impingement.</li> <li>• In-cylinder swirl improves homogeneity significantly, but it has proved to be an obstacle in any attempt in creating stratification.</li> </ul>
<p>Fajardo, C.M., Smith, J.D. Sick, V. (2005) [72]</p>	<p>Optical single cylinder research engine – 8-hole multi-hole injector</p>	<ul style="list-style-type: none"> <li>• Particle image velocimetry</li> <li>• Planar laser induced fluorescence</li> <li>• Chemiluminescence imaging</li> </ul>	<ul style="list-style-type: none"> <li>• A brief overview was given on some imaging techniques that are useful for studies of in-cylinder mixing, ignition and combustion.</li> <li>• Particle image velocimetry was implemented to measure velocity fields around the spark-plug in a firing engine.</li> <li>• The combination of imaging of LIF of toluene, plasma emission and OH* chemiluminescence with a single camera provides a useful tool for studies of cause and effect of cyclic variability on engine's performance, such as power fluctuation or ignition instabilities.</li> </ul>
<p>Wiles, M.A., Probst, D.M. Ghandhi, J.B (2005) [73]</p>	<p>Optical research engine test bed – centrally located spark-plug, wall-guided configuration with swirl and air-assisted injectors – valve deactivation system</p>	<ul style="list-style-type: none"> <li>• Planar Laser Induced Fluorescence</li> </ul>	<ul style="list-style-type: none"> <li>• The effect of in-cylinder vaporisation on mixing was found to be relatively small under normal engine operation</li> <li>• Under valve deactivated operation the effect of vaporisation was found to be more significant due to the decrease in bulk gas temperature</li> <li>• Bulk in-cylinder flow field has a controlling effect on the mixing of gasoline direct injection spray jets</li> </ul>

**Table 2-3: Literature relative to mixture preparation characterisation (continued).**

Wang, Y-J., Wang, J-X., Shuai, S-J., Lei, X-H. An, X-L. (2005) [74]	Constant volume chamber – 2-cylinder DI engine – swirl pressure atomiser	<ul style="list-style-type: none"> <li>• Mie imaging</li> <li>• Computational Fluid Dynamics</li> </ul>	<ul style="list-style-type: none"> <li>• Double injection strategy tested for improved fuel/air mixing and brake specific fuel consumption optimisation</li> <li>• There is found to be an optimum first injection timing which gives maximum BMEP and low HC and CO emissions (early injection leads to piston impingement and late to cylinder wall impingement)</li> <li>• There is an optimum timing for the second injection pulse as well. It was found to be around 230°CA.</li> <li>• Fuel quantity ratio between 1<sup>st</sup> and 2<sup>nd</sup> injection has a significant effect on mixture formation.</li> <li>• Overall, 15-24% lower fuel consumption was achieved relative to PFI engines.</li> </ul>
Skogsberg, M., Dahlander, P., Lindgren, R. Denbratt, I. (2005) [9]	Constant pressure spray chamber – optical DI engine – multi-hole 6hole injector with 50° overall spray angle	<ul style="list-style-type: none"> <li>• Direct imaging</li> <li>• Laser Induced Exciplex Fluorescence</li> <li>• Phase Doppler Anemometry</li> <li>• Computational Fluid Dynamics</li> </ul>	<ul style="list-style-type: none"> <li>• Fuel vapour is only found in the presence of liquid fuel throughout the injection process</li> <li>• At 20mm from the nozzle exit there is an outwards rolling vortex which separates combustible vapour from liquid fuel. Unfortunately this point is too far from the nozzle for positioning the spark-plug, because at TDC the piston crown is closer than 20mm to the nozzle exit</li> <li>• When injection duration is long, high axial spray velocities lower the pressure inside the spray preventing vapour transport away from the spray and thus reduce the spray cone angle.</li> <li>• It is found that the ratio between hole length and diameter (l/d) affects spray cone angle and size distributions. In detail, reducing l/d results in an increase in droplet size.</li> </ul>
McGee, J., Alger, T., Blobaum, E. Wooldridge, S. (2004) [75]	Optical single cylinder research engine with central spark plug and uneven valve lifts for swirl generation.	<ul style="list-style-type: none"> <li>• Planar laser induced fluorescence</li> </ul>	<ul style="list-style-type: none"> <li>• Analysis of the PLIF image measurement and correction procedure indicated an accumulated uncertainty of ±15% in the semi-quantitative measurements of fuel. Most of this was attributed to uncorrected background reflections.</li> <li>• Further quantification to equivalence ratio was found to be possible though inappropriate due to excessive additional uncertainties at the conditions tested – most notably unknown temperatures and residual gas amount.</li> <li>• Tracer selection among iso-octane candidates was found not to have a significant effect on PLIF results.</li> <li>• The angle of the rear piston bowl wall was important in determining the direction in which the fuel cloud emerged from the bowl.</li> <li>• The effect of fuel injector change was less evident in PLIF images while having a significant impact on measured data. The effect of injectors on fuel preparation was thought to have occurred primarily outside the plane of measurement.</li> </ul>

Table 2-3: Literature relative to mixture preparation characterisation (continued).

<p>Honda, T., Kawamoto, M., Katashiba, H., Sumida, M., Fukutomi, M. Kawajiri, K. (2004) [35]</p>	<p>Constant volume chamber – optical DI engine – multi-hole injector</p>	<ul style="list-style-type: none"> <li>• Laser Induced Exciplex Fluorescence</li> <li>• FID</li> <li>• Computational Fluid Dynamics</li> <li>• Emission monitoring</li> </ul>	<ul style="list-style-type: none"> <li>• Multi-hole nozzles are more suitable for spray guided direct injection spark ignition systems because of their strong penetration force, which is less affected by airflow</li> <li>• There is found to be a certain relation between hole length over diameter ratio (L/D) and jet angle. Moreover, wider single jet angles expand the mixture distribution</li> <li>• When running at stable combustion conditions, there were identified regions of unstable combustion due to rich in fuel air/fuel ratios. To improve this behaviour vaporisation characteristics need to be improved.</li> </ul>
<p>Frieden, D. Sick, V. (2003) [76]</p>	<p>Research single cylinder DI engine featuring a variable swirl intake port mechanism</p>	<ul style="list-style-type: none"> <li>• Laser Induced Fluorescence</li> </ul>	<ul style="list-style-type: none"> <li>• Two extreme bulk flow conditions, high and low swirl, were investigated at 600 and 2000rpm. Images of the fuel spray at both engine speeds indicate that the fuel was vaporized faster under high swirl conditions.</li> <li>• At 2000rpm the high swirl flow severely distorts the spray geometry, pulling it to one side of the combustion chamber resulting in elongated spray cross-sections. Such distortion was not found at low swirl test cases.</li> <li>• The equivalence ratio images at 20°BTDC indicated that for both engine speeds the high swirl flow produced less homogeneous charge at the time of ignition compared to the low swirl flow mode.</li> <li>• The high swirl condition resulted in lean equivalence ratios within the viewable area, which suggests the presence of rich fuel zones at the periphery of the cylinder where optical access is restricted, as the overall equivalence ratio had been set to 1.</li> <li>• For the high swirl condition at 2000rpm and for both swirl conditions at 600rpm significant amounts of fuel re-entered the viewing plane after the initial pass of the flame front. The equivalent ratio values of the re-entered fuel were well above stoichiometric which further proves that the periphery of the cylinder is fuel rich for the high swirl cases.</li> </ul>
<p>Stan, C., Stanciu, A., Troeger, R., Martorano, L., Tarantino, C., Antonelli, M. Lensi, R. (2003) [77]</p>	<p>Pressure pulse direct injection gasoline system attached on a turbo-/supercharged engine equipped with variable valve timing</p>	<ul style="list-style-type: none"> <li>• Computational fluid dynamics</li> <li>• Imaging</li> </ul>	<ul style="list-style-type: none"> <li>• Variable valve timing led to an improved volumetric efficiency, especially at low speeds</li> <li>• Combining supercharger and variable valve timing technology with direct injection gasoline engines, a decrease of the specific fuel consumption and improved emission behaviour can be reached.</li> <li>• The presented pressure pulse direct injection system allows mixture formation control, ignition timing and position of ignition sources.</li> </ul>

**Table 2-3: Literature relative to mixture preparation characterisation (continued).**

<p>Samson, E., Renou, B. Boukhalfa, A. (2003) [78]</p>	<p>Vertical wind tunnel adapted to unsteady combustion with the fuel/air mixture convected into a transparent open combustion chamber</p>	<ul style="list-style-type: none"> <li>• Laser sheet tomography</li> <li>• Planar laser induced fluorescence</li> </ul>	<ul style="list-style-type: none"> <li>• Local and global flame structure and local equivalence ratio in front of the flame have been simultaneously obtained by coupling PLIF on acetone and laser sheet tomography</li> <li>• Initial propagation of flames in a heterogeneous mixture with a local mean equivalence ratio close to unity is similar to that of homogeneous flames with a stoichiometric premixing.</li> <li>• During propagation the flame size for heterogeneous mixtures increases more slowly than for homogeneous cases. The local stoichiometric equivalence ratio sustains flame propagation into a mean leaner mixture.</li> <li>• The contribution of heterogeneities to local flame structures clearly appears from the flame curvature distribution analysis. A large-scale smoothing of the flame front can be observed due to the presence of equivalence ratio scales smaller than turbulent scales.</li> </ul>
<p>Moreau, J., Boree, J., Bazile, R. Charnay, G. (2003) [79]</p>	<p>Square compression chamber featuring a quasi-sinusoidal piston motion. A gas injector was used</p>	<ul style="list-style-type: none"> <li>• Particle Image Velocimetry</li> </ul>	<ul style="list-style-type: none"> <li>• A non-dimensional analysis has been performed in a view to reproduce engine conditions as far as momentum injection is concerned.</li> <li>• PIV measurements of the induction, injection and compression phases have shown that jet modifies tumble characteristics during injection. In detail the rotation centre location is modified.</li> <li>• Compression measurements have shown that injection modifies tumble breakdown process. The level of fluctuating energy at the end of compression is lower after a BDC injection than without injection.</li> <li>• Injecting directly in a rotating structure involves a modification in the energy transfer process. Breakdown of tumble occurs earlier and turbulence has more time to dissipate the kinetic energy of the flow.</li> <li>• In case of real gasoline injection, the effect should be greater due to the wider area of interaction and thus momentum transfer.</li> </ul>

**Table 2-3: Literature relative to mixture preparation characterisation (continued).**

<p>Alger, T., Hall, M. Matthews, R. (2002) [80]</p>	<p>Optical engine consisted of CLR engine block and a modified GM twin cam cylinder head having the injector in the spark plug hole and the spark plug between the intake valves.</p>	<ul style="list-style-type: none"> <li>• A fibre optic spark plug probe was used to measure the equivalence ratio at the spark gap</li> </ul>	<p><b>Early Injection Strategy</b></p> <ul style="list-style-type: none"> <li>• The fuel/air mixture homogeneity in the DISI engine prior to ignition had strong dependence on both injection timing and type of bulk flow.</li> <li>• In flow fields with significant in-cylinder motion the intracyclic variation (<math>\Phi_{mix}</math>) of mixture prior to ignition at the spark gap increased significantly as the SOI was retarded from 60° to 120° ATDC, representing a decrease in mixing.</li> <li>• The CoV of equivalence ratio at ignition (<math>\Phi_{ig}</math>) increased as the injection timing was retarded. The increase in cyclic variation in the equivalence ratio at the spark plug was followed by an increase in the CoV of IMEP in every flow field except the stock in which the CoV IMEP decreased with increasing CoV <math>\Phi_{ig}</math>.</li> <li>• The amount of time it takes for the fuel to first appear at the spark plug depends on the flow field.</li> </ul> <p><b>Late Injection Strategy</b></p> <ul style="list-style-type: none"> <li>• The CoV <math>\Phi_{ig}</math> increased and <math>\Phi_{ig}</math> decreased as the SOI timing was retarded. The value of <math>\Phi_{ig}</math> correlated very well with IMEP.</li> </ul>
<p>Ortmann, R., Arndt, S., Raimann, J., Grzeszik, R. Wuerfel, G. (2001) [3]</p>	<p>High pressure gasoline fuel injection test rig attached on a constant volume chamber – Single cylinder optical engine with wide and close spacing configuration – swirl and multi-hole injectors</p>	<ul style="list-style-type: none"> <li>• Mie Imaging</li> <li>• Lase Induced Exciplex Fluorescence</li> </ul>	<ul style="list-style-type: none"> <li>• Swirl injector spray geometry is found to be dependent on the ambient pressure. In addition variations of the spray design of the swirl injector are limited to angle, inclination and few spray patterns.</li> <li>• For the multi-hole injector spray geometry only varies in penetration with varying ambient pressure. There are many more spray design variations compared with the swirl injector and the fuel spray is quite stable under cyclic variations of the charge motion.</li> <li>• Fundamental numerical simulation showed a complete evaporation of the injected fuel for both injectors within 3ms.</li> <li>• Measurements of the droplet size at 10MPa fuel pressure are comparable fore both injectors.</li> <li>• In the wall guided combustion system the multi-hole injector performed better in terms of IMEP, shoot emissions for all injection pressures as a result of the higher air entrainment in the spray and the decreased wall film.</li> <li>• In the air guided combustion system enhanced air entrainment in the spray of the multi-hole injector causes wider ignition windows</li> </ul>

Table 2-3: Literature relative to mixture preparation characterisation (continued).

Gold, M., Li, G., Sapsford, S. Stokes, J. (2000) [81]	Spray rig – Non-firing four stroke single cylinder wide spacing direct injection Ricardo optical engine – Swirl injector	<ul style="list-style-type: none"> <li>• Mie scattering</li> <li>• Qualitative laser induced fluorescence</li> <li>• Phase Doppler anemometry</li> <li>• Computational fluid dynamics</li> </ul>	<ul style="list-style-type: none"> <li>• Under atmospheric conditions the CFD spray model was found to accurately predict the progression of droplets and vortex formation within the DISI engine.</li> <li>• Late stratified injection produced a narrow liquid core surrounded by a rich vapour cloud, which was seen to be transported by the reverse tumble out of the piston bowl towards the spark plug.</li> <li>• For the early injection operation there was some evidence of linear proportionality between droplet diameter and axial velocity. The larger droplets were in the leading edge and had either originated from the initial liquid sheet break up or form some smaller faster moving droplets coalescing into larger high velocity droplets.</li> <li>• The higher temperatures and pressures present within the compression stroke with, late injection operation resulted in a reduction of the injector cone angle together with lower velocities and droplet diameters.</li> <li>• Injection during the intake stroke presented higher spray structure fluctuations, resulting from the intake air flow, with evidence of piston impingement.</li> </ul>
Lee, S., Tong, K., Quay, B.D., Zello, J.V. Santavicca, D.A. (2000) [82]	Single cylinder optical engine featuring twin spark-plug combustion chamber – Modular intake system with swirl or tumble inserts for different in-cylinder flow generation	<ul style="list-style-type: none"> <li>• Planar Laser Induced Fluorescence</li> <li>• Unburned hydrocarbons monitoring</li> </ul>	<ul style="list-style-type: none"> <li>• In cylinder tumble and swirl improve engine's cold-start performance. Best cold-start behaviour in terms of unburned hydrocarbons was recorded with tumble in-cylinder flow.</li> <li>• Performance test results agree with the analysis of the pre-combustion fuel distribution images in terms of fuel vaporisation and fuel/air mixing. The higher signal intensity and lower intensity variation is achieved by the tumble system.</li> <li>• Combustion with enhanced swirl and/or tumble flows proceeds more rapidly, compared to the baseline neutral flow system. This allows the ignition timing to be retarded, providing more time for fuel vaporisation and fuel/air mixing.</li> </ul>
Ekenberg, M. Johansson, B. (2000) [83]	Firing single cylinder close spacing optical direct injection engine, with centrally located spark plug and two different piston crown designs. – Air assisted injector	<ul style="list-style-type: none"> <li>• Laser Induced Fluorescence</li> <li>• Combustion heat release analysis</li> </ul>	<ul style="list-style-type: none"> <li>• Planar LIF has been applied for measuring the in-cylinder mixture distribution. For the flat piston arrangement it was hard to achieve stratification of the fuel around the spark plug at the time of ignition.</li> <li>• By replacing the flat piston with a bowl piston better stratification was achieved around the spark plug at the time of ignition while the lean limit of the engine increased from <math>\phi = 1/1.3</math> to <math>1/3</math>.</li> </ul>

Table 2-3: Literature relative to mixture preparation characterisation (continued).

<p>Alger, T., Hall, M. Matthews, R.D. (2000) [84]</p>	<p>Firing four cylinder engine with optical access – swirl pressure atomiser</p>	<ul style="list-style-type: none"> <li>• Mie imaging</li> <li>• In-cylinder fibre optic probe for local equivalence ratio measurement</li> </ul>	<ul style="list-style-type: none"> <li>• When injecting early during the induction stroke, intake flow affects the spray development and rules surface wetting. Tumble flow leads to liner wall wetting, while swirling in-cylinder flow results in fuel impinging on the piston.</li> <li>• Bulk motion exists late in the compression stroke due to in-cylinder swirl or tumble flow.</li> <li>• High tumble flow-fields yield the highest equivalence ratio in the spark gap area than any other flow for any injection timing</li> <li>• Injection timing controls the amount of wall wetting and the effect of the bulk flow on the spray.</li> <li>• The best injection timing for high tumble in-cylinder flows is located around bottom dead centre and not early or late during induction or compression strokes respectively.</li> <li>• Fuel/air mixing is mainly independent of RPM but depends on vaporisation time and injector flow rate</li> <li>• At high RPM the increased gas motion compensates for the increased pressure to increase vaporisation.</li> <li>• As a result RPM directly affect equivalence ratio.</li> </ul>
<p>Kanda, M., Baika, T., Kato, S., Iwamuro, M., Koike, M. Saito, A. (2000) [31]</p>	<p>Toyota four cylinder firing direct injection engine with a shell-shaped piston cavity – Intake features a swirl control valve and a helical port – newly developed fan-shaped spray</p>	<ul style="list-style-type: none"> <li>• Fuel spray imaging</li> <li>• Laser Induced Fluorescence</li> </ul>	<ul style="list-style-type: none"> <li>• The fan spray injector can vary its droplet breakup length according to nozzle slit design characteristics. Nozzles with short breakup length are required in order to optimise the piston bowl shape for stratified operation.</li> <li>• The side wall shape of the cavity is important in controlling torque fluctuation by accelerating combustion.</li> <li>• The newly developed combustion system with a fan spray injector enlarges the stability range of stratified combustion relative to existing DI combustion systems.</li> <li>• The same system also presents full-load torque improvements at most speeds compared to standard DI configurations.</li> <li>• A 3L, 6 cylinder engine equipped with the above system demonstrated a 20% fuel economy improvement when tested in the Japanese 10-15 mode driving cycle.</li> </ul>

**Table 2-3: Literature relative to mixture preparation characterisation (continued).**

<p>Pontoppidan, M., Gaviani, G., Bella, G., Schilardi, M. Rocco, V. (2000) [85]</p>	<p>Firing four cylinder engine featuring optical access through a piston window and a pressure swirl atomiser</p>	<ul style="list-style-type: none"> <li>• Computational fluid dynamics</li> <li>• Combustion imaging with light intensity sensor</li> </ul>	<ul style="list-style-type: none"> <li>• On a small bore engine none of the mixture preparation layouts alone represent a “magical” solution, but each of them needs a high degree of flexibility of the components creating the combustion chamber boundary conditions in order to produce a high level lean combustion stability over the entire low load working area.</li> <li>• Variable valve train offers the potential of a cylinder-individual continuous airflow control without the head loss and back flow drawbacks of the mechanical secondary throttle solutions.</li> <li>• The only disadvantage for the time being is that it is still under development and therefore not cost-optimised.</li> </ul>
<p>Kakuhou, A., Urushihara, T., Itoh, T. Takagi, Y. (1999) [86]</p>	<p>Four-valve single cylinder optical engine with pent-roof type chamber, piston crown bowl and swirl control valve. (wide-spacing)</p>	<ul style="list-style-type: none"> <li>• Laser Doppler Velocimetry</li> <li>• Particle Image Velocimetry</li> <li>• Laser Induced Fluorescence</li> </ul>	<ul style="list-style-type: none"> <li>• The combined effect of the swirl motion in the cylinder head the cylindrical piston bowl positioned eccentrically to the cylinder central axis, forms an upward flow that rises from the piston crown near the cylinder centre area to the cylinder head in the latter half of the compression.</li> <li>• The fuel injected directly into the cylinder initially enters the piston bowl and then transported to the vicinity of the spark plug by the upward flow forming mixture stratification.</li> <li>• The ideal injection timings are determined from the balance between fuel trapping in the piston bowl and fuel film formation on the piston crown. <ul style="list-style-type: none"> <li>➤ Too early injection timing results in a fuel spray that is not trapped in the piston bowl and travels towards the exhaust side of the combustion chamber, which precludes mixture stratification and causes a large fluctuation in the mixture concentrations in the vicinity of the spark plug thus resulting in unstable combustion.</li> <li>➤ Too late injection timing results in higher mixture concentration in the vicinity of the spark plug however results in increased liquid film on the piston bowl.</li> </ul> </li> </ul>

**Table 2-3: Literature relative to mixture preparation characterisation (continued).**

Choi, K.H., Park, J.H., Lee, N.H., Yu, C.H. Noh, S.H. (1999) [87]	High-pressure chamber. Single cylinder optical engine with flat piston window as well as an opaque bowl shaped piston adaptor	<ul style="list-style-type: none"> <li>• Mie scattering</li> <li>• Phase Doppler Anemometry</li> <li>• Laser Doppler Velocimetry</li> <li>• Particle Image Velocimetry</li> </ul>	<ul style="list-style-type: none"> <li>• Swirl injector spray grows in dispersion but is suppressed in penetration with the development of a ring vortex produced by strong entrainment of air into spray.</li> <li>• Spray under high ambient pressure is changed into compact shape and is not developed into a hollow cone shape.</li> <li>• SMD from the swirl injector under room temperature condition was measured within 15~30<math>\mu</math>m. It was also found that as the air is strongly induced into the spray the droplet size becomes small and uniform very fast.</li> <li>• Visualization of the spray distribution after impingement on a flat or a bowl piston for two different injector positions proved, that for the particular engine arrangement the intake side injection seems to be most favourable for stratified mixture formation near the spark plug for the late compression injection strategy.</li> <li>• By strengthening the counter rotating tumble velocity and piston top shape into bowl structure was found to conserve the bulk motion toward the spark plug in the compression stroke.</li> </ul>
Arcoumanis, C., Gold, M.R., Whitelaw, J.H. Xu, H.M. (1999) [6]	Single cylinder research engine with shrouded valves for swirl and tumble ratios increase and local direct injection of propane/air mixture	<ul style="list-style-type: none"> <li>• Flame Ionisation Detection</li> <li>• High-speed flame imaging</li> </ul>	<ul style="list-style-type: none"> <li>• Local injection of a slightly rich mixture of propane/air at an engine speed of 1000RPM led to faster flame growth. Pressure measurements indicate that the locally rich zone enhanced the early flame development.</li> <li>• A controlled locally rich mixture is able to extend the lean driveability limit to an overall equivalence ratio of 0.61.</li> <li>• Strong inlet induced bulk flow minimises the effect of the local rich zone.</li> <li>• At lean overall mixture strengths the localised air fuel ratio is very important in achieving stable combustion and overcoming adverse in-cylinder flow conditions.</li> </ul>
Alger, T., Hall, M. Matthews, R. (1998) [88]	Optical engine consisted of CLR engine block and a modified GM twin cam cylinder head – weak and strong tumble was tested	<ul style="list-style-type: none"> <li>• Mie imaging</li> <li>• Fiber optic fuel vapour concentration measurement</li> </ul>	<ul style="list-style-type: none"> <li>• Intake flow configuration has a significant effect on fuel distribution. With increasing tumble the cylinder gases severely distort the fuel jet. Bulk motion due to tumble exists very late into the compression stroke.</li> <li>• Amount of in-cylinder tumble has a significant effect on the local equivalence ratio at TDC. At all engine speeds tested increased tumble resulted in an increase in the equivalence ratios at TDC from 40-100% for both early and late injection timings.</li> <li>• Piston wetting has a significant effect on equivalence ratio at TDC. Extended piston wetting lowers the equivalence ratio at TDC. Very early and late injection timings result in a low equivalence ratio at TDC because of piston wetting, in contrast to BDC injection.</li> </ul>

Table 2-3: Literature relative to mixture preparation characterisation (continued).

Ando, H. (1997) [4]	Four cylinder four valve engine using an upright straight intake port and a swirl injector	<ul style="list-style-type: none"> <li>• Pressure analysis</li> <li>• Laser light extinction</li> <li>• HC, NO<sub>x</sub>, CO<sub>2</sub> and CO emissions</li> <li>• Laser induced fluorescence</li> <li>• Schlieren photography</li> </ul>	<ul style="list-style-type: none"> <li>• Soot and CO emissions were controlled by a two-stage mixing process where soot and CO created in the late rich injection cloud (60°-80° BTDC) are oxidized and burned in the lean early injected mixture (280°BTDC)</li> <li>• Two stage mixing increased the low speed torque by 10% and allowed a compression ratio of 12:1 to be used</li> <li>• A steeper in-cylinder injection angle was used to improve the high speed fuel consumption with the benefit of higher EGR tolerance hence lower NO<sub>x</sub></li> <li>• A two stage combustion approach of injection in the expansion stroke reduced the catalyst 'light-up' time by the factor of 3 with improved cold start emissions</li> </ul>
Ohsuga, M, Shiraishi, T, Nogi, T, Nakayama, Y Sukegawa, Y - Hitachi Ltd (1997) [89]	Single cylinder four-valve engine with a flat top piston, utilizing a manifold swirl control air jet passage.	<ul style="list-style-type: none"> <li>• Laser Induced Fluorescence</li> <li>• Pressure curve analysis</li> </ul>	<ul style="list-style-type: none"> <li>• Central close spacing direct fuel injection with swirl inducing manifold resulted in stratification at the cylinder centre.</li> <li>• A low spray speed of 22m/s combined with a solid cone geometry while injecting at 240° BTDC improved combustion stability during transient and cold start conditions with the lean limit extended to an A/F ratio of 40:1</li> </ul>
Ghandhi, J.B Bracco, F.V (1996) [90]	Single cylinder research engine with ported configuration and intake swirl inserts	<ul style="list-style-type: none"> <li>• Laser Induced Fluorescence</li> <li>• Combustion analysis</li> </ul>	<ul style="list-style-type: none"> <li>• A large number of cycles, nearly 30%, were found with an average equivalence ratio near the spark-plug far leaner than the lean limit, but these cycles were able to ignite and combust fully. The expected cause for this behaviour is the mixture motion during the spark discharge.</li> <li>• There was a weak correlation between the local average equivalence ratio and the early combustion as measured by the pressure 10°CA after spark timing, the rate of pressure rise 5° after spark timing or the delay time for a 100kPa pressure rise. This weak correlation is considered to be the result of mixture motion. This results in a false measured fuel distribution at the time of ignition.</li> <li>• Direct injection systems are expected to experience these effects because of motions induced by the injected fuel jets.</li> </ul>

**Table 2-3: Literature relative to mixture preparation characterisation (continued).**

Kume, T., Iwamoto, Y., Lida, K., Murakami, M., Akishino, K. Ando, H. (1996) [91]	Two four valve engines one with an upright port and the other with a conventional port, with low and high intensity swirl injectors.	<ul style="list-style-type: none"> <li>• Phase Doppler Velocimetr</li> <li>• Hi speed photography</li> <li>• Pressure analysis</li> <li>• Flame radiation imaging</li> <li>• HC, NO<sub>x</sub>, smoke and O<sub>2</sub> emissions</li> </ul>	<ul style="list-style-type: none"> <li>• Stable combustion for partial load was realized at A/F ratios in excess of 40:1 by stratification through the use of upright intake ports and a piston cavity to form reverse tumble (TVR=1.8) combined with compression stroke injection using high intensity swirl injector.</li> <li>• Early intake stroke injection realized a homogeneous mixture distribution used in full load operation</li> <li>• The use of minimal throttling increased part load volumetric efficiency while at full load a further increase was gleaned from the charge cooling effect of the early injected fuel</li> <li>• Due to the charge cooling there was a lower octane requirement and hence a higher compression ratio of 12:1 could be used with subsequent 10% increase in the power output</li> <li>• EGR was shown to curb the increased NO<sub>x</sub> emissions due to the stratification.</li> </ul>
--	--	---	---

**Table 2-3: Literature relative to mixture preparation characterisation (continued).**

## 2.5 MISCELLANEOUS ENGINE EXPERIMENTS

Authors	Experimental Set-up	Techniques	Major Findings
Lang, O., Geiger, J., Habermann, K. Wittler, M. (2005) [92]	2.0Litre four cylinder naturally aspirated DI engine – 1.4Litre four cylinder turbocharged DI engine – swirl and multi-hole injectors	<ul style="list-style-type: none"> <li>• Computational fluid dynamics</li> <li>• Simple engine's operating parameters acquisition</li> </ul>	<ul style="list-style-type: none"> <li>• Multi-hole nozzles appear to have reduced wall wetting relative to swirl pressure atomisers.</li> <li>• For turbocharged direct injection spark ignition engine there is larger range of camshaft timing adjustment for the exhaust than intake at 1000RPM</li> <li>• A fuel consumption reduction of 13-18% was noticed compared to the PFI engine due to downsizing.</li> <li>• The combined use of turbocharger and direct injection create a very promising package. Direct injection technology with the increased compression ratio improves low-end torque reducing the effect of turbo-lag present in all turbocharged PFI engines.</li> <li>• Additional advantages in residual gas control can be gained from this coupling and another 6% fuel consumption reduction can be made possible.</li> </ul>

**Table 2-4: Literature of miscellaneous engine experiments.**

<p>Szekely, Gerald A. Alkidas, Alex C. (2005) [17]</p>	<p>Optical single cylinder research engine based on the spray-guided concept with a pentroof type combustion chamber and a high squish piston – Outward opening 90° injector, centrally located</p>	<ul style="list-style-type: none"> <li>• Simple engine data acquisition</li> <li>• Emissions monitoring</li> </ul>	<ul style="list-style-type: none"> <li>• This paper presents a complete overview of the spray guided concept by testing several parameters, such as double injection, injector lift altering, dwell time between injection pulses and intake induced swirl motion at 2000RPM and part load operation.</li> <li>• Increasing the injection duration by decreasing injector's lift, fuel consumption was improved and combustion duration was shortened, with no significant effect on emissions.</li> <li>• At each end of injection timing there is an optimal ignition timing presenting the best possible engine operation. This ignition window is very narrow though (<math>\pm 3^\circ\text{CA}</math>) and any other timing causes the engine's operation to deteriorate.</li> <li>• Air motion was found to have a negative effect on the stability of the ignition process and initial flame kernel development. Increasing swirl caused an increase in the CoV of IMEP. Minimum swirl resulted in minimum HC emissions, CoV of IMEP and fuel consumption.</li> <li>• Multiple injection did not lead to any improvements, at least at part load.</li> <li>• The more the injection pulses the shorter the delay between end of last injection and ignition timing.</li> <li>• With increasing dwell time between injection pulses, fuel consumption showed a slight increase as well as HC emissions due to longer mixing times, when compared with single injection.</li> <li>• The best results in fuel consumption for multiple injection strategy were seen when end of last injection pulse was placed at around 45-50°BTDC.</li> <li>• On the other hand, single injection has a wider injection timing range maintaining low fuel consumption.</li> <li>• Single injection produces the lowest CO of all. This means that single injection achieves the best mixing, which is followed by faster combustion and low smoke emissions.</li> </ul>
--	---	--	---

**Table 2-4: Literature of miscellaneous engine experiments (continued).**

<p>Kawamoto, M., Honda, T., Katashiba, H., Sumida, M., Fukutomi, N. Kawajiri, K. (2005) [93]</p>	<p>Optical single cylinder research engine equipped with a quartz liner and 2 multi-hole nozzles</p>	<ul style="list-style-type: none"> <li>• Simple combustion data acquisition</li> </ul>	<ul style="list-style-type: none"> <li>• Both tested configurations, side and centre injection, achieved spray guided direct injection spark ignition engine operation.</li> <li>• Centre injection achieved combustion at a continuous range of ignition timings. It also yielded a broader stable combustion area compared to the side injection concept.</li> <li>• Centre injection also produced slightly higher unburned HC emissions than side injection, due to the narrow spacing available for mixture formation.</li> <li>• Centre injection looks very promising and could be the leading concept in direct injection engine design with some improvements. By improving atomisation of the fuel spray and air entrainment the results will be faster fuel vaporisation and better homogenisation. Given these conditions, the centre injection concept combines many advantages compared to its side injection counterpart.</li> </ul>
<p>Szekely, Gerald A. Jr., Solomon, Arun S. Tsai, P.-H. (2004) [94]</p>	<p>Research single cylinder DI engine featuring a Reverse Tumble Wall Controlled combustion system</p>	<ul style="list-style-type: none"> <li>• Computational fluid dynamics</li> <li>• Basic engine data acquisition</li> <li>• Combustion analysis</li> </ul>	<ul style="list-style-type: none"> <li>• At the reverse Tumble Wall-Controlled combustion system dominant flow is the tumble plane that contains the axis of the spark-plug and injector, therefore sufficient time and path length should be provided for effective mixing in this plane.</li> <li>• There is an optimum piston bowl volume, this is 50-60% of the combustion chamber volume. If this volume is smaller, then the bowl cannot contain the mixture and if larger then the resulted overmixing causes misfires and increase in HC emissions.</li> <li>• The optimum overall spray cone angle is found to be around 90°.</li> <li>• The optimum combustion chamber developed leads to a world class reverse tumble wall controlled gasoline direct injection engine that was superior to the baseline port fuel injection engine as well as to all competitive tumble wall controlled gasoline direct injection systems.</li> </ul>

**Table 2-4: Literature of miscellaneous engine experiments (continued).**

<p>Lippert, A.M, El Tahry, S.H, Huebler, M.S, Parrish, S.E., Inoue, H, Noyori, T. (2004) [26]</p>	<p>Constant volume chamber – 4 cylinder DI engine with swirl control valve installed and equipped with fan-spray and multi-hole injectors</p>	<ul style="list-style-type: none"> <li>• Computational fluid dynamics</li> <li>• Phase Doppler interferometry</li> </ul>	<ul style="list-style-type: none"> <li>• The complex nature of full load operation was investigated during the development and optimisation of the WOT operation of a small bore SIDI engine.</li> <li>• Hot fuel reduces injected droplet sizes and overall spray cone angle.</li> <li>• Lack of mixing limits the air utilisation and hence limits the amount of heat release for improving vol. efficiency.</li> <li>• At low to medium engine speed mixing process and homogeneity at ignition timing are highly dependent on injection timing for low in-cylinder flow levels.</li> <li>• Mixing behaviour between high and low RPM is significantly different. At high RPM advanced injection id required because injecting late during intake stroke cannot overcome the momentum of inducted air.</li> <li>• Volumetric efficiency is strongly dependent on the amount of wall wetting, due to the effective heating effect of vaporisation off surfaces rather than intake charge. At high RPM, retarding injection increases vol. eff. This necessitates a trade off between mixing (advanced injection) and volumetric efficiency (retarded injection). At low to medium RPM is more advantageous to achieve sufficient mixing than volumetric efficiency. This can be done by either split injection or strong in-cylinder flows.</li> <li>• Swirl promotes mixing as well and it better solution because SCV is only a function of RPM and not also load.</li> <li>• Near complete mixing can be achieved with increased tumble at high RPM</li> </ul>
<p>Lippert, A.M, El Tahry, S.H, Huebler, M.S, Parrish, S.E., Inoue, H, Noyori, T, Nakama, K Abe, T. (2004) [27]</p>	<p>Constant volume chamber – 4 cylinder DI engine with swirl control valve installed and equipped with fan-spray, multi-hole and swirl injectors</p>	<ul style="list-style-type: none"> <li>• Computational fluid dynamics</li> <li>• Mie imaging</li> <li>• Phase Doppler interferometry</li> <li>• Basic engine data acquisition</li> </ul>	<ul style="list-style-type: none"> <li>• As far as the multi-hole injector is concerned, two findings should be pointed out: <ul style="list-style-type: none"> <li>➤ Large L/D ratios suppress the turbulence and create a more developed flow profile leading to narrower plumes</li> <li>➤ Atomisation is a strong function of injection pressure</li> </ul> </li> <li>• Combination of atomisation, penetration, air entrainment and momentum distribution are critical for successful injector selection</li> <li>• In the case of multi-hole injector, unequal penetration of the separate jets could cause impingement that is responsible for smoke emissions</li> <li>• Increased fuel jet penetration does not necessarily mean wall wetting; key element to achieve this is the amount of air entrainment.</li> <li>• At part- and lower loads/speeds, optimisation of engine operation requires containment of the fuel in the piston bowl. Multi-hole's individual jets are instrumental in reducing the penetration towards the head and spark plug.</li> <li>• The role of swirl for part-load operation is</li> </ul>

			<p>related to bulk transport of fuel/air mixture and not to enhance mixing.</p> <ul style="list-style-type: none"> <li>• Piston design is also very critical. Shallow piston bowls increase smoke emissions and the increase is even steeper when coupled with retarded injection timings.</li> </ul>
Landenfeld, T., Kufferath, A. Gerhardt, J. (2004) [34]	Real engine test bed. – swirl pressure atomiser and multi-hole injectors	<ul style="list-style-type: none"> <li>• Basic engine data acquisition</li> <li>• Emissions monitoring</li> </ul>	<ul style="list-style-type: none"> <li>• Optimisation of combustion in an engine using multi-hole injectors can lead to a reduction in HC emissions by 10%</li> <li>• Homogeneous split injection strategy is an effective way to achieve fast catalyst heating by efficient heat production in the exhaust while maintaining low HC emission levels.</li> <li>• Dominating effect during engine's starting phase is not the type of spray generation but the size and momentum of fuel droplets.</li> <li>• For short injection durations, needed when running in stratified mode and <math>AFR &gt; 35</math>, the multi-hole injector can build up a stable spray quicker than the swirl pressure atomiser and therefore better homogenisation can be achieved.</li> <li>• At high loads and 4000RPM slightly lower fuel consumption was recorded with the multi-hole injector; this is probably due to stable spray pattern with increasing chamber pressure.</li> </ul>
Lake, T., Stokes, J., Murphy, R., Osborne, R. Schamel, A. (2004) [95]	Real engine equipped with the Ricardo Lean Boost Direct Injection system	<ul style="list-style-type: none"> <li>• Basic engine data acquisition</li> </ul>	<ul style="list-style-type: none"> <li>• Low CO<sub>2</sub> gasoline engines are needed as an essential part of any profitable powertrain portfolio.</li> <li>• A good method of achieving low CO<sub>2</sub> is by raising the specific torque levels of the gasoline engine; this allows a volumetrically smaller engine to replace a large one – so called “downsizing”</li> <li>• Downsizing approaches that are applied well not only reduce pumping losses and friction, but deliver improved indicated efficiency benefits which in turn deliver improvements over a wide range of operating conditions with a direct impact to the vehicle owner.</li> <li>• This paper has considered various technologies to raise the specific torque levels of the gasoline engine and has shown that the best fuel economy is obtained with the Lean Boost Direct Injection approach</li> <li>• A substantial fuel economy benefit of more than 20% has been measured compared to the base naturally aspirated engine whilst being capable of meeting half EuroIV emissions over the NEDC cycle.</li> </ul>

**Table 2-4: Literature of miscellaneous engine experiments (continued).**

<p>Solomon, Arun S. Szekely, Gerald A. Jr. (2003) [96]</p>	<p>Real engine modified with a reverse-tumble wall-controlled direct-injection combustion system – Spark-plug centrally located and wide-spacing config. having the 90° swirl injector at the intake side.</p>	<ul style="list-style-type: none"> <li>• Basic engine data acquisition</li> <li>• Emissions monitoring</li> <li>• Combustion analysis</li> </ul>	<ul style="list-style-type: none"> <li>• Combustion efficiency was determined to be the single largest influential parameter in stratified charge combustion</li> <li>• Improving combustion efficiency simultaneous improvements in thermal efficiency, HC and NOx emissions and combustion stability can be had</li> <li>• There is an optimum End of Injection timing determined by combustion efficiency: <ul style="list-style-type: none"> <li>➤ Retarding EOI, combustion efficiency drops due to impingement of fuel on the piston, which causes the engine to operate in high smoke levels.</li> <li>➤ Advancing EOI, combustion efficiency drops again due to much time available for over-mixing and spray arriving too early for proper wall guidance from the piston; this causes combustion instability.</li> </ul> </li> <li>• The reverse-tumble wall-controlled DI combustion system proved to be much more tolerant to EGR dilution than a conventional PFI engine, probably due to higher burning rate.</li> </ul>
<p>Eichlseder, H., Baumann, E., Mueller, P. Rubbert, S. (2000) [97]</p>	<p>Real four cylinder engine equipped with exhaust after-treatment systems – NOx trap</p>	<ul style="list-style-type: none"> <li>• Basic data acquisition over the NEDC</li> <li>• Combustion analysis</li> </ul>	<ul style="list-style-type: none"> <li>• Today the full fuel saving potential of a direct injection engine cannot be achieved under US and European boundary conditions</li> <li>• For both, lean and stoichiometric concepts, the combustion system is the core element for low emissions and good fuel economy</li> <li>• In the tension area of low emissions and low fuel consumption different DI concepts have specific strengths and weaknesses</li> <li>• Split injection creates a new flexibility during start- and warm-up phases helping to improve emissions behaviour until light-off</li> <li>• Stratified lean operation gives the highest fuel economy potential but it requires a new exhaust after-treatment technology and special fuel quality.</li> </ul>

**Table 2-4: Literature of miscellaneous engine experiments (continued).**

Koike, M., Saito, A., Tomoda, T. Yamamoto, Y. (2000) [30]	Engine and constant volume chamber test rigs for the development of a new combustion concept	<ul style="list-style-type: none"> <li>• Spray – mixture characterisation</li> <li>• Engine operating behaviour</li> </ul>	<ul style="list-style-type: none"> <li>• A new combustion system that produces a stratified mixture by a fan-spray and shell-shaped piston cavity has been developed. It does not require special charge motion like tumble or swirl.</li> <li>• Characteristics of the fan-spray are: <ul style="list-style-type: none"> <li>➢ Large penetration compared to hollow-cone spray</li> <li>➢ Uniform fuel distribution inside the spray</li> <li>➢ Stable and robust spray pattern, insensitive to ambient condition changes</li> </ul> </li> <li>• The new combustion system produces under-mixing of fuel, confirmed by LIF measurements.</li> <li>• The developed system improves fuel consumption as well as smoke, CO and HC emissions at middle load and engine speed</li> <li>• Thermodynamic analysis showed that this new system makes the burning velocity fast, especially at the end of combustion process. This causes increased heat release near TDC</li> <li>• HC emissions at low load are lower than that of conventional DI combustion systems, even at high EGR rates condition.</li> </ul>
Fry, M., King, J. White, C. (1999) [98]	Single cylinder engine was used to assess two alternative DISI systems reverse tumble charge motion with high pressure swirl-type fuel injector (RTGDI) and low pressure air-assist direct injection (AAGDI). An MPI version of the same engine was tested as a baseline	<ul style="list-style-type: none"> <li>• Full load and part load performance testing</li> <li>• Full load and part load emissions HC, CO, NO<sub>x</sub></li> <li>• CFD</li> <li>• Engine simulation GTPower</li> </ul>	<ul style="list-style-type: none"> <li>• Both the RTGDI and the AAGDI systems were successfully implemented into an engine and both run into stratified and homogeneous modes</li> <li>• AAGDI was more flexible in its operation at part load tolerating greater ranges of injection timing and AFR/EGR, whilst maintaining stable combustion</li> <li>• Both systems gave improvements to the VE at full load. The AAGDI gave improved full load performance while the RTGDI did not deliver the expected improvement in engine torque.</li> <li>• CFD is a key analytical tool in the development of DISI combustion systems for assessing different port/chamber/piston geometries.</li> <li>• Cycle simulation provides a great deal of information that is difficult to obtain experimentally an example being in-cylinder residual fraction.</li> </ul>

Table 2-4: Literature of miscellaneous engine experiments (continued)

<p>Geiger, J., Grigo, M., Lang, O., Wolters, P. Hupperich, P. (1999) [2]</p>	<p>Firing DI engine equipped with the Charge Motion Controlled Combustion System</p>	<ul style="list-style-type: none"> <li>• Computational fluid dynamics</li> <li>• Combustion analysis</li> <li>• Emissions monitoring</li> </ul>	<ul style="list-style-type: none"> <li>• The new charge motion controlled combustion system for gasoline engines with direct fuel injection shows an excellent fuel economy potential compared to other DI concepts.</li> <li>• It realises a stable operation all over the entire speed/load regime.</li> <li>• The influence of injection timing and spark advance on emissions and ignition stability is low, compared to other investigated concepts.</li> <li>• High EGR tolerance allows a significant reduction of the engine out NOx emissions.</li> <li>• The compact and centrally located combustion chamber enables thermodynamically optimal and knock-free combustion.</li> <li>• The combination of firing engine tests and optical investigations with CFD calculations enables an efficient process optimisation.</li> </ul>
<p>Pontoppidan, M., Gaviani, G., Bella, G., DeMaio, A. Rocco, V. (1999) [99]</p>	<p>Real four cylinder small displacement engine – swirl pressure and closed cap atomisers tested</p>	<ul style="list-style-type: none"> <li>• Computational fluid dynamics</li> <li>• Basic engine data acquisition</li> <li>• Combustion analysis</li> </ul>	<ul style="list-style-type: none"> <li>• The very high sensitivity of the small bore engine to fuel spray mean penetration velocity and spray angle is confirmed</li> <li>• The choice of a mixed (air and solid shape guided) mixture preparation concept seems to be the optimal design direction for the combustion chamber geometry</li> <li>• The two-stage injection strategy enables a lean stratified operation mode, but the ratio of intake stroke to compression stroke injected fuel, as well as the phase of the late injection, remain critical parameters.</li> <li>• A potential increase in cycle-to-cycle combustion instability is observed in the mid-load lean mode as well as in the transition area between lean stratified and homogeneous stoichiometric mixture.</li> <li>• Off-axis deviated spray geometries can be an important feature for the optimisation for the small bore concept. However with this approach, particular efforts must be made in the atomiser design to ensure that the spray angles as well as mean penetration velocity are kept low.</li> </ul>

**Table 2-4: Literature of miscellaneous engine experiments (continued).**

<p>Whitaker, P.A., Stokes, J. Lake, T.H. (1998) [100]</p>	<p>Four combustion systems:  <b>(a)</b> Ricardo side port, central injector and central plug engine with central piston bowl optimised for wall guided operation  <b>(b)</b> Ricardo side port central injector and plug with exhaust side piston bowl designed for air guided operation  <b>(c)</b> Ricardo top entry port engine with inlet side piston bowl  <b>(d)</b> Toyota D4 engine ( side port, inlet side injector and piston bowl, swirling) adapted to run as a Hydra single cylinder engine</p>	<ul style="list-style-type: none"> <li>• Pressure analysis</li> <li>• HC and NO<sub>x</sub> emissions</li> </ul>	<ul style="list-style-type: none"> <li>• A variety of direct injection systems are capable of stable stratified and homogeneous operation</li> <li>• Combustion systems that provide satisfactory stratified performance may not necessarily demonstrate the expected benefits when operated at homogeneous mode</li> <li>• The side port, side injector swirling configuration provided the best unthrottled stratified results by using high swirl ratios as well as variable swirl control for achieving acceptable full load performance</li> <li>• The central injector central spark plug configuration with standard tumbling intake ports provides the best homogeneous results while promising results were obtained in the development of the stratified operation</li> <li>• Top entry systems has demonstrated excellent all around capability. It provides low emissions and excellent stability with lean AFRs and high EGR rates under stratified operation. Competitive homogeneous results were achieved with low levels of air motion</li> <li>• Side port HC emissions reduce with up to 20% EGR after when they increase. To the tolerance limit an 86% NO<sub>x</sub> reduction carries a 9% HC penalty</li> <li>• For the top entry engine HC emissions continue to decrease with increasing EGR rate up to the tolerance limit inn which an 80% NO<sub>x</sub> and a 42% HC reduction is achieved</li> </ul>
<p>Harada, J., Tomita, T., Mizuno, H., Mashiki, Z. Ito, Y. (1997) [101]</p>	<p>Four cylinder four valve having an involute piston cavity with a helical and straight port using a swirl control valve</p>	<ul style="list-style-type: none"> <li>• Fuel spray and flame imaging</li> <li>• In-cylinder gas sampling</li> <li>• Heat release and pressure analysis</li> <li>• HC, NO<sub>x</sub> and CO emissions</li> </ul>	<ul style="list-style-type: none"> <li>• Fuel economy improvements of 22% and A/F ratios greater than 30:1 were realized with the new design</li> <li>• Three injection strategies were employed using 'drive by wire' control of the throttle, injection and swirl valve to achieve stratified ultra lean stoichiometric and two stage injection strategy (for smooth transient operation)</li> <li>• The injection strategies together with a storage-reduction catalyst avoided smoke emissions and combined with EGR produced low NO<sub>x</sub>, HC and CO emissions.</li> <li>• The partial load combustion of the DI engine at an A/F ratio of 27:1 was more stable and faster than the conventional stoichiometric engine.</li> <li>• Some throttle control was still required to maintain the necessary exhaust temperature for the catalyst and a vacuum for the braking system</li> </ul>

**Table 2-4: Literature of miscellaneous engine experiments (continued).**

## 2.6 SUMMARY OF LITERATURE REVIEW

An extensive body of literature has been reviewed in this chapter in order to provide the foundation for the understanding and analysis of the subsequent results. In what follows, an attempt was made to provide a critical analysis, albeit brief, of the approach followed by the different investigators in resolving the internal flow and spray characteristics of high-pressure gasoline engine injectors, and the fuel/air mixing and performance in direct-injection spark-ignition engines.

Initially, knowledge of the internal nozzle flow in high-pressure injectors represents the first step in understanding the emerging spray structure. The experimental approach followed in the characterisation of the internal nozzle flow is by using enlarged transparent nozzles to obtain indirect information about the real-size nozzles used in gasoline DI engines. This technique, although able to identify both geometric and dynamic cavitation patterns, is unable to represent the flow velocities and Reynolds numbers present in nozzles under engine operating conditions. Taking into account the above issues, the approach used in this thesis has been to employ scaled-up transparent model nozzles under equivalent cavitating conditions to real-size injectors, assuming cavitation number (CN) similarity (refer to Chapter 3 for definition). This systematic approach allowed, for the first time, to identify the various cavitation patterns from inception to fully cavitating flow. In addition, by coupling the results with the emerging spray structure observations, it was confirmed that cavitation can improve the spray characteristics by enhancing the primary break-up and the subsequent atomisation of the liquid fuel, findings on which most of the reviewed papers in the open literature have concluded. Another general conclusion has been that the development of the different cavitation patterns inside the nozzle has been typically connected with decreasing nozzle discharge coefficients and increasing velocities in the non-cavitating flow regions.

Following the in-nozzle investigations, knowledge of the fuel spray characteristics is essential in understanding the atomisation mechanisms and their dependency on injection pressure and thermodynamic conditions. The majority of scientific publications in this field underline the dependency of atomisation on injection pressure. High injection pressures are able to reduce droplets SMD (Sauter Mean Diameter) to minimum levels of 12-15 $\mu\text{m}$ , contributing in this way to efficient and

quick vaporisation of the fuel. On the other hand, the increased droplet velocities resulting from elevated fuel pressures tend to increase the liquid fuel penetration lengths, leading to impingement of liquid fuel on surfaces which generally reduces its vaporisation potential and contributes to exhaust emissions increase. In this study the aforementioned findings have been confirmed by several experiments where injection and chamber pressures were varied along with ambient temperature. In an attempt to reduce spray tip penetration without compromising the atomisation quality, multiple injections have been employed. This resulted in reduced duration of multiple injection events. The general conclusion has been the positive effect of reduced injection durations on atomisation quality and penetration lengths.

At last, but not least, the performance of the above characteristics under engine operating conditions remains the most important factor on injector type selection and engine design trends. The scientific community has thoroughly investigated several types of high-pressure injectors as well as several engine design configurations. The major conclusion has been that in-cylinder air flow and fuel impingement control the formed mixture quality and distribution. The contribution of this relevant experimental work presented in this thesis has been the extensive testing of the multiple injection strategy in a 5-valve, twin-spark engine under variable intake swirl conditions. A general conclusion that can be drawn is that multiple injection strategy offers certain advantages which, when coupled with appropriate intake flow conditions and combustion chamber design, present a promising candidate for future developments in gasoline direct injection engines.

Finally, it can be argued that the review of the literature on different gasoline direct injection concepts has revealed that there is adequate experimental information, including the results presented in subsequent chapters, to allow further development and eventually establishment of a “clean” internal combustion gasoline engine. Whether this engine will be overshadowed by technologically advanced fuel cell concepts or the rapidly growing hybrid systems remains to be seen.

## *Chapter 3*

### *Internal Nozzle Flow*

#### **3.1 INVESTIGATED LARGE-SCALE TRANSPARENT NOZZLE**

As mentioned above, it is essential to examine the flow through scaled up injectors where, particularly, three-dimensional model nozzles can represent the exact geometry of real-size production or research injectors. The present thesis focuses exclusively on the newly arrived, diesel-technology derived, multi-hole nozzle injector and its various nozzle configurations.

Multi-hole nozzles are made up of several holes positioned in the nozzle's tip "dead" volume, according to the desired spray shape. Design flexibility in spray pattern configuration and hole positioning is one of the main advantages of the multi-hole nozzle concept. Among the various multi-hole nozzle designs, which include symmetric and non-symmetric sprays emerging from 6 or 12 holes, the simplest 6-hole nozzle design was chosen for the investigation of the internal nozzle flow for the purpose of the present study. As previously mentioned, six holes are symmetrically positioned in the nozzle tip "dead" volume, each one of them at an angle of  $45^\circ$  to the injector axis, as can be seen in Figure 3.1, forming an overall spray cone angle of  $90^\circ$ . All the dimensions of this prototype real-size multi-hole nozzle were enhanced by a factor of 29 and the transparent large-scale model (Figure 3.2) was manufactured from an acrylic material with a refractive index matching of 1.49. Three-dimensional views of the transparent model are presented in Figure 3.2.

The diameter of the cylindrical injection holes with filleted edges is  $140\mu\text{m}$  featuring a  $0.2\text{mm}$  fillet radius and an overall length of  $0.3\text{mm}$  in the real-size injector nozzle. These values correspond to a nominal hole diameter and length of  $4.1\text{mm}$  and  $8.7\text{mm}$  respectively for the large-scale model. The resulted length over diameter (L/D) ratio is of the order of 2.12.

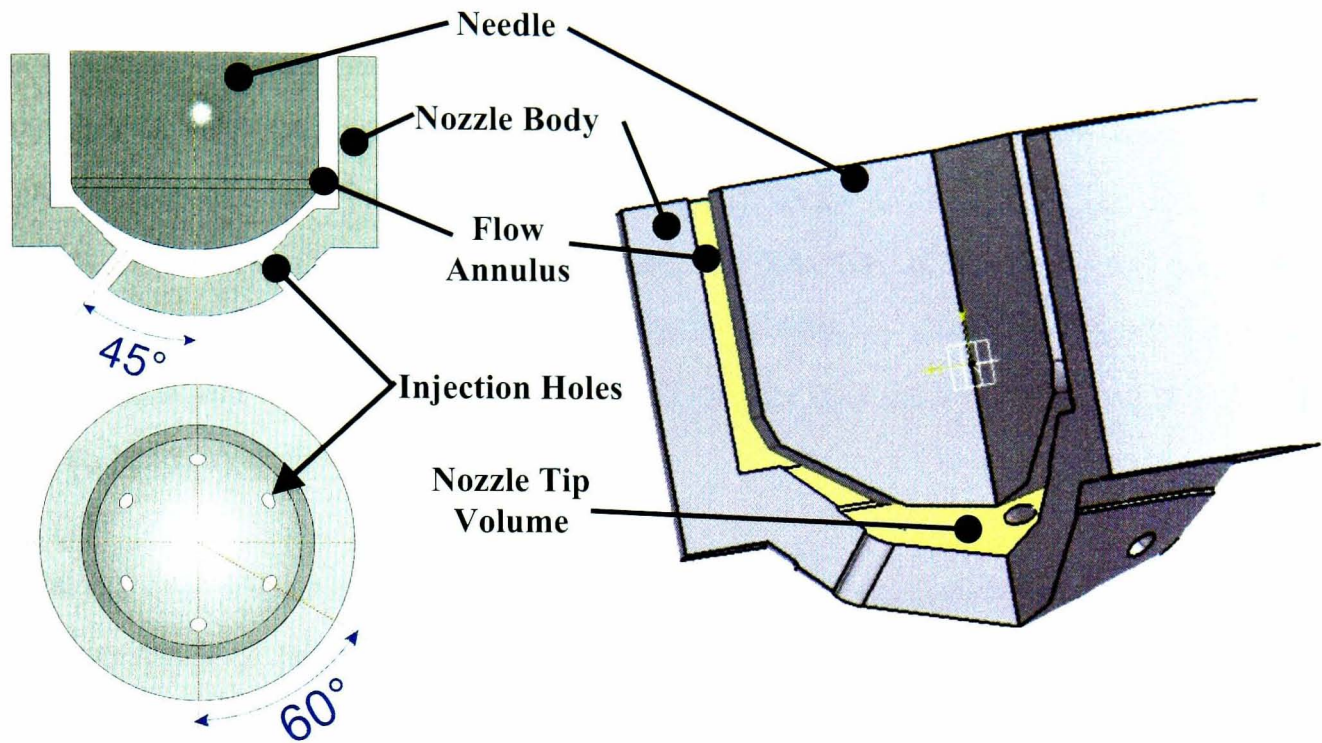


Figure 3.1: Geometry of the 6-hole fully symmetric injection nozzle.

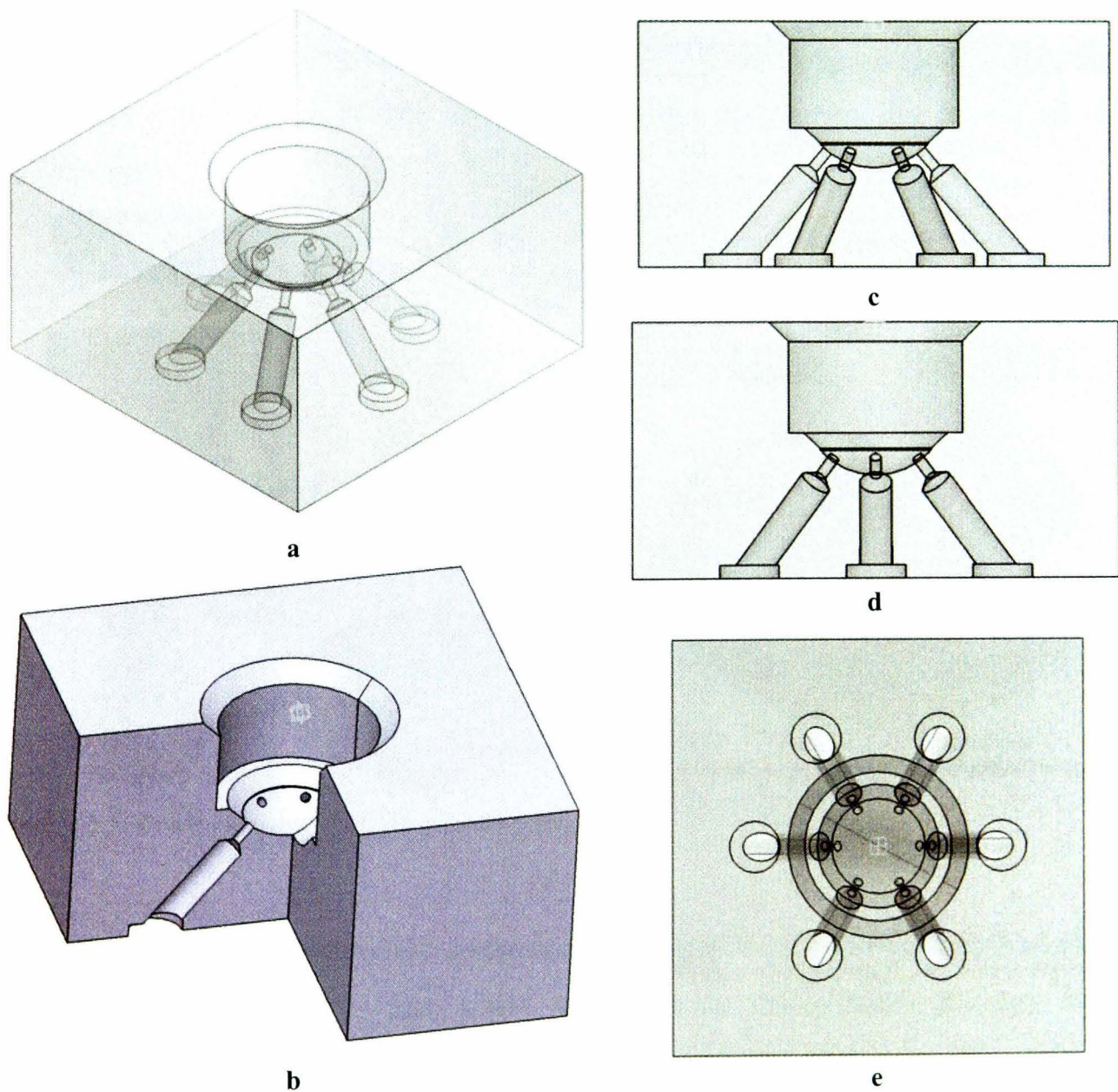


Figure 3.2: Three-dimensional models of the large-scale 6-hole nozzle. (a). Isometric view of Perspex nozzle. (b). Prospective cut-out. (c), (d). Front and side view, respectively and (e). Bottom view.

The enlarged nozzle is designed in a closed flow circuit configuration and thus has expanding flow holes downstream of the injection holes to minimise back flow and pressure drop. These back flow holes, which are larger in diameter than the injection holes, collect the emerging liquid and direct it into the tubes leading to the suction pump (see Section 3.2). This design makes it possible to shape the nozzle body as a block with flat outer surfaces, which has obvious advantages for imaging and laser measurement purposes.

It is not only necessary to model the geometry of the actual injection nozzle, but also the geometry of the flow passages inside the injector upstream of the nozzle for the sake of dynamic flow similarity (Figure 3.3); the latter is mainly achieved in terms of matching the Reynolds number ( $Re$ ) of the enlarged model to that of the real-size nozzle. This task was accomplished by enlarging the real-size geometry from the volume around the needle shoulder downstream to the nozzle, except that the length of the flow passage along the needle was shortened slightly, due to overall size limitations.

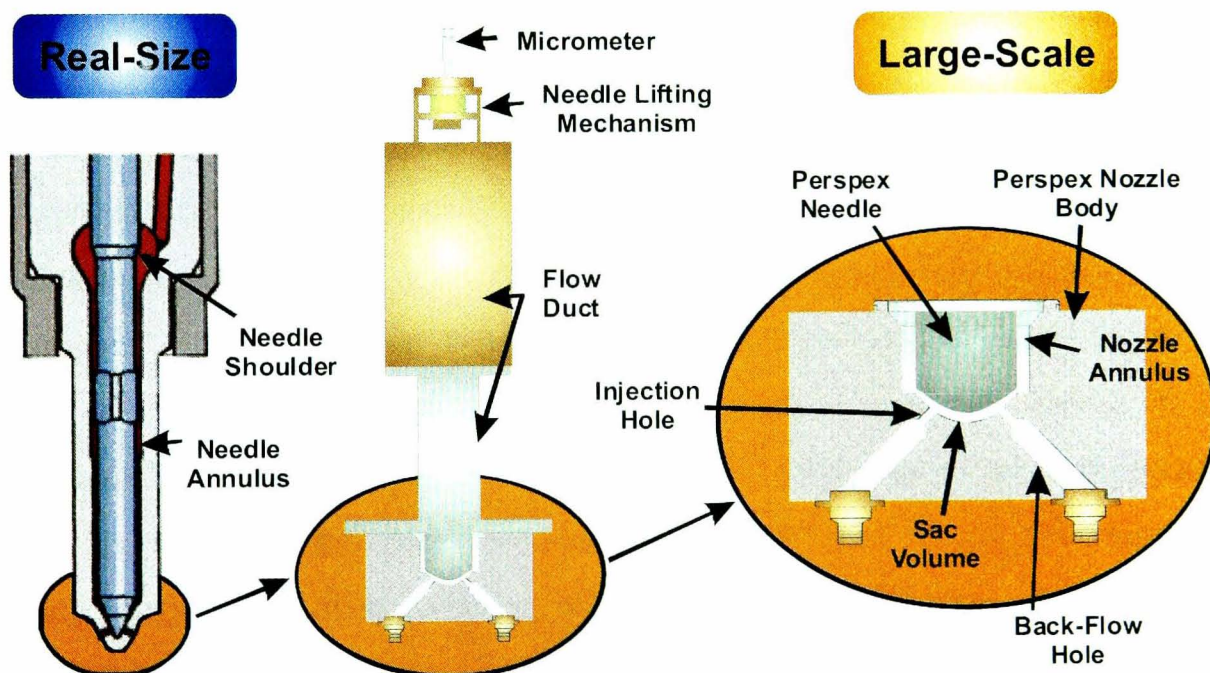


Figure 3.3: From real-size to large-scale injector.

In order to make the enlarged nozzle easily changeable it is fixed with a clamping mechanism under the flow duct, which represents the lower needle annulus. An O-ring between the metal flange and the Perspex nozzle body provides sufficient sealing. The model Perspex / acrylic needle has a large male thread at its upper end and thus can be fixed into the lower end of the enlarged metal needle part through a corresponding female thread (Figure 3.4)



**Figure 3.4: Enlarged transparent and metal needle parts.**

### 3.2 ENLARGED INJECTOR TEST-RIG

Initially, the motivation for building an enlarged transparent model of a nozzle has been the utilisation of the refractive index matching principle. This technique, which has been extensively used among our research group's activities [43, 44, 51, 102], makes possible the application of imaging and laser measurement techniques to fluid flows through complicated geometries, which are usually not optically accessible. When the refractive index of the working fluid is identical to that of the material from which the flow geometry was manufactured, optical access without any distortion of light at the liquid-solid interfaces can be obtained satisfactorily. Given the material of the transparent three-dimensional nozzle model, its refractive index is 1.49, as mentioned above. The only liquid that matches this property of the acrylic nozzle is a mixture of 32% by volume of Tetraline (1,2,3,4-Tetrahydronaphthalene) and 68% by volume of oil of Turpentine, which, at 25°C, has a refractive index of 1.49. Unfortunately, this mixture has an unpleasant smell, which discourages long exposure times. According to data sheets that describe the properties of the two compounds, inhaling fumes of the above mixture and skin contact could cause several irritations that affect human health. Based on health and safety considerations and the fact that detailed flow analysis using laser techniques was beyond the purposes of this study, it was decided to use water as the working fluid. Water has a refractive index of 1.33, a value considerably smaller than that of the acrylic material of the transparent nozzle. Although light distortion at the liquid-solid interfaces was expected, it was discerned that this distortion would not considerably affect the results as the main experimental technique would be imaging with the use of constant light source and not laser measurement techniques that require accurate positioning of a relatively small control volume.

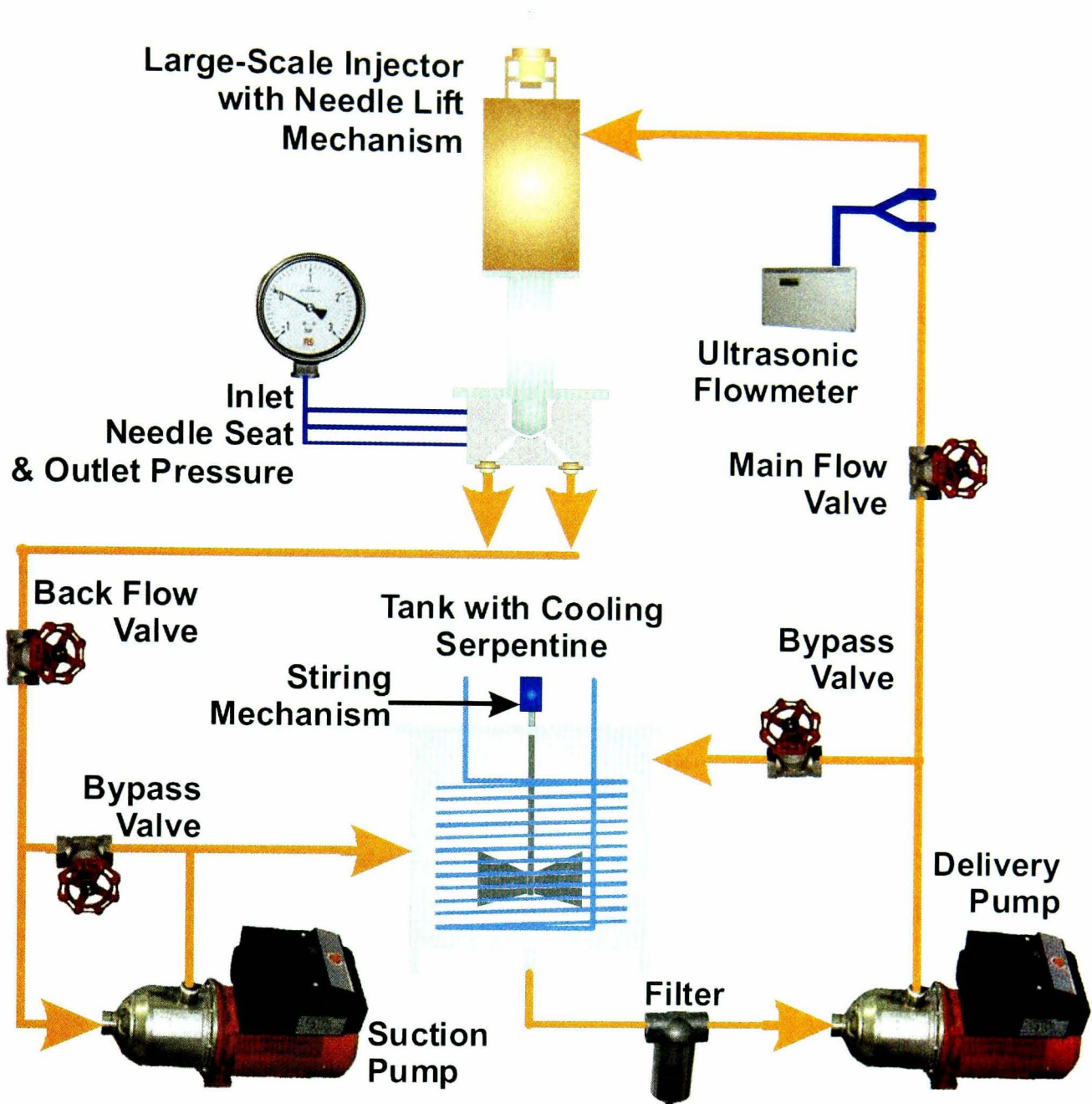


Figure 3.5: Schematic of the large-scale injector test rig.

A schematic overview of the experimental setup with incorporated large-scale model injector is shown in Figure 3.5. The illustrated system has been designed by members of our research group [41, 43, 44, 46, 47] and has actually been built by the author and Dr. Hartwig Roth [102]. The existence of the delivery and suction pumps, combined with the fact that it is a closed loop flow circuit, results in a working fluid temperature rise. To compensate for this heat up of the working liquid, due to pump-generated thermal energy, a closed loop cooling serpentine is installed in the 90ltr storage tank. A temperature controller, responsible for the flow control of the cooling fluid, ensured that the working liquid temperature was kept almost constant at around 25°C. A stirrer, installed in the storage tank, was used to extinguish any steep temperature gradient fields present in the working liquid. In this manner the temperature sensitive properties of the system fluid, like density, kinematic viscosity,

vapour pressure and surface tension, were maintained constant at all times. The flow rate of the large-scale injector is primarily controlled by the variable speed pumps, over a wide range of values. Further fine adjustment of the flow rate is achieved by means of the various flow and bypass valves installed. Accurate measurement of the overall flow rate is provided by an ultrasonic flow meter that is installed upstream in the large-scale injector in a fixed length feed pipe. The three-dimensional nozzle model provides the individual pressure measurement locations for accurate monitoring of the inlet, needle seat and outlet pressure values. Inlet and outlet pressures are of great interest in such experiments and they can be adjusted independently by restricting the inflow and/or outflow of the injector. The pressure difference between inlet and outlet, as well as, the difference between the outlet and vapour pressure of the working liquid represent a characteristic number of injector nozzle flow, the cavitation number (CN), which is defined as follows

$$CN = \frac{P_{inj} - P_{back}}{P_{back} - P_{vapour}}$$

Where  $P_{inj}$  is the inlet (injection) pressure,  $P_{back}$  is the outlet (back-) pressure and  $P_{vapour}$  is the vapour pressure of the working liquid (in the present study:  $P_{vapour, water} \approx 0.04 \text{ bar @ } 25 \pm 3^\circ \text{C}$ ). Cavitation number is a non-dimensional parameter that is used to classify operating conditions of injector nozzle flows and it is directly connected to the appearance of cavitation structures in the above flow fields. More specifically, the larger the CN the more possible it is for cavitation to develop inside the injector nozzle holes. In order to reach sub-atmospheric outlet pressures and, therefore, simulate cavitation numbers of interest, a variable speed suction pump was installed in addition to the main feed pump. This made flow conditions at higher cavitation and Reynolds numbers possible. To prevent the liquid from unnecessary contact with air, the spray development at the injection hole exit was avoided by collecting the emerging liquid streams through the expanding back flow holes and tubes, and, subsequently, directing the fluid via the suction pump into the tank in order to close the flow loop.

The aforementioned experimental setup is effectively a steady state flow test rig for in-nozzle flow visualisation purposes. In other words, the dynamic phenomena introduced due to the needle opening and closing events are absent. There is no dynamic needle movement; the needle is fixed to a certain lift simulating the desired

real-size needle lift conditions. Its position is fixed manually from the “needle lift mechanism” (Figure 3.5) and a micrometer is responsible for providing the exact position of the enlarged needle. The actual lift in the model is also scaled-up according to the enlargement factor of the injector nozzle.

The liquid flow through the injector multi-hole nozzle, and especially through its exit holes, is believed to be highly turbulent [36, 41, 43, 44, 47, 49, 67, 102-104]. Although the experiment is run at steady state conditions, all flow features, and particularly cavitation phenomena at injection holes, are expected to behave transiently and to have short time scales. This behaviour is virtually impossible to capture with conventional imaging (CCD camera) techniques. Since it is important to gain knowledge about the dynamics of cavitation inception and formation processes for various flow conditions, high-speed digital video technique was the primary method used for this study.

### **3.3 HIGH-SPEED DIGITAL VIDEO TECHNIQUE**

#### **3.3.1 Experimental Setup**

To capture the development of the cavitating injector flow inside the enlarged model nozzle, a high-speed digital video system (Photron Ultima APX) was set up in conjunction with the enlarged injector test rig. A schematic set-up of the 10bit video system is illustrated in Figure 3.6. The “mega-pixel Photron ultima APX” system is able to take between 60 and 2,000 frames per second with full resolution of 1,028 x 1,028 pixels. Higher frame rates of 3,000 up to 120,000 frames per second were possible at progressively reduced resolution. A strong halogen floodlight together with some halogen spotlights provided sufficient light for the non-intensified CCD imaging chip even at the highest used frames rates. The camera was operated by its control unit, which in turn was controlled by special software installed on the image collection computer. The software was responsible for programming critical operating parameters, such as desired frame rate, exposure time and triggering signals, to the camera’s control unit. Unlike other high-speed digital video systems, this system allowed the operator to set the shutter speed independently of the desired frame rate. All obtained images were saved at the image buffer, located in the camera’s control unit, and downloaded onto a computer via a high-speed cable connection.

As illustrated in Figure 3.6, two high-speed cameras were used for this experiment. This system allows for the synchronisation of more than one camera. By interconnecting the control units of the two cameras, synchronisation is achieved, and images can be obtained at exactly the same time. This important feature allows for the simultaneous imaging of the area of interest from two different viewpoints, providing a better understanding of the three-dimensional flow patterns present at the large-scale nozzle.



**Figure 3.6:** Schematic of HSDV imaging in large-scale 3-D model nozzle.

The first camera (HSDV Camera 1 in Figure 3.6) was set in a side view of the model, while the second camera (HSDV Camera 2 in Figure 3.6) was installed below the large-scale nozzle and imaged the bottom view of the three-dimensional model. In Figure 3.7, a schematic of the side camera imaging areas and viewpoints is presented. As is illustrated, three different viewpoints were selected, in an attempt to fully characterise the flow patterns. The first viewpoint (r-h-s top in Figure 3.7) included all injection holes visible from the front view of the model (see Figure 3.2c), 4 holes in total, sac annulus and the volume around the needle tip. Although light distortion is evident, due to the use of water as working fluid and the mismatch in refractive indices, this view was selected with the purpose of demonstrating simple flow streamlines by seeding the flow through the nozzle with air bubbles.

The second and most important view-port focuses in one of the holes. It can be seen in r-h-s bottom of Figure 3.7. As flow from the sac annulus enters the injection hole, it accelerates and the resulting in-hole fluid velocities are high enough for a common camera to capture. Therefore, an increased frame rate is required in order to fully capture the cavitation development. As mentioned above, the main working principal of high-speed digital video systems is that the higher the frame-rate is, the smaller the image resolution. In an attempt to use as high frame rate as possible for efficient cavitation imaging, the image resolution had to be greatly reduced. This meant that it could not accommodate the area of interest. To maximise the imaging area, the camera had to be aligned to the orientation of the injection hole, which forms a  $45^\circ$  angle to the injector axis. Therefore, the camera was rotated almost  $45^\circ$  and the resulting image presents the injection hole horizontally. This camera viewpoint was selected for synchronisation with the second, bottom camera, which was also set to image the same injection hole.

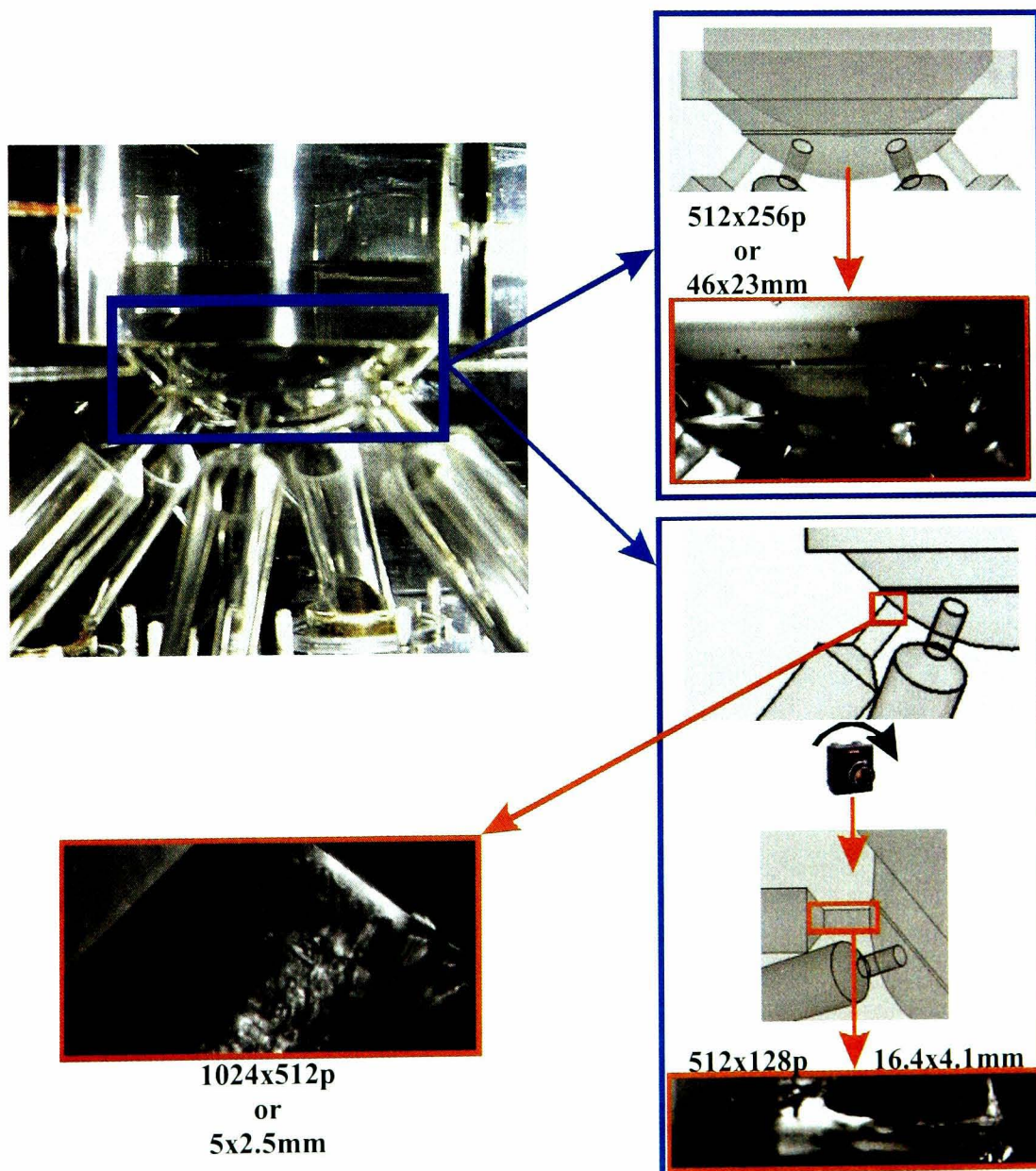
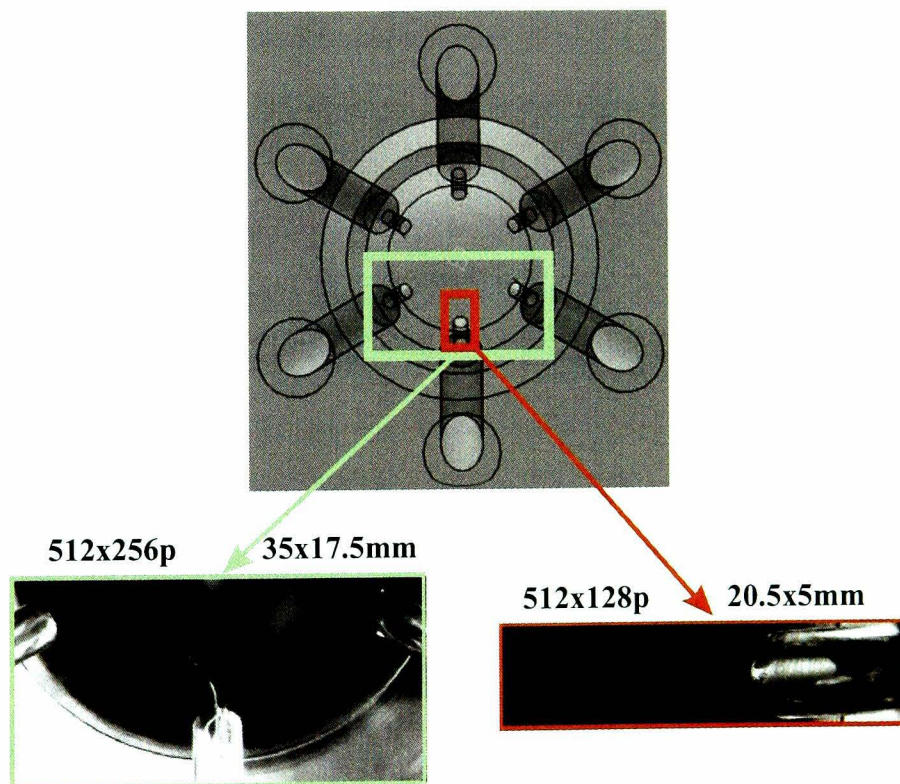


Figure 3.7: Schematic of imaging areas and viewpoints for the side camera (HSDV Camera 1).

The third view-port visible in Figure 3.7 focuses on cavitation structures present in the injection hole. Using a high-magnification lense setup, an area of 5 x 2.5mm was visualised. Cavitation patterns in injection holes are highly dependent on the cavitation number of the nozzle. By varying this parameter, the transition from smooth to rough cavitation surface was captured.

The second HSDV camera provides two different bottom views of the nozzle model. Based on previous similar work in diesel multi-hole injection nozzles [41, 43] cavitation appears to be in the form of string structures. This type of cavitation exists mainly in the injector's sac volume, interconnecting two or more holes, or stretching from one hole to the needle face. These structures are easily identified in the bottom view images. Therefore, the l-h-s image in Figure 3.8 focuses on half the sac volume including 3 injection holes while the r-h-s image in Figure 3.8 focuses exclusively on the same injection hole as the previously described side camera; these are the two synchronised images.



**Figure 3.8:** Schematic of the imaging areas as viewed from the bottom camera (HSDV Camera 2).

### 3.3.2 Image Processing

As previously mentioned, the camera's software was responsible for the control of the high-speed digital video system and the acquisition of images. Unlike other high-speed imaging systems, it conveniently adjusted the acquisition frame rate separately

than the camera shutter speed or, in photographic terms, the exposure time. In this experiment the main frame-rate was set approximately to 15,000 frames per second, and varied according to the velocity field of each imaged area. Higher frame rates were not selected due to limitations in image resolution. At the same time, due to sufficient lighting provided, exposure times were kept as minimum as possible. Typical exposure times of  $1/50000$ s, or  $20\mu\text{s}$ , provided sufficiently sharp images, since the transient imaged phenomena were of medium speed rate. Finally, the software used provided several choices with regard to the output image format. The majority of data images were saved in RAW Bayer format. The selection of the image format was made based on the actual supported colour depth of 10-bit.

The selected image format required certain post-processing for obtaining adequate image quality and easily comparable images. At first, due to the nature of the experiment, the lighting configuration used to capture images had to have a certain arrangement, like distance and orientation, with regard to the three-dimensional injector model. The reason for the use of this specific lighting arrangement is due to the sensitivity of the acrylic material to the elevated temperatures caused by the heat generated by the high-power lighting device. Moreover, the mismatch in refractive indices amongst the nozzle material, the working fluid and the air bubbles generated by cavitation phenomena inside the nozzle, resulted in random light refraction. The area of interest is then imaged at low light conditions. Colour-based information is not lost but a conversion in the greyscale is needed, from linear to logarithmic, for the dark areas to be shifted towards higher intensity values while the already light areas remain almost untouched. Effectively, the conversion of a linear greyscale to logarithmic alters the gamma ( $\gamma$ ) value of the colormap. This is the safest way of adjusting the brightness of an image without neglecting critical information hidden in the pixel intensity values. Following the colormap correction, the data images had to be masked for covering background light reflections that severely affect the contrast; higher contrast is translated into a sharper and more detailed image. All the image processing was done through the development of an in-house custom-made software using the Matlab platform.

### 3.4 EXPERIMENTAL RESULTS

Investigations of cavitation inside large-scale three-dimensional model nozzles of gasoline high-pressure injectors can provide useful information for improving the physical understanding of the cavitation phenomenon and its dependency on various parameters, such as nozzle geometry and flow conditions. Representative images of in-nozzle flow patterns and the various forms of cavitation are presented here. The steady-state flow conditions examined in terms of flow rates and pressures covered the range from low to full load of real-size production injectors, while the needle lift positions corresponded to that of full lift. Simultaneous matching of the Reynolds and cavitation numbers has allowed direct comparison between the cavitation regimes present in real-size and enlarged model nozzles. As illustrated in previous studies investigating nozzle cavitation in diesel injectors [43, 102], this phenomenon has its origin in areas of low local pressure. Usually, these areas are found in the core of the recirculation zones formed in the upper corner of the injection hole inlet.

#### 3.4.1 Internal nozzle flow patterns

A first step towards better understanding of the phenomena that take place inside the nozzle of high-pressure gasoline injectors is a simple flow mapping for effective visualisation of the dominant flow patterns. There are various ways of achieving high-quality visualisation and ultimately extracting flow streamlines derived from images. Most of the techniques used are based on flow seeding using various solid or other particles (flakes) of lightweight (almost neutrally buoyant) and flow non-intrusive shape. Unfortunately, the nature of the large-scale model test rig prohibits the use of metal or special plastic flakes for effective flow seeding. Therefore, it was determined that the best solution was the use of air bubbles, which were introduced in the flow upstream of the enlarged injector by a small diameter nozzle.

The selection of the seeding type proved quite efficient but the results may not fully represent the expected flow patterns due to the large size of the air bubbles and associated buoyancy effects. In the case of multi-hole nozzles, the primary inlet flow to the holes comes from the annular flow in the upper half. This was expected, since the liquid located just upstream the hole inlet, after passing the needle seat area, would seek the “easiest” way-out of the nozzle, i.e. where the pressure is lowest. As it can be seen in the sequence of high-speed images presented in Figure 3.9, the air

bubble, marked by a red circle in image number 1, is located directly upstream the injection hole as it crosses the needle seat area. In the next two images (numbers 2 and 3) the deformation of the bubble shape is evident, due to the mean flow gradient and turbulence associated with the low-pressure area introduced by the hole inlet further downstream. The bubble was finally dragged into the injection hole, and in image number 4 has already disappeared. As previously mentioned, this behaviour was expected and well confirmed.

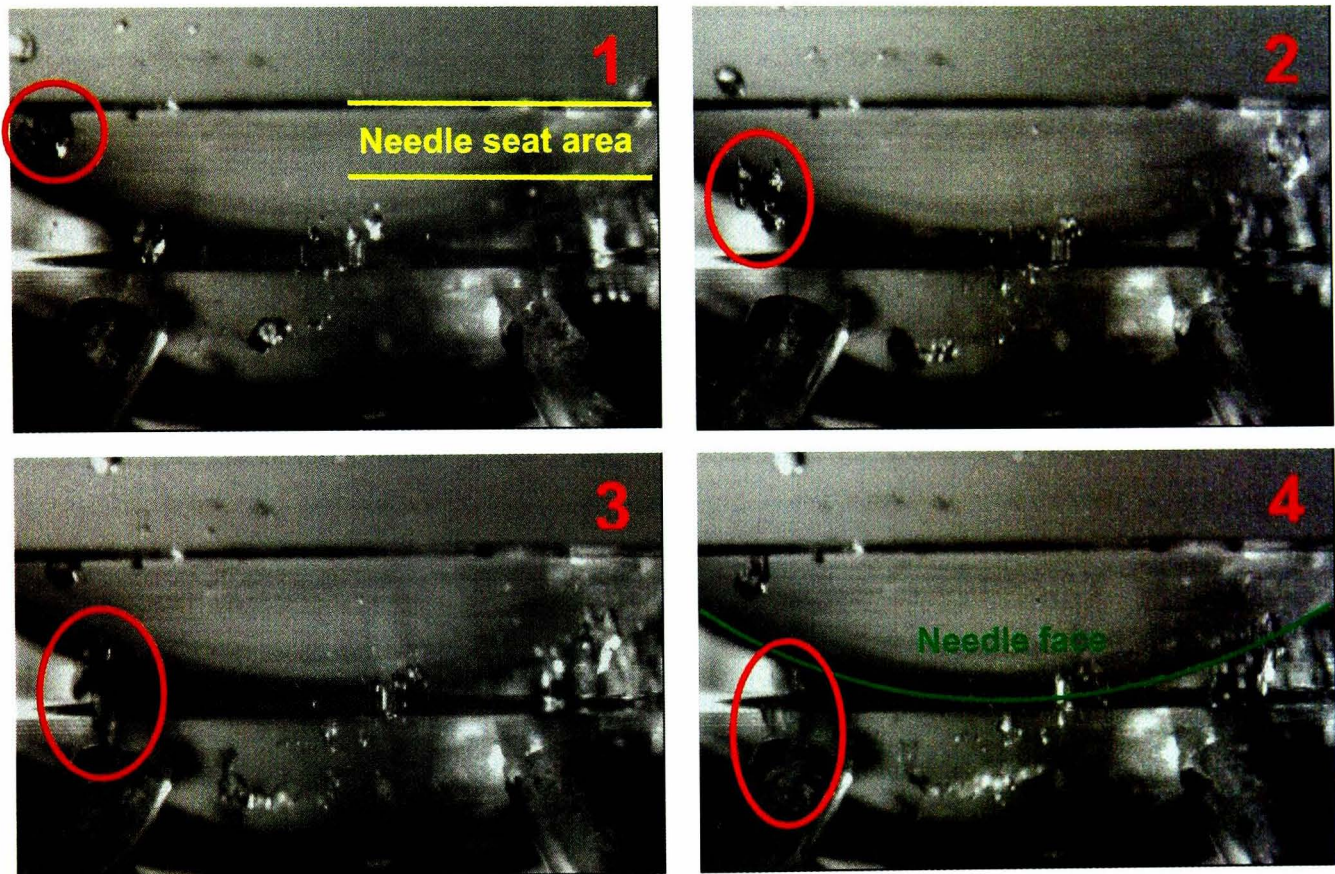


**Figure 3.9: Image sequence demonstrating primary inlet flow to the injection hole.**

There are only six injection holes in the investigated nozzle and, based on the previously presented finding, it is important to identify the flow patterns around the entire flow annulus and sac volume. Since the nozzle design is axis-symmetric, the area of interest would then be the region in-between two adjacent injection holes. As liquid passes through the needle seat area, there is not an apparent exit on its way, but a strong velocity gradient that is initiated from the low-pressure regions at the two neighbouring injection holes. The flow is then directed to the closest hole by changing its initial direction creating a secondary inlet flow towards the injection holes; it is mainly side flow and is complemented by an additional small stream that enters the hole from the bottom. Figure 3.10 demonstrates the above described flow behaviour. At the middle point of the inter-hole distance, the liquid faces strong shear forces that

come from the equal strength pressure gradients. The marked bubble in the image sequence presented in Figure 3.10 starts to split as it approaches the injection holes; see image number 2. Initially it forms two elongated groups of bubbles but, as it maintains its momentum, the bottom part is further detached forming effectively the third smaller group of bubbles observed in the fourth image in the sequence. The left and right circles, in image number 5, mark the bubbles that turn towards the left- and right-injection holes, respectively, forming the side entry flow for these holes. The bottom part of the initial bubble is not dragged into any of the two injection holes, since it has passed the high-pressure gradient area due to its momentum. As illustrated in the last image of the sequence, this latter part of the bubble continues its way downstream where it finally reaches the bottom of the nozzle sac volume where it interacts with the flows coming down from the other inter-hole spaces. Liquid trapped in the sac volume seems to be mainly stagnant, as presented in Figure 3.11. Effectively there is no flow in that nozzle area unless there is newly arrived liquid, according to the previously described mechanism that induces certain low-scale flow by displacement of the existing stagnant liquid towards the exit holes.

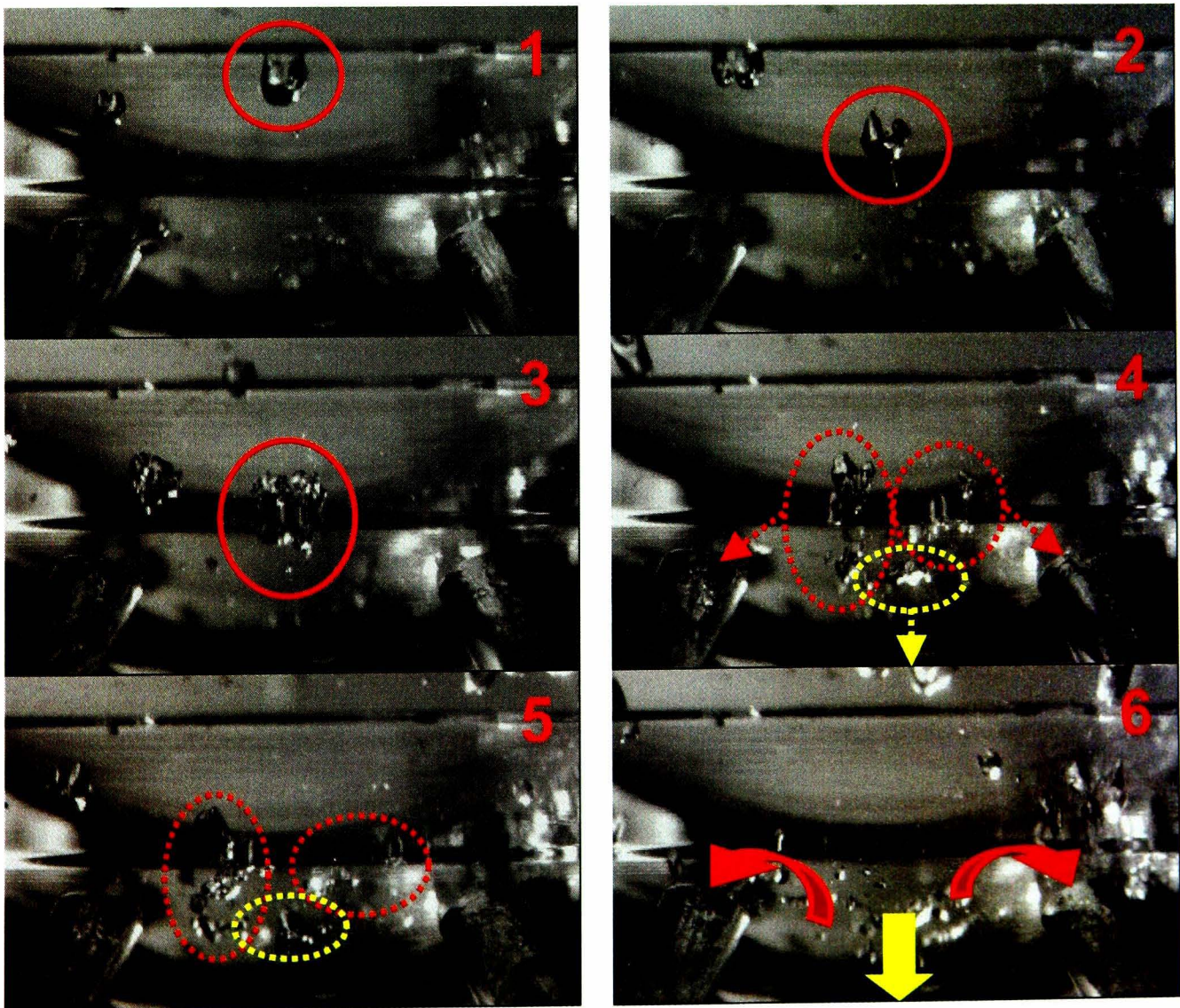


**Figure 3.10:** Image sequence demonstrating flow splitting in-between two injection holes.

The flow of the sac volume to the exit holes (bottom inlet flow) is of very low velocity and the contribution to the total inlet flow of the injection holes is minimum. Figure 3.11 shows a bottom view of the nozzle model including two injection holes where, effectively, only a portion of the nozzle sac volume is visualised. In this high-speed image sequence, a fine bubble is marked by the yellow circle. As flow passes in-between the two visible injection holes, it is directed towards the sac volume, as mentioned previously. Images number 3 and 4 were taken at a time interval of 1ms; this time frame provided sufficiently long time to visualise any movement in the highly transient flow-field of an injector nozzle. It is apparent from these images that there is not any defined movement of the marked bubble and the flow can be considered to be stagnant.

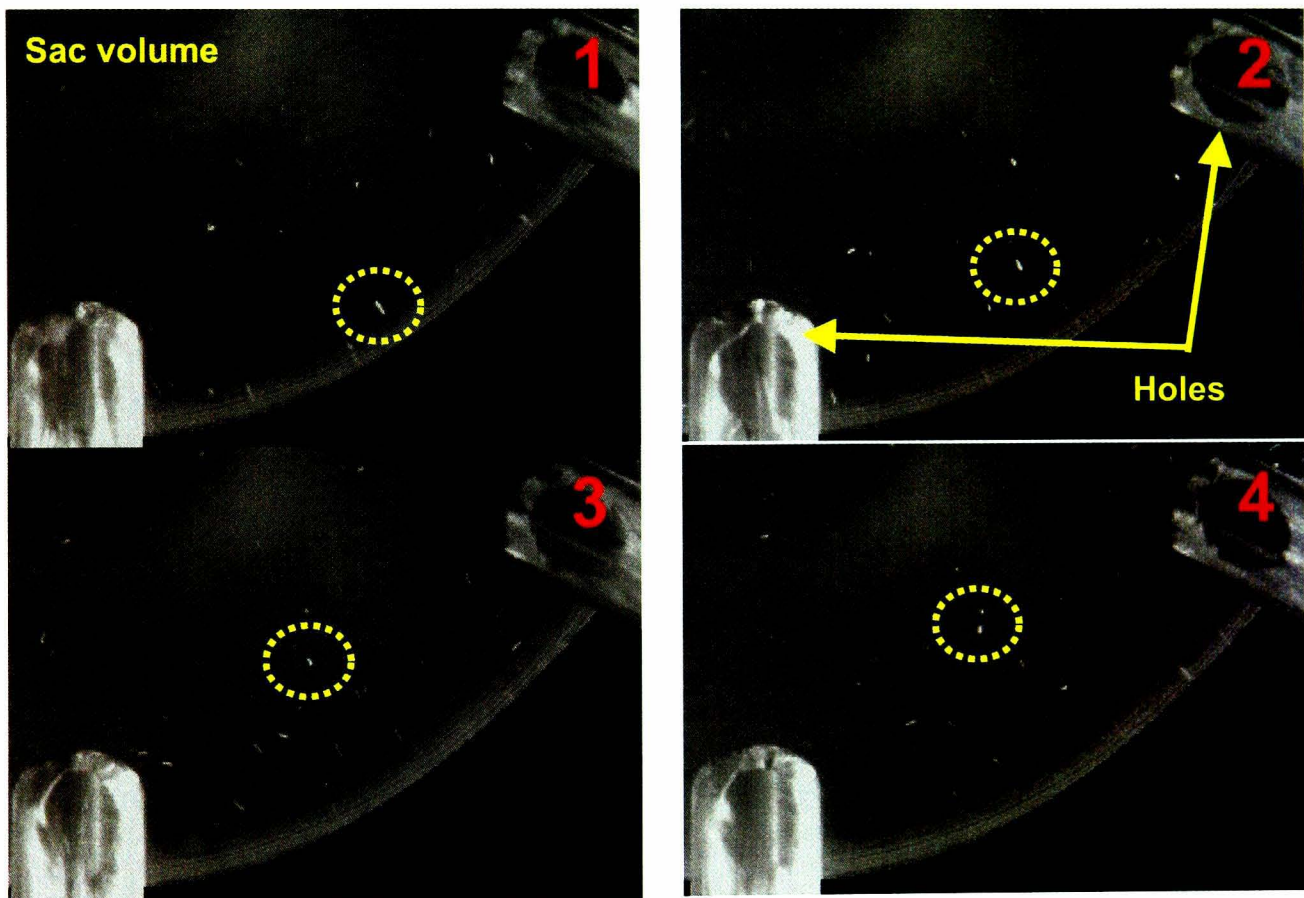


Figure 3.11: Image sequence demonstrating the low-scale flow at the sac volume.

### 3.4.2 Incipient cavitation

In order to identify and understand the dynamic behaviour of the various cavitation structures under different conditions, the enlarged injector test rig with the transparent multi-hole model nozzle was operated at different flow conditions and needle lifts, while the cavitating flow was visualised with the high-speed digital video camera. All experimental test conditions are listed in Table 3-1 through Table 3-2, where  $P_{inj}$  is

the absolute static inlet pressure,  $P_{back}$  is the absolute static outlet pressure and  $U_{inj}$  is the bulk velocity of the flow through an injection hole. The examined fluid flow and pressure conditions aimed to cover the equivalent range of low loads in terms of the cavitation numbers and low-to-high loads in terms of the flow rate through the nozzle, for a real-size production injector used in modern direct-injection spark-ignition engines. Matching cavitation numbers greater than 5, which represents the minimum under realistic injector operation in an engine, proved not to be feasible with the existing large-scale model test rig. On the contrary, the full operating range in terms of the flow rate through the nozzle was covered; the existing setup could operate at a range of Reynolds numbers between 30,000 and 72,000.

<b>Needle Lift = 0.51mm</b>						
<b>CN</b>	<b>Re</b>	<b><math>P_{inj}</math> [bar]</b>	<b><math>P_{back}</math> [bar]</b>	<b><math>U_{inj}</math> [m/s]</b>	<b>Flow Rate [l/s]</b>	<b>Frame Rate [1/s]</b>
<b>4.00</b>	<b>52614</b>	3.60	0.75	12.88	1.03	15000
<b>4.22</b>	<b>61899</b>	4.75	0.95	15.15	1.20	15000
<b>4.57</b>	<b>37139</b>	2.00	0.40	9.09	0.75	15000
<b>4.72</b>	<b>49519</b>	3.20	0.60	12.12	0.97	15000
<b>5.00</b>	<b>30949</b>	2.55	0.46	7.57	0.65	15000
<b>5.20</b>	<b>34044</b>	1.62	0.30	8.33	0.67	15000
<b>Needle Lift = 1.02mm</b>						
<b>CN</b>	<b>Re</b>	<b><math>P_{inj}</math> [bar]</b>	<b><math>P_{back}</math> [bar]</b>	<b><math>U_{inj}</math> [m/s]</b>	<b>Flow Rate [l/s]</b>	<b>Frame Rate [1/s]</b>
<b>2.40</b>	<b>34044</b>	1.43	0.45	8.33	0.69	15000
<b>3.00</b>	<b>34044</b>	1.43	0.39	8.33	0.69	15000
<b>3.22</b>	<b>40234</b>	1.75	0.45	9.85	0.80	15000
<b>3.75</b>	<b>61899</b>	3.78	0.85	15.15	1.15	15000
<b>Needle Lift = 1.53mm</b>						
<b>CN</b>	<b>Re</b>	<b><math>P_{inj}</math> [bar]</b>	<b><math>P_{back}</math> [bar]</b>	<b><math>U_{inj}</math> [m/s]</b>	<b>Flow Rate [l/s]</b>	<b>Frame Rate [1/s]</b>
<b>1.00</b>	<b>43329</b>	2.00	1.02	10.60	0.82	15000
<b>1.50</b>	<b>46424</b>	2.34	0.96	11.36	0.90	15000
<b>1.70</b>	<b>46424</b>	2.34	0.90	11.36	0.90	15000
<b>2.00</b>	<b>30330</b>	1.42	0.50	7.42	0.60	15000
<b>2.40</b>	<b>30330</b>	2.25	0.70	7.42	0.60	15000
<b>3.00</b>	<b>30330</b>	2.25	0.60	7.42	0.60	15000
<b>3.20</b>	<b>30330</b>	2.15	0.55	7.42	0.60	15000
<b>3.50</b>	<b>58804</b>	3.20	0.75	14.39	1.14	15000

Table 3-1: Flow conditions inside the large-scale multi-hole nozzle for needle lifts 0.51-1.53mm.

Table 3-1 shows experimental conditions for three different needle lifts of 0.51, 1.02 and 1.53mm, although none corresponds to the full lift of the real-size multi-hole

nozzle. In particular these values represent a quarter ( $\frac{1}{4}$ ), half ( $\frac{1}{2}$ ) and three quarters ( $\frac{3}{4}$ ) of the full needle lift of the real-size nozzle, respectively. The full lift, according to the FIE manufacturer is  $70\mu\text{m}$  which corresponds to  $2.04\text{mm}$  in the large-scale model. The experimental test conditions at the full needle lift operation are listed in Table 3-2. The selection of four different needle lift values is based on an attempt to parametrically study in-nozzle cavitation phenomena and their behaviour under the widest possible range of flow conditions. Unfortunately, in real engine applications, gasoline injectors of similar technology to the multi-hole nozzle are not able to vary the needle lift as a function of the engine's fuel requirement. Therefore, although a parametric study based on various needle lift positions does not simulate closely any realistic engine operation, it is nevertheless very helpful for the investigation of cavitation and its dependencies on flow conditions.

<b>Needle Lift = 2.04mm</b>						
<b>CN</b>	<b>Re</b>	<b>P<sub>inj</sub></b> [bar]	<b>P<sub>back</sub></b> [bar]	<b>U<sub>inj</sub></b> [m/s]	<b>Flow Rate</b> [l/s]	<b>Frame Rate</b> [1/s]
<b>0.62</b>	<b>37139</b>	2.40	1.50	9.09	0.75	15000
<b>0.73</b>	<b>37139</b>	2.30	1.35	9.09	0.75	15000
<b>0.78</b>	<b>37139</b>	2.20	1.25	9.09	0.75	15000
<b>0.89</b>	<b>37139</b>	2.05	1.10	9.09	0.75	15000
<b>1.00</b>	<b>58803</b>	3.30	1.63	14.39	1.14	15000
<b>1.27</b>	<b>58803</b>	3.30	1.48	14.39	1.14	15000
<b>1.50</b>	<b>49519</b>	2.50	1.03	12.12	0.97	15000
<b>1.50</b>	<b>58803</b>	3.30	1.35	14.39	1.14	15000
<b>1.70</b>	<b>49519</b>	2.50	0.96	12.12	0.97	15000
<b>1.70</b>	<b>58803</b>	3.30	1.25	14.39	1.14	15000
<b>2.00</b>	<b>37139</b>	2.12	0.74	9.09	0.75	15000
<b>2.00</b>	<b>58803</b>	3.30	1.13	14.39	1.14	15000
<b>2.40</b>	<b>37139</b>	1.77	0.55	9.09	0.75	15000
<b>2.40</b>	<b>58803</b>	3.30	0.99	14.39	1.14	15000
<b>2.70</b>	<b>37139</b>	1.75	0.51	9.09	0.75	15000
<b>3.00</b>	<b>49519</b>	2.20	0.59	12.12	0.97	15000
<b>3.00</b>	<b>58803</b>	3.30	0.86	14.39	1.14	15000
<b>3.00</b>	<b>72731</b>	5.00	1.29	17.80	1.40	15000
<b>3.20</b>	<b>37139</b>	1.52	0.40	9.09	0.75	15000
<b>3.20</b>	<b>58803</b>	3.00	0.75	14.39	1.14	15000

Table 3-2: Flow conditions inside the large-scale 3-D multi-hole model nozzle at full needle lift.

The results observed in the large-scale multi-hole nozzle have revealed that increasing the cavitation number resulted in the formation of different cavitation hole flow regimes. All of the investigated conditions confirmed that cavitation behaviour in the

nozzle of a gasoline multi-hole injector featuring an overall spray cone angle of  $90^\circ$  is highly dynamic and unstable. Initially, and surprisingly enough, “needle strings<sup>2</sup>” were identified prior to any other hole flow cavitation. At very low cavitation numbers, of the order of 0.5-0.7, strings originated at the needle surface facing an injection hole inlet, which extend downstream into the hole (Figure 3.12). This is believed to have its cause in a temporarily strong vortex flow around the hole axis, which leads to the above described string formation process due to the low pressure region in the core of this vortex. This mechanism becomes dominant as needle lift decreases. Thus, at lifts lower than full needle lift, the flow field alteration imposed due to the extensive throttling at the needle seat area and the reduced distance between the needle surface and the hole inlet result in robust needle string structures that are present at all times. With increasing cavitation number, “needle strings” tend to disappear mainly due to the flow field alterations imposed by hole cavitation that appears around the injection hole inlet. Further increase in the cavitation number causes “needle strings” to be replaced by in-hole cavitation strings, as described in following sections.

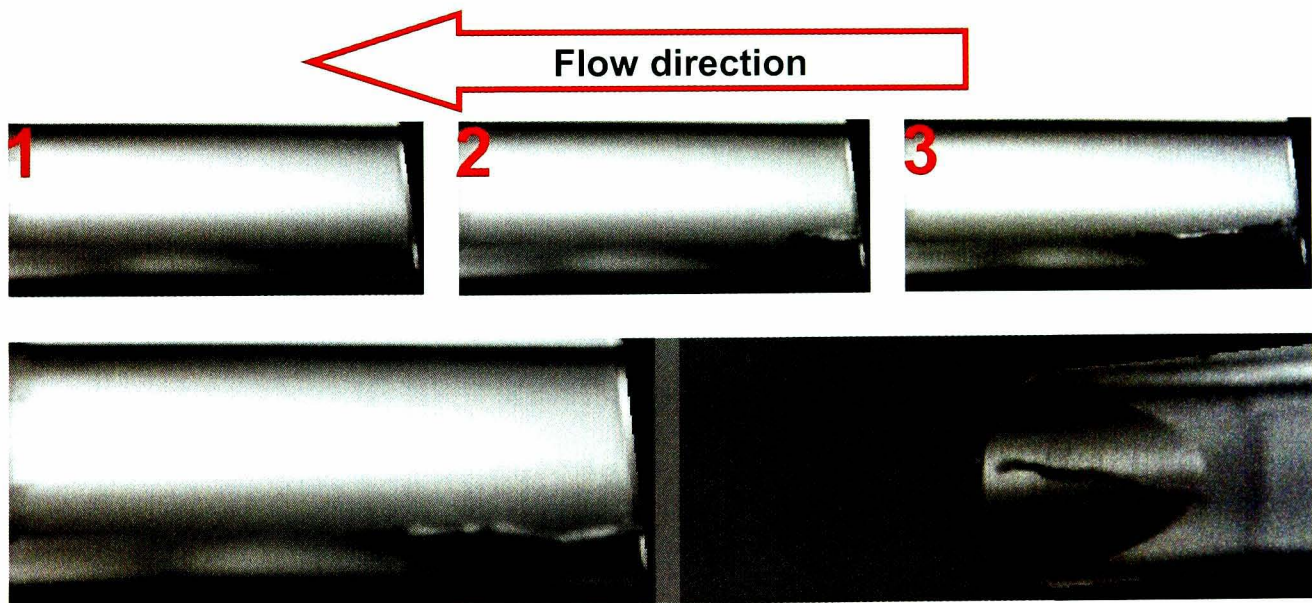


**Figure 3.12:** *Top row:* Image sequence of “needle string” development. *Bottom row:* combined side and bottom view images of a “needle string” taken simultaneously.

As mentioned above, at cavitation numbers in the range 0.7-0.9, bubble clouds appear in the upper hole corner (Figure 3.13 top row), while “needle strings” are still visible below them. These clouds are unstable and tend to detach off the hole surface quite

<sup>2</sup> A needle string has its origin on the injector needle since it appears to originate at the needle surface facing an injection hole inlet and to extend downstream into the hole. It is created by the vortex flow around the injection hole axis, which extends out of the hole onto the needle surface.

frequently and collapse further downstream the injection hole. In the image sequence presented at the bottom row of Figure 3.13, the interaction between the persisting “needle strings” and the bubble cloud in the upper hole entrance is clearly evident. A “needle string” structure could randomly move upwards, and as its low-pressure core region approaches the upper hole inner surface, causes further pressure drop which leads to a bubble cloud appearing in that region. Overall, these are the two mechanisms responsible for the first appearance of cavitation in the hole of a multi-hole large-scale model nozzle.

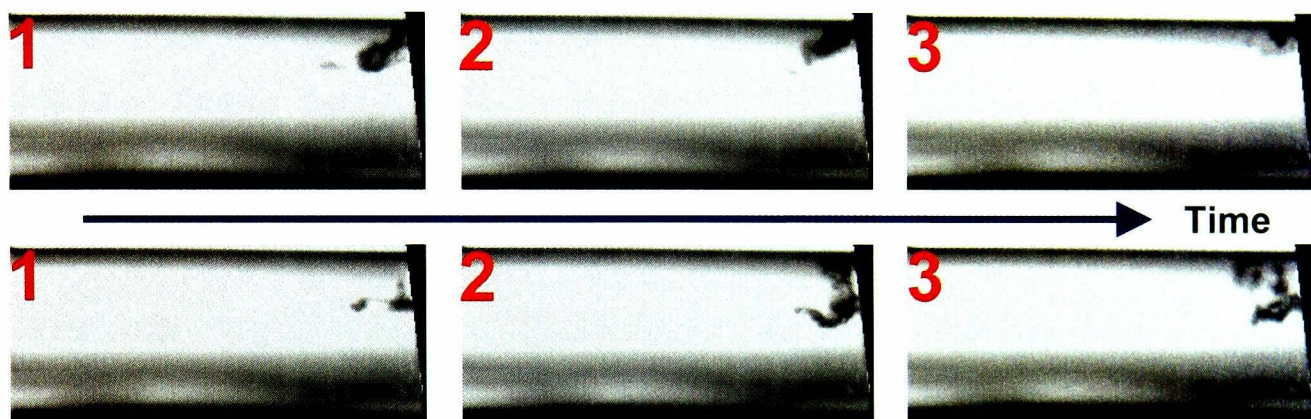


**Figure 3.13:** Side view cavitation visualisation at  $CN=0.73$ . *Top row:* image sequence of bubble cloud at upper hole corner. *Bottom row:* interaction between needle string and hole cavitation.

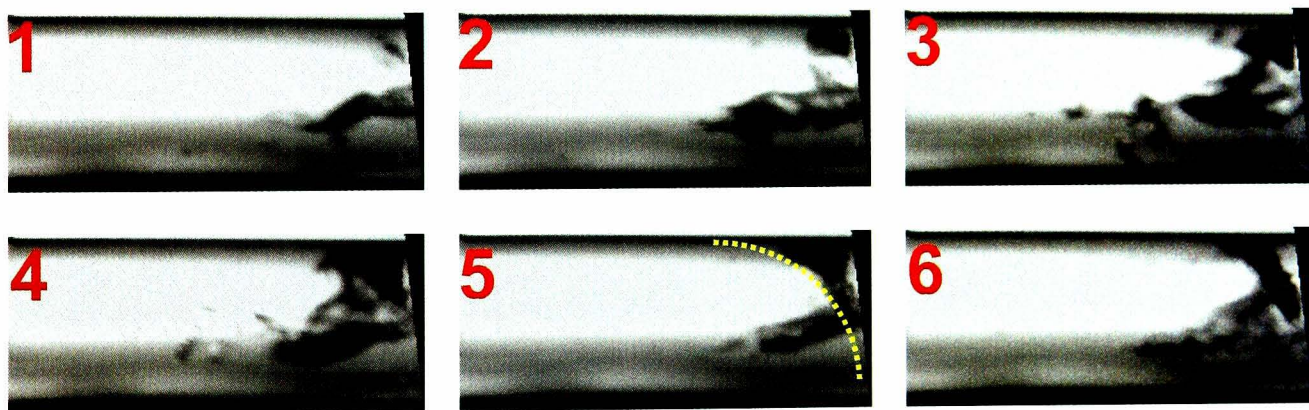


**Figure 3.14:** Demonstration of cavitation regime occupying the hole inlet from upper to side entrance walls at  $CN=0.9$  and full valve lift.

As cavitation number increases to values around 0.9, cavitation develops in three different ways. In Figure 3.14 a sequence of images demonstrates how a cloud created in the upper hole corner extends to occupy half of the hole entrance following the curved shape of the hole. The “needle string”, still visible at these cavitation numbers, does not seem to interfere with the formation and development of hole flow cavitation. In the first two images in Figure 3.14, it is clear how a small cloud is created at the top of the hole entrance, due to the low pressure region caused by the

rapid turning of the liquid as it enters the hole. In images 3 and 4, this cloud has taken a triangular shape and, ultimately, in the last two images it is shown to occupy almost half the hole entrance by following its curved perimeter. Given the highly transient nature of the flow regimes, the aforementioned mechanism is not unique. As Figure 3.15 demonstrates, there could be cavitation at the sidewalls of the hole entrance without the presence or connection to any cavitation regimes at the top entrance of the hole. In Figure 3.15, the “needle string” present in the first images disappears and, without the presence of a stable cloud at the top of the hole, small bubble clouds appear at the sidewalls to form a cavitation film which is highly unstable and quickly collapses. Finally, a more stable mechanism appears to form cavitation films that are canopy shaped and occupy most of the hole entrance perimeter simultaneously.

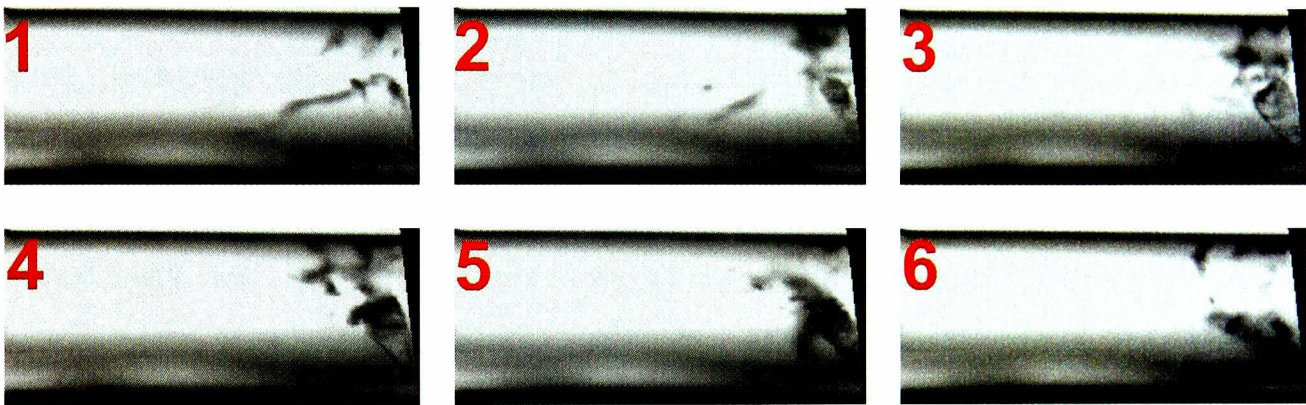


**Figure 3.15: Image sequence demonstrating cavitation at the side entrance walls at  $CN=0.9$  and full valve lift.**

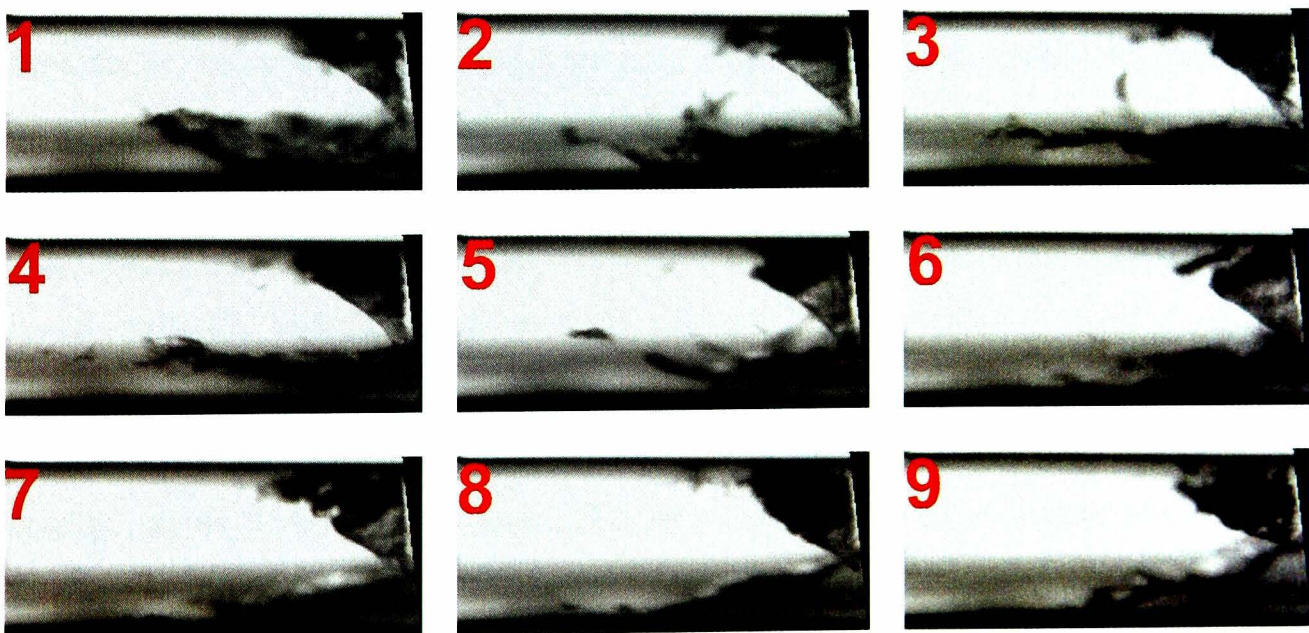


**Figure 3.16: Image sequence of canopy shaped cavitation film development at  $CN=0.9$  and full valve lift.**

This is presented in Figure 3.16 in a series of nine consecutive images. The relatively thin cavitation film, which is visible in the top right corner of each image in the

sequence, occupies simultaneously most of the hole entrance perimeter and maintains its shape for longer times compared to the previously described top- or side-generated vapour films. The difference in light intensity gives a rough estimation of the vapour film thickness, although dark areas at the top of the film are due to the film present at the background wall of the hole.

### 3.4.3 Developed cavitation

In general, in the large scale model the nozzle flow transitions from bubbly flow through pre-film to film stage cavitation as identified in the high-speed videos with increasing cavitation number. For almost all investigated cavitation numbers it seems that the cavitation structures are unstable due to the large pressure variations in the cavitation zones and the increased flow turbulence that dominates the internal nozzle flow. In the high-speed video image sequences it can be seen that the flow entering the injection hole from the side, as well as the cavitation strings, play a major role in further cavitation inception and development. For cavitation numbers smaller than 1, it has been discussed in previous sections that “needle strings” and bubble clouds represent the incipient cavitation. As cavitation number increases to values equal and greater than 1, the bubble clouds become more opaque and it is not possible anymore to distinguish between individual bubbles. Moreover, the beginning of the coalescence of cavitation bubbles forms larger voids, which lead to local vapour films (Figure 3.17a). A further increase of the cavitation number causes the flow to fully separate at the upper half of the nozzle hole inlet. This, in turn, induces the formation of a vapour film type cavitation (Figure 3.17b) where the relatively thin film follows the curved shape of the hole. Although these geometrically induced cavitation patterns were found not to depend on the Reynolds number (flow rate), the development of these cavitation structures was strongly affected by the cavitation number. Almost identical behaviour of cavitation structures and their development has been reported in diesel injectors [43, 44, 49, 102]. For both most commonly used diesel nozzle configurations (Conical Mini-Sac and Valve Covering Orifice) similar pre-film and film stage cavitation structures have been reported. These structures do not depend on Reynolds number unlike cavitation number and needle lift that affect the transition among the different stages. The similarities in internal nozzle flow between gasoline multi-hole and diesel injectors are of great significance since certain flow patterns of gasoline multi-hole nozzles can be explained according to the results of the ongoing research in diesel nozzles.

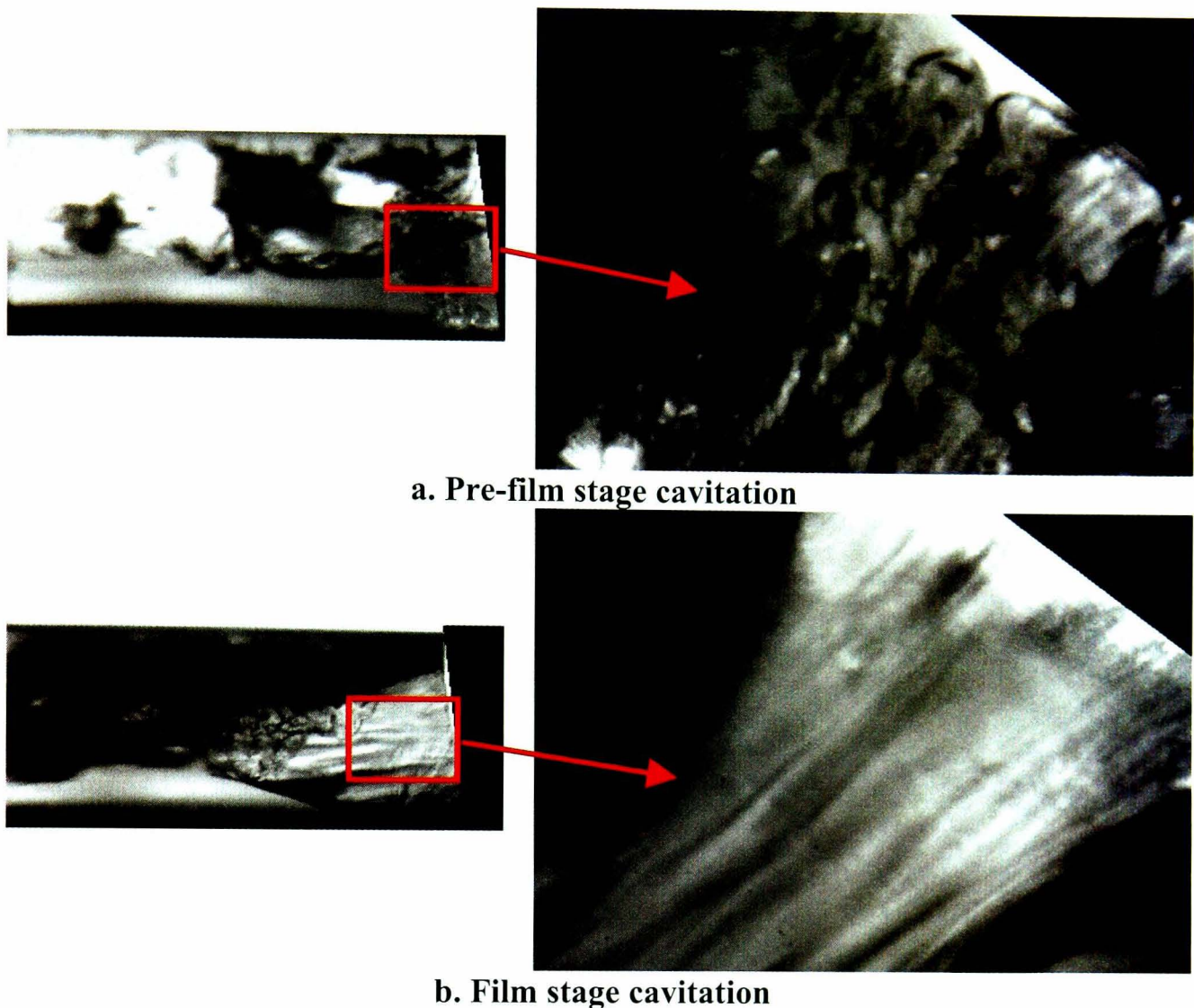


**Figure 3.17: Cavitation regimes inside the 3-D large-scale model nozzle**

Surprisingly enough, string-type cavitation structures were observed to be present in the holes but their creation mechanism is radically different than that of the “needle strings”. Although the geometry of the examined nozzle is axis-symmetric, a vortex structure was identified to be present in the volume between needle, needle seat and two adjacent holes. The vortex and string formation was attributed to the interaction between the high momentum annulus flow and the cross flow, which occurs due to the intermittent throttling of individual holes by already existing recirculation zones or cavitation at their entry. As a result, the flow conditions at the vortex core lead to the formation of a low-pressure region and, subsequently, of cavitation bubbles, which coalesce immediately into a continuous vapour string along the core of the vortex (Figure 3.18). This string is initiated inside one injection hole by a strong vortex around the hole axis. As presented in the image sequence in Figure 3.19, it extends upstream to the hole inlet, where it triggers a bubble creation mechanism at the core of the vortex between two adjacent holes. The succession of bubbles forms a fine string structure that extends to the neighbouring injection hole. These strings

seem to develop transiently and intermittently between adjacent holes. The parts of the vortex entering the injection hole inlet area seem to diffuse to large conical clouds of bubbles, which then mix with the already established hole cavitation structures.

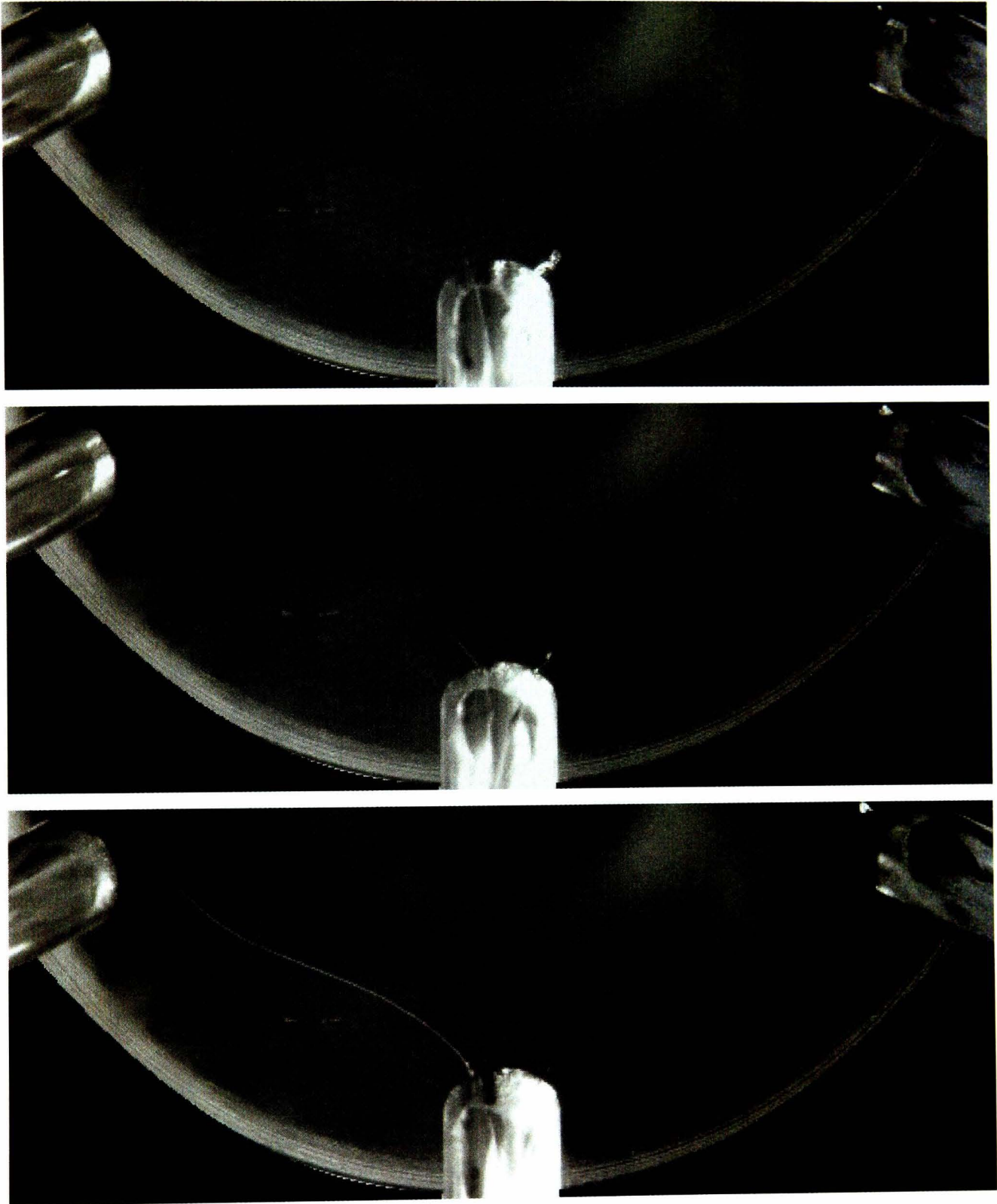


**Figure 3.18: Image sequence with developing cavitation string.**

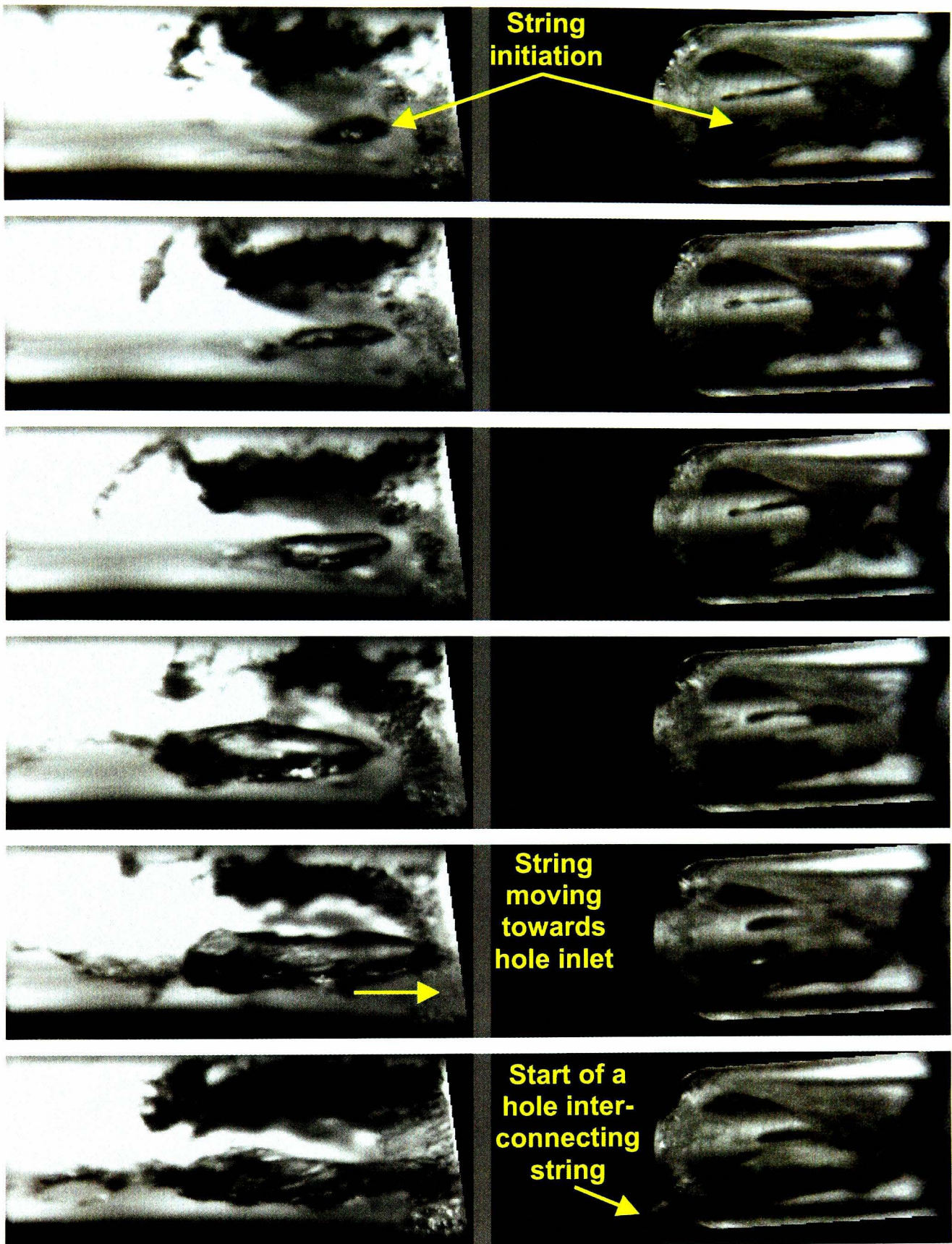


**Figure 3.19:** Image sequence with in-hole cavitation string creation mechanism at  $CN=1$ .

What might prove to have major practical importance is the interaction of these cavitation strings inside the hole with the cavitation structures already formed in the upper region of the injection hole, which may give rise to turbulence enhancement and hole-to-hole variations in the two-phase mixture exiting the hole. Thus, despite the axis-symmetric geometry of the vertical multi-hole nozzle, variations in the flow pattern between holes are likely to happen due to the complex two-phase flow present

in the sac volume and holes after the onset of cavitation. The actual influence of the highly transient strings on the in-hole cavitation structures inside multi-hole nozzles at cavitation numbers of the order of 1 is presented in a sequence of high-speed video images in Figure 3.20.

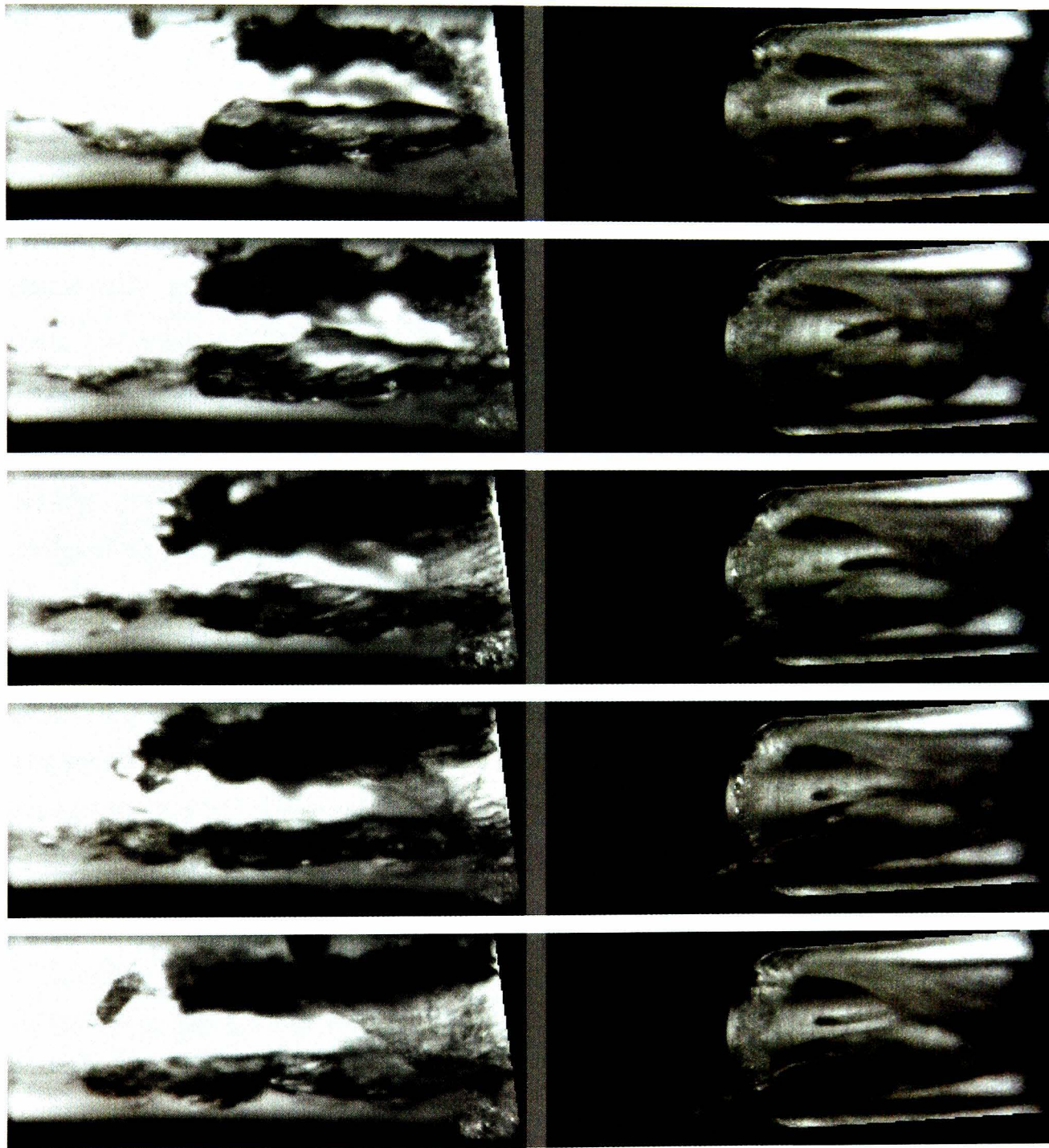


**Figure 3.20: Interaction between cavitation string and in-hole cavitation structures at  $CN=1$ .**

In the first image of the above sequence it is clear that cavitation around the hole inlet is unstable and not fully developed. At the same time, cavitation strings can be identified that do not extend to the hole inlet. At later images in the sequence, the cavitation string has been extended well beyond the hole boundaries. The vapour volume induced by the string reduces the effective flow area at the hole inlet and, in turn, fluid flow entering the hole is accelerated. A series of events are being triggered

and the resulting flow acceleration is responsible for further pressure drop in the potentially low-pressure regions. Finally, this behaviour enhances stabilisation of cavitation around the hole inlet boundary. As presented in the latter images of the above sequence, pre-film stage cavitation is well established and the detachment of the flow off the side hole walls is evident.

In general, pre-film stage cavitation could be identified at high-speed video images for cavitation numbers up to 2. The main characteristic of the observed cavitation regimes has been the highly unstable structures and their transient behaviour. More specifically, as cavitation number increases, film stage cavitation appears although it does not seem to be well established unless the cavitation number exceeds 2. Therefore, as the image sequence in Figure 3.21 shows, there is continuous alternation between pre-film and film stage cavitation. First images at the sequence present a bubbly cavitation pre-film, while in the latter ones the tendency for bubbles to coalesce and form a film structure is clearly evident. The above-described transient behaviour proved to be almost independent of the flow rate through the nozzle (Reynolds number), although it is highly dependent on the valve lift. Regarding the effect of the needle lift on the cavitation pattern development, it was observed that a low needle lift leads to more turbulent flow behaviour and thus bubblier cavitation (r-h-s of Figure 3.22). Increasing the needle lift gives rise to a more stable flow and the cavitation structures inside the injection holes transform into a more or less steady cavitation film (l-h-s of Figure 3.22). A direct comparison could be seen in Figure 3.22, where all images were taken at a cavitation number of 1.5, a Reynolds number of 46,500 at full lift and 49,000 at the lower lift for two different needle lifts of 2.04 and 1.53mm. The difference in the film structure is visible and the turbulent bubbly flow induced by the lower needle lift is clearly identified in the right-hand-side column of the figure.

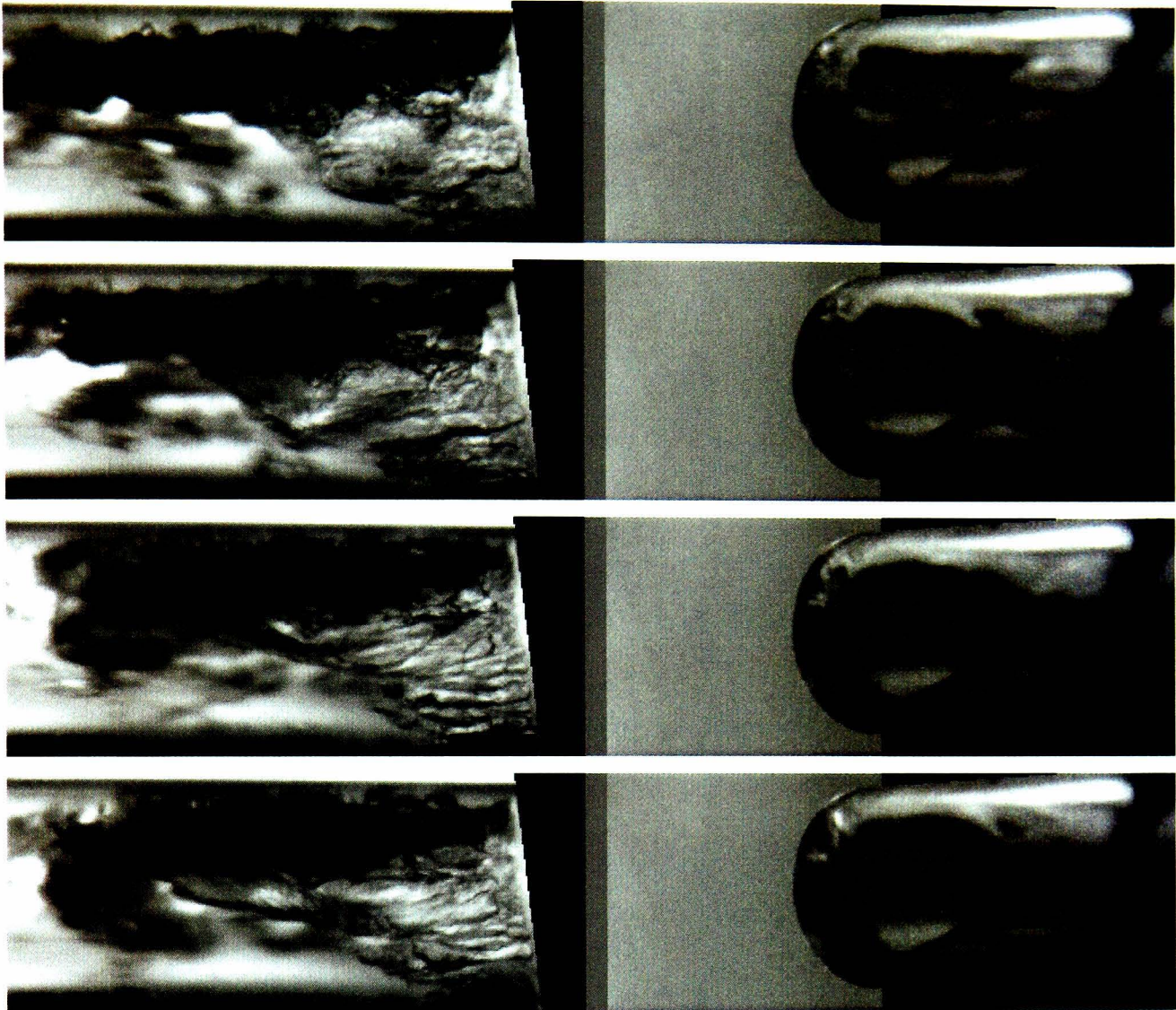
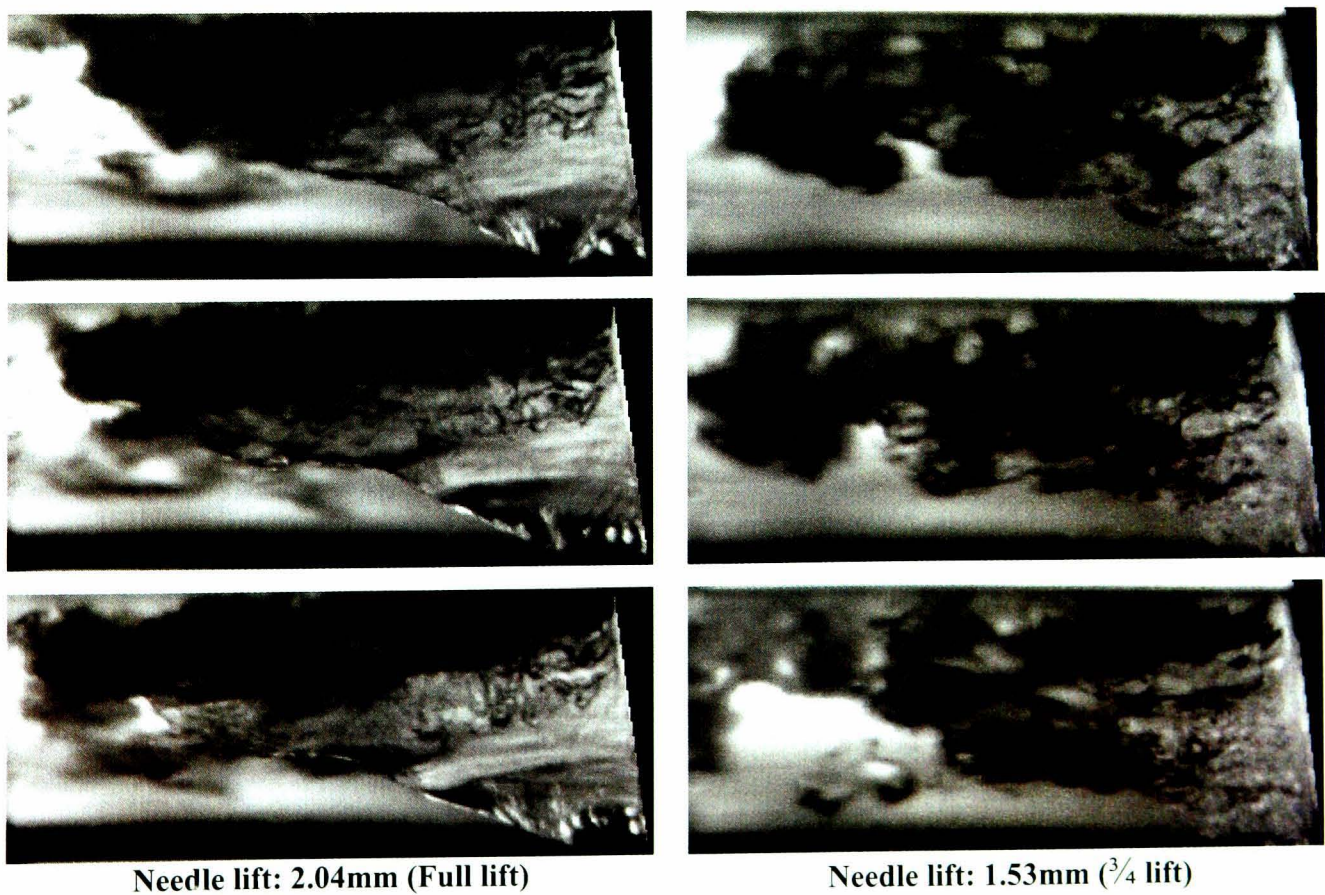


Figure 3.21: Alternation of pre-film to film stage cavitation at  $CN=2$ .

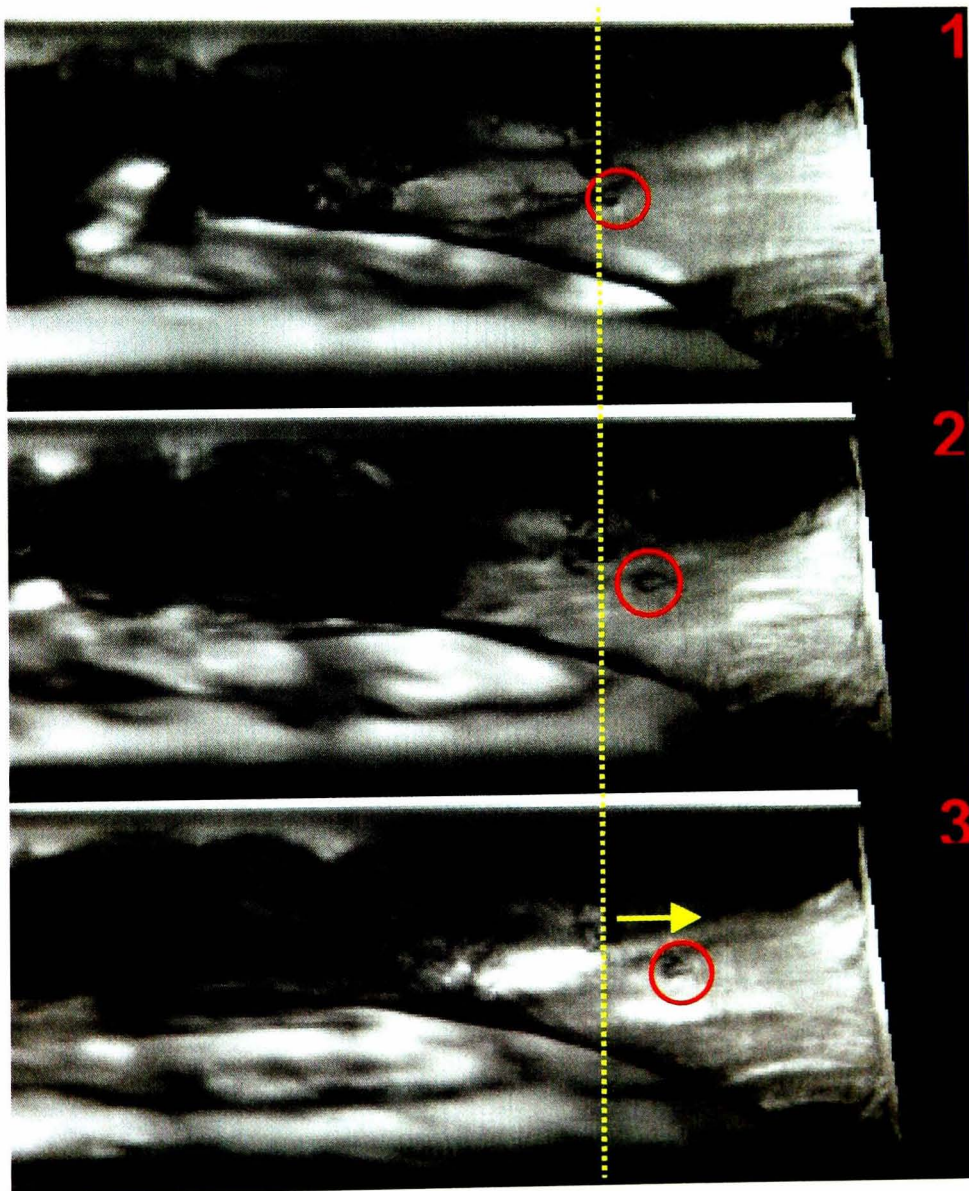


Needle lift: 2.04mm (Full lift)

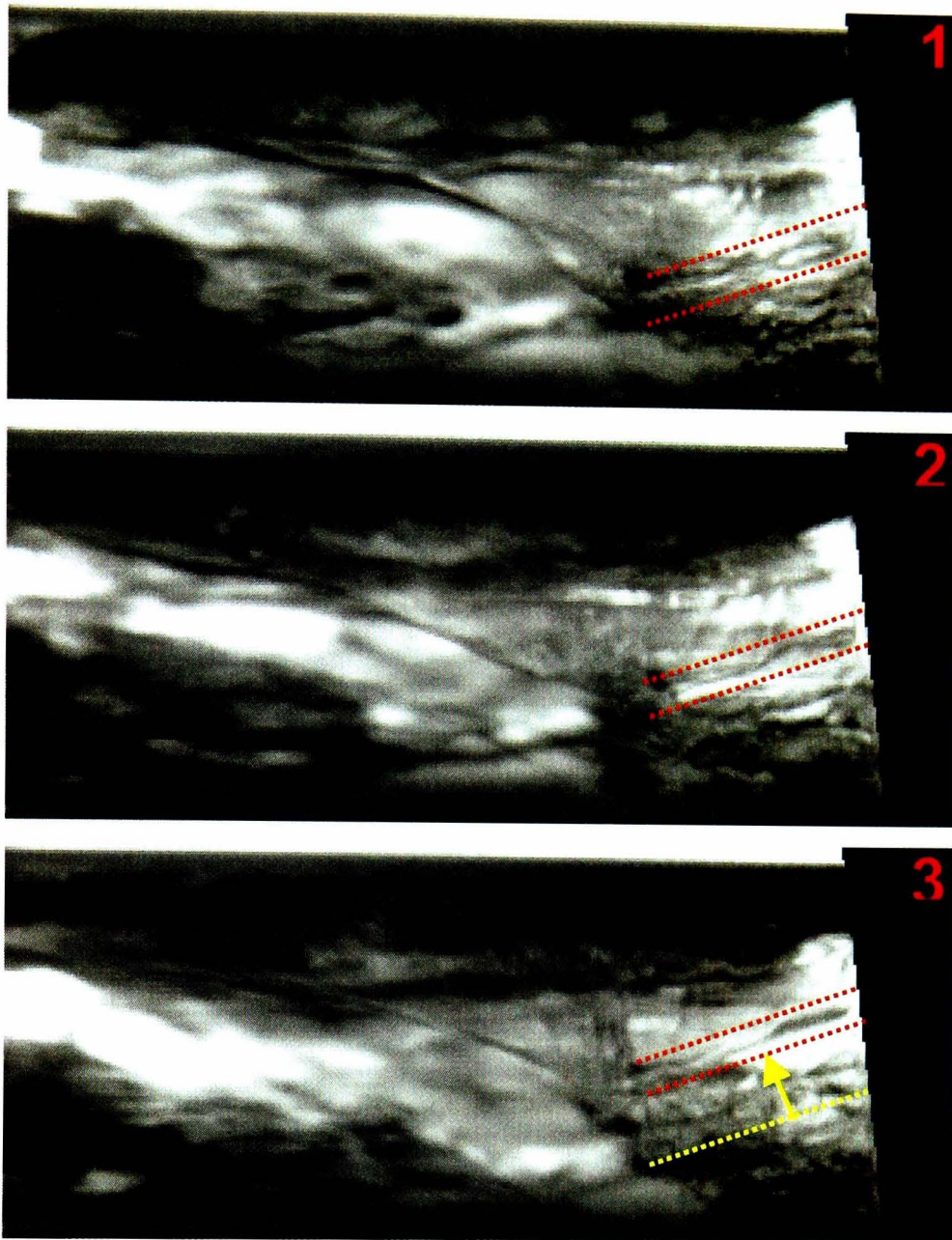
Needle lift: 1.53mm ( $\frac{3}{4}$  lift)

Figure 3.22: Effect of needle lift on cavitation structures ( $CN=1.5$ ,  $Re \sim 46,500$ ,  $\sim 49,000$ ).

In addition to the previously discussed phenomena, a recirculation zone was identified throughout the transitional period from pre-film to film stage cavitation. Given the unstable behaviour of both types of cavitation, bubbles that did not manage to integrate into the created film maintain their shape and attach to the hole side walls, thus allowing a kind of flow-seeding in that region. The flow inside the gaseous pocket that the detached cavitation film has created is almost stagnant and subject to pressure differences across that region. In some cases, the low-pressure at the hole entrance is enough to create a small recirculation zone inside that gaseous pocket. An example of such behaviour is presented in Figure 3.23 where a small bubble marked by a red circle moves towards the hole entrance. Furthermore, another more frequent flow structure inside the gaseous pocket that the cavitation film creates is presented in Figure 3.24. In this case, the flow moves upwards, from the bottom hole entrance wall towards the top hole wall and it is mainly visible due to the texture of the interaction interface between gas and liquid.



**Figure 3.23:** Representation of recirculation zone inside the gaseous pocket of film cavitation at  $CN=2.5$  and full valve lift.



**Figure 3.24: Flow structure inside the gaseous pocket of film cavitation at  $CN=2.5$  and full valve lift.**

At cavitation numbers higher than 2.5, film stage cavitation is well stabilised and the film thickness is substantially larger than at any lower cavitation number. A representative example is presented in Figure 3.25, where the cavitation number is set to 3 and the thickness of the vapour cloud blocks the light from reaching the camera, thus appearing darker than in previous conditions. Furthermore, as cavitation number increases, cavitation strings appear almost permanently in the injection hole and frequently develop into hole interconnecting strings. Neither the film stage cavitation patterns nor the in-hole cavitation strings seem to depend on the Reynolds number. Keeping the cavitation number and needle lift constant to 3 and full lift, respectively, a variation of the Reynolds number from 49,000 to 73,000 did not show any significant effect on both types of cavitation structure.

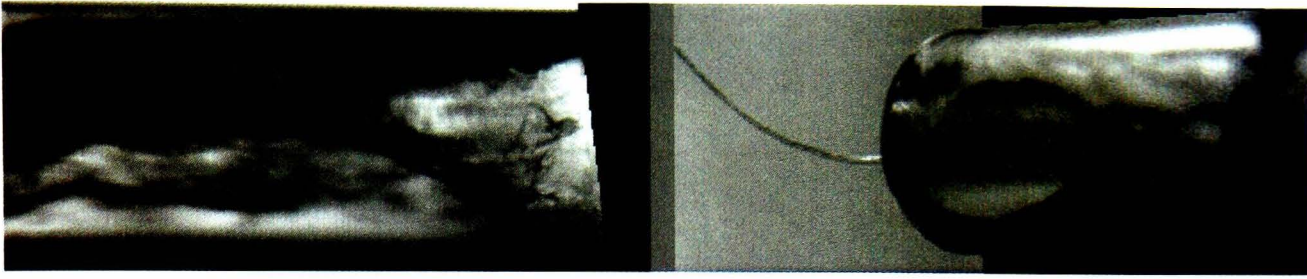


**Figure 3.25: Representative image of film stage cavitation at  $CN=3$  and full valve lift.**

Finally, high-speed video images confirmed that, apart from the cavitation number, the needle lift also affects to a significant degree the cavitation development at cavitation numbers greater than 3.5. At full needle lift conditions, the in-hole cavitation patterns seemed to stabilise in terms of vapour/liquid interface surface quality and volume of gaseous pocket at cavitation numbers greater than 2.5. At lower needle lifts, the afore-mentioned critical cavitation number ( $CN \sim 2.5$ ) seemed to shift towards higher values. As described previously, lower needle lifts cause a highly turbulent flow mainly because of the extensive flow throttling through the needle seat area. The generated turbulence is transferred to the injection hole and causes a breakdown of the film leading to a “bubblier” in-hole flow field, which in turn is responsible for shifting the pre-film stage cavitation at higher cavitation numbers. In a direct comparison (Figure 3.26) of representative images at full (2.04mm) and half needle lift (1.02mm) conditions at a cavitation number of 3.2 the difference in the vapour film structure is evident. In the case of half needle lift (bottom row in Figure 3.26) there is a bubbly pre-film stage cavitation structure. Furthermore, in the right-hand-side image (bottom view) cavitation is not well developed at the bottom entrance of the hole in the case of low needle lift. Structures of film stage cavitation at low needle lifts were observed at cavitation numbers as high as 5.2. In Figure 3.27, a direct comparison of film cavitation surface quality under different needle lifts is attempted and cavitation numbers of 3.2 (top row – 2.04mm) and 5.2 (bottom row – 0.51mm) are presented. Although film stage cavitation is visible in the bottom row image, the differences to the full lift image on the top row are significant. Specifically, the main volume of gas can be found almost around the hole axis rather than at the top hole wall. This is mainly due to the size of the cavitation string, which expands almost to two thirds of the hole cross-sectional area suppressing in this way geometric cavitation as at full lift conditions. Dashed yellow lines mark the expansion of the cavitation string, shown in the bottom image, while there is no cavitation string visible at the top image.

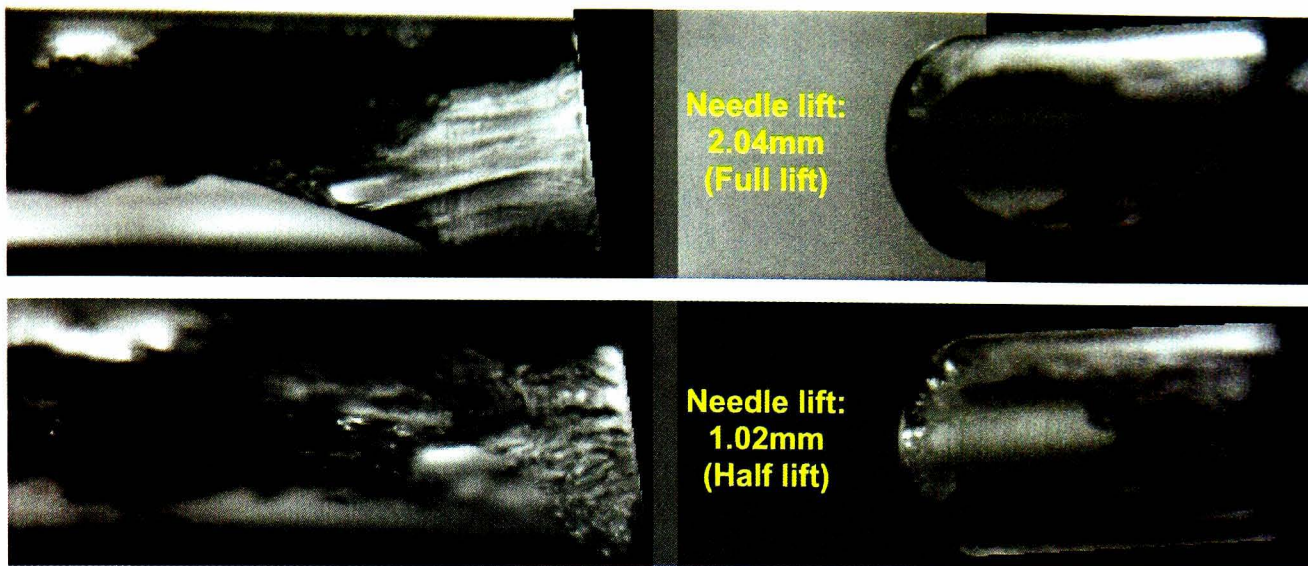


Figure 3.26: Effect of needle lift on cavitation structures at  $CN=3.2$ .

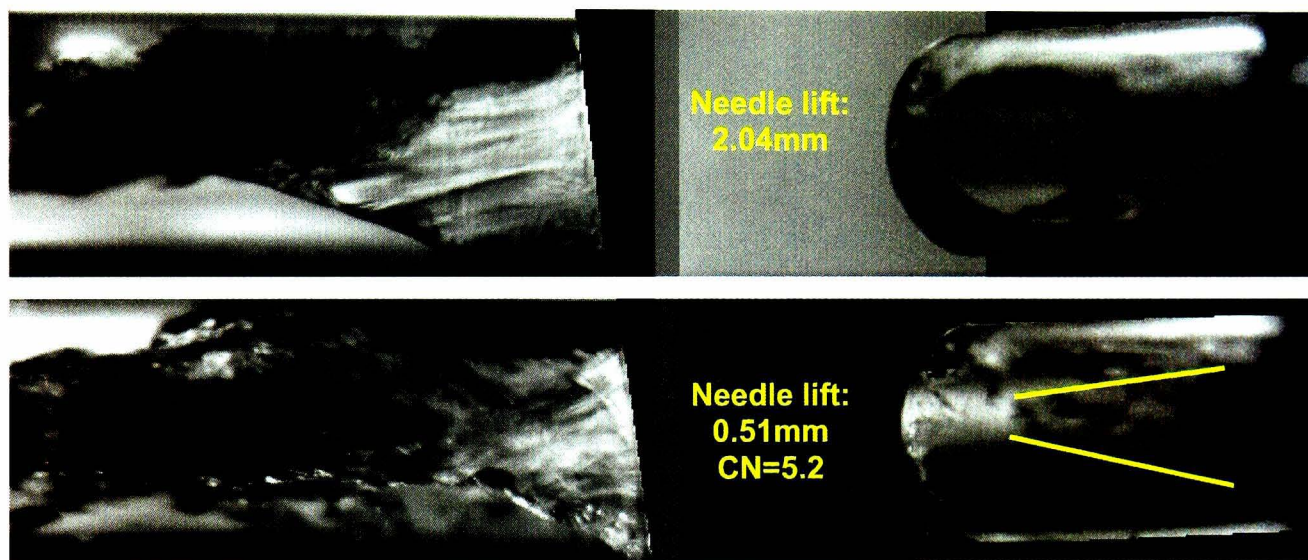


Figure 3.27: *Top row*: Full needle lift (2.04mm) at  $CN=3.2$ . *Bottom row*: One quarter of full needle lift (0.51mm) at  $CN=5.2$ .

### 3.5 SUMMARY

The transparent large-scale nozzle test rig proved to be extremely helpful in understanding the internal nozzle flow patterns in multi-hole injectors especially when coupled with the high-speed digital video technique. Internal nozzle flow dependencies on injector operating parameters have been visualised and well discussed. More specifically, the onset of cavitation in multi-hole injectors is of great importance, since such a change in the injection hole flow patterns affects considerably the injected spray. For the gasoline multi-hole nozzle that features a  $90^\circ$  overall spray cone angle, the onset of cavitation has been identified at flow conditions (flow rates and injection pressures) significantly lower than the expected operating field of such an injector. The aforementioned fact is adequate to classify the examined

multi-hole nozzle as a cavitating high-pressure nozzle. In addition, the cavitation structures and their dependency on Reynolds (flow rate) and cavitation numbers, as presented in previous sections, could allow improved understanding of the atomisation mechanism of multi-hole injectors and the emerging spray structure. Furthermore, in-hole cavitation development and cavitation string structures are expected to alter the geometric characteristics of the nozzle, thus resulting in injected liquid spray velocities significantly higher than the geometrically calculated ones. It is thus important to investigate the spray characteristics of multi-hole nozzles and, in particular, the temporal variation of the injected droplet velocities and size distribution under a wide range of operating conditions. This is considered to be a prerequisite towards a more complete understanding of high-pressure multi-hole gasoline injectors which offer promise as FIE systems in second-generation direct-injection gasoline engines.

## *Chapter 4*

### *Spray Characterisation*

The fuel injection system is one of the key elements that must be optimised if the DISI concept is to achieve its full potential as a viable alternative to the PFI engine in the coming years. The restriction of the fixed-location ignition source places great importance on mixture preparation in DISI engines where the mixing process is controlled primarily by the atomisation and transport of the liquid/vapour fuel towards the spark plug at the time of ignition. For injection during the intake stroke aiming at homogeneous mixtures, the high-pressure fuel injection system should produce, at the correct timing, a spray with tip penetration that chases the moving piston, since fuel impingement on the piston could have an adverse effect on hydrocarbon emissions. For late injection during the compression stroke aiming at stratified overall lean mixtures, the elevated in-cylinder gas pressure reduces spray penetration [7, 17, 34, 38, 94] producing a more compact spray that can more easily be directed towards the spark plug. Although through many years of research on multi-hole diesel sprays a comprehensive know-how has been established on direct injection high-pressure sprays, there is still a lot to be learned about gasoline sprays due to the different spray types, injection/ambient conditions and fuel properties. Therefore, the advent of the new generation DI gasoline engines has opened up a new and important research area on high pressure sprays. A wide range of experimental techniques have been employed with the most important being Phase Doppler Anemometry (PDA), Laser Doppler Velocimetry (LDV) [19, 25, 40, 55, 63], Mie scattering and LIF [58, 72, 75, 78, 81, 88, 105-110] or a combination of the above (laser-sheet droplet-sizing – LSD) [69, 72]. These techniques aim at providing single point droplet size and velocity information, identifying the atomisation process as well as revealing the spatial and temporal characteristics of the liquid / vapour phases of transient sprays for a range of nozzle designs.

Having studied the internal nozzle flow patterns generated in a six-hole injector, the next step was to examine the spray characteristics of different multi-hole nozzle configurations in terms of number of injection holes and nozzle hole positioning.

Therefore, five-, six- and twelve-hole nozzles were examined, incorporating central injection holes and fully symmetric or non-symmetric spray patterns. The aforementioned multi-hole injector types represent the 2<sup>nd</sup> generation of DI injectors, capable of operating under atmospheric and high-pressure ambient conditions in a close spacing configuration. In the present study Mie scattering and Phase Doppler Anemometry were employed for characterisation of the sprays, as they are capable of providing detailed information about the spray structure. A constant-volume spray chamber was used to investigate the effects of increased ambient and injection pressure conditions, at room or higher temperatures, on the spray structure. Such experiments have been useful in allowing an assessment of the injection system operating parameters on the ensemble averaged temporal and spatial spray development under quiescent flow conditions.

#### **4.1 INVESTIGATED MULTI-HOLE NOZZLE CONFIGURATIONS**

Initially, the aim of this study has been the investigation of the high-pressure gasoline multi-hole injector concept and the flexibility in nozzle design that it offers. Consequently, several nozzle configurations have been considered having their main differences in the number and position of injection holes. The design philosophy of multi-hole nozzles is based on guidelines derived from the corresponding diesel technology where a variety of injector geometries have been investigated thoroughly by several research groups worldwide. These guidelines suggest that the holes should be positioned on the periphery of an imaginary circle. The number of holes varies and the basic variations include nozzles featuring six-, eight- or twelve-hole pattern designs. The increased design flexibility of multi-hole nozzles is also evident in the investigated later on designs that come from slight modifications in the aforementioned six- and twelve-hole conventional symmetric nozzles. More specifically, there is a possibility of adding an extra central hole to any hole arrangement, as well as blocking one or more side holes. The design of the injection nozzle could be fully symmetric around the injector axis, or the holes could be positioned at random angles, always on the same circle periphery, forming a non-symmetric hole configuration. Finally, a very important design characteristic of multi-hole nozzles is the overall spray cone angle, which represents the relative angle formed between an injection hole axis and the injector's geometric axis.

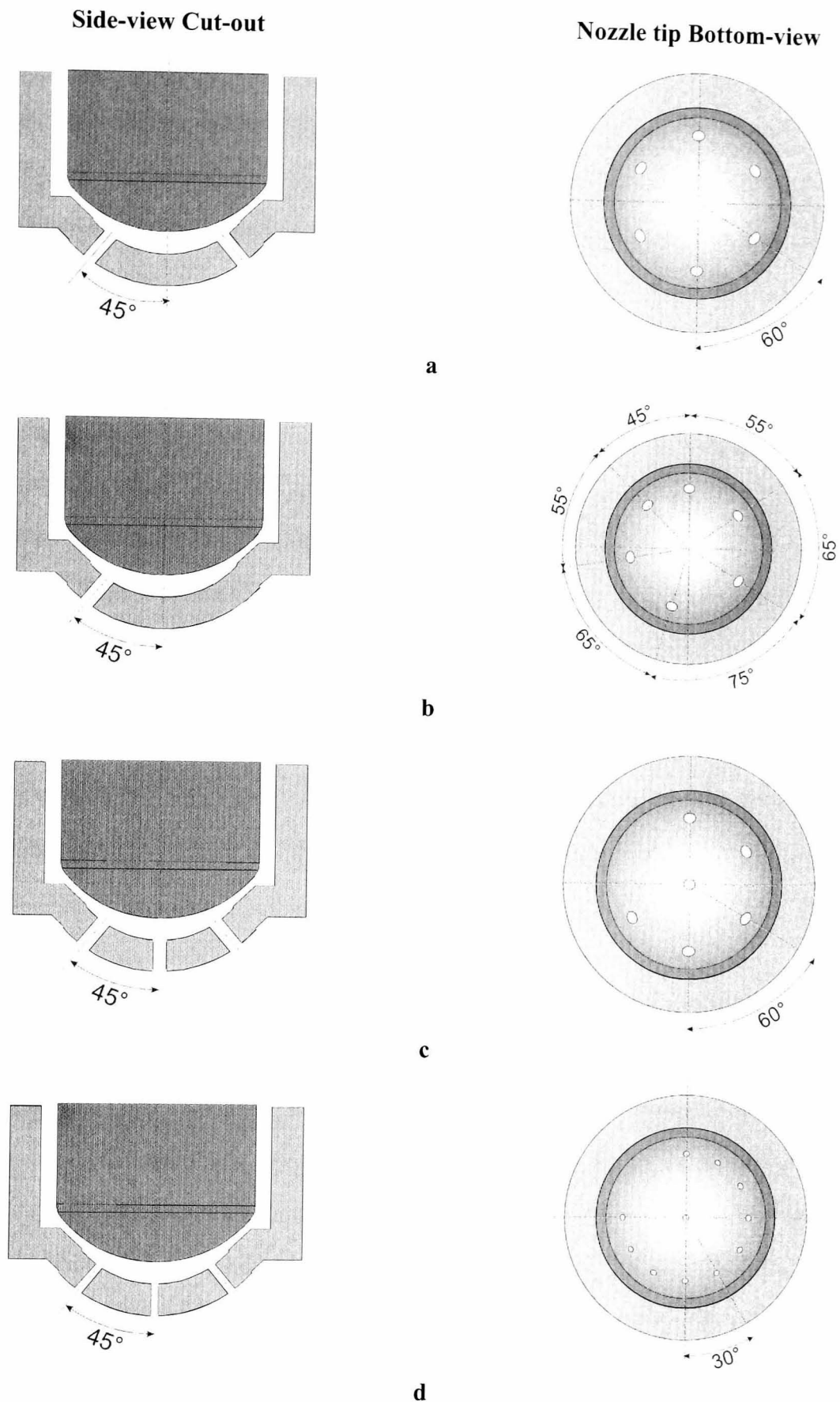


**Figure 4.1: Tested multi-hole nozzle configurations. (a). Symmetric 6-hole, (b). Asymmetric 6-hole, (c). 5-hole plus one central hole and (d). 12-hole nozzle with 2 missing peripheral holes and a central hole.**

In Figure 4.1 a schematic representation of all investigated nozzle designs is illustrated. The first two designs (Figure 4.1a and b) correspond to a six-hole nozzle

configuration. The first one represents a fully symmetric hole arrangement where the angular spacing between two adjacent holes is  $60^\circ$ . The second schematic features a non-symmetric design where the angular spacing varies from  $45^\circ$  to  $75^\circ$ . The third design (Figure 4.1c) comes from the symmetric six-hole nozzle family and features a central hole, while one side hole is blocked. The reason of blocking one or more side holes is the creation of a small gap for spark plug positioning in the case of a close-spacing, spray-guided combustion concept. The last schematic illustrated at Figure 4.1d is a twelve-hole design featuring a central injection hole and two blocked side-holes. In the case of the twelve-hole nozzle the angular spacing is kept constant at  $30^\circ$  and the hole diameter is reduced when compared to the six-hole nozzle hole size. The reduction in injection hole diameter has to be realised for the static flow rate of all nozzles to be kept constant, when the number of holes is doubled. More specifically, six-hole nozzles feature a hole diameter of  $140\mu\text{m}$  and a hole length of  $300\mu\text{m}$ , resulting in a “length to diameter” (L/D) ratio of 2.14. Twelve-hole patterned nozzles maintain the exact same hole length of  $300\mu\text{m}$ , while the hole diameter is reduced to  $100\mu\text{m}$  (for the total flow area to be kept constant), resulting in a L/D ratio of 3. All different designs illustrated at Figure 4.1 feature an overall nominal spray cone angle of  $90^\circ$ .

Multi-hole nozzles have been characterised as second-generation fuel injection equipment for gasoline direct-injection engines. The main differences, or more specifically, the main advantages of the multi-hole nozzles versus the first generation swirl pressure atomisers are presented in subsequent paragraphs. Currently, the third generation of high-pressure gasoline injectors has been released and the main difference compared to multi-hole nozzles is in the electronics driving the injector needle. Highly sophisticated piezo technology secures accurate and very fast opening and closing times of the injector needle, thus controlling in the best possible way the injection event duration. At present, multi-hole gasoline injectors do not exploit the advances in electronic technology and therefore a conventional high-voltage coil is responsible for controlling the movement of the injector needle. As a result, long needle opening and closing times have been measured that affect directly the actual injection duration. Every injection event is controlled by a triggering pulse of certain duration. Long needle opening and closing times result in actual injection duration considerably different than that determined by the injection signal. As illustrated in

Figure 4.2, for an electronic injection pulse of 1.5ms (blue line) the resulting actual injection duration, as measured from the needle trace (red line), is about 1.1ms. The long needle response times to any injection pulse changes constitutes a major drawback for the establishment of the multi-hole high-pressure gasoline injector as a promising fuel injection equipment for direct-injection spark-ignition engines.

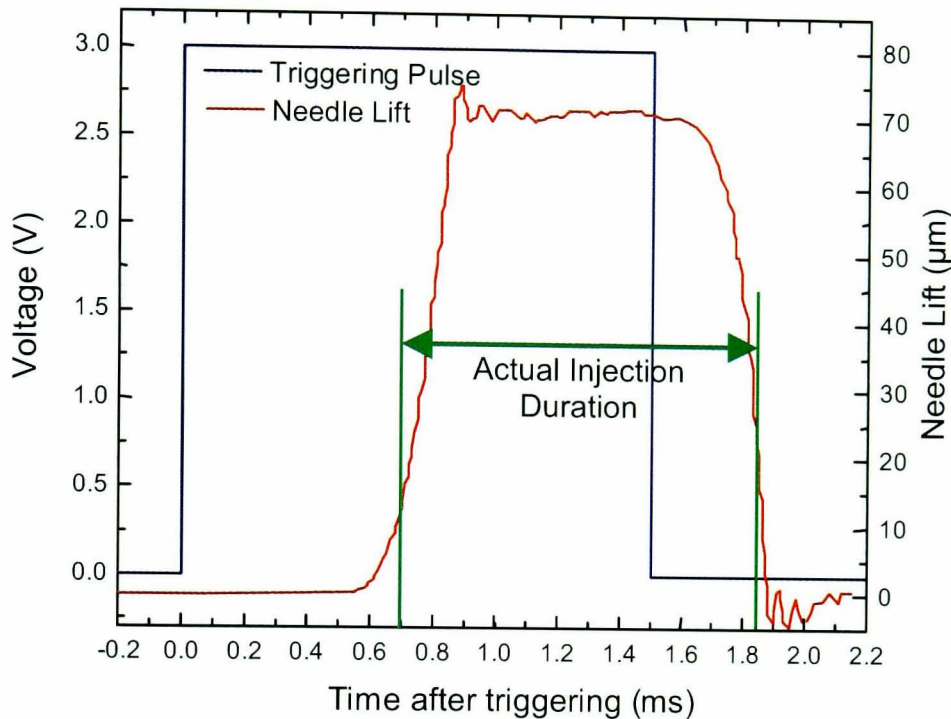


**Figure 4.2: Multi-hole injector triggering signal and typical needle lift diagram.**

As illustrated in the above graph (Figure 4.2), the needle opening delay is almost 0.7ms. This fact has also been confirmed by accurately timed images (section 4.5) that show liquid fuel exiting the nozzle holes at times 0.65-0.75ms after the electronic injection pulse has been applied to the injector coil. This relatively long needle opening delay sets an unfortunate limit on the minimum injection duration that multi-hole injectors can deliver. Additionally, stable injection events have been recorded at injection pulse durations greater than 0.9ms. Since the applied injection pressure does not assist the needle-opening event, the absolute rail pressure considerably affects injection pulse durations smaller than 0.9ms. The aforementioned needle opening delay also affects the minimum settings in parameters related to the multiple-injection strategy. Double-injection is well investigated among all major engine manufacturers as a very effective way of achieving both a minimum delay in reaching the catalyst light-off temperature and stable combustion under homogeneous and stratified operating conditions [5, 34, 74]. Apart from the individual pulse duration settings for both injection events, a critical parameter affecting the effectiveness of double-

injection is the delay between the two injection pulses, or also known as “dwell-time”. In real engine applications the dwell-time requirements vary from a minimum of almost 0.3ms to a maximum of a couple of milliseconds (always depending on engine speed). It is evident that dwell-times of 0.3-0.5ms are not officially supported from the multi-hole injector. The word “officially” has been chosen to declare that according to experiments carried out for the present work, multi-hole injectors could support shorter dwell-times than the needle opening delay. Their behaviour is stable apart from the second injection event, in a double-injection sequence, which appears to have an elongated duration relative to the injection pulse applied.

Prior to any experiments involving the aforementioned multi-hole injectors, a volumetric capacity characterisation was carried out in terms of injection pressure and injection pulse duration. The results, as presented in Figure 4.3 and Figure 4.5, confirm the expected trends. Volumetric capacity among all tested nozzles does not differ considerably. Additionally, it is proportional to injection pressure and injection pulse duration, as expected. More specifically, in Figure 4.3 a direct comparison of the four different multi-hole nozzle designs is illustrated. Useful conclusions extracted of this graph could be summarised as follows: injection pulse durations smaller than

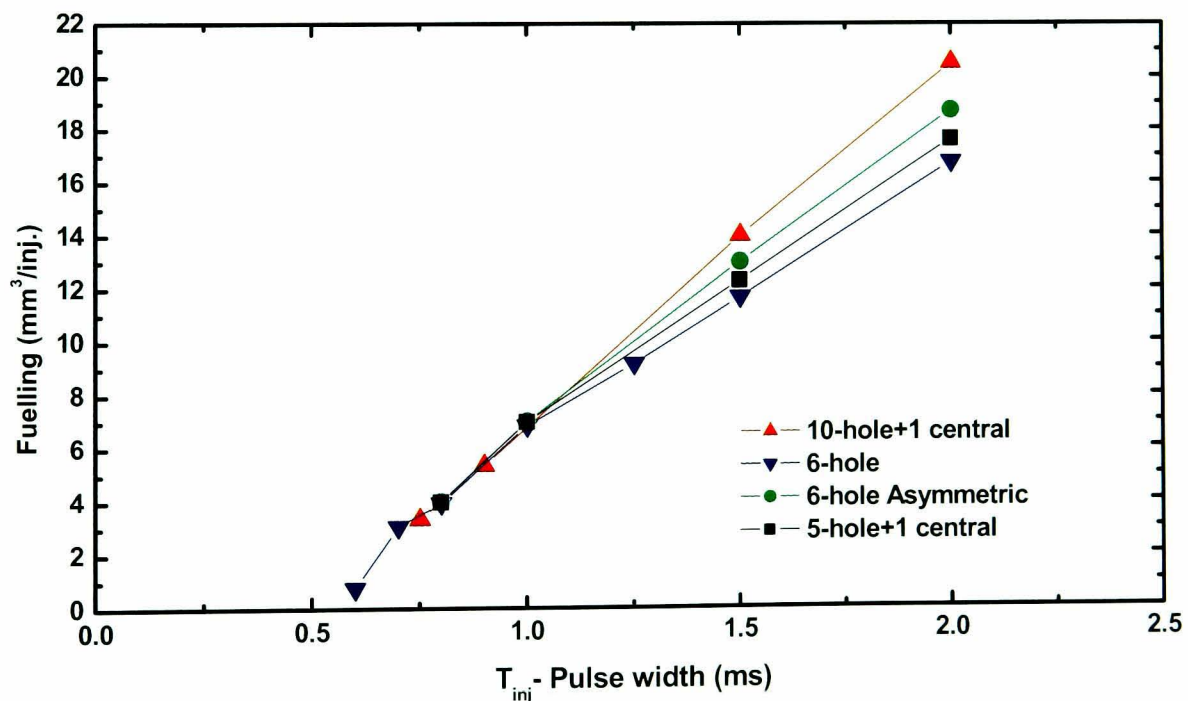


**Figure 4.3: Direct comparison of volumetric capacity of all tested multi-hole injectors at 120bar injection pressure.**

1ms present a non-linear fuel flow-rate curve, while durations greater than 1ms exhibit acceptable linearity and differentiations among the four designs. Additionally,

although the total flow area between the 12-hole pattern nozzle (in graph “10-hole+1 central) and the 6-hole one is almost identical, the first shows higher volumetric capacity compared to the latter one, as high as 16%. The reason for the increased volumetric capacity of the 12-hole nozzle is directly related to the internal geometry of that nozzle. All manufacturing details for the internal geometry are identical for both nozzles apart from the injection hole diameter, which is reduced for the 12-hole nozzle for the total flow area to be kept constant. The latter, combined with the fact that the radius of curvature at the hole inlet is identical for both nozzles, alters significantly the geometric cavitation development that takes place in the injection hole. The radius of curvature of the hole inlet to the hole diameter ratio ( $r/D$ ) directly affects geometric cavitation patterns [111, 112], since higher  $r/D$  values are translated into smooth turning of the flow into the injection hole, while small  $r/D$  values force the incoming annulus flow to turn suddenly and therefore, the unavoidable pressure drop creates cavitation regimes at the hole inlet. As a result, cavitation structures of the 12-hole nozzle are much lighter compared to the 6-hole nozzle case. More specifically, Figure 4.4 illustrates the difference in the effective flow area of an individual hole for both nozzles, utilising the computational fluid mechanics simulation code developed by the research group [113]. The aforementioned mechanism results in higher measured dynamic flow rates of the 12-hole nozzle compared to the 6-hole one.

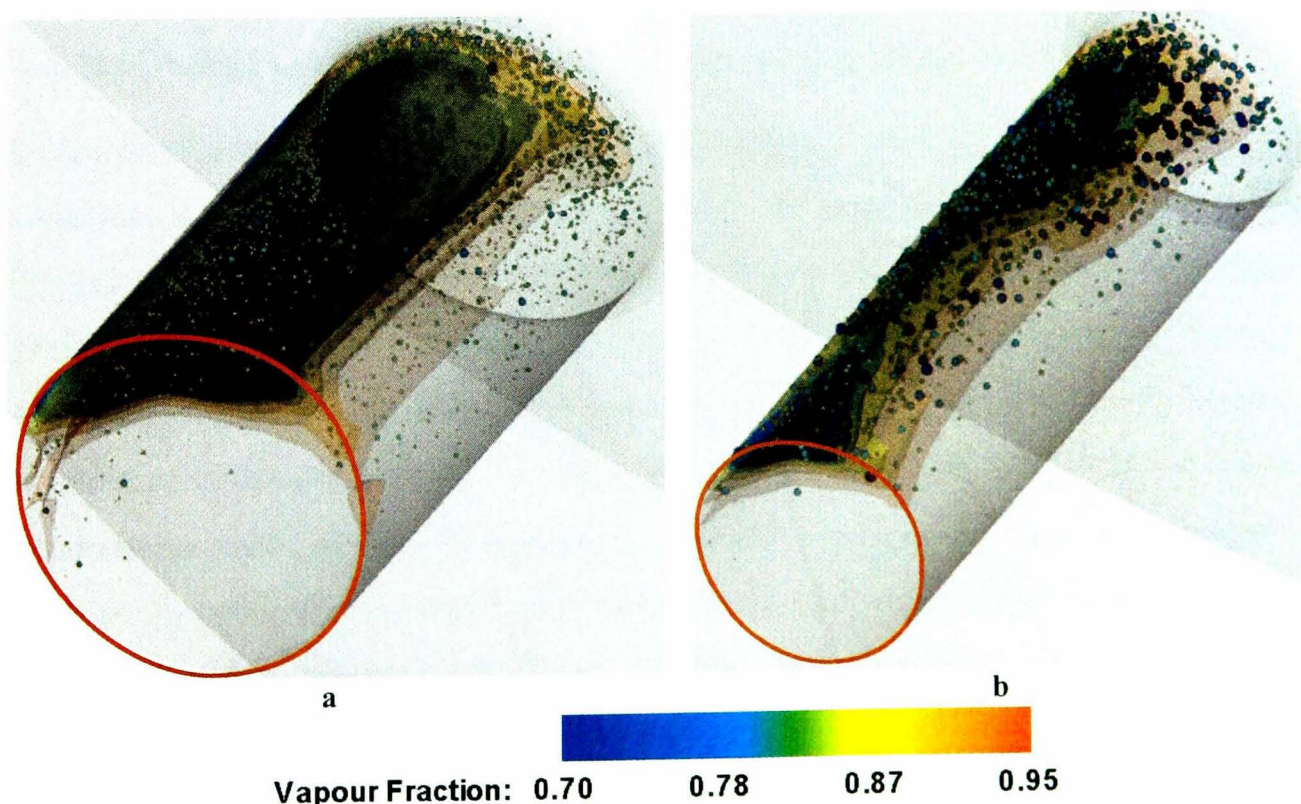


**Figure 4.4: Iso-surface of vapour fraction for (a). 6- and (b). 12-hole nozzles [113].**

Finally, in Figure 4.5, a comparison in volumetric capacity is illustrated between different injection pressures for two multi-hole nozzles. It is evident that injection pressure controls the dynamic volumetric flow rate as expected. In Figure 4.5a, the highest tested injection pressure of 200bar is plotted along with the standard 120bar pressure. It is illustrated at Figure 4.5b that the differences between 120 and 200bar are not of the same order as the differences between 80 and 120bar. Small differences are expected between the 6- and 12-hole nozzles, although the reason could also lie in the internal nozzle flow development. Increasing the injection pressure from 80bar to 120bar causes the majority of in-nozzle flow phenomena to develop considerably, leaving little room for further significant modifications initiated by the higher injection pressure.

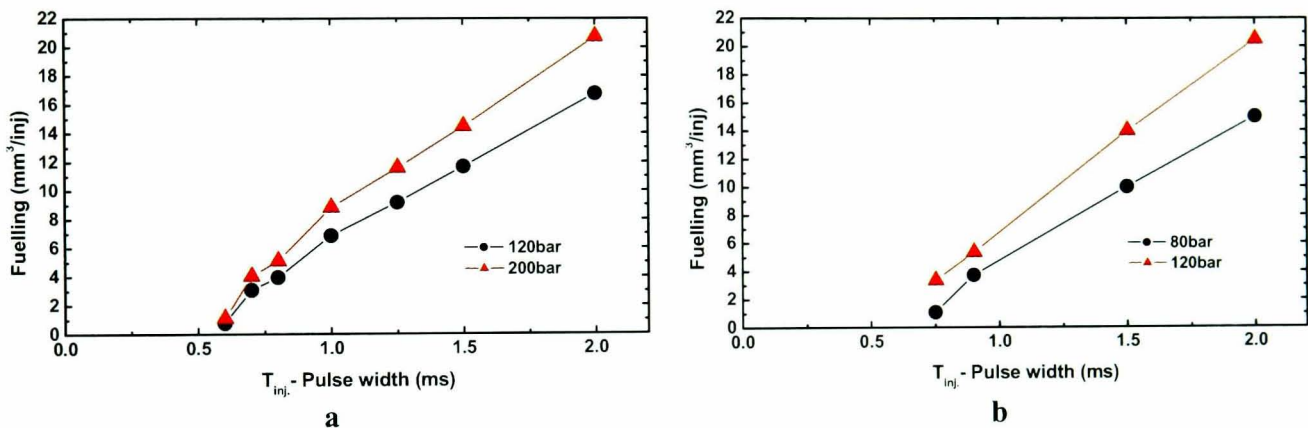


**Figure 4.5: Volumetric capacity of (a). 6-hole symmetric injector and (b). 12-hole injector with a central hole and two blocked side holes.**

## 4.2 HIGH-PRESSURE\TEMPERATURE CHAMBER TEST RIG

Qualitative and quantitative spray measurements, such as spray imaging and simultaneous velocity and droplet size distribution measurements, require excellent control on ambient thermodynamic conditions. For better understanding of the effects of the internal nozzle flow on spray formation and atomisation mechanisms, extensive Mie scattering and Phase Doppler Anemometry (PDA) measurements were essential. A constant volume chamber was employed for the realisation of the aforementioned experiments under quiescent flow conditions. More specifically, spray characteristics such as tip penetration, overall spray cone angle and cycle-to-cycle variation under various chamber pressure conditions for the four multi-hole injectors, could be measured. The experiments were aiming to characterise the spray under three operating injection pressures of 80, 120 and 200bar (where applicable) and chamber pressures corresponding to fuel injection during induction and compression strokes in

an engine. Therefore, apart from the chamber pressure variation, the system design allowed the variation of ambient chamber temperature for simulating realistic operating conditions.

#### 4.2.1 Experimental set-up

In Figure 4.6 a schematic representation of the high-pressure\temperature constant volume chamber and the high-pressure injection system is illustrated. The constant volume chamber, located at the middle of the figure, is made of stainless steel and is equipped with three quartz windows. A powerful electric heater for maintaining the chamber's temperature at the desirable levels has replaced the fourth window. The chamber is connected to a pressurised nitrogen bottle for accurate setting of the required chamber pressure (up to 25bar). The high-pressure nitrogen supply pipeline is also heated by a second electric heater. Both heating elements are controlled from the same control unit. The temperature regulation is based on extensive feedback provided by six thermocouples, appropriately installed in the constant volume chamber. The nitrogen flow through the CVC is not continuous. Quiescent flow conditions are achieved with a solenoid valve that is installed in the chamber's exhaust pipe. The exhaust pipe and solenoid valve is essential equipment for discharging the chamber contents after each injection.

The common rail system, shown schematically in Figure 4.6, has been specifically built with one injector outlet for the work of this thesis. A three-piston-type pump coupled to an electric motor is responsible for delivering high-pressure fuel (up to 200bar) to the common rail. The nominal fuel injection pressure is kept at the desired levels inside the common rail by a fuel pressure regulator. The latter is a rotary valve regulator attached on the common rail. Fuel pressure regulation is done automatically, according to the user setting value; by throttling the fuel return line. The common rail is attached on the constant volume chamber and a pipe with specific diameter and length is responsible for delivering high-pressure fuel to the injector. The restrictions in high-pressure fuel line diameter and length are applied in order to simulate realistic engine operating conditions. The length of the pipe is critical due to high-pressure

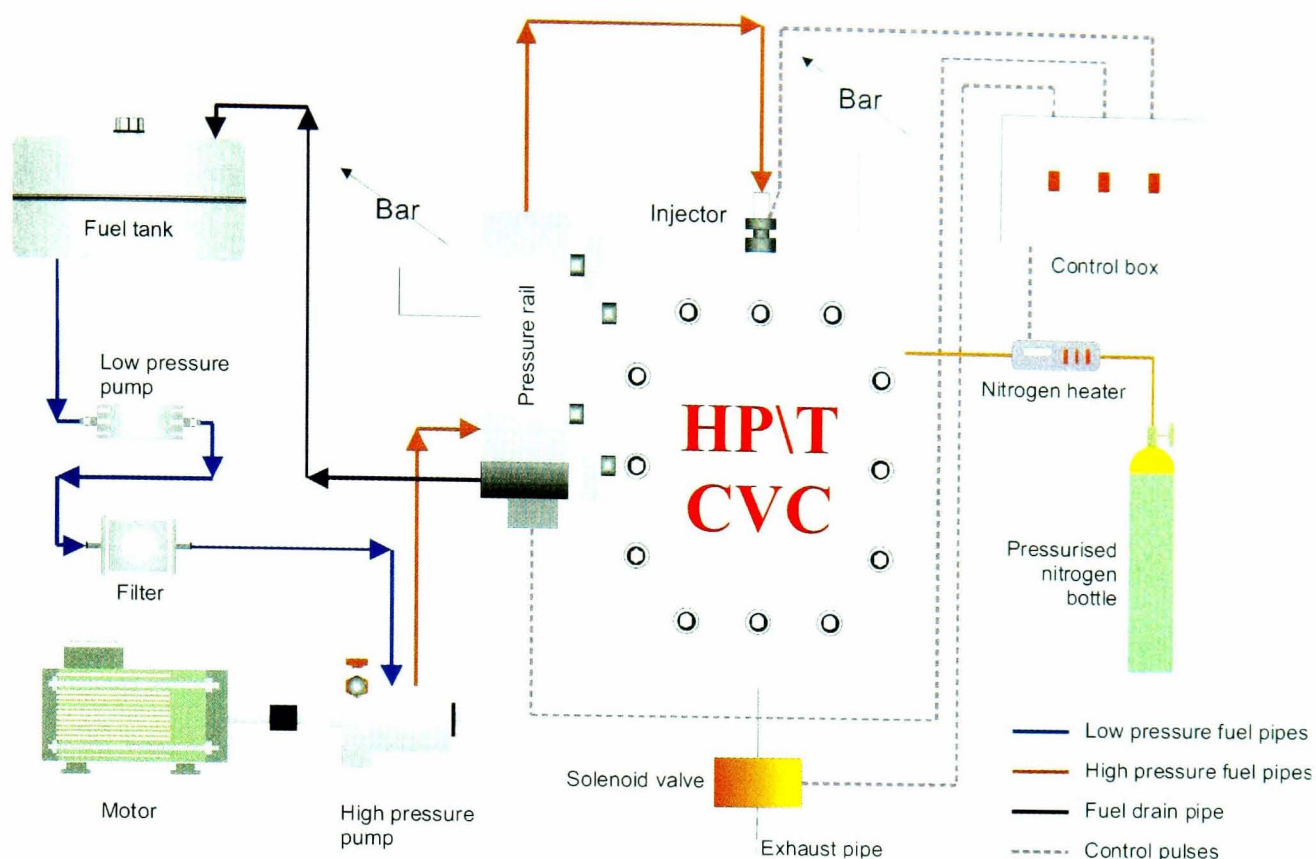


**Figure 4.6: Schematic of the high-pressure/temperature constant volume chamber (HP\T CVC) test rig and the high-pressure injection system.**

waves developed from the injector's solenoid opening and closing events. These pressure waves travel from the injector back to the common rail and vice versa. It has been proven that such pressure waves affect the spray characteristics [24]. The injector is mounted on the top face of the constant volume chamber. A mounting adaptor secures the sealing of the chamber for every kind of high-pressure injector. As illustrated in Figure 4.6, gravity is responsible for delivering fuel to the low-pressure fuel pump from the tank. The low-pressure fuel pump pressurises the fuel up to 3bar and delivers it to the high-pressure fuel pump, after it has been filtered. Two pressure gauges, installed in the constant volume chamber and the high-pressure common rail, provide information on the pressure levels reached and complete the CVC test rig. The afore-described test rig has been developed entirely at City University, and the laboratories of the Energy and the Environment Research Centre, from Dr. J.M. Nouri and the author, utilising valuable support by the groups technical staff.

Isooctane has been selected as the working fluid, since it is safer to use and more convenient for optical studies compared to gasoline, due to the absence of heavy oily compounds that lead to extensive window fouling. In addition to that, isooctane is a single-compound fuel that features stable properties, in contrast to commercial grade

gasoline, which varies in constitution according to production companies. Isooctane has a density, kinematic viscosity and surface tension of  $692\text{kg/m}^3$ ,  $0.78\text{cSt}$  and  $0.0188\text{N/m}$ , respectively.

#### 4.2.2 Control and monitoring of experiments

The final essential part of the previously described constant-volume chamber test rig is the control and data acquisition equipment. A dedicated injector and equipment control system had to be developed in order to guarantee accurate and repeatable measurements. The requirements for this system included triggering of single or multiple injection events together with the appropriate illumination and visualisation devices. Acquired data, such as images or velocity and droplet size distribution files, and all injection parameters for each measurement had to be stored on a PC for further evaluation and analysis. The hardware used was a National Instruments PCI-6602 32bit general-purpose timer/counter card [114, 115] featuring eight individual counter/timers and a number of digital input/output lines suitable for delivering flexible TTL signals as and when required. This guaranteed sufficient high-speed injection pulses and triggering signals for the camera and flashlight. The full potential of this timer card regarding the necessities for this work were exploited with the programming language Microsoft Visual Basic 6.0, which enabled the fairly straightforward in-house development of a graphical user interface (Figure 4.7) for controlling the hardware through a PC. For the visualisation process the program was used in its automated operation mode with adjustable delays between the imaging events depending on the charging time of the flash light source (up to 40s for single-flash unit).

The Fast Shutter Sensicam CCD camera was connected to the PC via an optical data cable and a PCO image acquisition card [116]. The trigger and imaging parameters were set with the PCO system software, which also managed the acquired images and made simple batch image processing possible. The high-speed digital video camera utilised an IEEE1394 (FireWire) communication protocol with its control software.

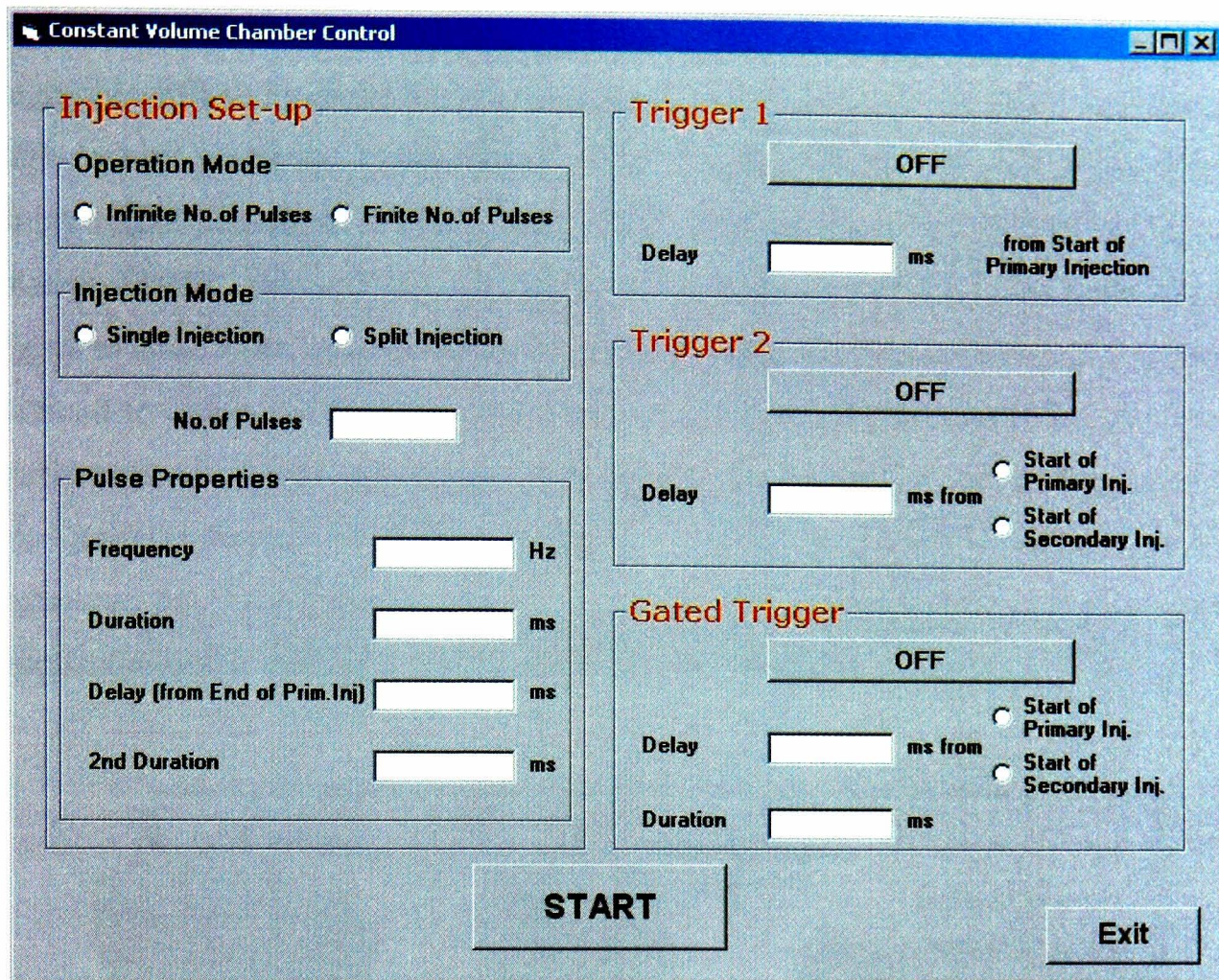
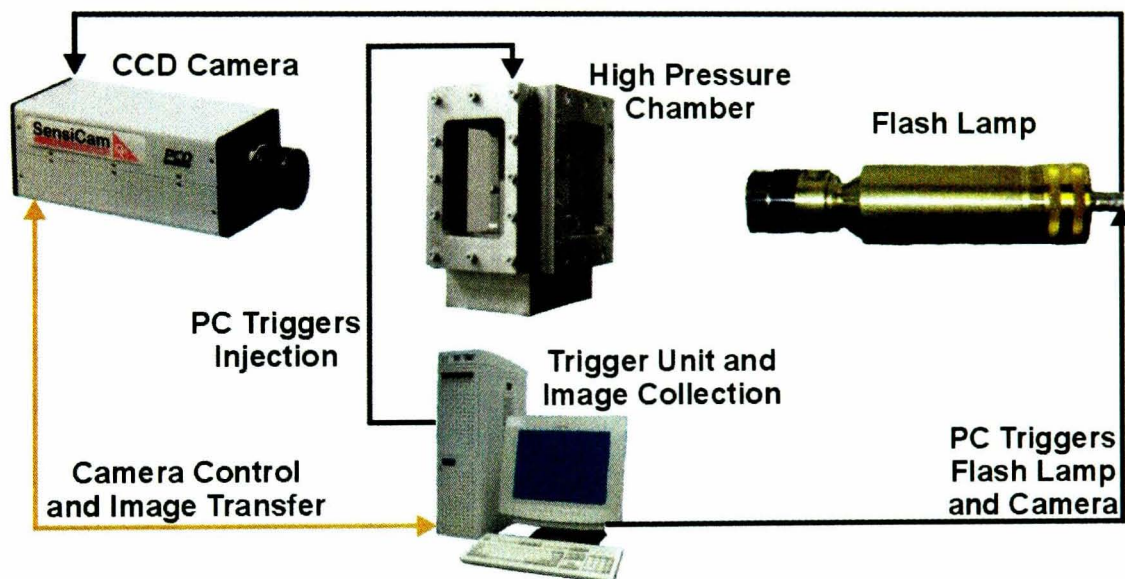


Figure 4.7: User-interface of the *Chamber Control* software.

### 4.3 MIE-SCATTERING VISUALISATION

One of the most frequently used techniques for the extraction of qualitative information regarding the fuel droplet behaviour of a high-pressure liquid spray inside a constant volume chamber or even an engine's cylinder is the Lorenz-Mie scattering technique. More specifically, Mie scattering is an elastic scattering technique where light of the same wavelength to the incident radiation is scattered from particles or droplets, which move with the flow [117]. The light intensity according to Lorenz-Mie theory is a complex function depending upon the droplet diameter, the scattering angle, and the refractive index of the droplet, the polarisation and the wavelength of the incident radiation. According to [118] however, for spherical droplets of diameter greater than  $1\ \mu\text{m}$ , the Mie scattered light intensity can be considered as being approximately proportional to the square of the droplet diameter. This property would render the technique attractive for quantitative in-cylinder mixture distribution investigations especially in cases where gaseous fuel is injected into an air stream where the fuel part could be modelled by a stream of particles [119]. However, there

are various problems that can limit the accuracy and validity of the results. Firstly, the negligible diffusivity of the particles compared to the gas phase can lead to spuriously high-density gradients. Furthermore, reliable measurements cannot be attained in flows where considerable body forces such as buoyancy or centrifugal forces are present. Finally, although large particles, in diameter, are usually required for a good signal to noise ratio, a compromise has to be found as the larger the particle the more difficult to follow the flow length-scales. Additionally, medium populated with large particles would not be adequately optically thin for the incident light intensity to be kept uniform throughout the measuring area [117]. For the above reasons the Mie technique has found limited use as a quantitative technique and is instead more frequently used to visualise spray and even flame structures.



**Figure 4.8:** Schematic of the Mie scattering visualisation set-up.

Figure 4.8 illustrates the schematic set-up for the Mie scattering visualisation of the high-pressure gasoline multi-hole spray. The CCD camera used for the still spray imaging, was a 12bit fast shutter Sensicam with a resolution of 1280x1024 pixels and a minimum exposure time of 100ns. It was fitted with a zoom lens and connected to a PC via an image acquisition card. The PC also had a timer card installed that triggered both the flash lamp illumination and the camera. All internal camera settings could be adjusted with the image acquisition software and the obtained pictures were downloaded onto the PC. A Xenon spark light provided the required illumination. The light source unit utilised a lenses system that enabled the redirection of the produced light into two separate flexible optical fibres, which converted the bulk light intensity

to point-light. The flexible optical fibres were positioned anywhere close to the imaging area quite easily and increased the effectiveness of the imaging set-up.

High-pressure fuel sprays present highly transient behaviour, hence a sequence of short exposed images should be obtained for the injection event to be visualised effectively. The CCD camera and flash light illumination imposed limitations on the maximum frame rate. Mainly because of the charging period of the Xenon spark light, which required a maximum of 40s after each discharge; and secondly due to the CCD chip read-out period that was fixed to 120ms. The aforementioned limitations allowed the acquisition of only one image at each injection event. A total of 20 images were acquired at every time-step (time After Start Of Injection – ASOI) for adequate sample population that would provide representative statistical analysis after image post-processing. The latter involved mean spray-tip penetration and overall spray cone angle calculations (Figure 4.9b-c) at each time-step for all investigated conditions. The post-processing of the acquired images was performed by in-house, highly customisable software, developed on the Matlab platform. Additionally, in an attempt to investigate the ability of the multi-hole injector to generate repeatable spray patterns, several test cases were focused mainly on the central fuel jet (where applicable) due to its default instability. This instability is owed in the position of the central injection hole that is located in the middle of the nozzle's sac volume; an area characterised by unstable flow conditions as presented in the third chapter. Furthermore, high-magnification images were obtained using a telescopic lens for the exact start of injection (SOI) to be identified accurately. Start of injection is the zero time in all the results presented in subsequent paragraphs; it is defined as the time the first liquid exits the injection hole.

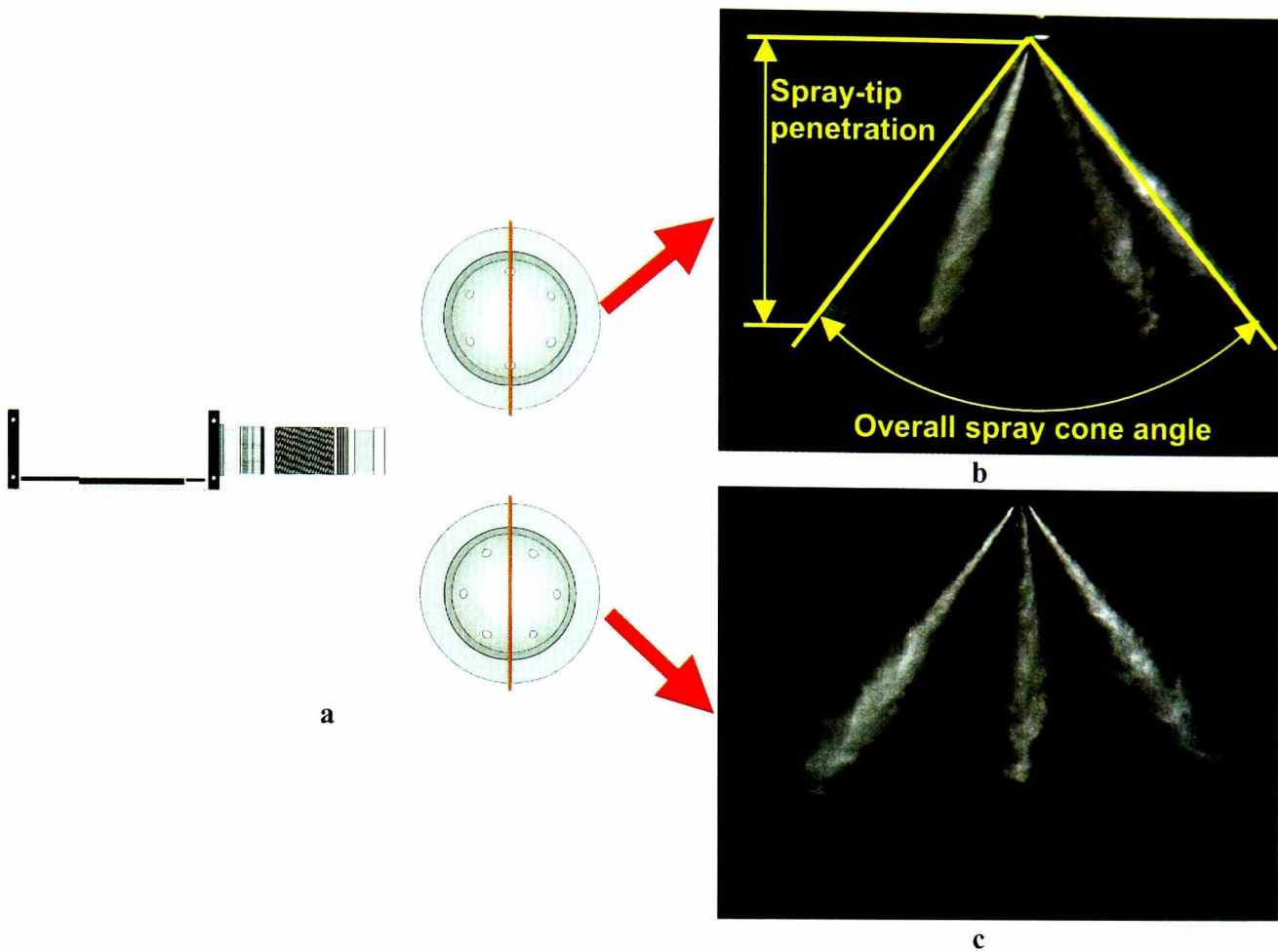


**Figure 4.9:** (a). Spray regions of interest and imaging planes. (b). Definition of spray quantitative parameters and (c). Spray image used to compare test cases.

Still spray imaging provided very useful information on multi-hole spray structures and spray dependencies on injection and chamber pressures and ambient temperature. However, the development of a single injection event and the stages through which the atomised liquid changes velocity and size distribution were unknown. The short injection pulse duration of 1.5ms prohibited the use of a double shutter Sensicam CCD camera. Hence high-speed digital video recording seemed to be the only feasible solution. The camera used was a Photron APX, as presented in Chapter 3. The desired frame rate for adequate spray visualisation results was identified at the range of 15,000 to 50,000 frames per second. Although the limitations in image resolution were severe, it was decided to align the narrow imaging areas of 1024x128 pixels (15,000fps) that could also be reduced down to 256x64 pixels (50,000fps) with one of the fuel jets. Sample images of the above settings are illustrated in Figure 4.10. The results proved to be of great interest and comparisons between several test cases revealed useful information on the multi-hole spray development mechanism.

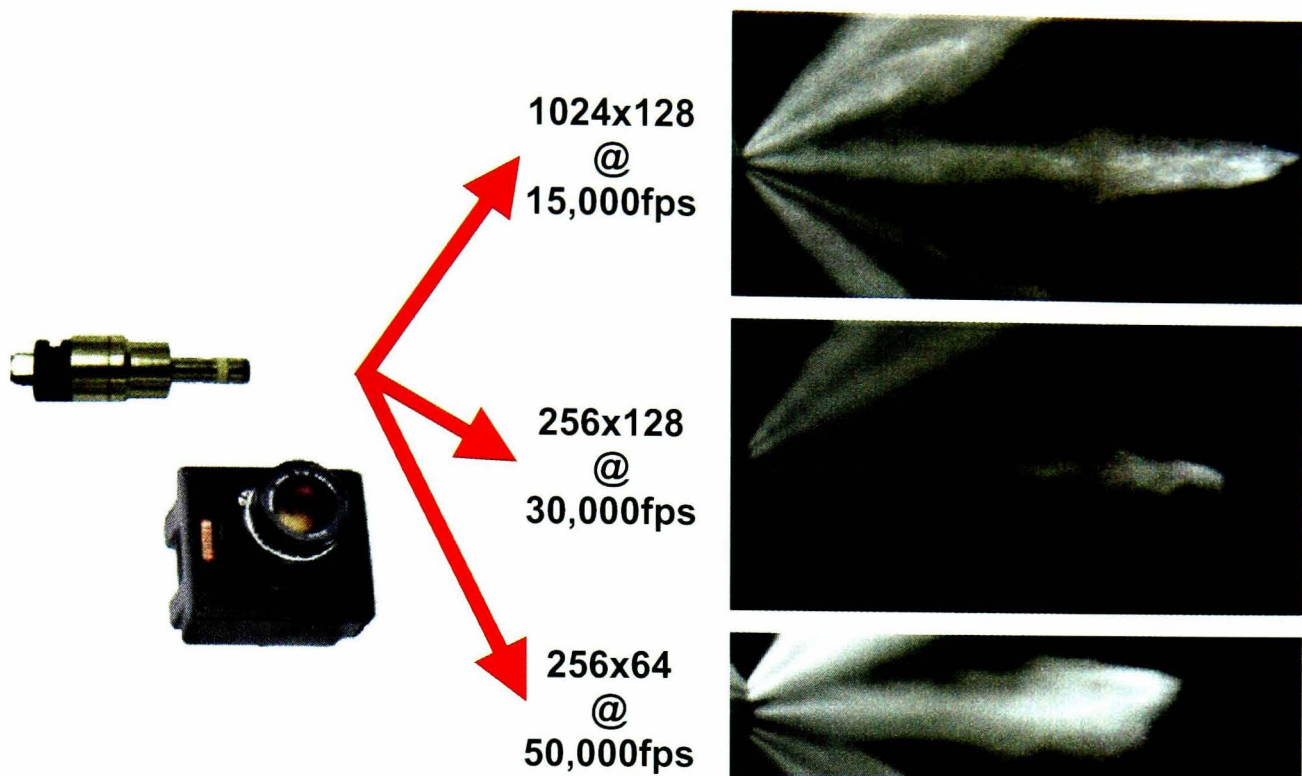


Figure 4.10: Imaging areas and spatial resolution of selected frame rates for HSDV.

#### 4.4 PHASE-DOPPLER ANEMOMETRY

Mie scattering visualisation revealed important information on multi-hole high-pressure gasoline fuel sprays. More specifically, the effects of injection and chamber pressures, the ambient chamber temperature and double-pulsed injection on spray development were assessed. The aforementioned findings allowed the researcher to obtain a general overview of the mechanisms governing atomisation and supplied limited but useful quantitative information on spray tip penetration and overall spray cone angle. However, the need of global spray characterisation for multi-hole injectors remained to be seen. There were basic questions, regarding the effect of an increase in injection pressure from 80 to 200bar on droplet size distribution, as well as, the main differences between central and side fuel jets, which needed urgent attention. Quantitative measurements of droplet size distributions and velocity fields could provide the answers and help the most in understanding all the details about multi-hole gasoline fuel sprays. Phase Doppler anemometry (PDA) is a non-intrusive optical technique that allows the simultaneous measurement of droplet velocity and size. It is a more complete version of laser Doppler anemometry (LDA) first described by Durst *et al* (1976). A typical PDA set-up consists of a laser tube, a light frequency phase shifter (Bragg-cell), a laser-beam splitter, a transmitting optical unit, a receiving optical unit and a signal processor [19, 63, 120].

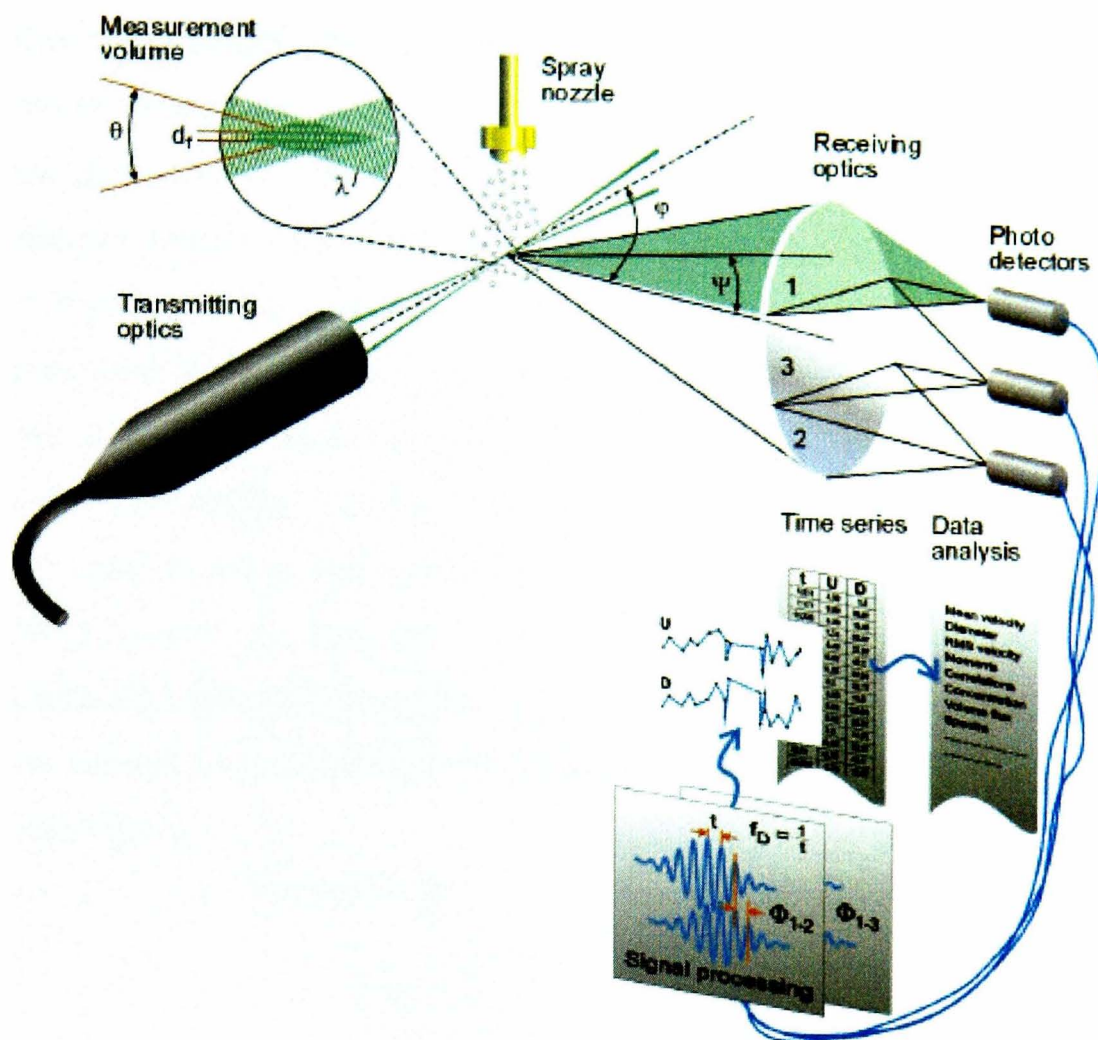


Figure 4.11: Schematic of the measurements principle of PDA (Source: Dantec Dynamics).

When a droplet passes through the measuring volume, it scatters light at all directions. Receiving optics is placed at an off-axis location and projects a portion of the scattered light onto multiple photo-detectors. Due to the structure of the measuring volume (it is made of fringes created by the intersection of two individual laser beams) and the photo-multipliers position, scattered light is converted into Doppler bursts. The frequency of the Doppler bursts is linearly proportional to the particle velocity. Each photo-detector captures the same burst signal although, due to their relative positions, there is a phase shift in signals acquired by each detector. This phase shift has been shown to be directly proportional to the droplet diameter.

More specifically, light scattering is where the phase-Doppler anemometry technique is based. Visualised ray tracing can provide better understanding of how light is scattered by a spherical droplet. As illustrated in Figure 4.12, the incident light beam is partially reflected at the surface of the particle and partially refracted into the particle. Upon exiting the particle without any further internal reflection, the scattered beam is known as 1<sup>st</sup> order refraction. Higher order refraction (2<sup>nd</sup> order refraction)

also arises after internal reflections and subsequent refraction out of the particle into the surrounding medium. Second order refraction is responsible for the rainbow effect in backscatter, thus it could be used in the phase-Doppler technique under special circumstances. On the other hand, first order refraction is more suitable for phase-Doppler measurements, although a compromise has to be made between the dominance of 1<sup>st</sup> order refraction at 70° receiving angle and a higher scattered light amplitude at lower scattering angles (15°-45°). The scattering characteristics of a particle depend strongly on the refractive index. More specifically, the relative refractive index between the particle ( $n_p$ ) and the medium ( $n_M$ ), which is effectively the ratio of  $n_p$  over  $n_m$ , determines principle differences in scattering modes. For relative refractive indices larger than unity (e.g. water/fuel droplets in air) first order refraction dominated the forward direction and these scattering characteristics are well documented [121].

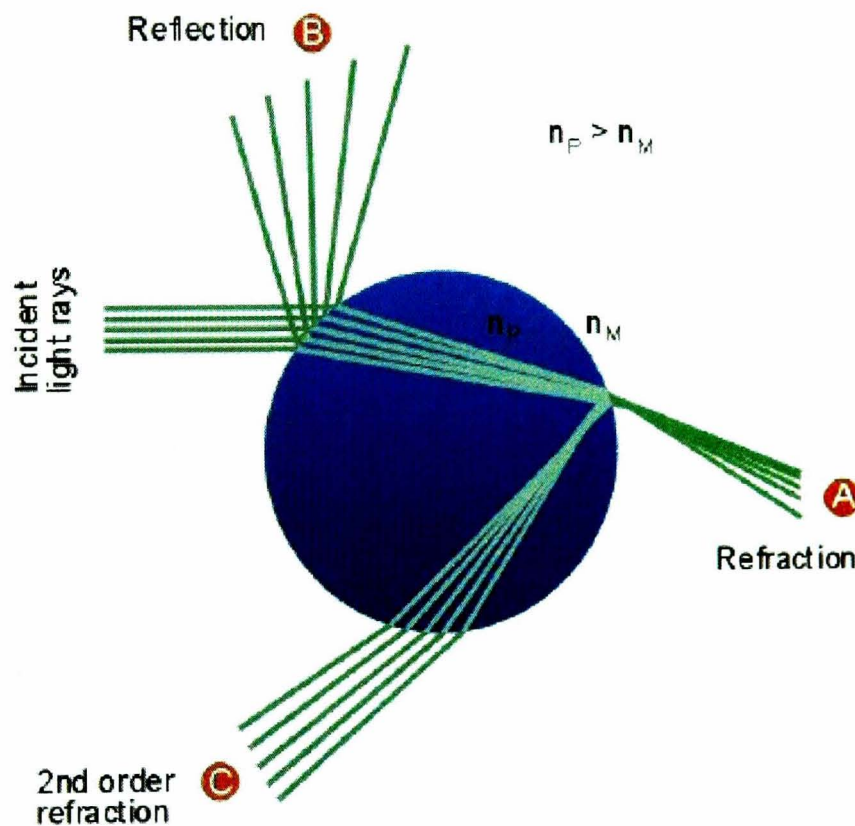


Figure 4.12: Scattered light from a spherical particle (Source: Dantec Dynamics).

As illustrated in the top left corner of Figure 4.11, the measurement volume of a PDA system is formed by the intersection of two laser beams. The focused laser beams intersect and form an ellipsoid shaped pattern of bright and dark stripes, so called fringes. The spacing of these fringes is determined by the light wavelength and the angle between the two laser beams that is set by the transmitting optics. The laser tube output beam features a multi-colour wavelength that ranges from 420 to 520nm. A

laser beam splitter separates the output beam into green (514nm) and blue (488nm) wavelengths. Both of these laser beams are further split into two green and two blue beams by another set of beam splitters. The majority of PDA/LDA systems feature a frequency shift between the two laser beams of same wavelength generated by means of a Bragg-cell. This frequency shift makes the fringe pattern of the control volume move at a constant velocity. Stagnant particles will generate a signal corresponding to the shift frequency. Particles moving at positive or negative velocities will generate positive and negative signal frequencies relative to the shift frequency, respectively. Therefore, systems without frequency shift cannot distinguish the flow direction, unlike the frequency shift based systems that can effectively distinguish positive and negative particle velocities and provide a zero velocity measurement, where applicable. Finally, when a particle traverses the control volume, the scattered light fluctuates in intensity at a frequency equal to the velocity ( $U$ ) of the particle, divided by the fringe separation distance ( $s$ ), as shown in Figure 4.13.

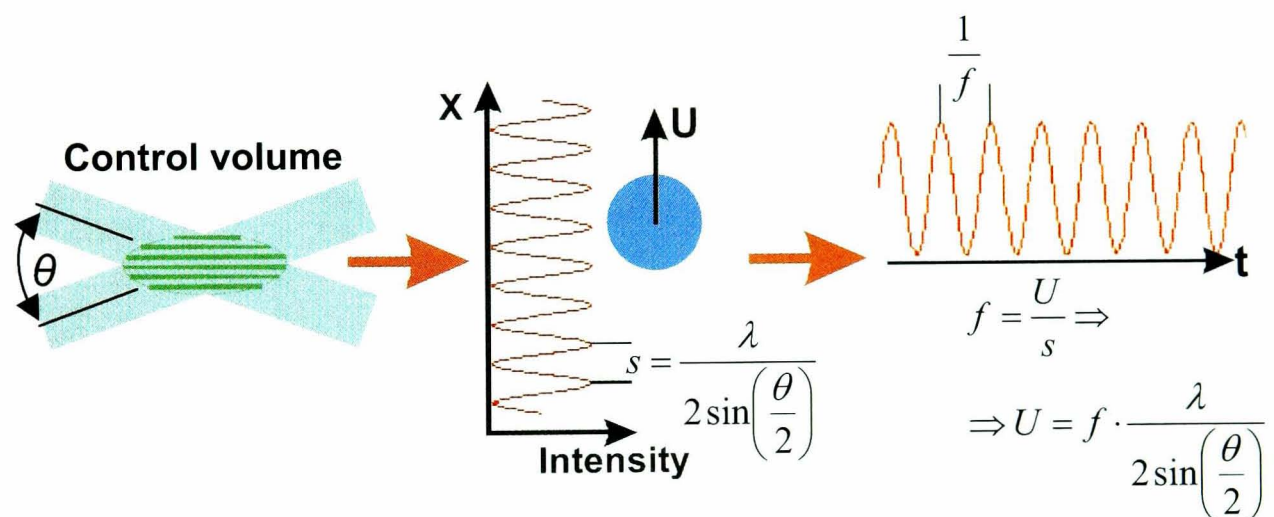


Figure 4.13: Doppler Velocity measurement principle.

Velocity measurements require one photo-multiplier for the generation of the time-based signal and the velocity value calculation. The same principle does not apply to size measurements though, and for accurate particle sizing information, more than one photo-multipliers are needed. In the case of two photodiodes, particle size measurement is achieved by measuring the time delay of the scattered light signal that is captured by the first detector at time ( $t$ ) and the second detector at time ( $t+\Delta t$ ), as shown in Equation 4-1, where  $T$  is the period of one cycle of the signal.

$$\Delta\phi = 2\pi \frac{\Delta t}{T} \quad [4-1]$$

The phase difference ( $\Delta\phi$ ), calculated by the above equation, increases with

increasing particle size. Since phase is a modulo  $2\pi$  function, it cannot exceed this value, i.e.  $360^\circ$ . Therefore, if a particle is large enough and causes the phase to go beyond a  $2\pi$  jump, a two-detector PDA system could not discriminate between this size and a much smaller particle. Hence, three-detector systems are used, where two individual phase differences are obtained from two detector-pairs having different relative positions. Three-detector PDA systems (D1-3 in Figure 4.14) show certain advantages and apart from overcoming the  $2\pi$  ambiguity, the measurable size range is increased and high measurement resolution is maintained. A processor attached to the system measures the phase shift between the two signals, which is proportional to the droplet radius of curvature, thus allowing determination of the droplet diameter, according to the calculation illustrated in Figure 4.14, where  $\Phi$  depends on the dominant mode of scattered light (reflection or refraction).

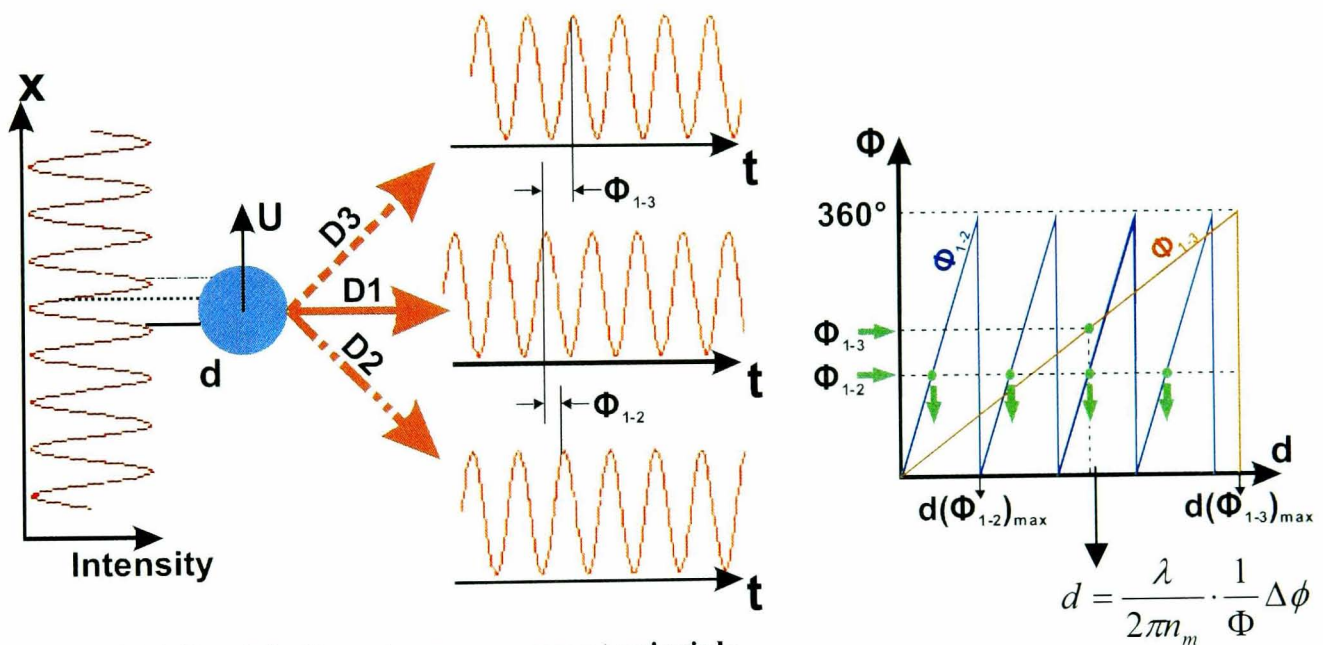


Figure 4.14: Particle diameter measurement principle.

In the present study, a 2-D PDA system was used that enabled the simultaneous measurement of the two velocity components and diameter of a particle and is illustrated in Figure 4.15. A wall mounted Argon-ion laser supplied the laser light beam with a maximum power output of 1.5W, and was aligned with an optical unit, which included the laser beam splitter and the Bragg-cell. This unit was responsible for splitting the laser beam into two pairs of different wavelengths; each pair consisted of two equal intensity beams that featured a 40MHz frequency shift

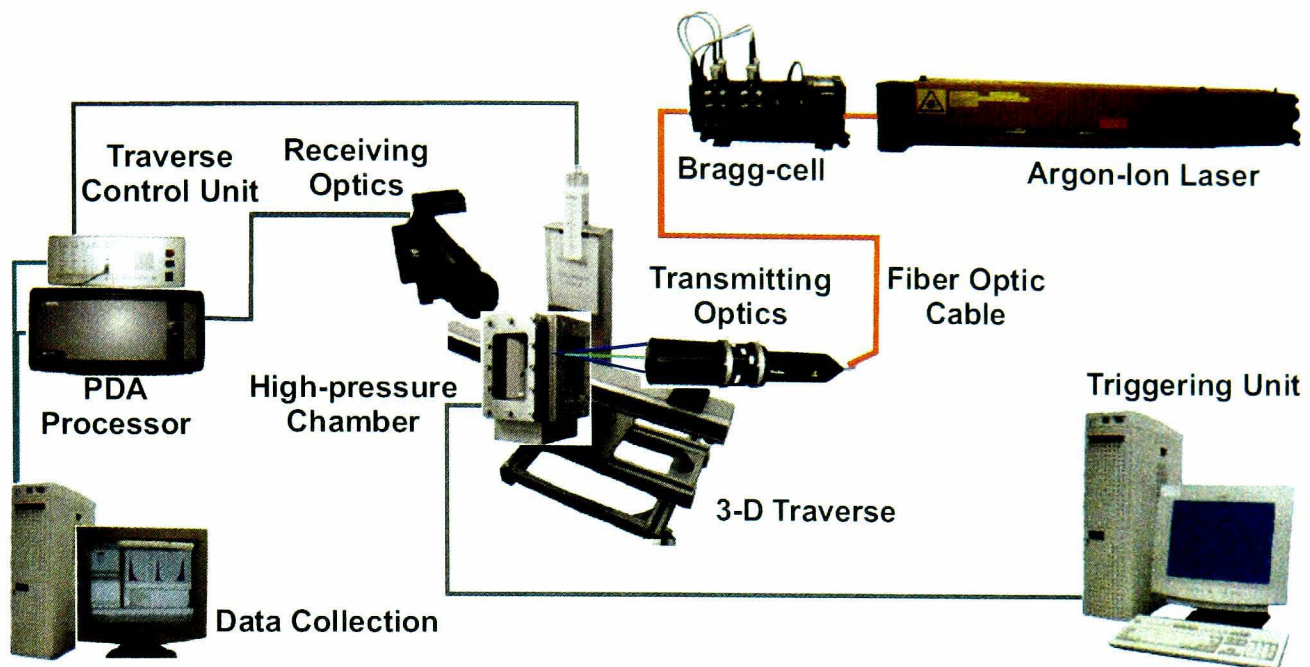


Figure 4.15: Schematic of the Dantec 2D PDA system.

provided by the Bragg-cell. The first pair was green light at a wavelength of 514.5nm, responsible for the axial velocity component, while the second pair was blue light at 488nm wavelength providing the radial velocity component. The transfer of the laser beams to the transmitting optics was through a fibre optic cable. The collimating and focusing lenses formed an intersection volume, consisting of elliptical disc shaped fringes, with major and minor axes of approximately 2.863 and 0.092mm for the green, and 2.716 and 0.088mm for the blue component. The PDA receiving unit consisted of a 310mm focal length lens that focused the collected light onto the four photo-multipliers through a slit of 0.1mm width in order to minimise the major axis of the measuring volume and to ensure that multi-particle detection is avoided. The receiving optics was positioned at  $70^\circ$  (see Figure 4.16) to the plane of the two green laser beams to ensure that refraction dominated the scattered light. Transmitting and receiving optics were both mounted on a three dimensional electronic traversing mechanism with a positional sensitivity of 0.01mm in the x-y plane and 0.1mm in the vertical, z, direction, minimising any positional error. The signal from the four photo-multipliers was transmitted to the processor unit where all the data processing was carried out. The processor was connected to a desktop computer via an Ethernet adaptor, where all the acquired data were saved for further analysis. The measurement period was defined by the injection duration for each test case. This period varied from 2.5 – 4.5ms (for 1.5 – 3.5ms injection duration), so did the total number of samples collected each time that were of the order of 10,000 samples per millisecond

of measurement. The total number of samples was collected over many injection cycles.

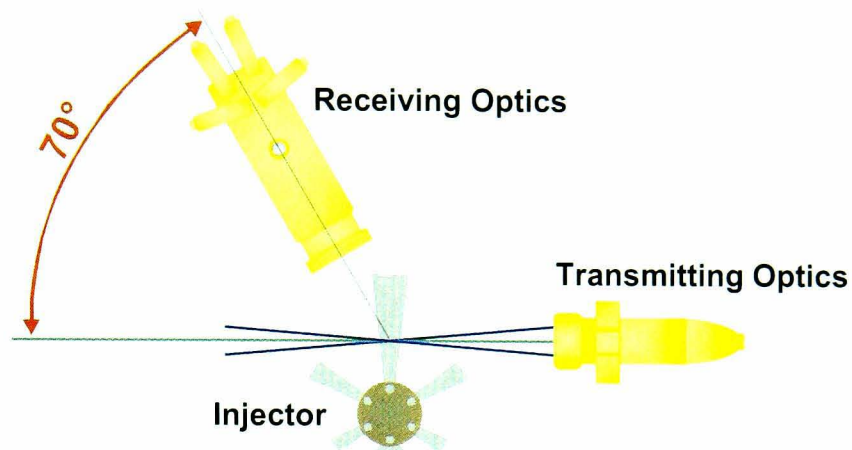


Figure 4.16: Top view of the PDA optics set-up.

The measurement period was divided in narrow time windows of 0.1ms for further post-processing of the collected data. These data consisted of time, axial and radial velocity vectors as well as droplet size information. Post-processing involved calculation of ensemble-averaged values of droplet mean and root mean square (RMS) velocities and arithmetic mean (AMD) and Sauter mean (SMD) droplet diameters, according to the following equations:

	<b>Total Droplet Velocity</b>	<b>Mean</b>	<b>Root Mean Square</b>
<b>Velocity</b>	$U_{total,i} = \vec{u}_i + \vec{v}_i$	$\bar{U}_{total} = \frac{\sum U_{total,i}}{N}$	$U_{RMS} = \sqrt{\frac{\sum (\bar{U}_{total} - U_{total,i})^2}{N}}$
	<b>Arithmetic Mean</b>	<b>Sauter Mean Diameter (Volume/Surface)</b>	
<b>Size</b>	$d_{10} = \frac{\sum N_i \cdot d_i}{\sum N_{total}}$	$d_{32} = \frac{\sum N_i \cdot d_i^3}{\sum N_i \cdot d_i^2}$	

Post-processing of the acquired data was done by custom, in-house developed, software in Compaq Visual FORTRAN 6. The whole process was done automatically for all acquired velocity profiles and size distributions for every test case. Visual representation of the results was performed by specialised macro-commands written for visualisation package TecPlot.

## 4.5 EXPERIMENTAL RESULTS

Direct injection gasoline engines have been one of the main research areas for the majority of automotive manufacturers for the last decade. Starting from the first generation direct injection spark-ignition (DISI) engines, where a swirl pressure atomiser utilised the piston and engine liner walls to provide an ignitable air/fuel mixture at the spark plug location, a compact and more environmental friendly configuration was thought to be the way ahead. The latter, second generation DISI engines, became a reality, when fuel injection equipment manufacturers provided the market with injectors capable of producing robust and easily directed spray shapes. Second generation combustion concept is mainly focused on spray-guided configurations, where the absence of fuel-wall interaction offers certain advantages in unburned hydrocarbon emissions. The first strong candidate for spray-guided engine operation has been the high-pressure gasoline multi-hole injector. Although multi-hole injectors are well established in diesel engines, important differences between diesel and gasoline combustion concepts has created the need to redesign and re-evaluate multi-hole nozzles for best results in spark-ignited engines. Changes in the overall spray cone angle, the nominal injection pressure and the internal nozzle geometry in general, necessitate extensive investigations and complete spray characterisation prior to any engine test.

Key factors in multi-hole injectors spray characterisation that will define possible engine modifications, like combustion chamber design and injection strategies, could be summarised in the stability of the overall spray cone angle in terms of chamber pressure, spray tip penetration distance and particle size distribution. The present chapter focuses exclusively on investigations related to the aforementioned characteristics for several multi-hole nozzle designs. Furthermore, following the advances in engine management strategies, the ability of multi-hole injectors in multiple injections is investigated. Spray stability and behaviour under various operating conditions have been evaluated for the case of double injection events with varying delay time (dwell-time).

The presentation of the results is divided in two major sections. The first one presents mostly qualitative and partly quantitative (spray tip penetration, spray cone angle) data, which derived from spray visualisation under various conditions. The last

section appears to be more specialised, and quantitative velocity field and size distribution profiles are presented. For better understanding of the presented data a brief explanation of the terminology used is essential. Firstly, injector nozzles are classified according to their hole-pattern. More specifically, injectors featuring six holes, as well as nozzles with blocked holes (i.e. 6-1(blocked)+1central holes) are all referred to as 6-hole-patterned nozzles. According to the same classification, the one and only 12-hole patterned nozzle examined, features two blocked and one central holes (12-2+1central holes). In addition to that, the zero time for all presented data refers to the start of injection (SOI) and not the electronic start. The difference between the two is the needle opening delay of each injector. Start of injection is defined, as the time the first liquid fuel droplets appear to exit one of the holes. Injection duration, on the other hand, is exclusively defined by the electronic injection pulse width (e.g. duration of 1.5ms results in actual injection time of almost 1.2ms and varies slightly according to injector needle response). Finally, all chamber pressure values presented are absolute pressure values (atmospheric pressure is 1bar).

#### **4.5.1 Mie scattering visualisation**

The experimental conditions of visualisation experiments, for all tested multi-hole nozzles, were selected upon different targets that were defined by the need of better understanding of the parameters affecting the spray development. Initially, the investigation was focused on the effects of injection and chamber pressures, under constant thermodynamic conditions, on initial and later stages of spray development and spray shape repeatability. More specifically, chamber pressure values were selected to be in accordance to typical cylinder pressures encountered during the intake and compression stages of an internal combustion engine. Therefore, atmospheric chamber pressures (1bar) reflect the in-cylinder pressure levels during induction; elevated pressures, of 4-12bar, simulate cases of injection during the compression stroke. The latter is based on the fact that modern direct-injection spark-ignition engines feature compression ratios of the order of 10-12:1, values that could possibly lead to in-cylinder pressures, during compression stroke, in the range of 5-20bar. One immediately realises that the injection event could be placed at a wide timing window that cylinder pressures as high as around 18-20bar (possible peak in-cylinder pressure at Top Dead Centre) could be encountered. Experimental conditions for the three nozzles tested are presented in Table 4-1. More specifically, for the exact

identification of the Start of Injection (SOI) highly magnified images of the injector nozzle were acquired. Furthermore, images of smaller magnification, but focused on the initial spray stages, decoded the effects of injection and chamber pressures on the fuel spray in a maximum distance of 10mm from the nozzle exit. Finally, imaging of the overall spray produced enabled various comparisons between different nozzles and conditions, as well as spray shape repeatability experiments.

<b>5 (6-1) + 1central holes</b>				
<b>Injection Pressure</b> $P_{inj.}$ [bar]	<b>Chamber Pressure</b> $P_{back}$ [bar]	<b>Injection Duration</b> $t_{inj.}$ [ms]	<b>Ambient Temperature</b> [°C]	<b>Region of Interest</b>
80	1 / 4 / 8 / 12	1.5	~30	Highly magnified injector nozzle exit [3.5x4mm].
100	1 / 4 / 8 / 12	1.5	~30	
120	1 / 4 / 8 / 12	1.5	~30	
80	1 / 8 / 12	1.5	~30	Nozzle exit close-up imaging [15x20mm].
100	1 / 8 / 12	1.5	~30	
120	1 / 8 / 12	1.5	~30	
120	12	1.5	~30	Central jet repeatability from 2 viewing angles.
80	1 / 4 / 8	1.5	~30	Overall spray development [50x60mm].
100	1 / 4 / 8	1.5	~30	
120	1 / 4 / 8	1.5	~30	
<b>6 holes</b>				
<b>Injection Pressure</b> $P_{inj.}$ [bar]	<b>Chamber Pressure</b> $P_{back}$ [bar]	<b>Injection Duration</b> $t_{inj.}$ [ms]	<b>Ambient Temperature</b> [°C]	<b>Region of Interest</b>
120	1 / 4 / 8 / 12	1.5	~30	Overall spray development [55x70mm].
200	1 / 4 / 8 / 12	1.5	~30	
<b>10 (12-2) + 1central holes</b>				
<b>Injection Pressure</b> $P_{inj.}$ [bar]	<b>Chamber Pressure</b> $P_{back}$ [bar]	<b>Injection Duration</b> $t_{inj.}$ [ms]	<b>Ambient Temperature</b> [°C]	<b>Region of Interest</b>
80	1 / 6	1.5	~30	Highly magnified nozzle exit [10x20mm].
120	1	1.5	~30	
80	1 / 4 / 8	1.5	~30	Overall spray development [55x70mm] for 3 different injection durations.
80	1	0.75 / 0.9	~30	
120	1 / 4 / 8	1.5	~30	
120	1	0.75 / 0.9	~30	

**Table 4-1: Still imaging test conditions for three different multi-hole nozzles.**

Following the extraction of useful information on the overall spray development mechanism, it was decided to proceed by simulating engine operating thermodynamic

conditions in the constant volume chamber, since the ultimate target has always been the implementation of multi-hole injectors in direct injection spark-ignition engines. This second phase of spray visualisation was mainly characterised by elevated chamber ambient temperatures and testing of double injection pulses, as presented in Table 4-2.

<b>6 holes – Asymmetric</b>				
<b>Injection Pressure</b> $P_{inj.}$ [bar]	<b>Chamber Pressure</b> $P_{back}$ [bar]	<b>Injection Duration</b> $t_1-t_{dwell}-t_2$ [ms]	<b>Ambient Temp.</b> [°C]	<b>Engine condition simulated</b>
80	1	1-0.5-1	~40-50	Injection during induction stroke, where pressure is close to 1bar and temperature ~45°C (Double injection for effective warm-up and operational stability).
80	1	1-0.7-1	~40-50	
80	1	1-1-1	~40-50	
80	1	2-1-2	~40-50	
120	1	1-0.5-1	~40-50	
120	1	1-1-1	~40-50	
80	1 / 3 / 6	1.5-0-0	~90	Injection at early compression stroke.
120	1 / 3 / 6	1.5-0-0	~90	
80	1	1.5-0-0	~120	Test case for evaporation simulation
120	1	1.5-0-0	~120	
<b>10 (12-2) + 1 central holes</b>				
<b>Injection Pressure</b> $P_{inj.}$ [bar]	<b>Chamber Pressure</b> $P_{back}$ [bar]	<b>Injection Duration</b> $t_1-t_{dwell}-t_2$ [ms]	<b>Ambient Temp.</b> [°C]	<b>Engine condition simulated</b>
80	1	1-0.5-1	~40-50	Injection during induction stroke, where pressure is close to 1bar and temperature ~45°C (Double injection for effective warm-up and operational stability).
80	1	1-0.7-1	~40-50	
80	1	1-1-1	~40-50	
80	1	2-1-2	~40-50	
120	1	1-0.5-1	~40-50	
120	1	1-1-1	~40-50	
80	1 / 3 / 6	1.5-0-0	~90	Injection at early compression stroke.
120	1 / 3 / 6	1.5-0-0	~90	
80	1	1.5-0-0	~120	Test case for evaporation simulation
120	1	1.5-0-0	~120	

**Table 4-2: Still imaging test conditions for two different multi-hole nozzles simulating engine-operating conditions.**

Finally, in Table 4-3, high-speed imaging experimental conditions are presented. High-speed digital video recording offered the maximum in double injection investigations. The effects of time delay between the two injection pulses (Dwell-time), as well as the connection between injection pressure and minimum possible injection duration were investigated. Utilising frame rates up to 50,000 frames per

second, a clear view of the injector behaviour under double pulse operation was obtained.

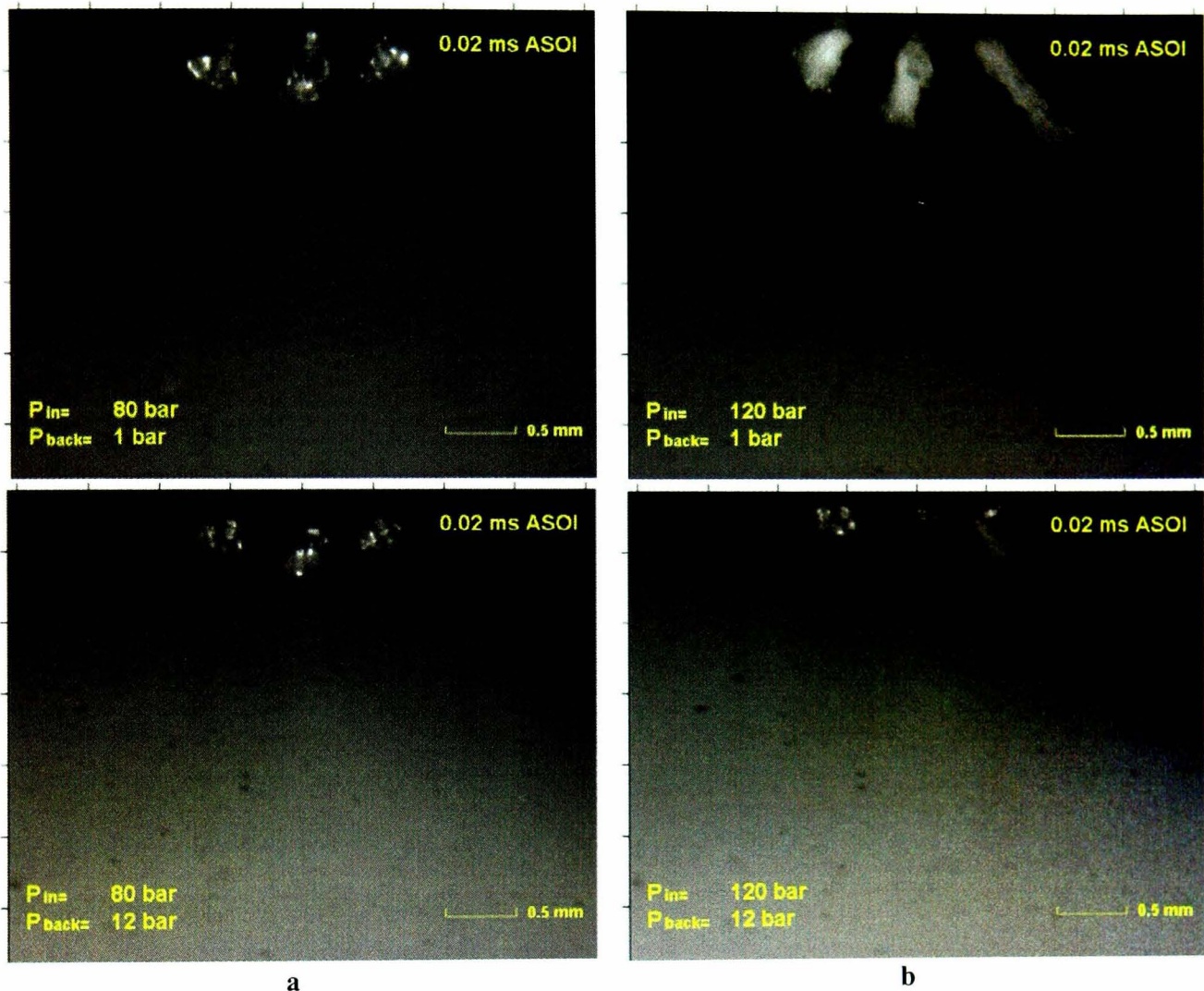
10 (12-2) + 1 central holes				
Injection Pressure $P_{inj}$ [bar]	Chamber Pressure $P_{back}$ [bar]	Injection Duration $t_1-t_{dwell}-t_2$ [ms]	Ambient Temp. [°C]	Region of Interest – Frame Rate [fps]
40	1	1-0.3-1	~30	Injector nozzle exit @ 30,000fps
40	1	1-0.5-1	~30	
40	6	1-0.5-1	~30	
60	1	1-0.3-1	~30	Injector nozzle exit @ 30,000fps
60	1	1-0.5-1	~30	
60	6	1-0.5-1	~30	
80	1	1-0.3-1	~30	Injector nozzle exit @ 15,000 / 30,000 / 50,000fps
80	1	1-0.5-1	~30	
80	1	1-0.7-1	~30	
80	1	0.75-0-0	~30	
80	1	0.9-0-0	~30	
80	1 / 4 / 8	1.5-0-0	~30	
80	6	1-0.5-1	~30	
120	1	1-0.3-1	~30	Injector nozzle exit @ 15,000 / 30,000 / 50,000fps
120	1	1-0.5-1	~30	
120	1	1-0.7-1	~30	
120	1	0.75-0-0	~30	
120	1	0.9-0-0	~30	
120	1 / 4 / 8	1.5-0-0	~30	
120	6	1-0.5-1	~30	

Table 4-3: High-speed imaging test conditions.

### Start of Injection (SOI)

The Start of Injection time is very critical for all visualisation experiments related to high-pressure sprays. It is used as the “zero time” for all presented images. Hence, the exact identification of the time the first liquid droplets exit the nozzles holes had to be done prior to any other investigation. Using a high-magnification telescopic lens, sprays from six- and twelve-hole nozzles, both featuring a central hole, were imaged at time-steps of 0.05ms after the injection signal. Any possible effects of injection or chamber pressures on SOI time were investigated, while the injection duration was set constant to 1.5ms. Following the processing of the acquired images, it was decided that the start of injection for both nozzles is 0.6ms after the electronic start of injection. More specifically, the delay of the needle-opening event, as well as the time needed for the liquid to fill the sac volume and start exiting the holes, is found to be 0.6ms. Injection and chamber pressures effects on the SOI time are negligible. The

actual differences between 80 and 120bar injection pressures and 1-12bar chamber pressures is of the order of 0.05ms; thus varying from 0.58-0.63ms. In Figure 4.17, an example of the first visible liquid exiting the holes is illustrated, for two injection pressures (Figure 4.17a and b) and chamber pressures (top row: 1bar and bottom row: 12bar).



**Figure 4.17: Start of injection identification for the 5+1 central holes nozzle at (a). 80bar and (b). 120bar injection pressures. (Image resolution: 1280x1024; spatial resolution: 0.003x0.0068mm/pixel).**

The second injector investigated, a 12-hole patterned nozzle, produced similar results. As illustrated in Figure 4.18, with defined SOI at 0.6ms, injection pressure affects marginally the needle opening delay. In the case of 0.05ms after SOI (top row of Figure 4.18) and 120bar injection pressure, liquid is not clearly visible at the hole exit, while this is not the case for 80bar. Bottom row of Figure 4.18 illustrates images taken at 0.1ms ASOI, and at that time liquid fuel exiting the nozzle is clearly visible. Illustrated images at Figure 4.17 and Figure 4.18 are not of the same magnification. Based on this fact and judging upon the most accurate image, 0.6ms is set as the global SOI for all multi-hole nozzles.

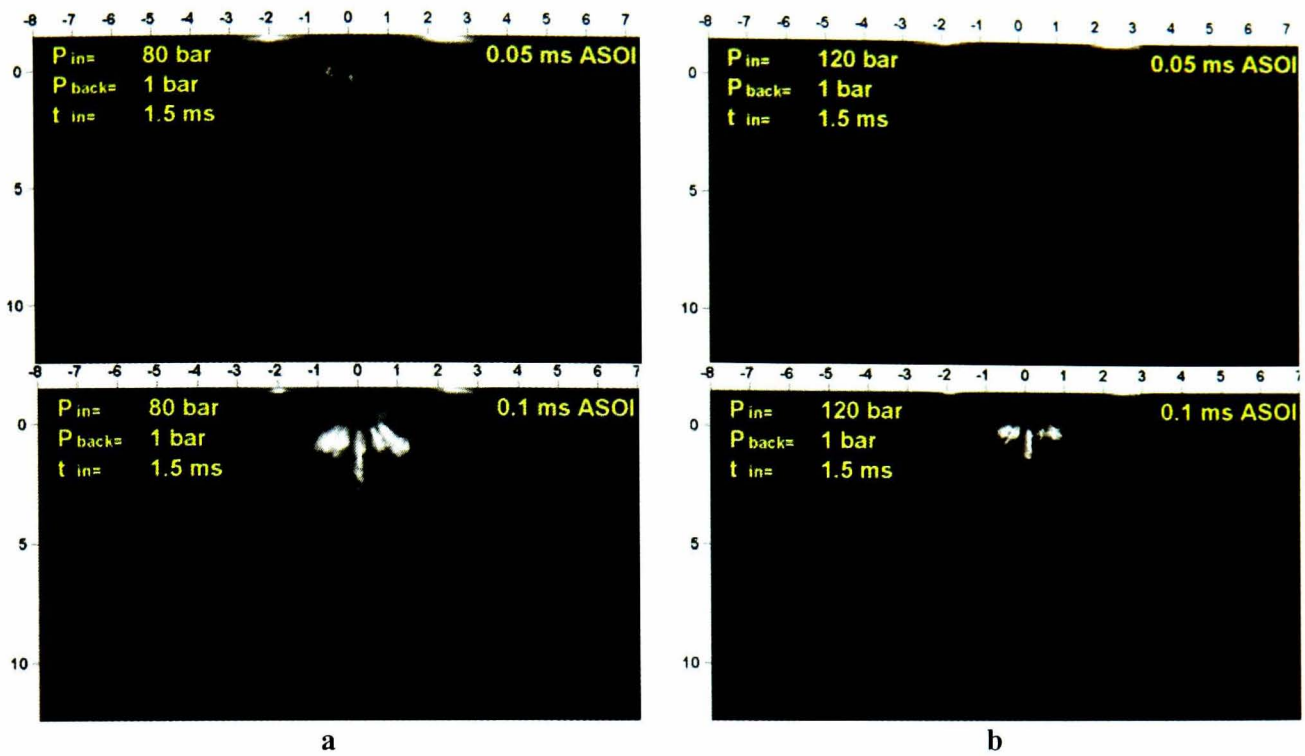


Figure 4.18: Effect of injection pressure on SOI time for a 10 (12-2) + 1 central holes nozzle. (a). 80 and (b). 120bar. (Image resolution: 640x512; spatial resolution: 0.025x0.039mm/pixel).

### High-pressure spray development

The initial stages of spray development present a highly transient behaviour. The time taken by the in-hole flow to develop fully and produce atomised spray is visible on the spray itself. As soon as the first liquid droplets emerge from the nozzle holes, the spray is not atomised, as illustrated in Figure 4.20. It takes something less than 0.1ms for the injector to produce fully atomised spray, as it is presented in the fourth image of the sequence presented in Figure 4.20. In the first, second and third images of the same sequence, one could assume that each fuel jet probably consists of pure, non-atomised liquid and this absence of liquid droplets limits considerably the Mie-scattered light intensity.

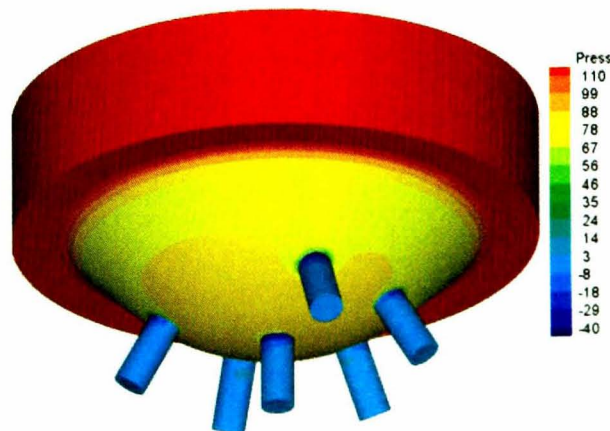


Figure 4.19: Predicted pressure distribution inside the injection nozzle, showing the pressure-drop taking place at the needle seat area [38].

Internal nozzle flow is mainly determined by the pressure drop at the needle seat area and the entrance to the injection holes. For the particular injector design investigated here, the needle seat pressure drop can be substantial relative to the rail pressure, as shown in Figure 4.19. This is reflected in the spray velocity and the resulting droplet size during the transient phase of the needle opening and closing events. During that period, droplet velocities are much smaller than in the main injection phase and droplet diameters significantly larger. Also, even at fully developed spray where the needle has stabilised, the actual injection pressure is about 90% of the rail pressure, according to simulation results carried out by the CFD branch of the research group [24, 38]. Furthermore, this is supported from the shape of the first liquid exiting the holes, which could be compared to a mushroom's head. This mushroom-shaped jet is interpreted as low tip-velocity that is forced to that deformation from the following liquid, which features increased velocity. The higher velocity liquid masses that follow displace the slow-moving tip, and are responsible for the mushroom-shaped liquid jet. The aforementioned mechanism does not change with increasing injection pressure, although it becomes more evident with increasing chamber pressure.

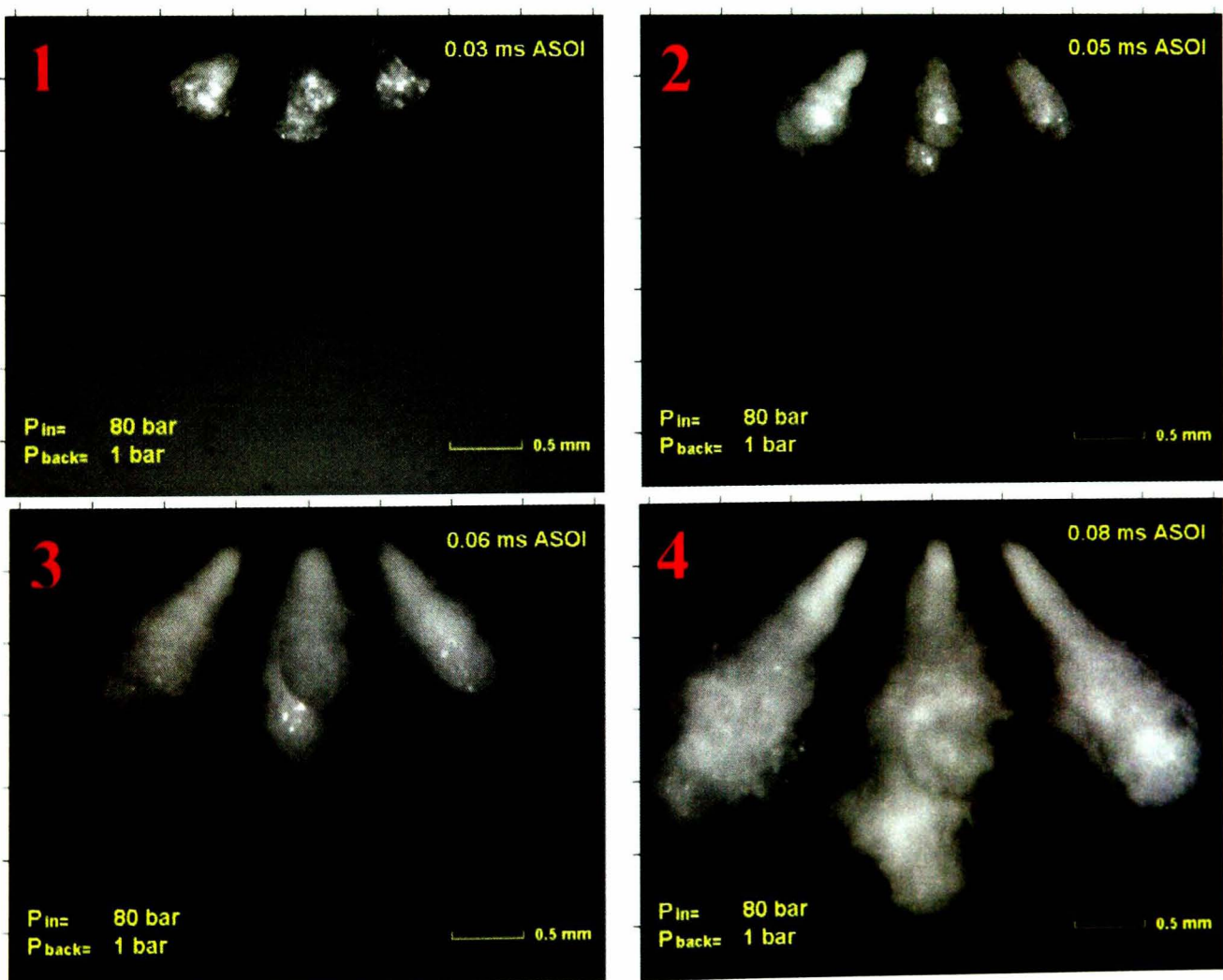
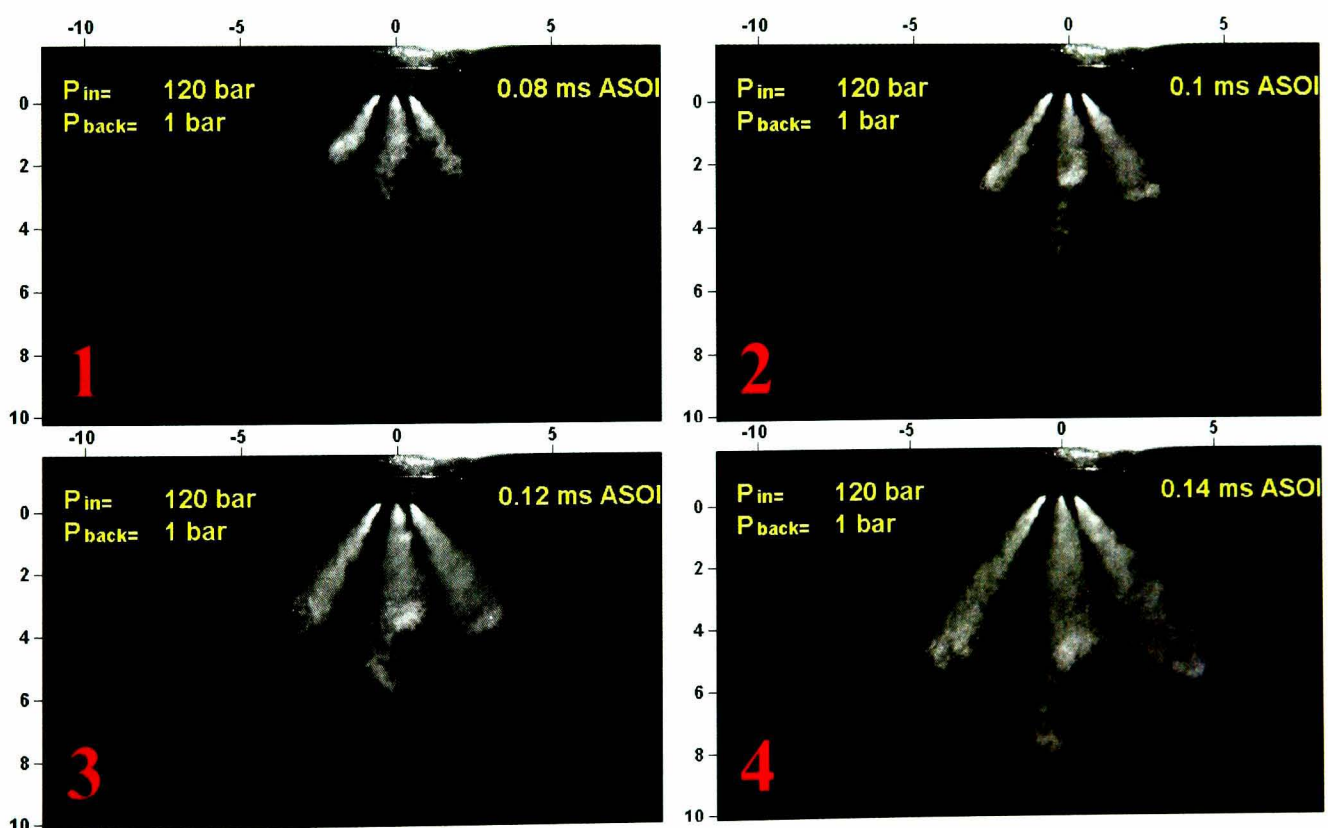


Figure 4.20: Sequential images of the initial spray development of 5+1 central holes injector.

(Image resolution: 1280x1024; spatial resolution: 0.003x0.0068mm/pixel).

According to the fourth image of the sequence presented in Figure 4.20, it is evident that the primary break-up of the spray would happen at around 0.1ms ASOI and at a distance of 1-2.5mm from the nozzle tip, according to injection and chamber pressures (see section 4.6 for details). Images focusing on a wider viewing window of 15x20mm present a satisfactory overview of the initial spray behaviour, as illustrated in Figure 4.21. Observation of the four images presented and more specifically, the shape development of an individual jet, shows that the spray could be characterised as fully developed only at 0.12-0.14ms ASOI and later. At these time ASOI, a single jet has sufficiently widened its angle, which means that internal nozzle flow has fully stabilised and cavitation-generated atomisation is at maximum levels. The small droplets produced following the primary break-up have decreased fuel mass, thus their velocity reduces rapidly. As a result, these small-sized droplets are vulnerable to ambient air motion and they are drifted away from the main jet by spray-induced air-entrainment.



**Figure 4.21: First stages of fully developed spray for the 5+1 central holes nozzle. (Image resolution: 640x512; spatial resolution: 0.035x0.035mm/pixel).**

The mechanism of air-entrainment is best illustrated in Figure 4.22, where an image of a fully developed spray is presented. The constant volume chamber suppresses any air motion since there is not any cross-flow during the injection event. Nevertheless, there is air motion in the CVC that is induced by the high-pressure spray. The air-fuel

spray interface is subjected to significant shear forces and this is the cause of recirculation zones generation. These vortices, as illustrated in Figure 4.22, become wider, as distance from nozzle tip increases, and form a fishbone structure due to the dispersion of slow-moving light droplets.

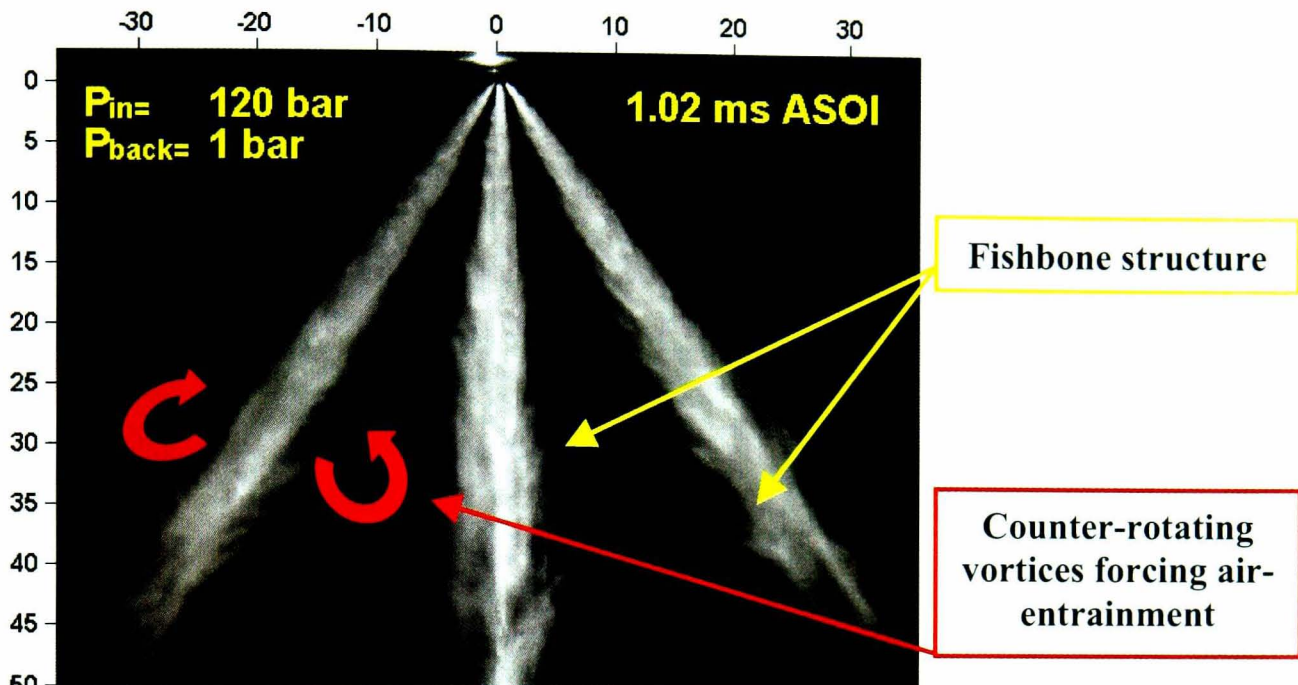
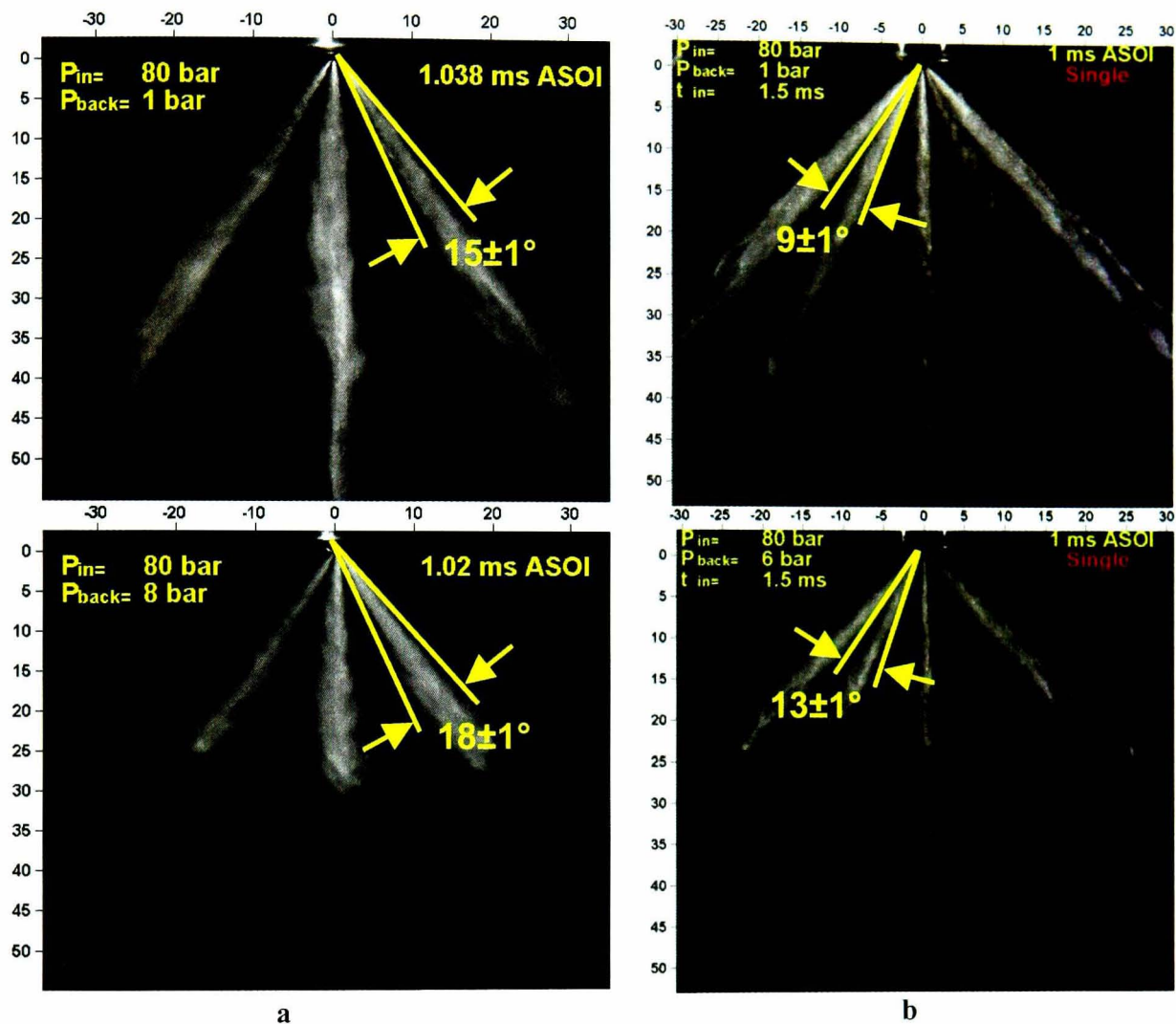


Figure 4.22: Example of air-entrainment in a 5+1 central holes injector spray.

Taking further the observations on the individual jet angle, a comparison between a 6- and a 12-hole injector spray reveals useful information on the effect of internal nozzle geometry to the injected spray. Based on certain know-how obtained from extended investigations on diesel sprays, it is well established that the ratio of the hole-length over the hole-diameter ( $L/D$ ) is responsible for the final shape of the jet produced. In principle, large values of  $L/D$  produce thin jets featuring a relatively small jet cone angle and a long liquid core length. On the contrary, jets produced by lower  $L/D$  values exhibit a large jet cone angle and the liquid core length is shorter, contributing, in principal, in quick and efficient evaporation of the fuel droplets [9, 27, 35]. Among all investigated nozzles a comparison between nozzles of different  $L/D$  value is possible. One of the 6-hole nozzles (five plus one central holes) features an  $L/D$  value of 2.14, while the 12-hole nozzle (ten plus one central holes) has a reduced hole diameter and the resulting  $L/D$  ratio is 3. As illustrated in Figure 4.23a, the 6-hole nozzle produces a jet cone angle of  $15^\circ$ . This value does not change with injection pressure, but it grows larger ( $\sim 18^\circ$ ), as expected, with increasing chamber pressure. The effect of chamber pressure on the jet cone angle is due to the increased drag applied on single droplets and results in large velocity losses. Furthermore, in Figure

4.23b, similar operating conditions for the twelve-hole nozzle, result in a jet cone angle of maximum  $10^\circ$ . The aforementioned results support and verify the already established connection of the geometrical L/D ratio to the resulted spray shape that derived from investigations on diesel multi-hole injectors.



**Figure 4.23:** Comparison of the individual jet cone angle for (a). 6- and (b). 12-hole nozzles. *Top row* is atmospheric and *bottom row* is higher chamber pressure. (Image resolution: (a,b) 640x512; spatial resolution: (a) 0.11x0.108mm/pixel, (b) 0.096x0.108mm/p).

In general, spray propagation and atomisation mechanisms related to gasoline multi-hole injectors are in tight bonds with diesel multi-hole injectors and the physical phenomena behind these mechanisms are almost identical. Small differentiations appear that are closely related to the needed geometry changes. For instance, a gasoline multi-hole spray features a maximum overall spray cone angle of around  $90^\circ$ , value much smaller compared to diesel sprays. In addition to that, given the operating cycle differences between diesel and gasoline engines, one would never expect a central injection hole in a diesel injector. On the contrary, gasoline nozzles feature central holes for achieving better homogenisation of the air/fuel mixture in the cylinder. Central injection holes are positioned in the middle of the nozzle's sac

volume and their existence disturbs the almost stagnant flow that rules that region of the nozzle. Based on results presented in Chapter 3 regarding the internal nozzle flow, it is evident that central jets are more likely to present unstable shapes than any other side jet. This theory is also strengthened by the fact that central injection holes are most likely utilised when there are blocked side holes. This behaviour has been verified in certain experiments, and examples of central jet instability are illustrated in Figure 4.24.

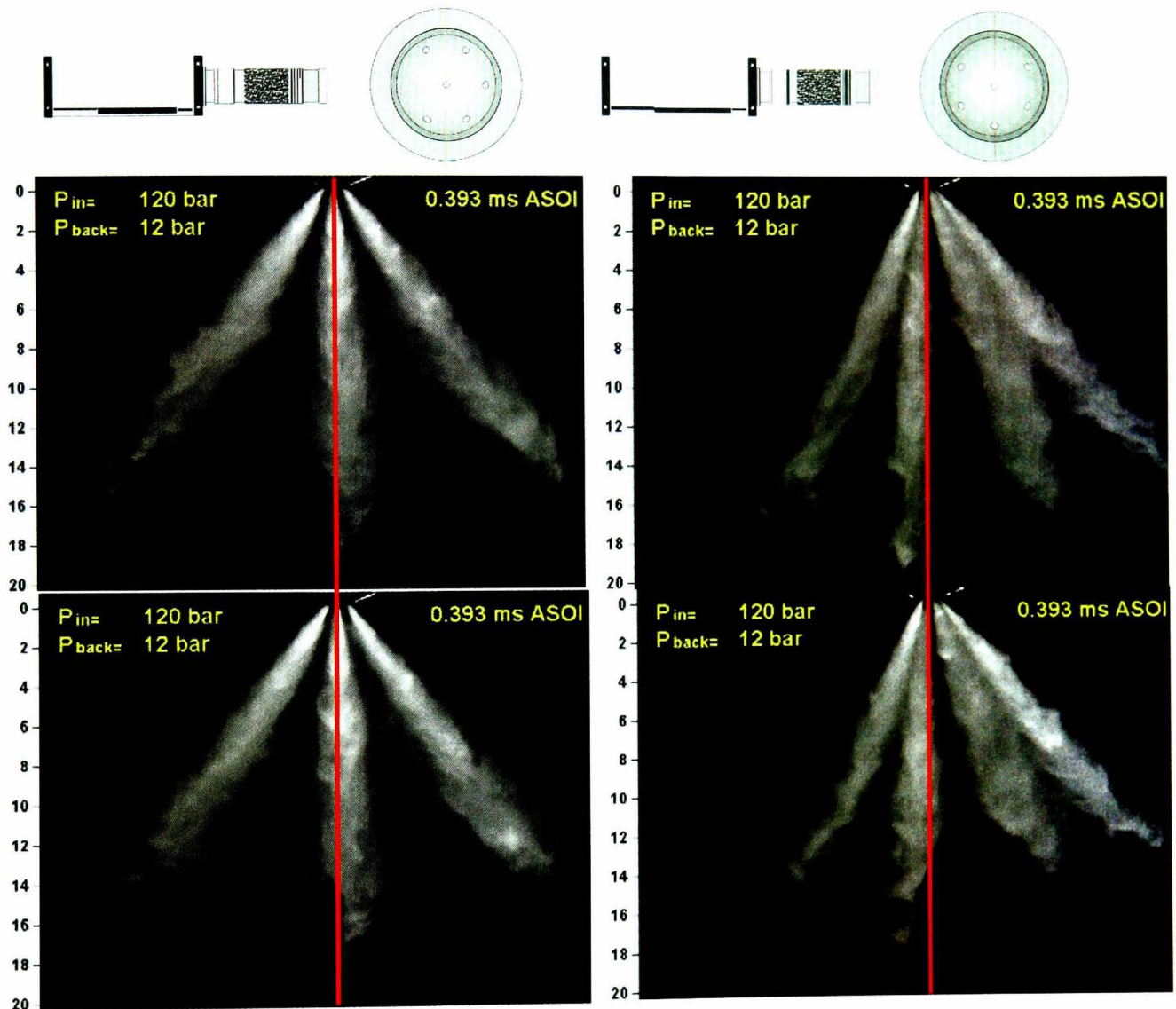


**Figure 4.24: Comparison of images of central jet shape of a 5+1 central holes injector taken at identical conditions but on two different imaging planes. (Image resolution: 640x512; spatial resolution: 0.046x0.046mm/pixel).**

Left hand column in Figure 4.24 illustrates images where the missing injection hole does not lie on the imaging plane. On the contrary, at right hand column images, the injector has been rotated and the blocked side hole lies on the imaging plane. Initially, an important observation is related to the tip penetration length of the central jet, which appears larger than all side jets. This behaviour is expected, since central injection holes are not positioned at an angle, relative to the injector's axis of

symmetry, and droplet velocities are expected higher than any side injection holes. Extraction of quantitative results from spray images, are presented in Figure 4.25, and confirm the longer penetration lengths of the central spray tip relative to the side jets. Apart from the long penetration length, images at left hand column, present the central jet almost symmetrically shaped around the injector axis (red line). The same observation cannot be verified from the right hand column images, where the central jet is imaged from a different angle. It appears to lean towards the side where the blocked injection hole is positioned. This behaviour is believed to be due to a combination of the non-symmetrical in-nozzle flow, imposed by the missing hole, the non-stable in-hole flow conditions, imposed by the weak flow field in the middle of the sac volume and the dynamics of the spray itself, where air-entrainment to the central jet is enhanced unilaterally.

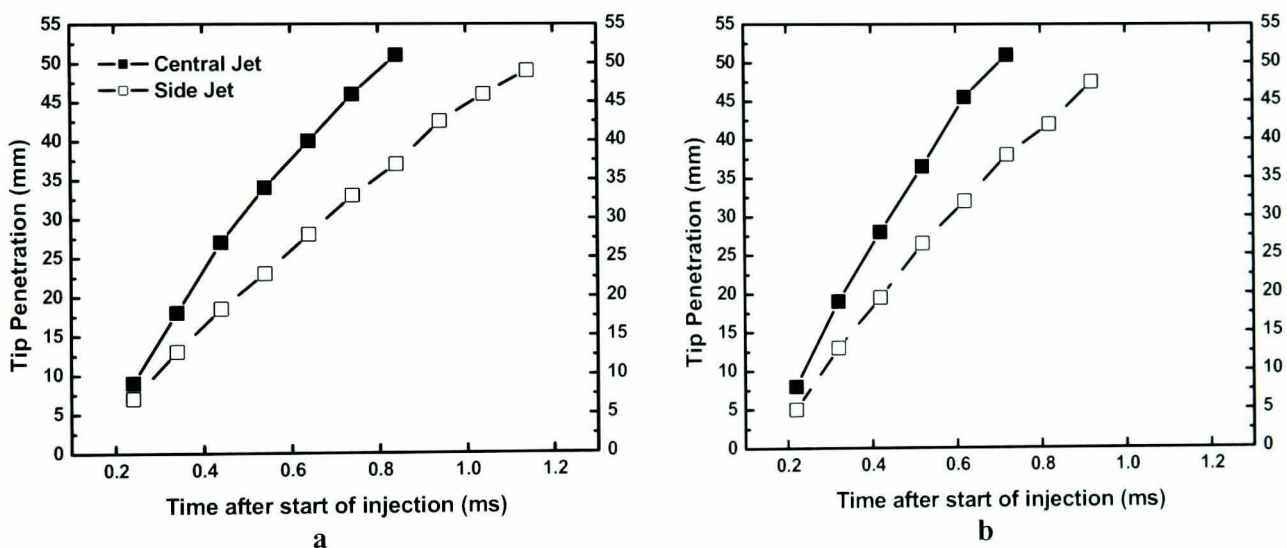
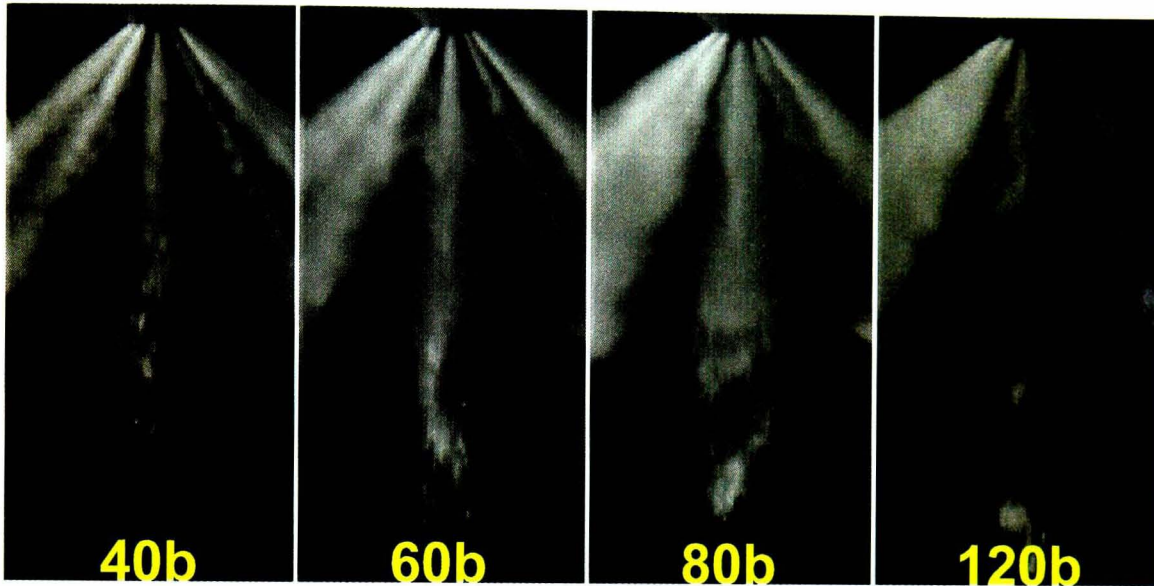


Figure 4.25: Spray tip penetration lengths of central and side jets as calculated from Mie images at (a). 80bar and (b). 120bar injection pressures.

### Effect of injection pressure

Multi-hole nozzles operate in a wide range of injection pressures, starting from the lowest acceptable value of 60bar and increasing to 120bar, or even 200bar in some cases. The lower limit in injection pressure is defined from the desired atomisation quality and not any operating limitations. The major effect of injection pressure on high-pressure fuel sprays has always been connected to liquid atomisation. The higher the injection pressure the better and more effective the spray atomisation. Figure 4.26 illustrates images taken at identical conditions at four different injection pressures. Although the advantages, in terms of atomisation, of 120b injection pressure relative to 40b are crystal clear, the same rule does not apply when increasing the pressure from 120b to 200b. The multi-hole nozzle, as a fully cavitating nozzle, utilises

cavitation as an atomisation mechanism. According to results presented in previous chapters, fully developed in-hole cavitation has been observed at conditions corresponding to injection pressures lower than 120b. Based on these observations, it is concluded that there is a limit in injection pressures, in terms of atomisation enhancement; values higher than this limit contribute minimum or limited advantages when compared to the simultaneous higher energy consumption of the high-pressure pump.



**Figure 4.26: Effect of injection pressure on spray atomisation.**

Finally, another effect of injection pressure on spray development is the increase of spray tip penetration length with increasing injection pressure. Pressures of 80,100,120 and 200bar appear to affect the distance between the spray tip and the nozzle, when injecting at similar chamber pressures. This behaviour is based on the increased droplet velocities initiated by high injection pressures and it could be seen as a possible way of controlling the spray tip penetration length. The ability to control penetration lengths of gasoline high-pressure sprays is of great importance, since in gasoline DI engines any wall impingement of the fuel spray results in increased exhaust gas emissions. A visual representation of the effect of injection pressure on spray tip penetration length is illustrated in Figure 4.27 through Figure 4.28.

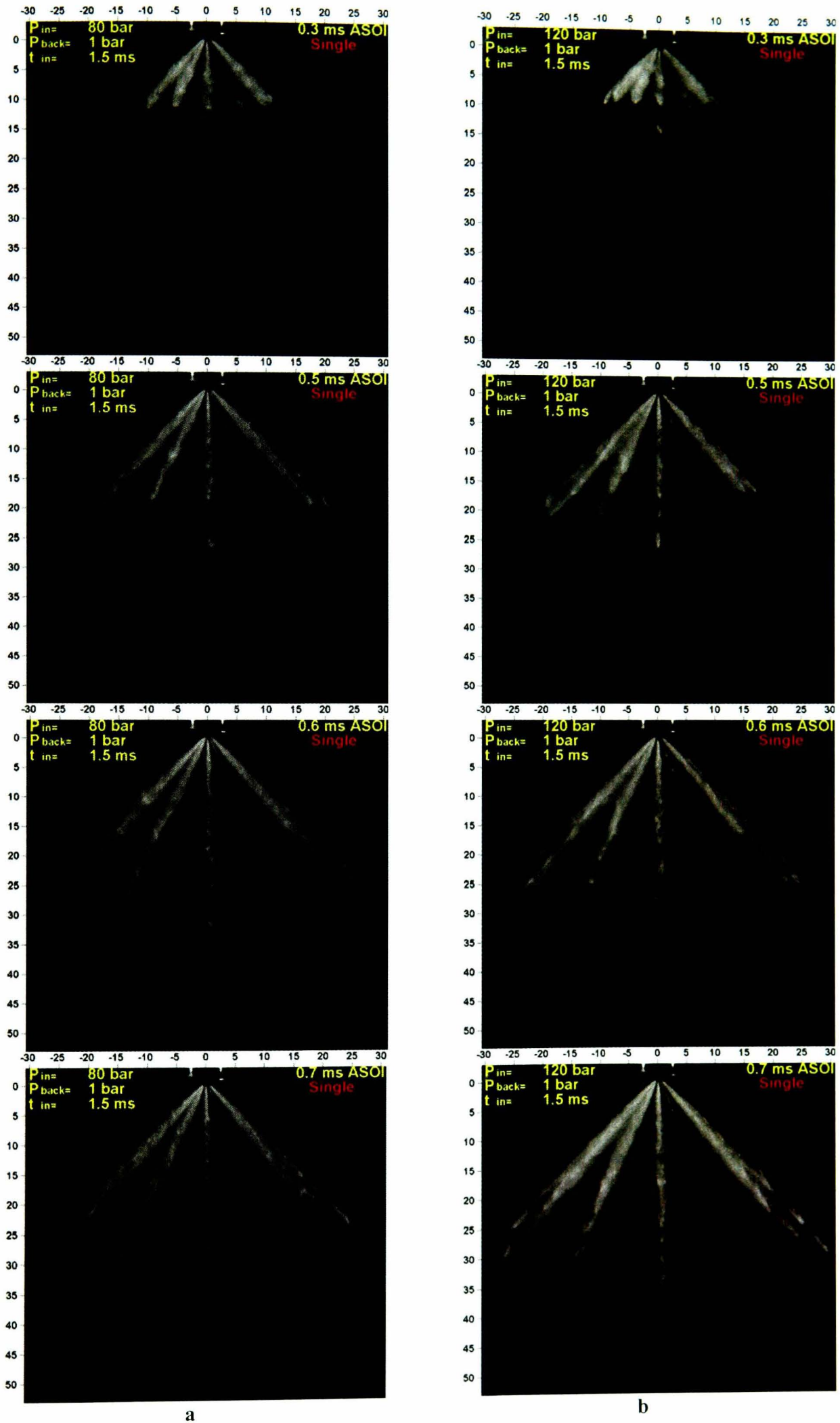


Figure 4.27: Time-dependent comparison of a 10 (12-2) + 1 central holes spray injected at injection pressures of (a). 80 and (b). 120bar. (Image resolution: 640x512; spatial resolution: 0.094x0.107mm/pixel)

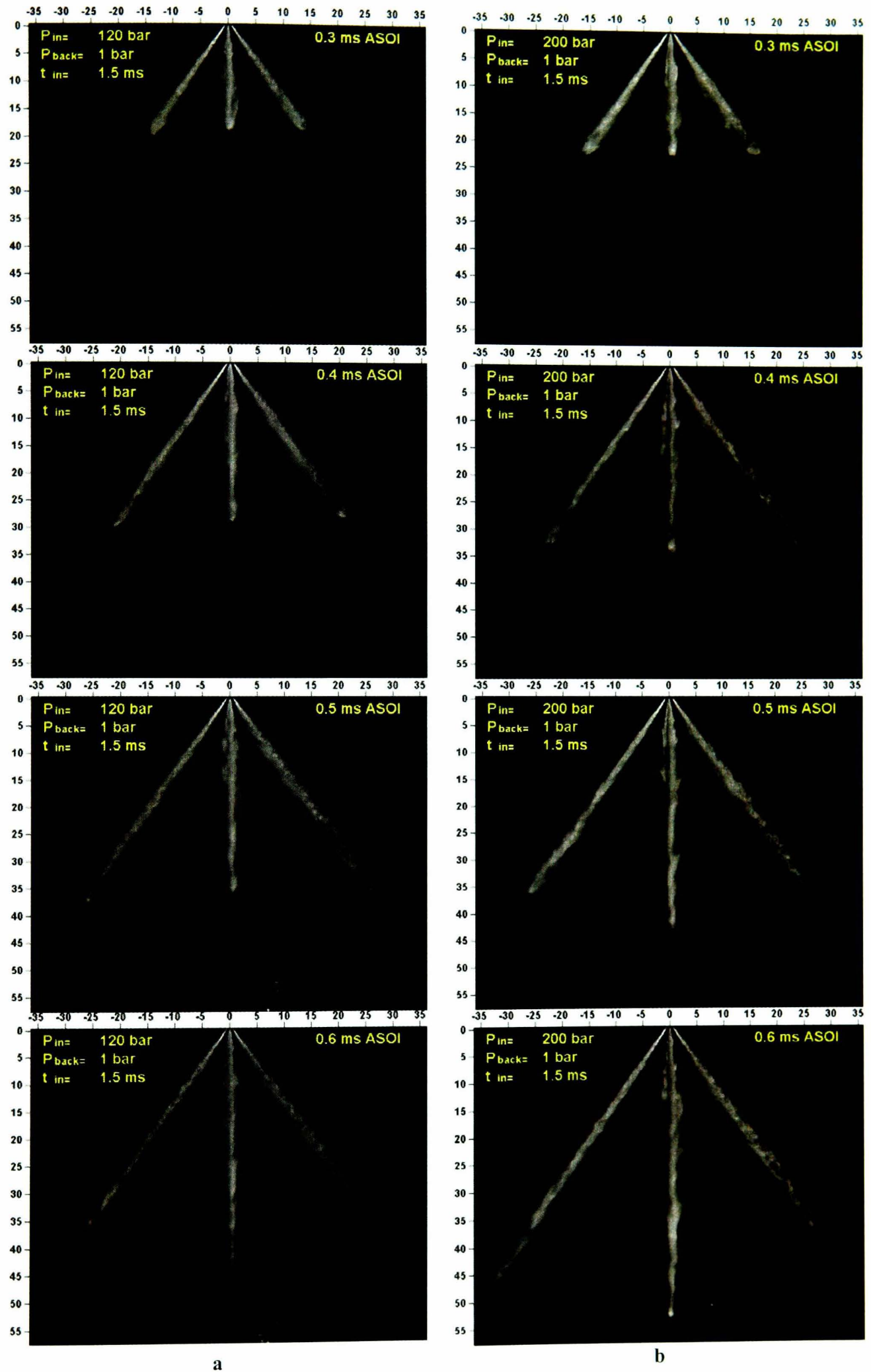


Figure 4.28: Time-dependent comparison of a 6-hole spray injected at injection pressures of (a). 120 and (b). 200bar. (Image resolution: 640x512; spatial resolution: 0.11x0.108mm/pixel)

Following certain post-processing applied in the above-presented images, sets of graphs (Figure 4.29 and 30) have been created, presenting tip penetration values for all nozzles tested.

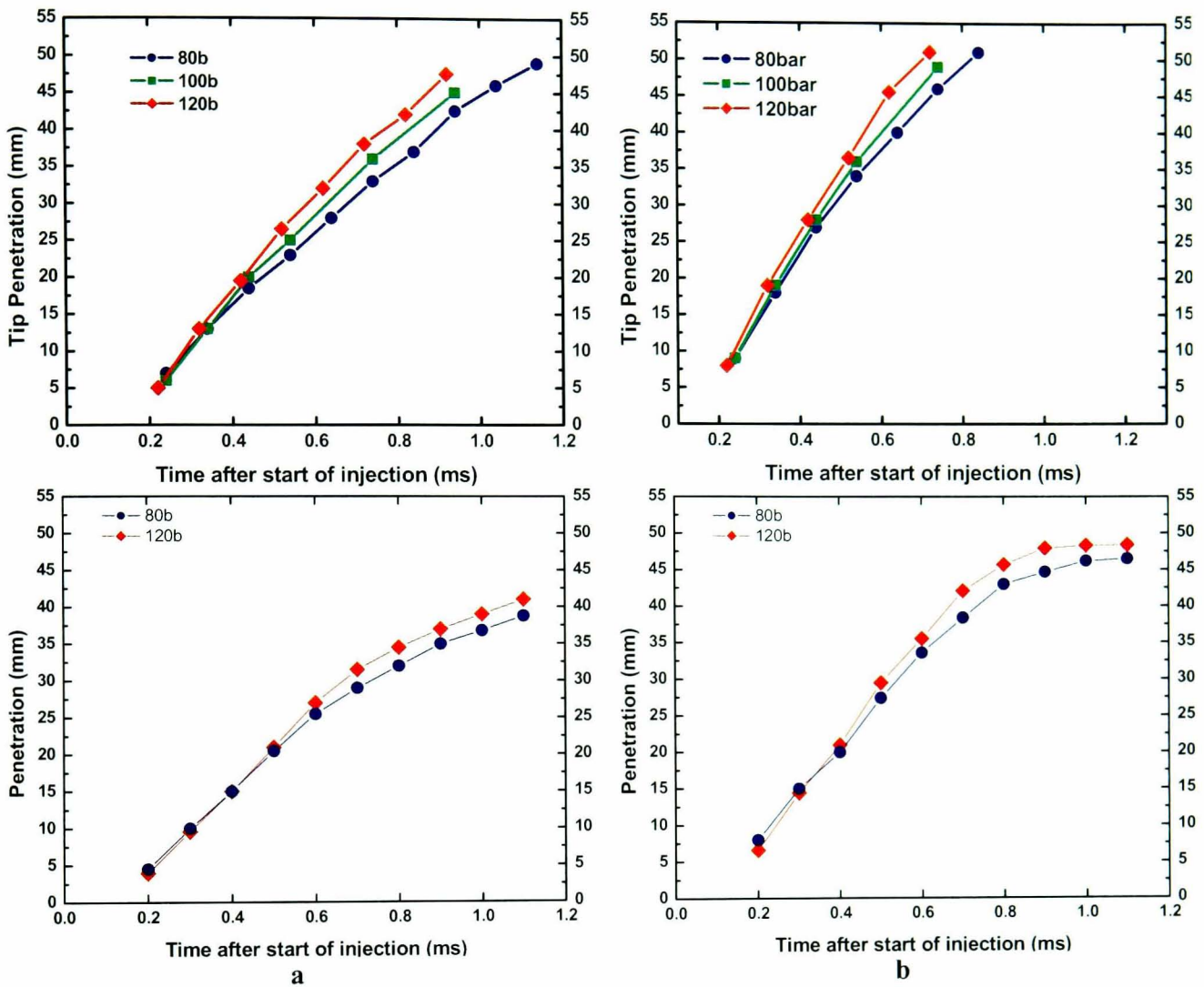


Figure 4.29: Effect of injection pressure on (a). side and (b). central jet tip penetration lengths for 5+1 central holes (top row) and 10 (12-2) + 1 central holes (bottom row) nozzles.

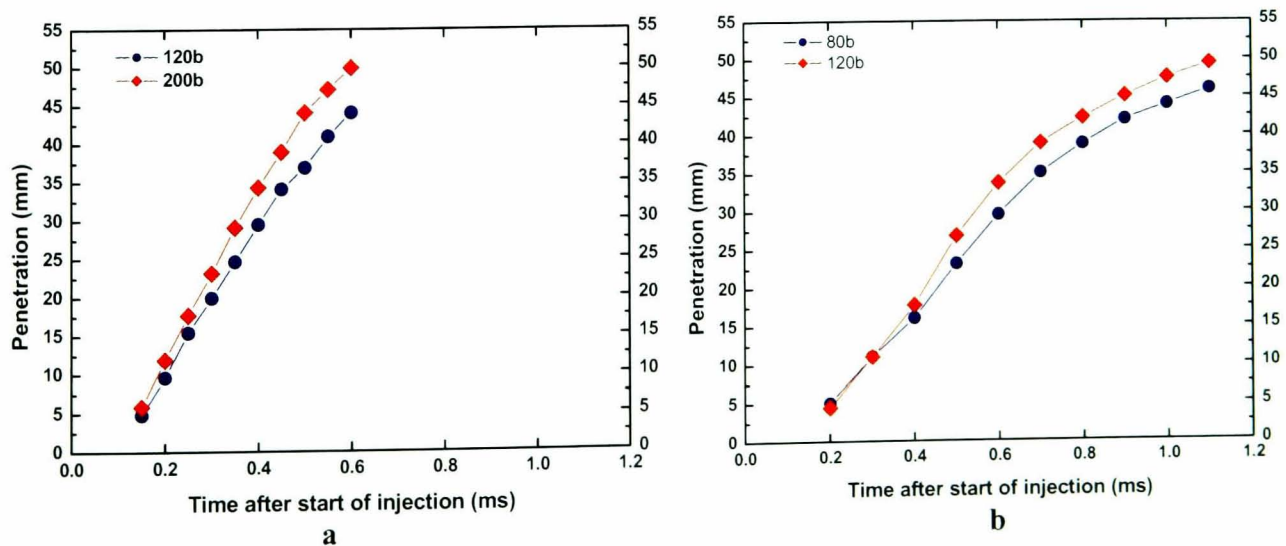


Figure 4.30: Effect of injection pressure on spray tip penetration lengths for (a). 6-hole symmetric and (b). 6-hole asymmetric injectors.

The above summary of spray tip penetration lengths for all tested multi-hole nozzle configurations demonstrates that, within the measured ranges, injection pressure marginally affects the distance the high-pressure spray would travel. For example, at 0.6ms ASOI, when the spray is fully developed, the increase in injection pressure from 80 to 120bar lead to increased spray tip penetration of up to 16% and 8% for the 5 + 1 central holes and the 10 + 1 central holes injectors, respectively. The latter suggests that spray tip penetration of the 10 + 1 central holes injector is less affected by injection pressure than the one of 5 + 1 central holes. It is also evident from Figure 4.29 that the overall spray tip penetration of the 10 + 1 central holes injector is less than the one of 5 + 1 central holes injector by up to 15% (data corresponding to side jets), suggesting that better atomisation and faster evaporation are achieved with the 10 + 1 central holes nozzle.

### Effect of chamber pressure

The effect of ambient chamber pressure on spray development is remarkable and straightforward. Effectively, increased chamber pressure is translated into higher gas density, which is what spray droplets sense. More specifically, as droplets emerge from the nozzle holes they face a considerably dense (depends on chamber pressure value) gaseous medium that causes droplets to rapidly reduce their velocity. The sudden spray velocity reduction possibly leads to droplet coalescence, which, in turn, could result in formation of large diameter droplets. Furthermore, individual jets become compact in size, spray tip penetration is reduced remarkably and air-entrainment lies at minimum levels. Figure 4.31 and Figure 4.32 illustrate an overview of chamber pressure effect on sprays from two different multi-hole nozzles.

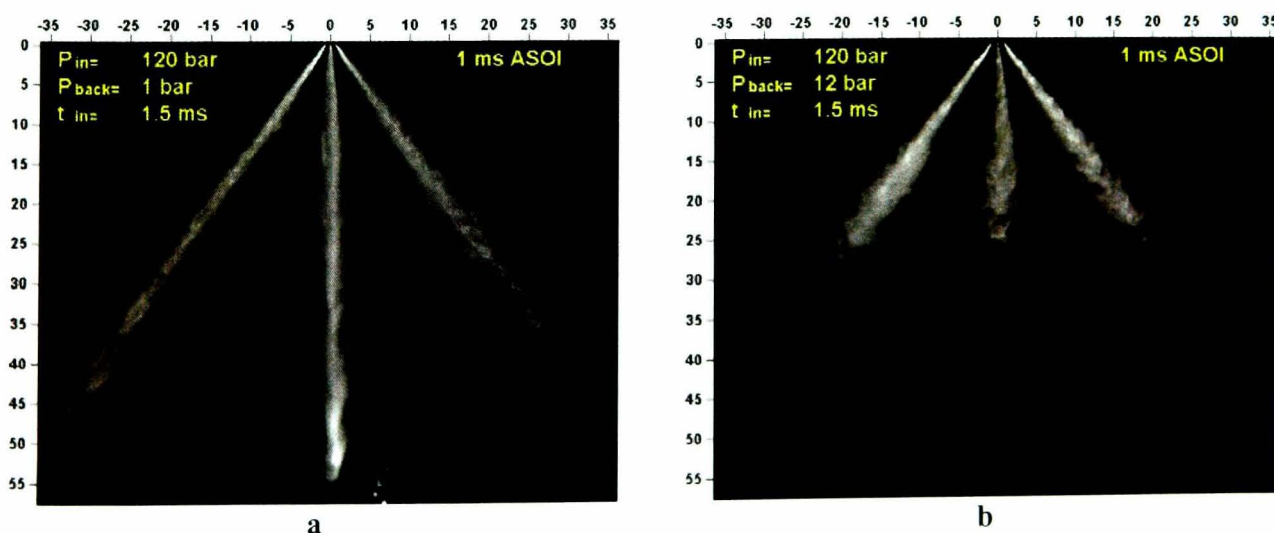


Figure 4.31: Effect of chamber pressure on a 6-hole nozzle spray. (a). 1bar and (b). 12bar.

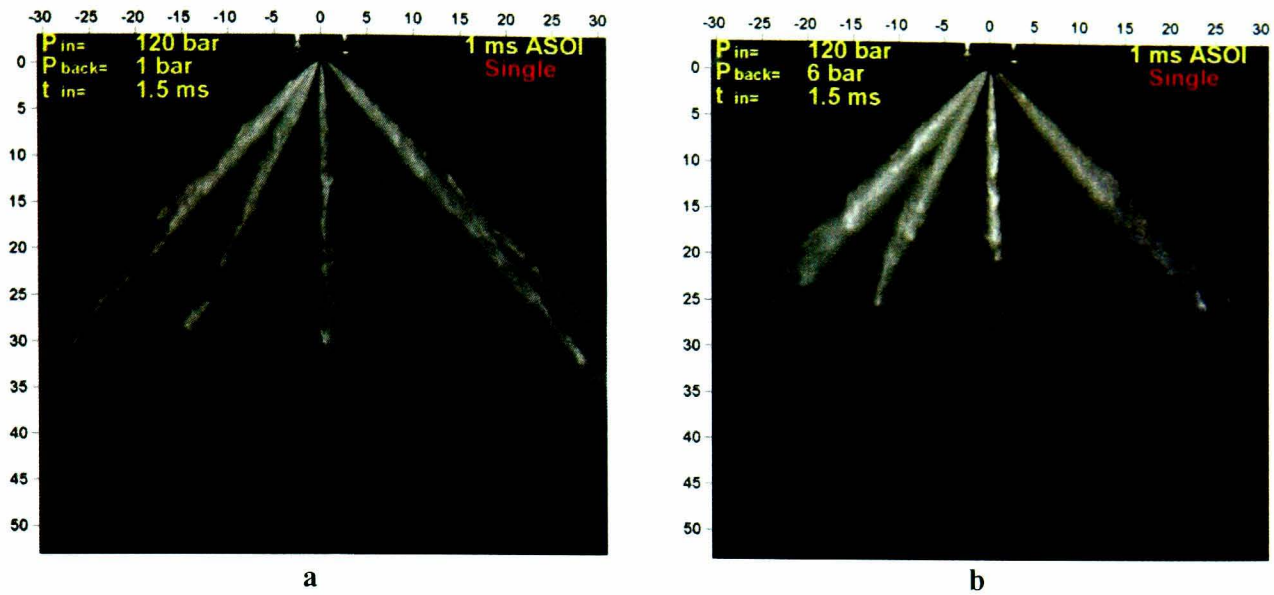


Figure 4.32: Effect of chamber pressure on a 10 (12-2) + 1 central hole nozzle spray. (a). 1bar and (b). 6bar.

Apart from the individual jets shape, chamber pressure also affects spray tip penetration length. As mentioned above, droplet velocity losses lead to reduced spray tip penetration lengths. This reduction is strongly related to the applied chamber pressure, as illustrated in the following graphs (Figure 4.33 and Figure 4.34). In general, results show that spray tip penetration at elevated chamber pressures decreases progressively with time ASOI. More specifically, at 0.2ms ASOI, the reduction in penetration length is of the order of 2 to 5% and increases to around 24% and 30% at 0.6ms and 1.1ms ASOI, respectively, as chamber pressure increases from atmospheric to 6bar (Figure 4.33). Further increase in chamber pressure to 12bar results in a reduction of spray tip penetration of 50%, at 0.6ms ASOI (Figure 4.34).

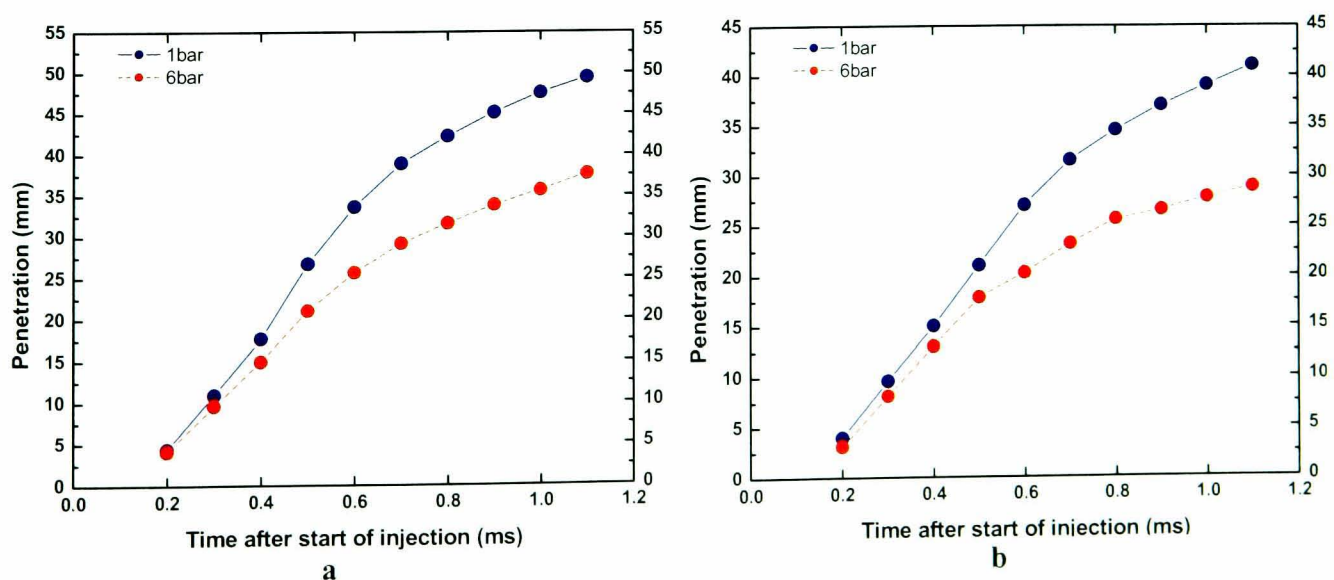
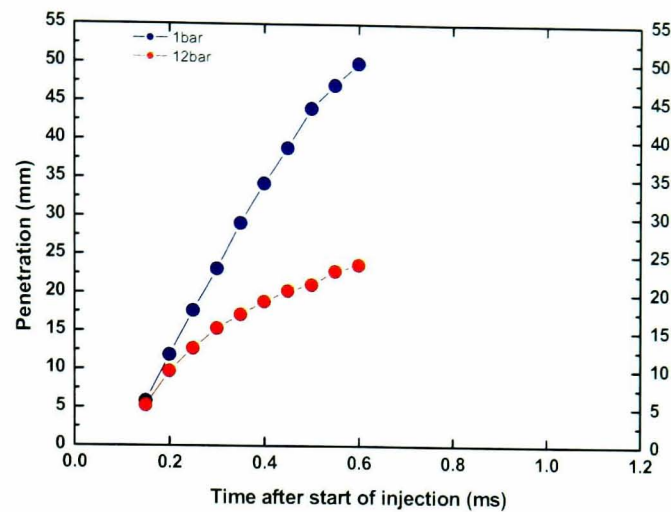


Figure 4.33: Effect of chamber pressure on spray tip penetration length at 120bar injection pressure for (a). 6-hole asymmetric and (b). 10 (12-2) + 1 central holes nozzles.



**Figure 4.34: Effect of chamber pressure on spray tip penetration length at 200bar injection pressure for the 6-hole symmetric nozzle.**

Multi-hole gasoline injectors have been released in order to replace the first generation injectors, known as swirl pressure atomisers. The latter present a main disadvantage related to the spray shape stability. Investigations carried out by a number of research groups worldwide, showed that spray shapes from swirl pressure atomisers are a function of chamber pressure. More specifically, injection at chamber pressures higher than atmospheric results in a reduction of the overall spray cone angle. This reduction is remarkable and effectively spray shape collapses. Similar changes in basic spray shape characteristics create difficulties in engine manufacturers, due to the imposed complexity in engine design and management. The position of the high-pressure injector in an engine's combustion chamber is carefully selected and defines basic engine design features, such as piston-crown shape (cavity/flat) and spark-plug position. In the unfortunate situation where spray shape is a function of chamber pressure and in-cylinder flow field in general; it is evident that stable engine operation cannot be achieved.

Multi-hole injectors have been introduced in order to overcome the spray shape dependence of the swirl pressure atomisers on chamber pressure. Thus, the critical spray characteristic is the overall spray cone angle, which, in multi-hole nozzles, is defined during manufacturing by the relative angle between the injection hole axis and the injector axis of symmetry. The majority of all investigated nozzles, in the present work, featured a nominal overall spray cone angle of  $90^\circ$ . Following experiments at different injection and chamber pressures, it has been revealed that overall spray cone angle remains unaffected. Even in cases where the measured cone

angle appeared smaller than the nominal value, it remained at the same levels. Chamber pressure mainly affects individual jets, the alteration in spray shape characteristics is marginal though and therefore global spray shape remains unchanged, as illustrated in Figure 4.35.

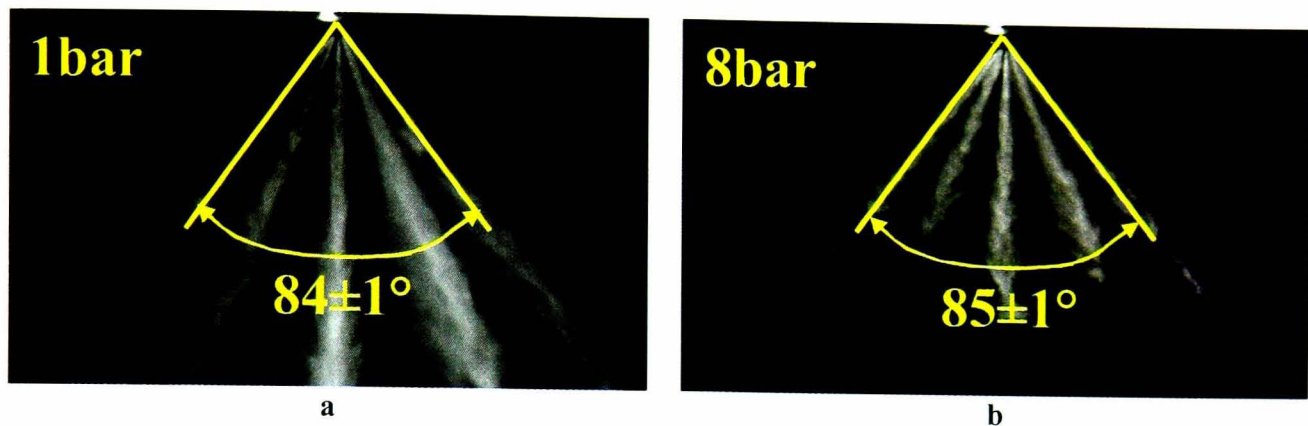


**Figure 4.35:** Comparison of overall spray cone angle between (a). 1bar and (b). 8bar chamber pressures, for an injection pressure of 80bar.

The measured overall spray cone angle values for two representative multi-hole nozzles under all tested conditions are presented in Table 4-4. The results show that the overall spray cone angles of all multi-hole nozzle designs investigated present significant stability against chamber pressure changes, with a maximum deviation of about 3.5% that can partly be attributed to uncertainties induced by processing.

6 holes			
Injection pressure [bar]	Chamber pressure [bar]		
	1	8	12
120	79 ±1	81 ±1	81 ±2
200	80 ±1	81 ±1	80 ±2
10(12-2)+1 central holes			
Injection pressure [bar]	Chamber pressure [bar]		
	1	4	8
80	85 ±1	86 ±2	88 ±2.5
100	85 ±1	86 ±2	86 ±2
120	84 ±1	82 ±1	84 ±2

**Table 4-4:** Overall spray cone angle for two multi-hole nozzles.

### Effect of ambient chamber temperature

Stratified engine operation is achieved only by late fuel injection in the compression stroke. A small quantity of fuel that is capable of delivering a combustible air/fuel mixture around the spark-plug vicinity is needed. Apart from the important spray

shape stability under high chamber pressures, spray shape repeatability is required under increased chamber ambient temperature conditions. During the first stages of the compression stroke, cylinder pressure is very close to atmospheric values and temperature is only increased by a maximum of  $15^{\circ}$ - $20^{\circ}$ , a difference that is caused by heat exchange between the inducted air and the induction manifold walls. At later stages of the compression stroke, cylinder pressure and temperature start increasing exponentially before maximum values are reached at piston's top dead centre. Hence, it should be considered as a fact that the majority of late injection events occur at temperatures higher than  $40^{\circ}$ - $50^{\circ}$ . In an attempt to simulate realistic engine operating conditions in a constant volume chamber, a high-energy heater is utilised and resulted chamber temperatures could reach a maximum value of  $120^{\circ}$ . Following the extended spray investigations at temperatures of  $40^{\circ}$ - $50^{\circ}$ , it was decided to visualise multi-hole sprays under elevated temperature conditions of  $90^{\circ}$  and  $120^{\circ}$ . The latter value was selected to be above the boiling point of isooctane ( $102^{\circ}$ - $105^{\circ}$  @1bar) for evaporating conditions to be simulated. Since the Mie scattering technique is based on scattered light by liquid droplets only the remained non-yet-vaporised spray could be captured. Hence, the results could not be compared unless a combination of a direct comparison of more than one condition is realised. More specifically, assuming that the base spray image for characterising evaporation would be at the lowest available temperature, the combination of images taken at the base and a higher temperature would provide important qualitative information on the relative percentage of liquid already vaporised (Figure 4.36).

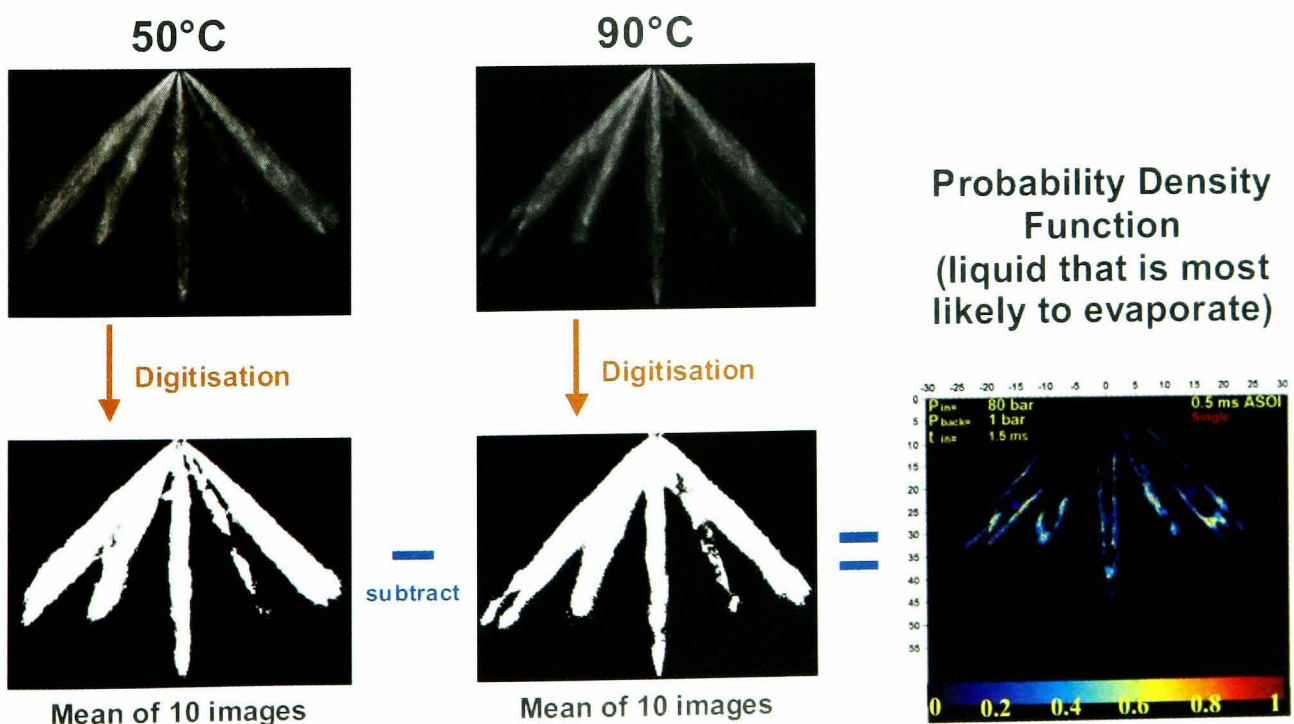


Figure 4.36: Schematic representation of the processing procedure.

Figure 4.37 and Figure 4.38 illustrate the temperature effect on spray droplet vaporisation for a 10(12-2) + 1 central holes and a 6-holes asymmetric nozzles for sprays injected at 80bar into atmospheric chamber pressure. Similar data exist for a higher injection pressure of 120bar, although the results are very similar to the ones presented below. This is probably due to minor improvements in atomisation and effectively vaporisation that is difficult to be captured by a visualisation experiment. A more specific analysis on the images illustrated below, would conclude that the contribution of 90°C in spray vaporisation relative to 50°C is according to expectations. Ninety degrees Celsius is lower than the boiling point of isooctane, however small amounts of liquid are expected to vaporise during the main injection event and this would most likely happen at the edges of the individual fuel spray jets. As illustrated in Figure 4.37a and Figure 4.38a, the vaporised liquid is effectively a contour of the high-pressure fuel jets at 50°. This behaviour would not change considerably as time ASOI increases, although an increase in probability of vaporised fuel is visible at the spray tips.

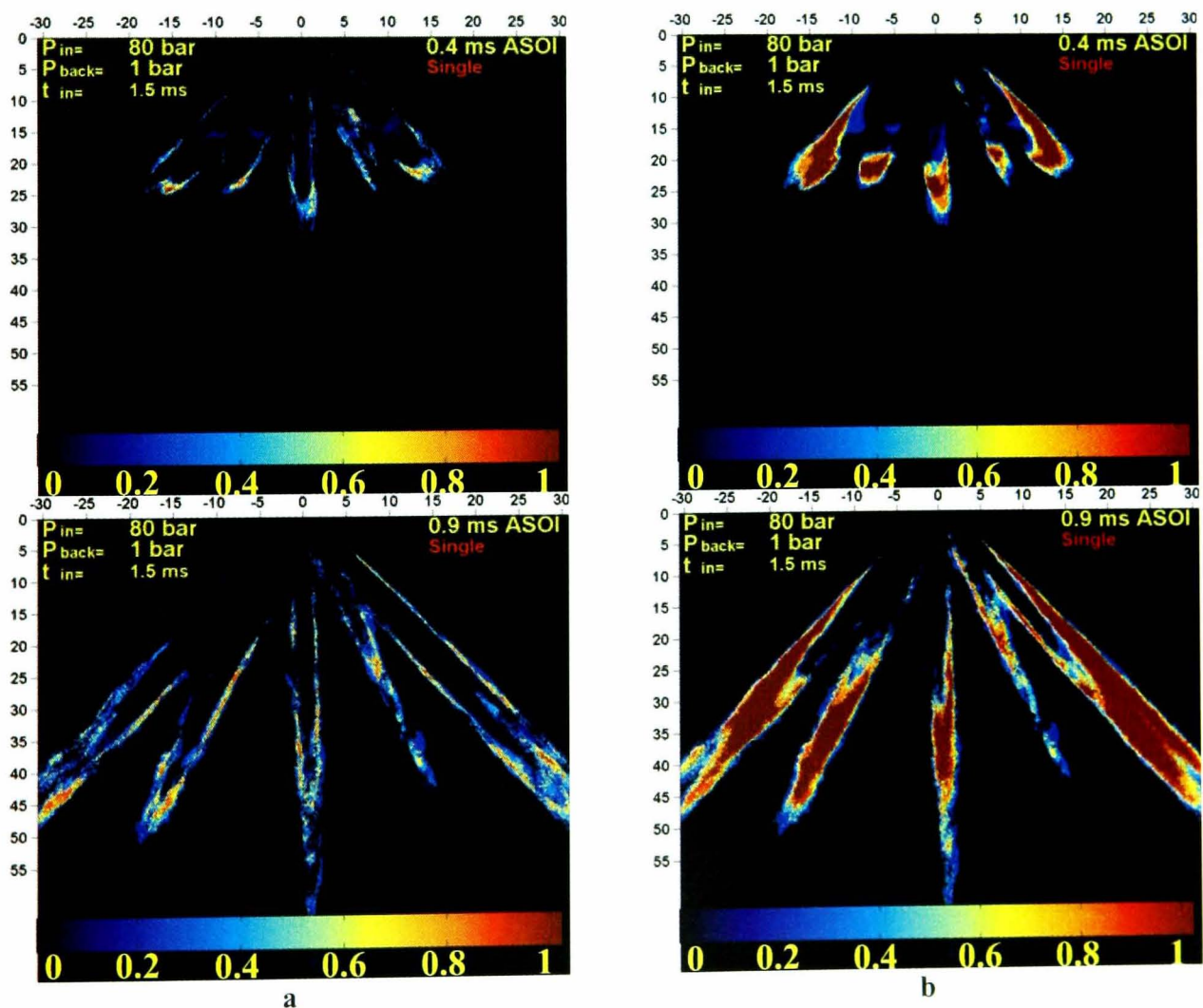
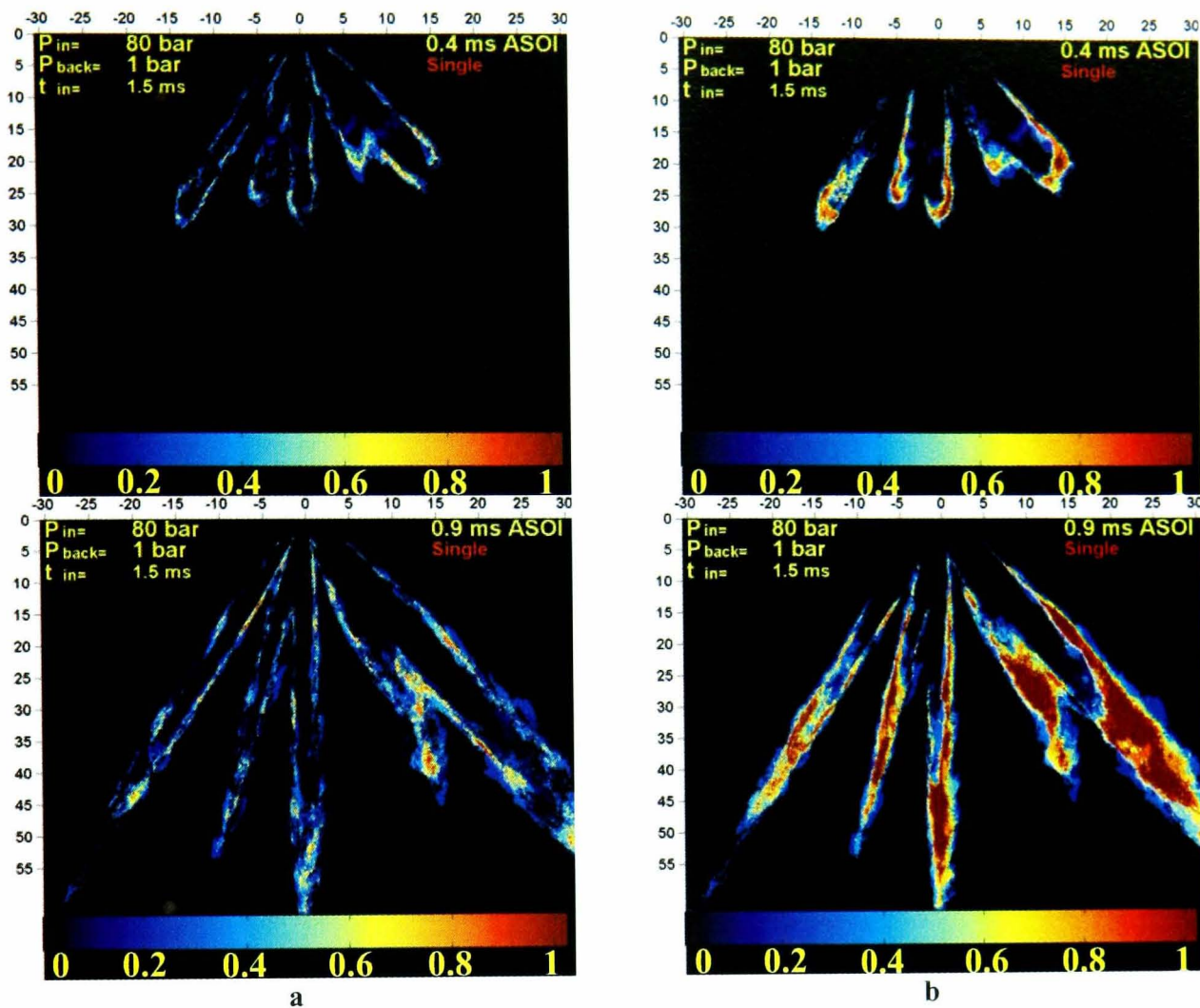


Figure 4.37: Temperature effect on droplet vaporisation for the 10 (12-2) + 1 central holes nozzle at two times after SOI (*top row*: 0.4ms and *bottom row*: 0.9ms ASOI) expressed as probability density function for temperatures (a). 50° to 90° and (b). 50° to 120°.



**Figure 4.38:** Temperature effect on droplet vaporisation for the 6-hole asymmetric nozzle at two times after SOI (*top row: 0.4ms and bottom row: 0.9ms ASOI*) expressed as probability density function for temperatures (a). 50° to 90° and (b). 50° to 120°.

Finally, as chamber temperature increases to values higher than 105° (boiling point of isooctane) the reduction in the visualised spray quantity is evident. Careful observation of Figure 4.37b and Figure 4.38b would show that in the case of injection into a chamber of 120°C the impact on fuel vaporisation is enormous even at early times of injection. The maximum spray tip penetration length is reached at 0.4ms ASOI, at all tested injection pressures. The reason lies on the fact that vaporisation rates are high enough to vaporise a considerable amount of liquid in short time scales. Furthermore, an important differentiation of the 12- and 6-hole injectors has been revealed. The thin jets produced by 12-hole nozzles feature better vaporisation potential compared to their 6-hole counterparts. More specifically, the increased fuel mass distribution achieved by a 12-hole nozzle presents higher evaporation rates than any other nozzle tested.

### Double-injection performance of multi-hole injectors

Double injection strategy has proved to be an effective way of minimising engine's and catalyst warm-up time [17, 34, 74], a period during which, the emissions are at highest levels. In addition to that, double injection efficiently contributes in the formation of a combustible air/fuel mixture around the spark-plug electrode. Division of the total injection duration into two parts, results in reduced spray tip penetration for both injection events, thus fuel impingement on cylinder walls and piston crown is avoided. According to engine's load requirements different timing of the two injection events is instructed. More specifically, homogeneous stoichiometric mixture is achieved by placing the first injection event during the induction stroke and the second during early compression stroke stages. Furthermore, a common strategy for creating stratified overall lean, in fuel, mixture instructs placing of the first injection early in the compression stroke followed by the second injection event shortly after.

The aforementioned details on engine management developments immediately set the requirements for fuel injection equipment as far as the delay time between the two injection events are concerned. This delay time is often referred to as the “dwell time” and it could vary from a minimum of 0.1ms to two or so milliseconds. The definitions of all double injection related values are illustrated in Figure 4.39.

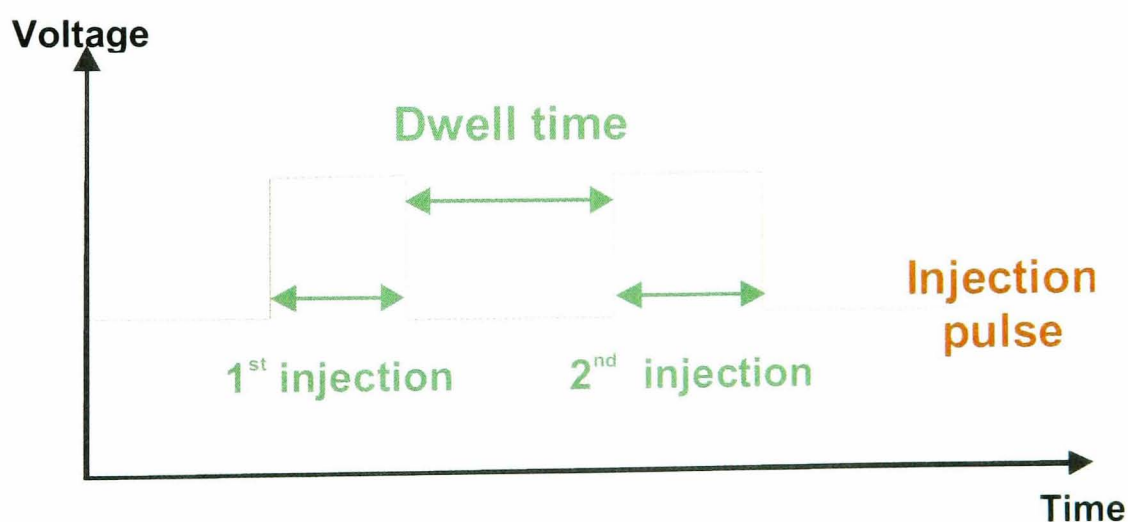
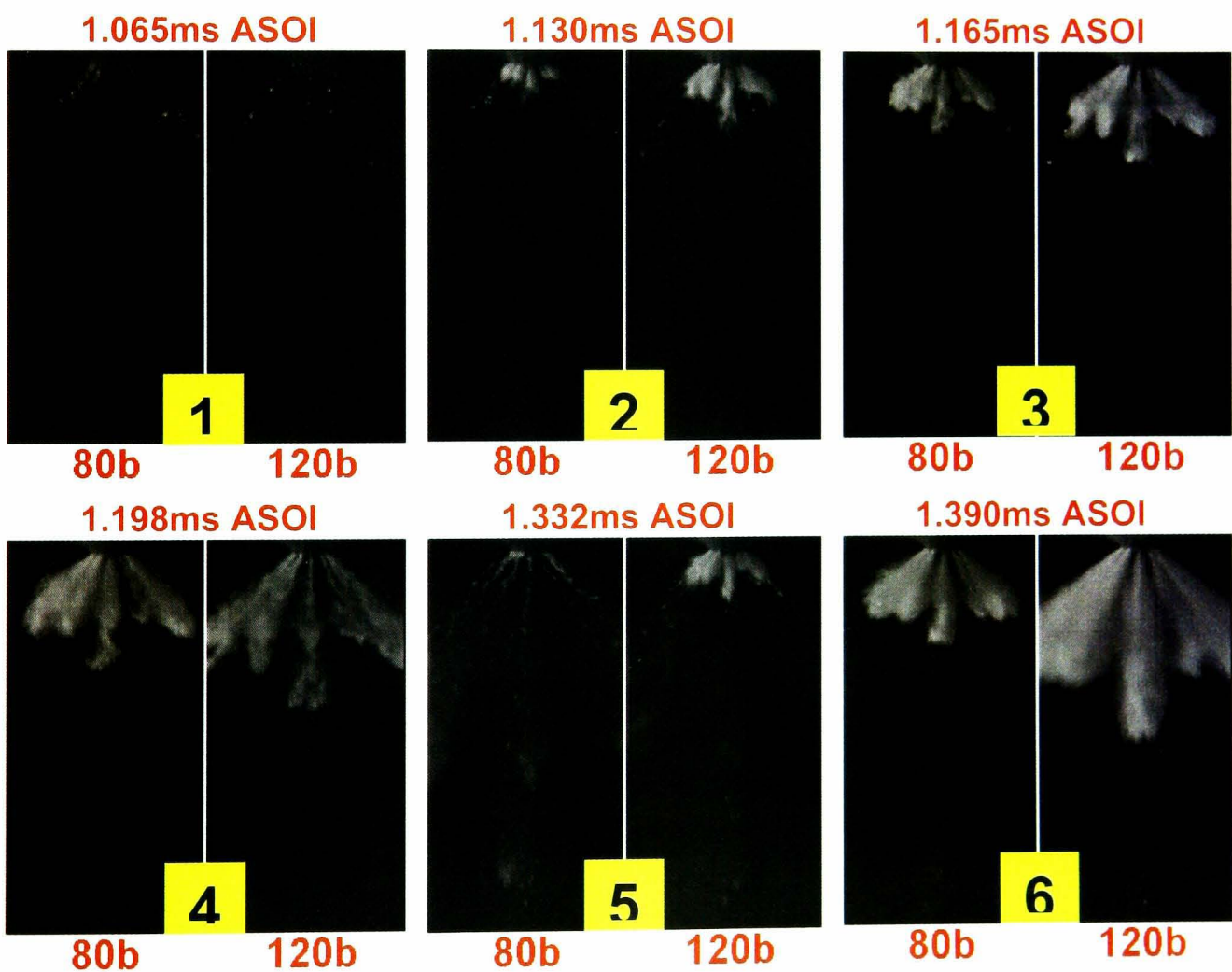


Figure 4.39: Definitions of injection duration and “Dwell time” in double injection.

Still spray imaging revealed that during both injection events spray behaviour is identical to the single injection spray propagation. The start of injection (SOI) for the first injection event is found to be 0.6ms, while for the second injection this time is highly dependent on the dwell time. More specifically, multi-hole injectors that are

coil-driven, feature a certain needle closing delay time, which has been identified to be around 0.3ms. In the unfortunate event where the dwell time is of the order of the closing delay time (0.3-0.5ms) the behaviour of the second injection changes dramatically. On the other hand, dwell times greater than 0.5ms secure normal development of the second injection event, as presented in previous paragraphs.

High-speed spray imaging recorded a pre-spray of very short duration that is chronologically located prior to the second injection event, when dwell times are in the 0.3-0.5ms time window. This behaviour is due to short dwell time settings that do not leave the required “relaxing” time for the needle and the driving coil to recharge. Furthermore, injection pressure significantly affects the start of second injection. A representative sequence of images is illustrated in Figure 4.40.



**Figure 4.40: Double injection with symmetric duration pulses of 1ms injection duration and 0.3ms dwell time. Time sequence of high-speed images acquired during the dwell time period.**

In the first image of the above sequence, the first injection event has just finished. Around 0.07ms later (image 2), while the dwell time is set to 0.3ms, pre-spray comes

out of the nozzle for almost another 0.17ms (second to fifth images). Fifth and sixth images illustrate the start of the second injection event. Apart from the pre-spray that is visible in the above time-sequenced images, the emergence of the second injection has occurred sooner (fifth image) in the case of 120bar injection pressure. This is believed to happen due to the fact that the required time has not been given to the needle to be kept closed, and as a result, the higher injection pressure contributes in a fast needle-opening event. This abnormality disappears when dwell times are greater than 0.5ms.

Finally, high-speed imaging proved to be a useful tool in multi-hole injectors spray characterisation, since it revealed an important effect of injection duration on injector behaviour. According to captured images, injection durations shorter than 0.9ms are highly dependent on injection pressure. More specifically, an injection duration setting of 0.7ms produces the expected spray pattern at 80bar injection pressure, but as injection pressure rises at values greater than 100bar, the resulted spray is significantly affected; due to the increased pressure applied on the needle, the latter requires more time to open at full lift.

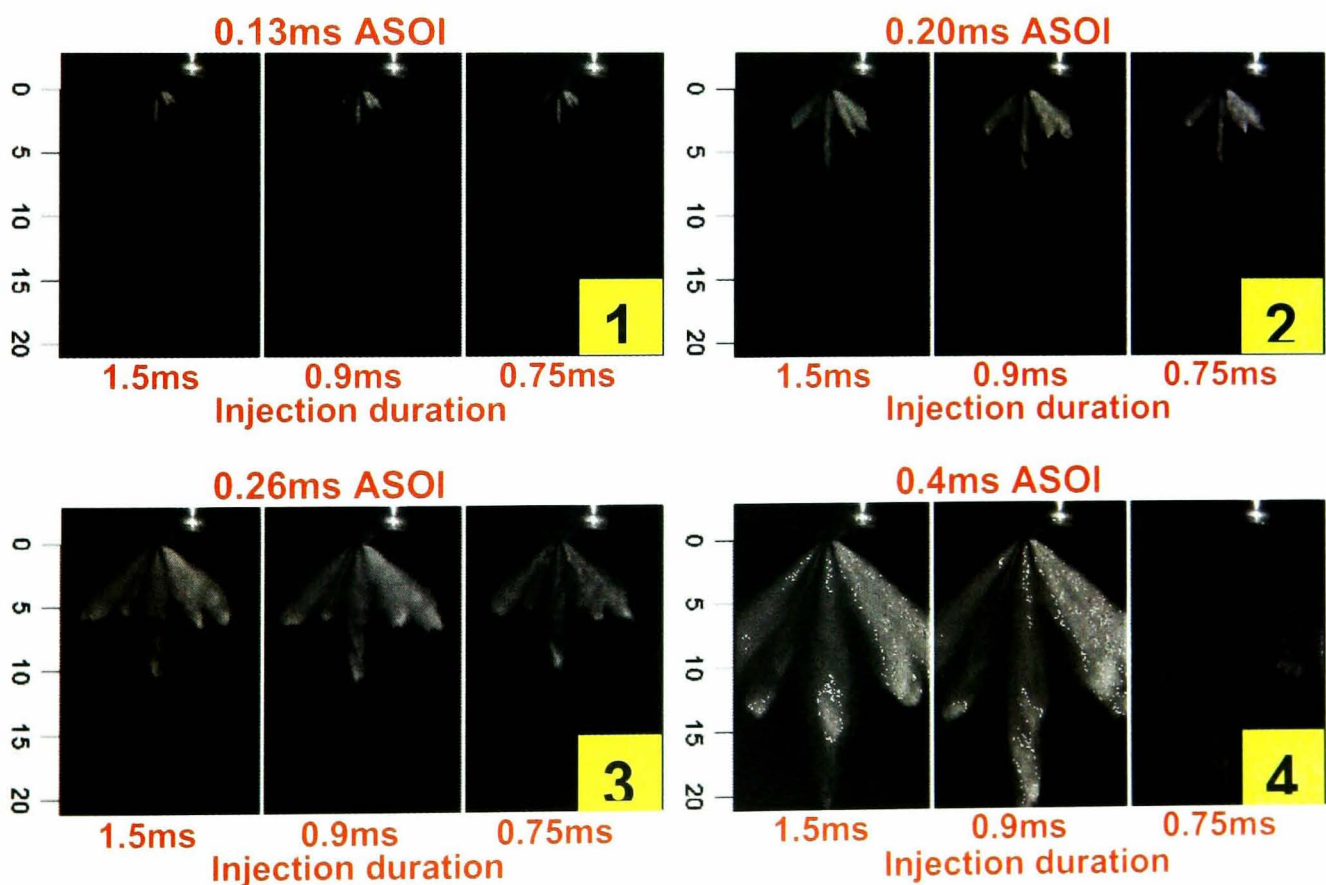


Figure 4.41: Time-dependent comparison of different injection durations at 120bar injection pressure.

Figure 4.41 illustrates a time-dependent comparison of three different injection durations at 120bar injection pressure. All the images share the same time-base and the difference in spray propagation is visible from the third image onwards. At this time, 0.26ms ASOI, in the case of 0.75ms injection duration (most-right frame in each image) the spray starts fading out and finally it disappears. This behaviour is the result of the needle not opening at full lift and closing before the designated time due to the short duration injection pulse coupled with the increased injection pressure of 120bar. Such behaviour is not visible at injection pressures lower than 120bar.

#### **4.5.2 Phase – Doppler anemometry**

Still and high-speed spray imaging is a useful tool widely used in the initial stages of a spray characterisation experiment. It provides global spray development details and important qualitative information on several parameters affecting a high-pressure fuel spray. Nevertheless, quantitative droplet information is essential in completing a spray characterisation investigation. Droplet velocity fields and size distribution information as well as their behaviour under various thermodynamic ambient chamber conditions would conclude whether multi-hole injectors are promising fuel injection equipment candidates.

Three of the multi-hole nozzle designs, described in previous chapters, have been tested thoroughly in a constant volume chamber. Droplet velocity and size distribution data have been acquired using a two-dimensional phase – Doppler anemometry system. Single injection experimental conditions for all tested nozzles are presented in Table 4-5 through Table 4-7 and double injection test cases for two of the nozzles in Table 4-8.

6 holes				
Injection Pressure $P_{inj.}$ [bar]	Chamber Pressure $P_{back}$ [bar]	Injection Duration $t_{inj.}$ [ms]	Ambient Temperature [°C]	Measurement Plane
120	1 / 12	1.5	~25	2, 10 and 30mm from the nozzle exit.
200	1 / 12	1.5	~25	

Table 4-5: Test conditions for the 6-hole symmetric nozzle.

6 holes – Asymmetric				
Injection Pressure $P_{inj.}$ [bar]	Chamber Pressure $P_{back}$ [bar]	Injection Duration $t_{inj.}$ [ms]	Ambient Temperature [°C]	Measurement Plane
80	1	1.5 / 2.5 / 3.5	~50	2.5 and 10mm from the nozzle exit.
120	1	1.5 / 2.5 / 3.5	~50	
80	1 / 3 / 6	0.7 / 1.5	~90	
120	1 / 3 / 6	0.7 / 1.5	~90	
80	1 / 3 / 6	0.7 / 1.5	~115	
120	1	1.5	~115	

Table 4-6: Test conditions for the 6-hole – Asymmetric nozzle.

10(12-2) + 1 central holes				
Injection Pressure $P_{inj.}$ [bar]	Chamber Pressure $P_{back}$ [bar]	Injection Duration $t_{inj.}$ [ms]	Ambient Temperature [°C]	Measurement Plane
80	1	1.5 / 2.5 / 3.5	~50	2.5 and 10mm from the nozzle exit – side jet.
120	1	1.5 / 2.5 / 3.5	~50	
80	1 / 3 / 6	1.5	~90	
120	1 / 3 / 6	1.5	~90	
80	1 / 3	1.5	~90	2.5 and 10mm from the nozzle exit – central jet.
120	1 / 3	1.5	~90	

Table 4-7: Test conditions for the 12-hole symmetric nozzle.

6 holes – Asymmetric				
Injection Pressure $P_{inj.}$ [bar]	Chamber Pressure $P_{back}$ [bar]	Injection Duration $t_1-t_{dwell}-t_2$ [ms]	Ambient Temp. [°C]	Measurement Plane
80	1	1-0.3-1	~50	2.5 and 10mm from the nozzle exit – side jet.
80	1	1-0.5-1	~50	
80	1	1-1-1	~50	
80	1	1-1-0.7	~50	
120	1	1-0.5-1	~50	
120	1	1-1-1	~50	
80	1 / 3 / 6	1-0.3-1	~90	2.5 and 10mm from the nozzle exit – side jet.
80	1 / 3 / 6	1-0.5-1	~90	
80	1 / 3 / 6	1-1-1	~90	
120	1 / 3 / 6	1-1-1	~90	
80	1	1-0.3-1	~115	2.5 and 10mm from the nozzle exit – side jet.
80	1	1-0.5-1	~115	
80	1	1-1-1	~115	
120	1	1-1-1	~115	
10(12-2) + 1 central holes				
Injection Pressure $P_{inj.}$ [bar]	Chamber Pressure $P_{back}$ [bar]	Injection Duration $t_1-t_{dwell}-t_2$ [ms]	Ambient Temp. [°C]	Measurement Plane
80	1	1-0.5-1	~50	2.5 and 10mm from the nozzle exit – side jet.
80	1	1-0.7-1	~50	
80	1	1-1-1	~50	
80	1	2-1-2	~50	
120	1	1-0.5-1	~50	
120	1	1-1-1	~50	

Table 4-8: Double injection test cases for the 6-hole – Asymmetric and the 12-hole symmetric nozzles.

Figure 4.42 illustrates the measurements grid for all PDA experiments and the definition of the resultant velocity vector. The selection of measurement planes was based on the primary and secondary droplet break-up lengths, which are believed to be less than 2.5mm and 10mm respectively. In addition to that, simultaneous acquisition of radial and axial velocity vectors of a single droplet, allowed the accurate calculation of the resultant velocity vector, including its direction angle  $\theta$  that is linked to the overall spray cone angle.

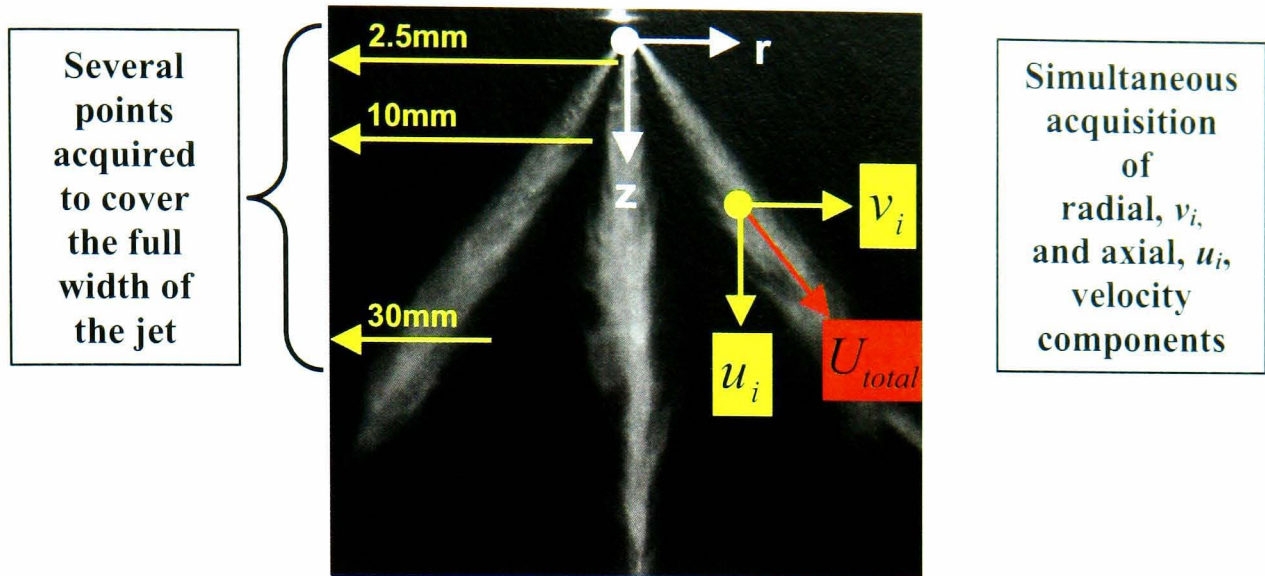
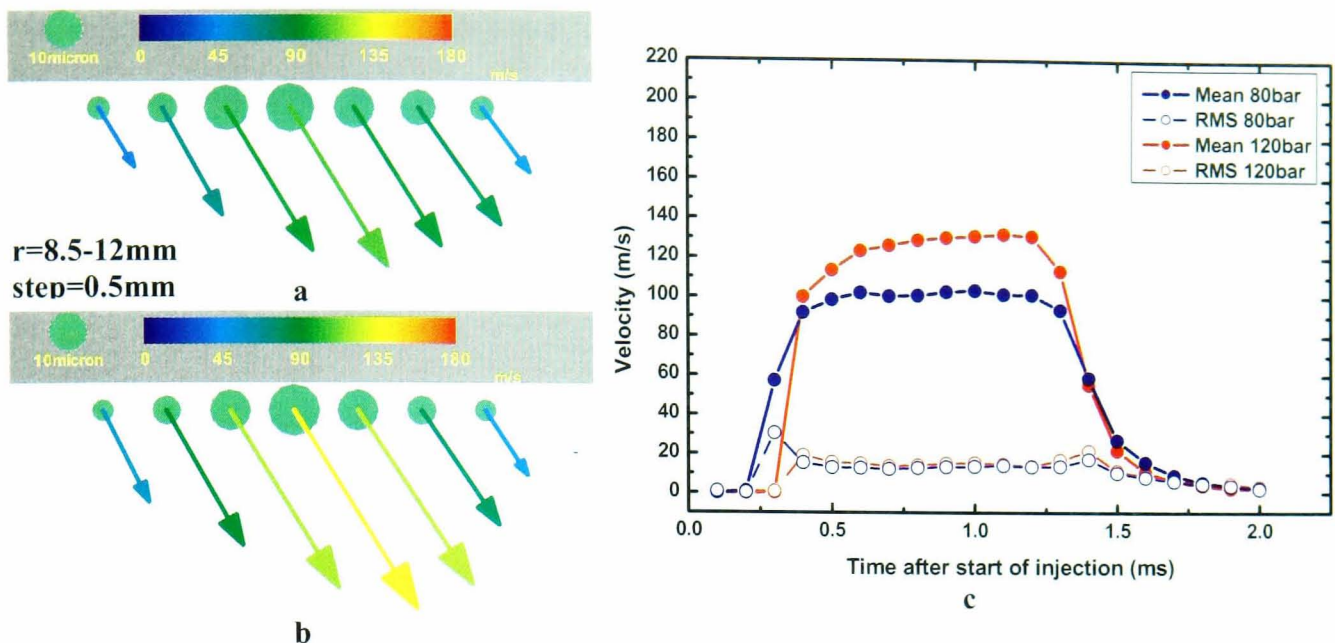


Figure 4.42: PDA measurements grid and resultant velocity vector definition.

### Droplet velocity profiles

Temporal and spatial velocity profiles are presented in this section, quantifying effects of injector operational parameters on droplet velocities. Temporal profiles present the variation in droplet velocities throughout the injection process at one measuring point that is located at the centre of the jet. Spatial velocity profiles present all measuring points located at a cross-section of the jet at certain time after start of injection that is representative of the main injection process. The effect of injection pressure in 12- and 6-hole nozzles is illustrated in Figure 4.43 and Figure 4.44. The temporal variation of velocity profiles illustrated describe fully the injection process, with velocities increasing sharply during the needle opening period, they remain at their maximum value during the main injection event before velocities drop sharply to zero following the needle closing event. As expected, increasing injection pressure causes droplet velocities to rise. More specifically, an increase of 40bar (80-120bar) results in 30m/s (~100-~130m/s) velocity rise at 10mm distance from the nozzle exit, while in the 6-hole nozzle, increasing injection pressure by 80bar (120-200bar) causes droplet velocities to increase by almost 60m/s (~120-180m/s).



**Figure 4.43:** Effect of injection pressure on droplet velocities at 10mm from the nozzle exit for the 10(12-2) + 1 central holes nozzle. Spatial representation at 0.9ms ASOI of (a). 80b and (b). 120b. (c). Temporal velocity profiles for 1.5ms injection duration at 1bar chamber pressure at the centre point of the jet ( $r=10\text{mm}$ ).

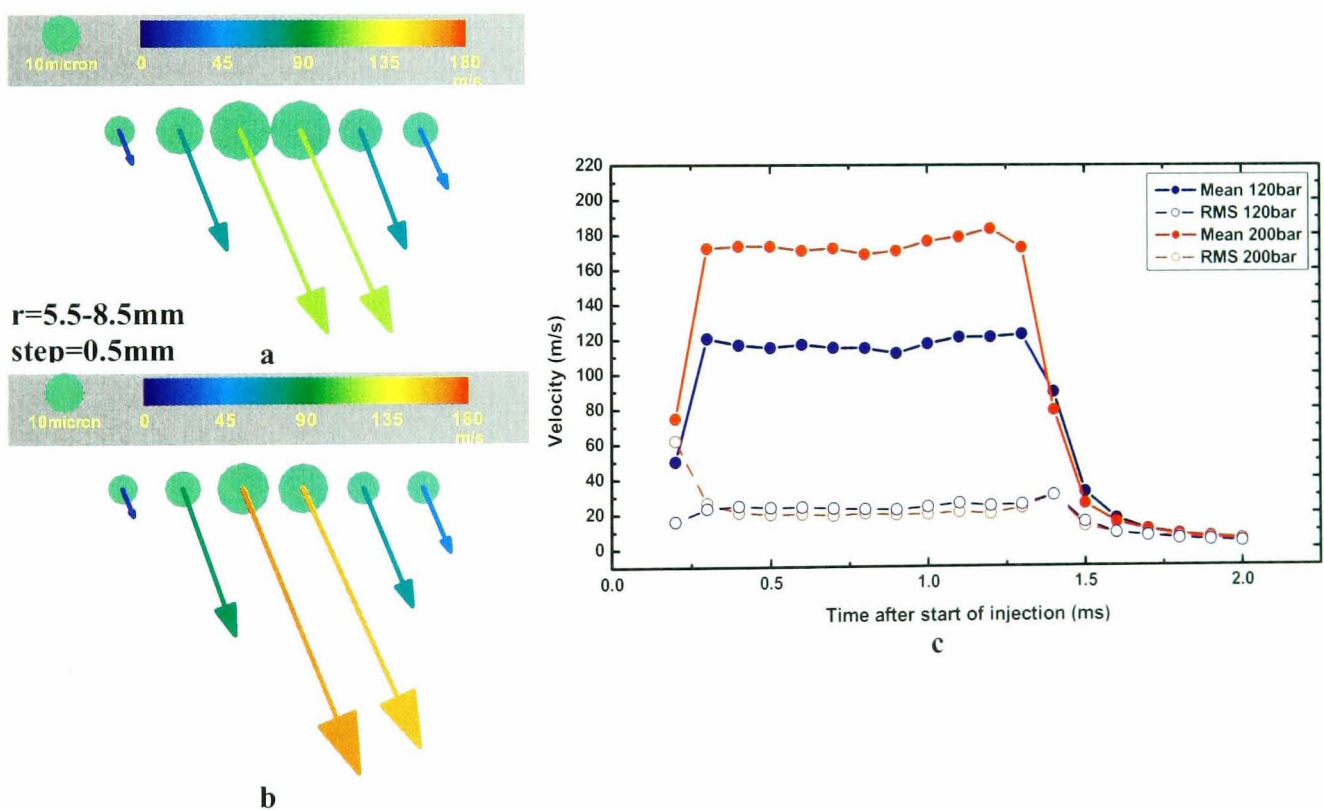


**Figure 4.44:** Effect of injection pressure on droplet velocities at 10mm from nozzle exit for the 6-hole symmetric nozzle. Spatial representation at 0.9ms ASOI of (a). 120b and (b). 200b. (c). Temporal velocity profiles for 1.5ms injection duration at 1bar chamber pressure at the centre point of the jet ( $r=7\text{mm}$ ).

The spatial velocity distributions of Figure 4.43 and Figure 4.44 present absolute droplet velocities vectors coloured according to the magnitude colour bar. The results show a jet-like profile with peak velocity values at the centre of the jet. The effect of

injection pressure is clearly evident with higher velocities at higher injection pressure, as aforementioned. An interesting observation is related to the trajectory of all droplets across the jet, which is of similar angle and in accordance to the overall spray cone angle values extracted from spray visualisation images.

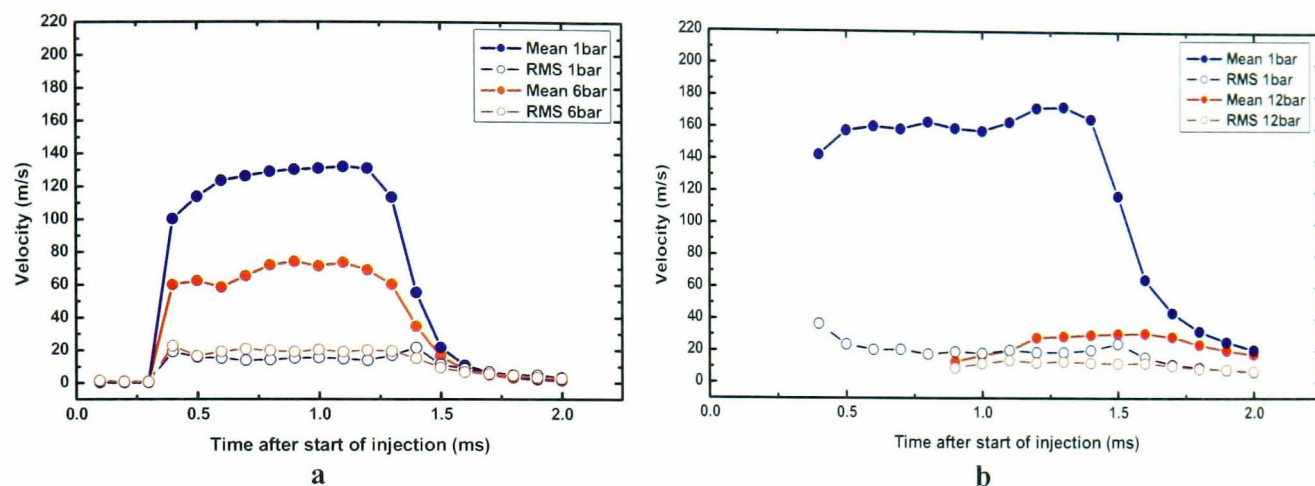


**Figure 4.45: Effect of chamber pressure: (a). 10 (12-2) + 1 central holes nozzle at 10mm from nozzle exit at 80bar injection pressure and (b). 6-hole symmetric nozzle at 30mm from nozzle exit at 200bar injection pressure at the centre points of the jets ( $r_a=10$  and  $r_b=7$ mm).**

The effect of chamber pressure on droplet velocities, illustrated in Figure 4.45, evidently leads to substantially reduced mean velocities at 6, as well as, 12bar chamber pressures. In the case of 6bar chamber pressure (Figure 4.45a) the reduction in the resultant velocities is up to 50% during the main part of the spray. Furthermore, at Figure 4.45b, where chamber pressure is increased from 1 to 12bar for a 6-hole nozzle, the reduction in droplet velocities is up to fourfold at 30mm distance from the nozzle exit. However, the droplet mean and RMS velocity values tend to be similar at all illustrated chamber pressures in the tail of the spray. It is also evident that the droplet arrival time at  $z=30$ mm has been delayed by 0.5ms at the 12bar chamber pressure case (Figure 4.45b), which matches with the reduction in spray tip penetration length estimated from the CCD images. The angle between a single jet and the injector's axis, as calculated from the mean axial and radial velocities, is found to be  $86 \pm 2^\circ$  for the 12-hole and  $80 \pm 2^\circ$  for the 6-hole nozzles. This overall spray cone angle remains constant for all tested chamber pressures, demonstrating its independence from chamber pressure variations, in agreement with the spray visualisation results. It is useful to stress the importance of spray angle stability in spray-guided systems where successful ignition depends on precise delivery of the spray edge recirculation onto the spark plug gap at the time of ignition.

In real engine operating conditions, a single high-pressure injector is responsible for delivering stoichiometric or lean air/fuel mixture according to engines load requirements. More specifically, the injector is asked to operate at long injection durations to achieve stoichiometric mixtures, as well as short duration in order to inject the minimum quantity of fuel required. This variation in injection durations should not affect the performance of the high-pressure injector in spray shape stability and atomisation quality. Experimental results from injection durations of 0.7 to 3.5ms showed that spray characteristics of multi-hole injectors remain unchanged as injection duration increases. On the other hand, the needle driving mechanism limits the minimum feasible injection duration to the lowest value of 0.9ms.

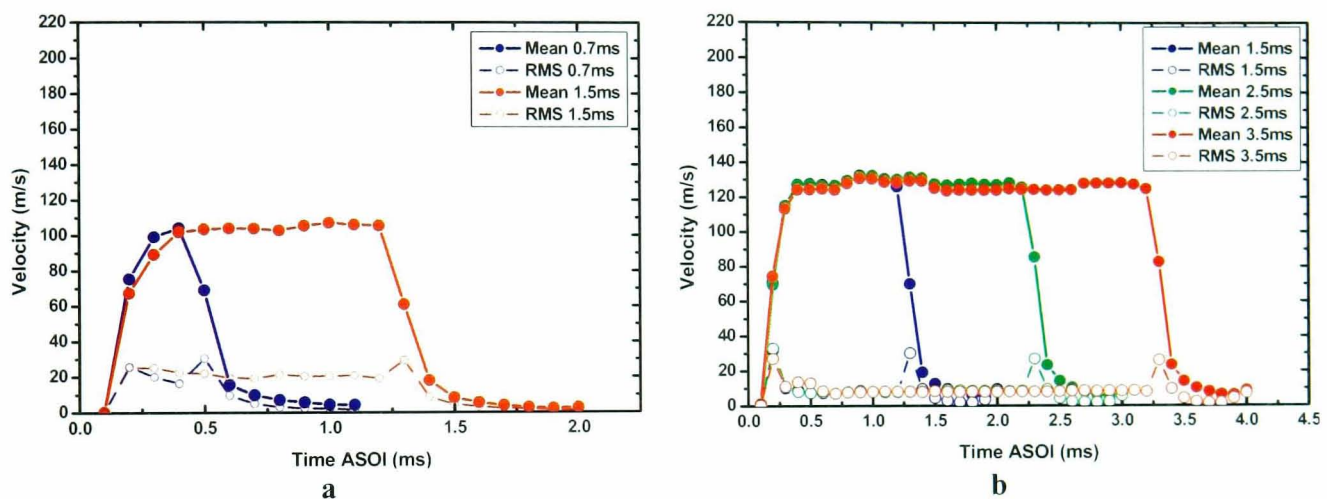


**Figure 4.46: Effect of injection duration at 80bar injection pressure and 1bar chamber pressure in (a). 6-hole asymmetric and (b). 10 (12-2) + 1 central holes nozzles.**

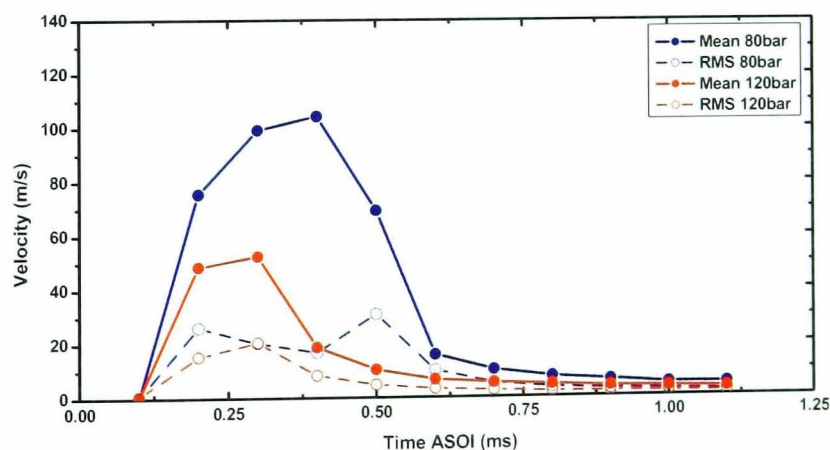


**Figure 4.47: Effect of injection pressure on the minimum injection duration of 0.7ms**

Figure 4.46a illustrates the mean and RMS velocity values of 0.7 and 1.5ms injection durations at 80bar injection pressure. It is evident that 0.7ms should be the shortest possible duration, since by the time droplet velocities have reached their maximum values injection finishes. This is not the case for 120bar injection pressure though, where higher injection pressure limits the needle acceleration during the opening

event. As a result, the needle does not open fully before it is asked to close again and spray repeatability is not acceptable (Figure 4.47). On the other hand, right-hand side of Figure 4.46 illustrates multi-hole injector performance at durations higher than 1.5ms. As expected, there is not a significant effect on droplet velocities and the measured RMS values indicate that spray stability is not an issue at long injection durations.

Ambient chamber temperature is expected to have minor effects on droplet velocities due to enhanced vaporisation of the spray at temperatures higher than 50°C. More specifically, droplets located at the outer spray perimeter are more likely to reduce their mass, due to smaller sizes and lower velocities that increase the travel time inside the high-temperature environment. Any possible momentum losses will occur in a distance further than 10mm from the nozzle exit, which is the main measuring location of the PDA experiments, because the time for evaporation is then sufficiently provided.

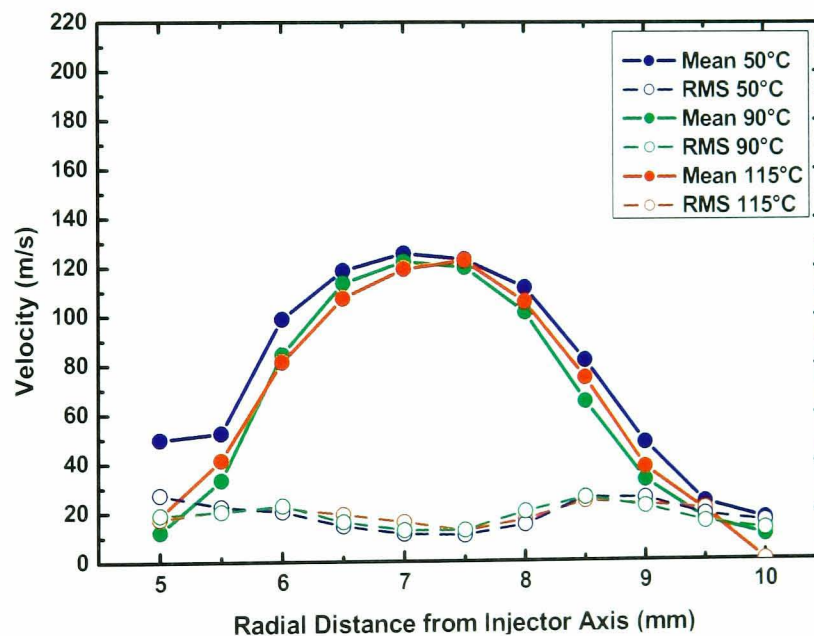


**Figure 4.48:** Effect of ambient chamber temperature on droplet velocities for a 6-hole asymmetric nozzle at 80bar injection pressure at 10mm from the nozzle exit.

As illustrated in Figure 4.48, the temperature effect on spray droplet velocities is minor as the presented velocity profiles for all measured ambient temperatures are highly uniform.

Following the analysis of the majority of possible thermodynamic conditions and injector operating parameters that characterise the operating environment of a high-

pressure injector, the performance of multi-hole injectors in double-injection conditions will indicate whether second generation injectors are promising fuel injection equipment candidates. As presented in previous sections of this chapter (section 4.5.1) double injection in multi-hole injectors is highly dependent on the minimum feasible dwell time imposed by the needle driving mechanism. Initially, an example of triggering and needle response time for double injection is illustrated in Figure 4.49.

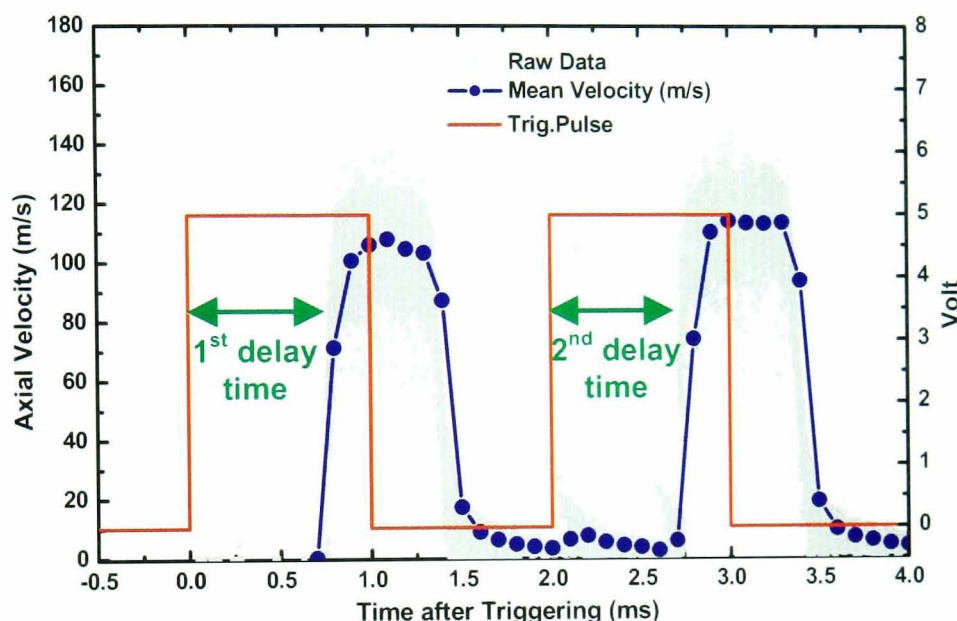


**Figure 4.49:** Double injection triggering and needle response time.

The important characteristic of the above graph is pointed out with the green coloured arrows. The delay time for the needle-opening event in the first injection is somewhat longer than the equivalent time for the second injection event. The difference is not clearly visible in the above graph, however it is of the order of 0.1ms. The importance of a shorter needle opening delay time between the two injections is insignificant, although the possible resulting longer injection duration of the second injection event is highly significant. The fast needle opening in the second injection causes the latter to have slightly longer duration compared to the first one even at fully symmetrical triggering pulses. In addition to that, the fast pick-up in velocities, initiated by the increased needle response, imposes a relative alteration on injected fuel quantity compared to the first injection event.

In general, double injection does not present any significant changes in droplet velocities compared to single injection. Figure 4.50 illustrates the effect of injection pressure at a distance of 2.5mm from the nozzle exit, where the expected increased

droplet velocities are clearly visible. Furthermore, the effect of dwell time, previously presented in section 4.5.1, has been quantified. According to data presented in Figure 4.51, short dwell times of 0.3-0.5ms produce a non-negligible spray, prior to the second injection event, with velocities varying from 60 to 80m/s, while dwell times of 1ms do not produce a pre-spray. It is also evident that for all cases presented here, RMS and mean droplet velocity profiles of the first and second injection are quite similar.

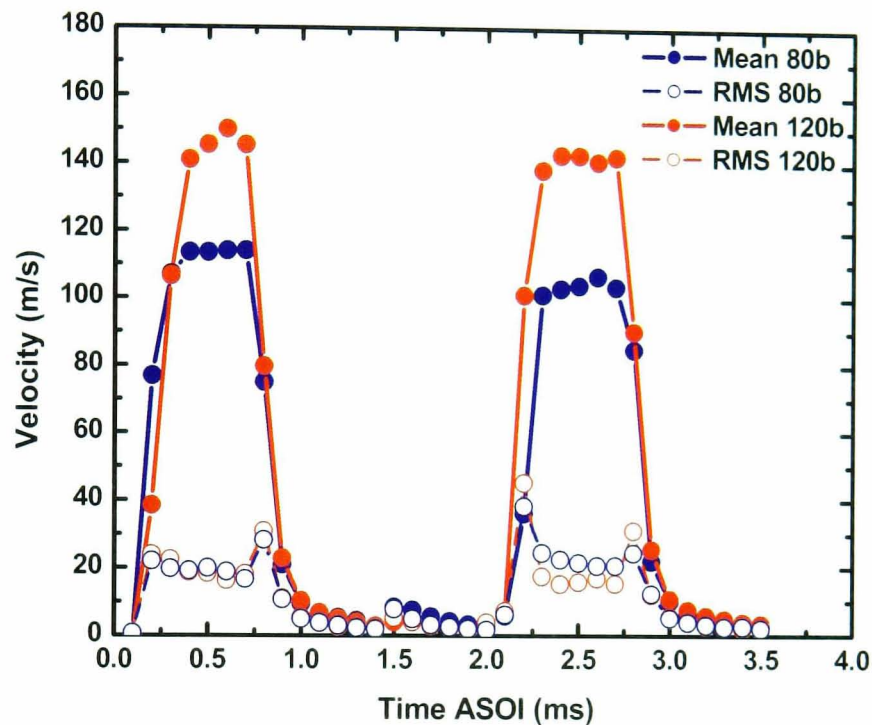


Figure 4.50: Effect of injection pressure on double injection for a 6-hole asymmetric nozzle injecting at 1bar chamber pressure; values measured at 2.5mm from the nozzle exit.

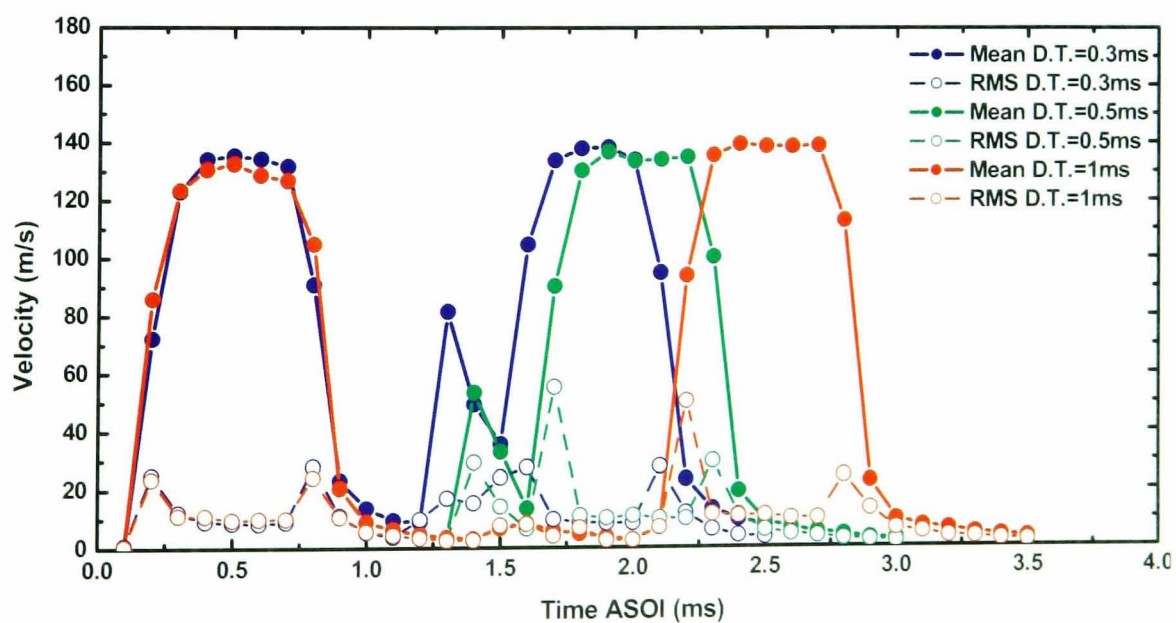
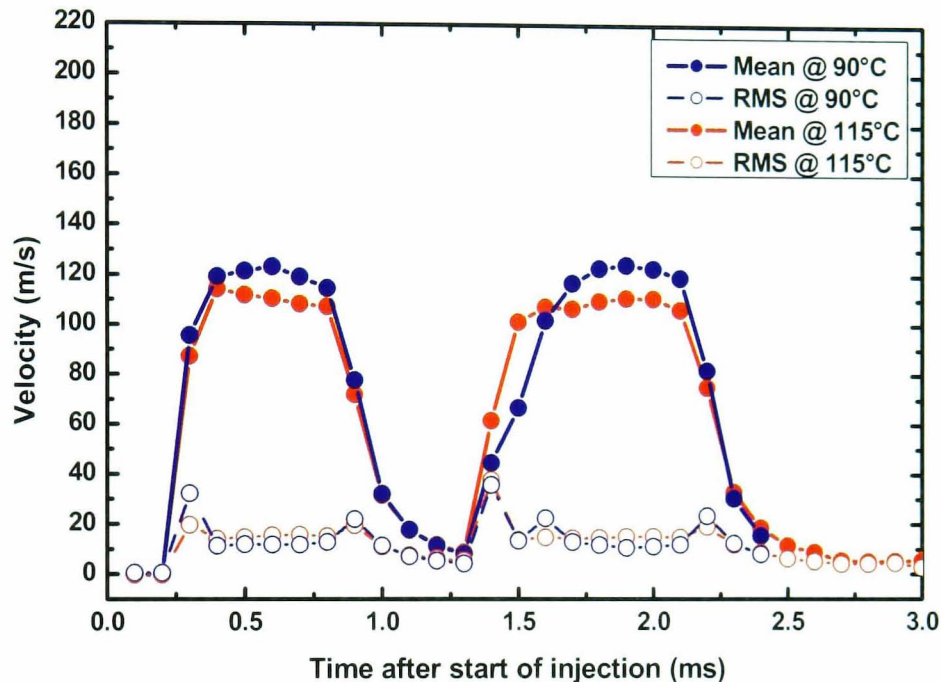


Figure 4.51: Effect of dwell time on double injection for a 6-hole asymmetric nozzle. Values measured at 2.5mm from the nozzle exit at 80bar injection pressure.

At 2.5mm from the nozzle exit this pre-spray is non-negligible and alters the velocity fields significantly. However, further downstream, at 10mm from the nozzle exit, this pre-spray is totally disappeared. Of course it has not vaporised, but higher velocity droplets from the second injection event catch up the slower moving pre-spray droplets and mix together, causing a less steeper velocity pick-up for the second injection and therefore broadening the velocity profile. This effect is clearly visible in Figure 4.52, where velocities measured at 10mm from the nozzle exit are presented.



**Figure 4.52: Double injection droplet velocities from a 6-hole nozzle at 80bar injection pressure and at 10mm from nozzle exit**

In addition to that the above figure also demonstrates the rather insignificant effect of ambient chamber temperature on double injection spray velocity fields. The slightly lower velocities, in the case of 115°C compared to 90°C, are possibly observed due to the increased vaporisation rates imposed by high temperatures that reduce the droplet mass, thus reducing droplet momentum.

Finally, a direct comparison between the 6- and the 12-hole nozzles clarifies important details on multi-hole injectors operating principles. There are two basic differences between the two investigated nozzles: the hole length over diameter ratio ( $L/D$ ) of the 10(12-2) + 1 central holes injector is larger, compared to the 6-hole asymmetric nozzle, and secondly, the latter features six holes asymmetrically positioned in the sac volume that is effectively translated into six non-identical jets. The lack of an axis of symmetry, in terms of spray shape, causes certain disruptions in internal nozzle flow that directly affect the emerging jets. More specifically, the angle

between the injector's axis and each jet is not constant and it could vary significantly, that variation in angle could be greater than  $2^\circ$ , a value measured for the 12-hole symmetric nozzle. In addition to that, individual jet shapes differ considerably and the lack of an axis of symmetry for each jet is due to the non-symmetric internal nozzle flow. The aforementioned divergence in a jet's angle is illustrated in Figure 4.53.

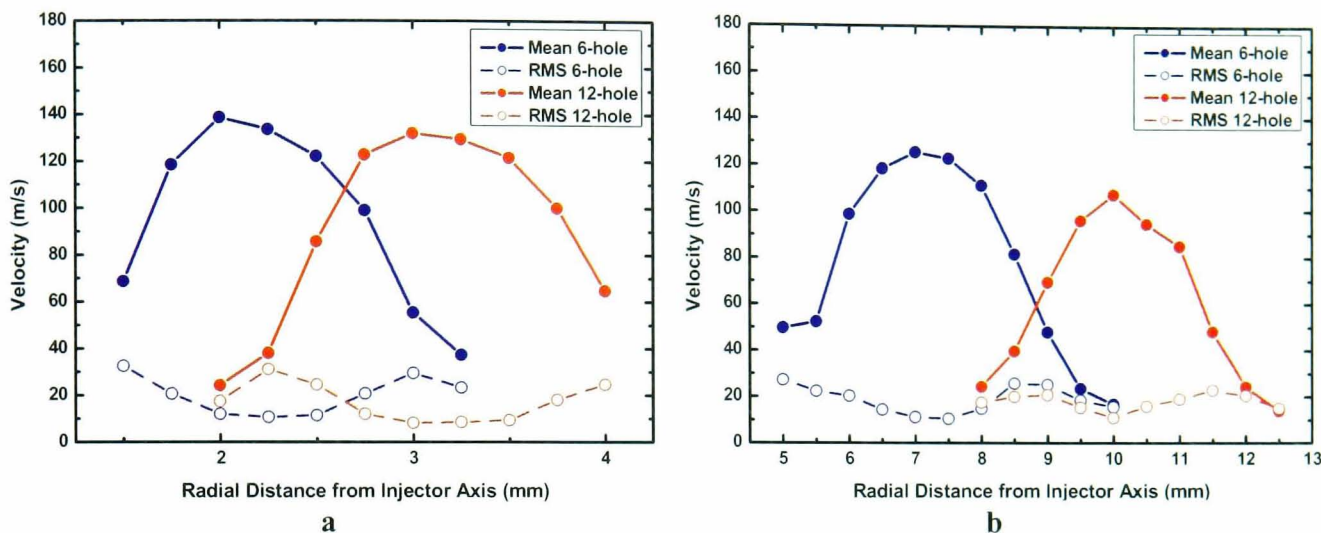


**Figure 4.53: Effect of L/D ratio on droplet velocities for 80bar injection pressure, 1bar chamber pressure at (a). 2.5mm and (b). 10mm from the nozzle exit.**

Velocity fields measured at 10mm from the nozzle exit, as presented in Figure 4.53b, present a slight reduction for the 12-hole nozzle compared to the 6-hole one. This differentiation in droplet velocities, at a distance greater than 2mm from the nozzle exit, is believed to have its cause in smaller droplet sizes produced by the 12-hole nozzle. Better atomisation quality of the latter nozzle results in small droplets that lose their momentum quicker than slightly larger droplets, which are generated by a smaller L/D ratio nozzle. Detailed analysis of the aforementioned effect can be found in the next paragraph, where droplet size distributions are presented.

### Droplet size distribution

Following the observation previously mentioned concerning the size distribution of 6- and 12-hole nozzles, the relative droplet size data are illustrated in Figure 4.54. From the two graphs presented for two distances from the nozzle exit, the Sauter mean diameter (SMD) values of the 6-hole injector are always larger than the 12-hole one. The same trend is gradually reflected on the mean diameter (AMD) values as the distance from the nozzle increases. Based on this fact, it is evident that droplets generated by large L/D ratio nozzles, are more likely to lose their momentum as they are exposed to ambient chamber conditions. Small SMD values denote the existence of small volume droplets that feature increased external area, a combination that

enhances droplet evaporation.

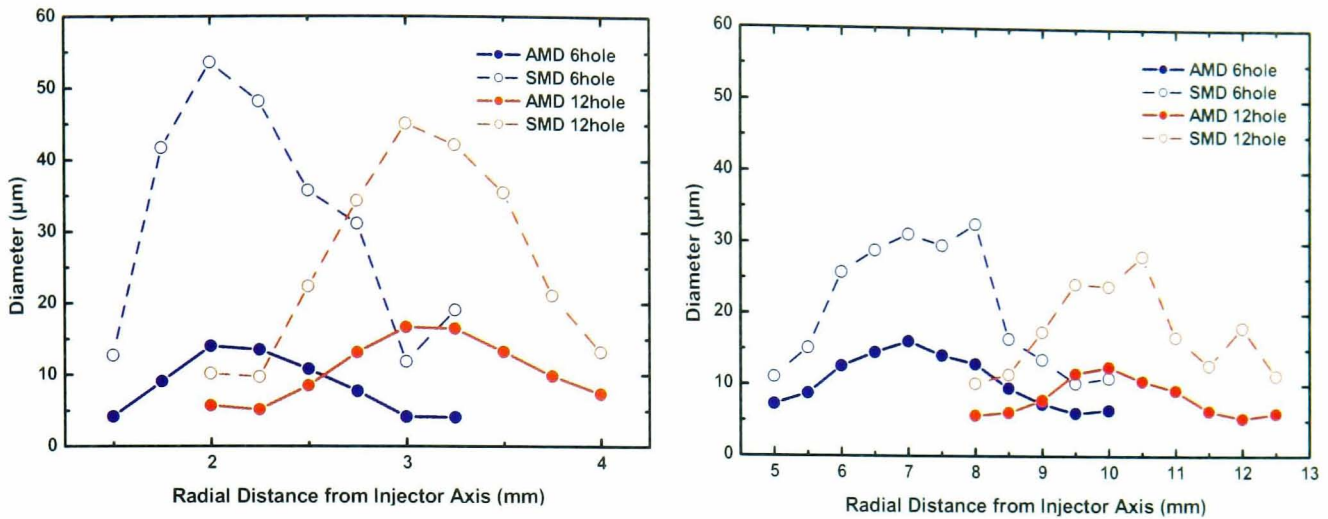


**Figure 4.54:** Effect of L/D ratio on droplet size distribution for 80bar injection and 1bar chamber pressures at 0.9ms ASOI at (a). 2.5mm and (b). 10mm from the nozzle exit.

Increased chamber ambient temperature also enhances droplet evaporation. After a single droplet has travelled for a short time in high-temperature environment, its diameter is drastically reduced. The effect of ambient temperature on droplet size distribution is illustrated in Figure 4.55.

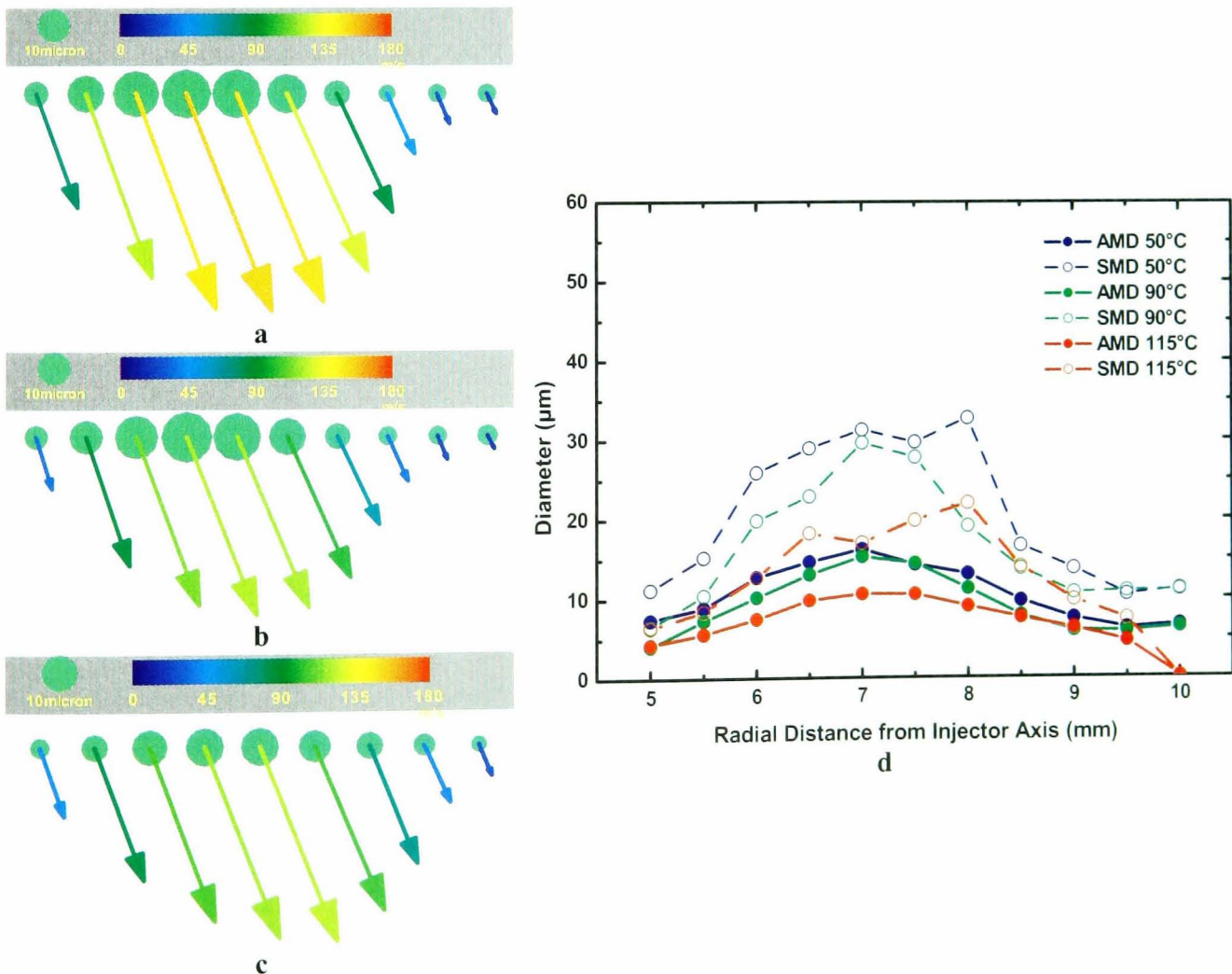


**Figure 4.55:** Spatial representation of ambient chamber temperature effect on droplet size distribution for a 6-hole asymmetric injector at 10mm from the nozzle exit at 0.9ms ASOI. (a). 50°C, (b). 90°C, (c). 115°C and (d). AMD and SMD values.

Increasing temperature from 50 to 90°C does not seem to have a significant effect on droplet sizes. Further increase though, causes a reduction of up to 5µm in AMD and 10µm in SMD values, in the core of the jet, which correspond to a reduction of 38% and 33%, respectively. A significant observation that is linked to the previously mentioned fact of reduced droplet momentum is also verified according to Figure 4.55a, b and c. From 50°C to 115°C and while droplet size decreases, droplet velocities seem to follow the same trend and their mean values are also decreased.

In direct injection gasoline engines, increased chamber temperature is often coupled with elevated chamber pressures. Engine stratified operation is achieved by late injection of fuel during the compression stroke, where the in-cylinder pressure could vary from 3 to 15bar, for naturally aspirated engines and 5-20bar for turbo-charged engines. In general, elevated chamber pressures cause the droplets to slow down, a more compact-sized spray is created and large droplet diameters are possibly formed due to droplet coalescence. The results of the aforementioned mechanism are visible at distances greater than 10mm from the nozzle exit. Figure 4.56 presents size distribution for a 6-hole symmetric spray injected at 200bar at 30mm from the nozzle exit. The difference in droplet sizes, between atmospheric and 12bar chamber pressures, is clearly visible.

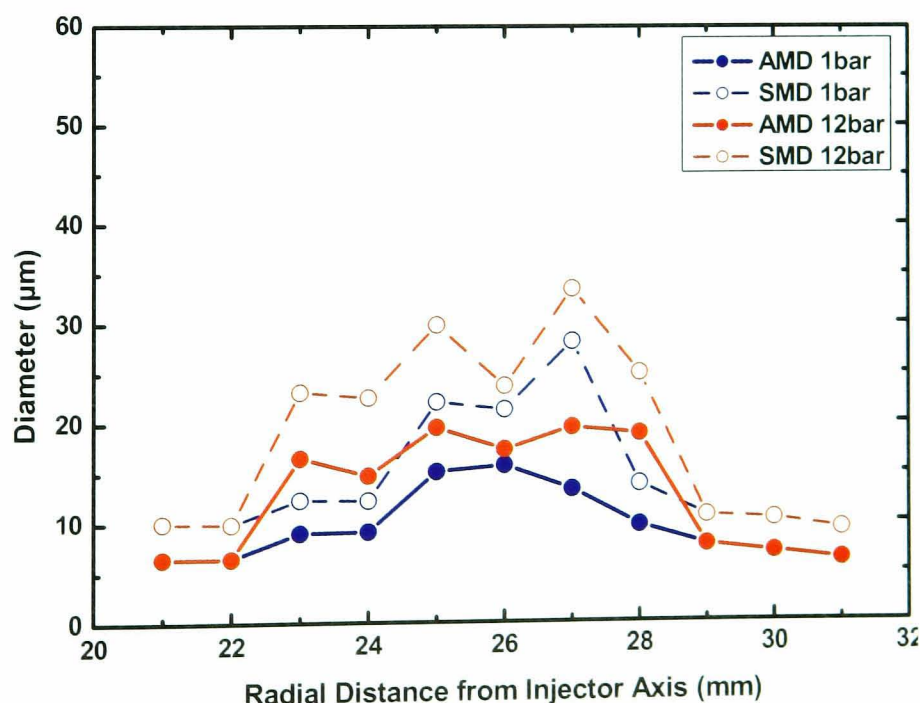


**Figure 4.56:** Effect of chamber pressure for a 6-hole injector at 30mm from the nozzle exit injecting at 200bar.

Droplet sizing measurements are always referred to the complete injection event and neither spatial representation at certain time steps nor temporal variation graphs at a single point could secure a satisfactory description of the effect. An example is illustrated in Figure 4.57, where at 10mm from the nozzle exit of a 12-hole injector there are not any significant changes in droplet size distribution. Therefore, a better representation of the phenomenon is achieved, when the comparison is based on the number of droplets that crossed the measuring plane during the injection event, excluding only the tail of the spray. More specifically, a comparison of the normalised probability density function graph leads in more accurate conclusions. In Figure 4.57b, the difference in droplet diameter between 1 and 6bar chamber pressures is found to be almost 55%. The spatial profile presented in the left-hand side of the same figure does not direct the reader to the same conclusion.

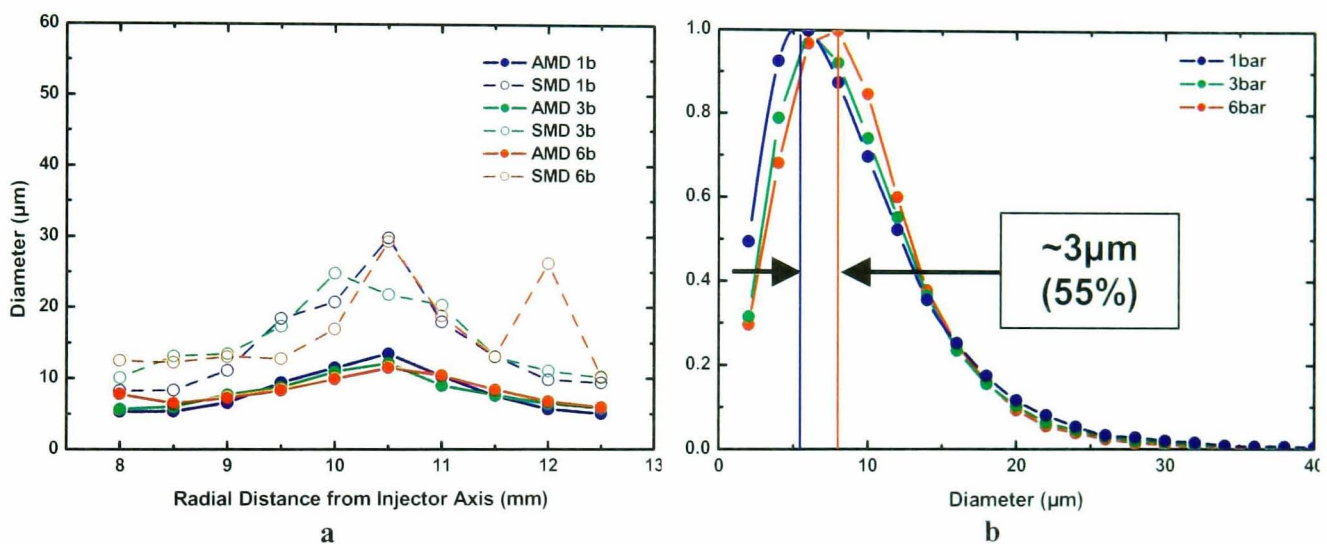


**Figure 4.57: Effect of chamber pressure for a 10 (12-2) + 1 central holes injector at 10mm from the nozzle exit at 80bar injection pressure. (a). Spatial profile and (b). Normalised size distribution graph for the entire injection duration and the total jet cross-section.**

Temporal sizing profiles could lead to similar misjudgement of the effect of injection duration on droplet sizes. Increased injection duration from 1.5 to 3.5ms does not affect the velocity profiles, however a slight increase in the AMD of the total number of droplets that crossed the measurement plane during the complete injection event is observed. According to Figure 4.58, the confusion that is caused by the spatial sizing profile in terms of accurate estimation of the difference in droplet diameters is totally cleared when analysing the normalised size distribution graph for the entire injection duration. Increased droplet diameters are a particular characteristic of long injection durations for multi-hole injectors. The injected fuel quantity in 3.5ms is relatively

large compared to 1.5ms duration, and atomisation mechanisms of the multi-hole nozzle are slightly disturbed. More specifically, air-entrainment in a multi-hole spray is highly dependent on the transient nature of the spray itself. The disturbances that the tip and the tail of the spray introduce to the chamber's bulk flow enhance air-entrainment. In addition to that, droplets injected at later times may coalesce with those injected earlier due to the increased drag that the earlier injected droplets sense. Therefore, more time is available for possible droplet coalescence to take place when injection duration is long and droplet sizes rise significantly.

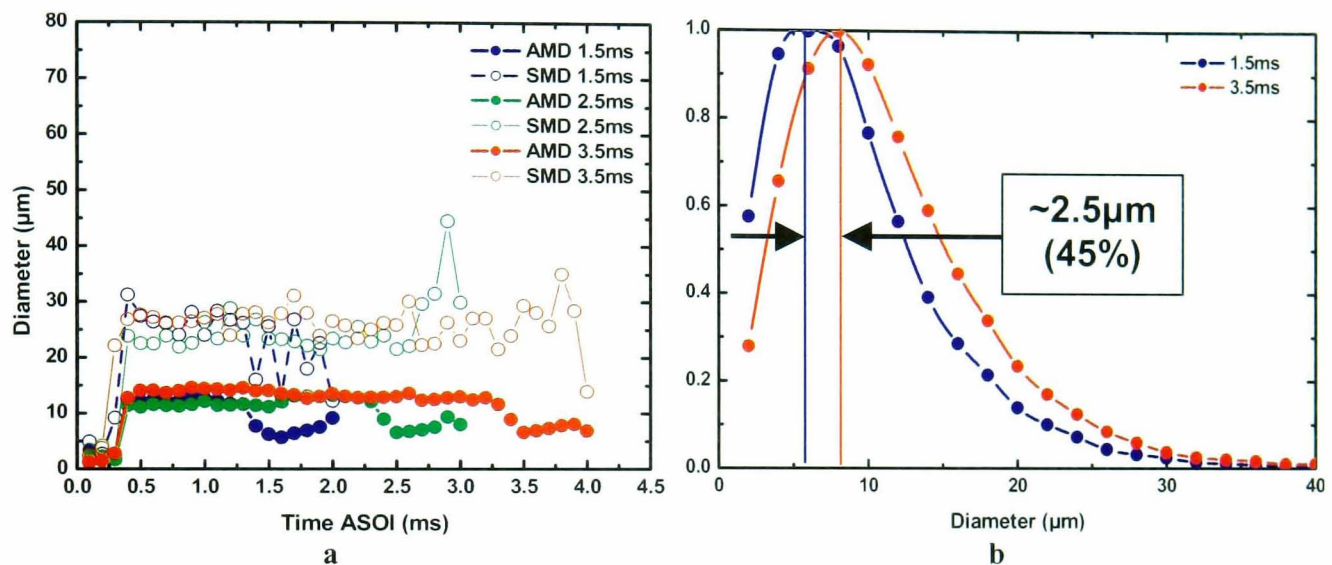


**Figure 4.58: Effect of injection duration for a 10(12-2) + 1 central holes injector at 10mm from the nozzle exit at 80bar injection pressure. (a). Spatial sizing profile and (b). Normalised size distribution graph for the entire injection duration and the total jet cross-section.**

Multi-hole injectors operate over a wide range of injection pressures, and the final selection is usually based on the desired atomisation quality. Normal injection pressures for the first generation of multi-hole injectors are 80-120bar. A later released injector that features six holes could also operate at pressures higher than 120bar; however there is a maximum injection pressure of 200bar that should not be exceeded. We know, however, that multi-hole injectors tested in F1 engines have reached 500bar (but with a different pump!). Extended investigations of the effect of injection pressure on droplet size distribution have not entirely confirmed the myth that the higher the injection pressure the better the atomisation quality. More specifically, in a 10 (12-2) + 1 central holes injector an increase of injection pressure from 80 to 120bar does not seem to improve atomisation. As illustrated in Figure 4.59, at two distances from the nozzle exit (2.5 and 10mm) 80 and 120bar injection pressures effectively produce droplets of similar size.

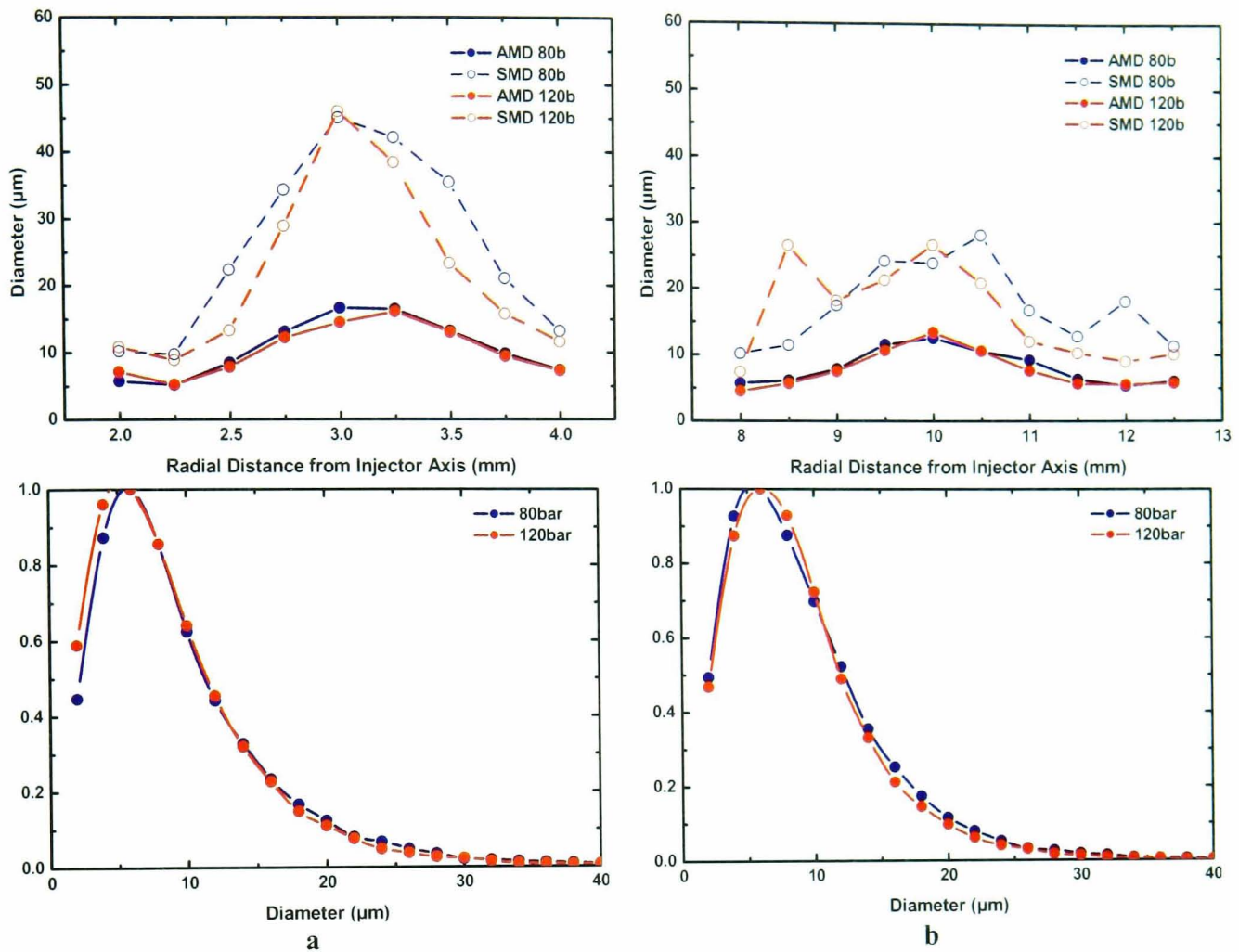


**Figure 4.59:** Effect of injection pressure for a 10 (12-2) + 1 central holes injector at atmospheric chamber pressure. *Top row:* Spatial sizing profiles at 0.9ms ASOI at (a). 2.5mm and (b). 10mm from the nozzle exit. *Bottom row:* Normalised size distribution graphs for the entire injection duration and the total jet cross-section at (a) 2.5mm and (b) 10mm from the nozzle exit.

A further increase in injection pressure marginally affects droplet size distribution. In the case of a six-hole nozzle, atomisation improvements caused by an 80bar (120-200bar) increase in injection pressure are rather small and disproportional to the extra amount of energy spent by the high-pressure pump to pressurise fuel to such high levels. More specifically, as illustrated in Figure 4.60, for a 65% increase in injection pressure (120-200bar) a maximum of 25% ( $\sim 2\mu\text{m}$ ) is gained in AMD values. The same trend is also visible in the spatial droplet size profile at 10mm from the nozzle exit, where, although AMD values for 200bar injection pressure appear lower than 120bar, such a minor gain in droplet sizes does not justify the energy cost for increased injection pressure.

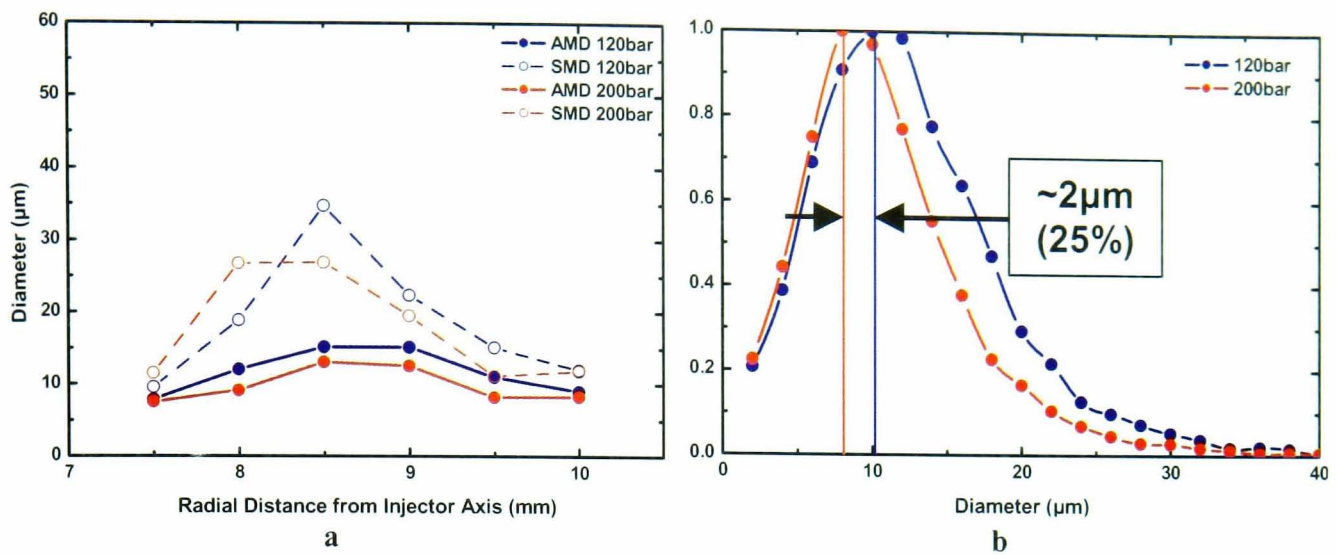


**Figure 4.60: Effect of injection pressure for a six-hole injector at atmospheric chamber pressure. (a). Spatial sizing profile at 10mm from the nozzle exit at 0.9ms ASOI and (b). Normalised size distribution graph for the entire injection duration and the total jet cross-section.**

Finally, the droplet size distribution of the spray at double injection does not show any significant changes relative to what has been mentioned so far. In fact both injection events follow the same trends, as presented in previous paragraphs. There is one extra operating parameter in the case of double injection that affects droplet size distribution in a predictable manner, and this is the dwell time. The previously analysed pre-spray that is formed during short dwell times, i.e. between the two injection events, consists mainly of large-sized droplets. The reason is simple and it comes from the mechanism that creates this pre-spray. This is the needle instability caused by short dwell times that forces the needle to open while it has not been shut completely. As a result, the needle does not open fully, thus creating a form of a pre-spray that is characterised by large droplets, since atomisation mechanisms are not effective for needle lifts other than full lift.

As illustrated in Figure 4.61, in the interval between the two injection events (marked region) droplet sizes are larger than the sizes achieved during injection. The only difference is that in the case of 0.3ms dwell time (Figure 4.61a) there is a pre-spray and the validated samples can be as many as 3,000. On the contrary, a dwell time of 1ms (Figure 4.61b) does not produce a pre-spray and validated samples during that period may not exceed 500! The 500 samples come from liquid ligaments that exit the injection holes after the needle has closed. At that time, all the liquid left in the sac volume emerges from the injection holes without any atomisation due to the lack of upstream pressure and is captured by the PDA system as a few large droplets.

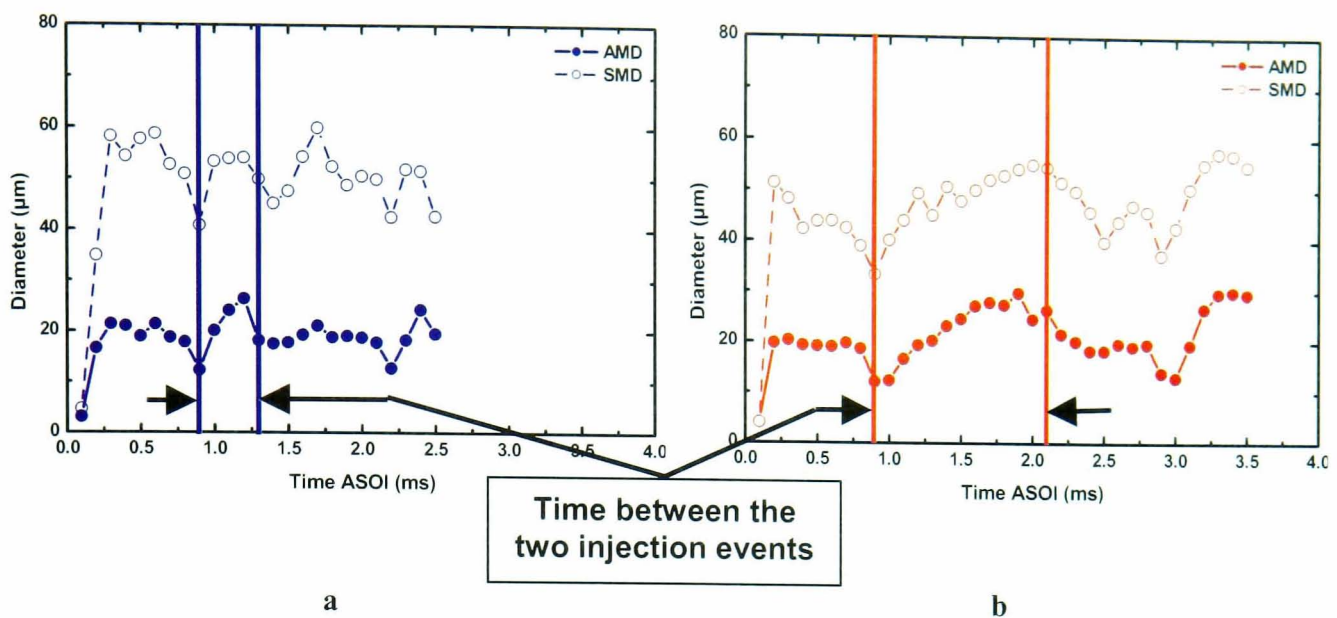


**Figure 4.61:** Effect of dwell time for a 6-hole asymmetric nozzle at 80bar injection pressure, at 2.5mm from the nozzle exit. (a). Dwell time of 0.3ms and (b). Dwell time of 1ms.

## 4.6 SUMMARY

Spray characterisation of gasoline high-pressure multi-hole injectors in a constant-volume high-pressure/temperature chamber revealed important information on the performance of these second-generation injectors. The combination of Mie scattering visualisation and phase-Doppler anemometry experiments proved to be a powerful tool in this high-pressure spray investigation. Several multi-hole injector geometries have been tested and the effects of various operating parameters have been quantified. Complete understanding of high-pressure sprays behaviour in terms of stability and structure is essential for successful implementation of such injectors to advanced gasoline direct-injection engines.

High magnification imaging revealed that the needle opening delay, after the injection pulse has been applied to the injector coil, is around 0.6ms. For all tested injectors, the start of injection oscillates around the value of 0.6ms after triggering, so it is set as a global start of injection for the second-generation coil-driven multi-hole injectors. The needle driving mechanism also limits the minimum feasible injection duration. As a result, durations shorter than 0.9ms cannot be realised at all injection pressures due to the increased needle opening delay and the reduced needle opening acceleration. On the other hand, long injection durations result in a slight increase in the mean droplet diameters. Further spray imaging experiments demonstrated the air-entrainment mechanism in individual jets. High-pressure injection induces certain ambient airflow

patterns that could be summarised as pairs of counter-rotating vortices attached to surrounding individual spray jets. These vortices contribute to the widening of these single fuel jets that exhibit fishbone structures, which ultimately enhance air-entrainment. In most of the cases, the aforementioned mechanism stabilises the shape of the side jets of a multi-hole nozzle. Nevertheless, the separation between side and central jets cannot be avoided. The existence of a central jet is almost associated with a blocked side hole for the positioning of the spark plug. Blocked side holes result in non-uniform internal nozzle flow that is closely linked to central jet instabilities. In general, central jets in multi-hole injectors do not exhibit high repeatability and are characterised by the highest droplet velocities of the nozzle with increased spray tip penetration lengths.

The most important advantage of multi-hole injectors, relative to the first-generation swirl pressure atomisers, is the independence of the overall spray cone angle on chamber pressure. Increased chamber pressure alters significantly the spray development by confining sprays into compact jets and reducing their tip penetration, but the overall spray cone angle remains unaffected. More specifically, chamber pressures greater than 3bar result in reduced droplet velocities and increased size distributions. Furthermore, the spray cone angle is independent of injection pressure. Increasing injection pressures from 80 to 120 and to 200bar leads to higher spray droplet velocities but, interestingly enough, size distributions do not show the expected reduction. More specifically, an increase of injection pressure from 120 to 200bar achieved a maximum reduction in the size of the injected droplets of 25%; a number that is rather low relative to the 80bar increase in injection pressure. A more drastic effect on droplet size is achieved with ambient chamber temperature. Increasing chamber temperatures from 50°C to 120°C resulted in a mean droplet diameter reduction of 35-40%. Furthermore, spray tip penetration lengths were reduced and a marginal reduction in droplet velocities was also observed.

Following understanding from diesel injectors, an attempt was made to associate gasoline high-pressure spray behaviour with key parameters in multi-hole nozzle design. The most important design parameter in multi-hole nozzles is the ratio of the injection hole length to its diameter. In diesel nozzles, there is evidence that the  $L/D$  ratio controls fuel atomisation and spray tip penetration length. The same trend has

been confirmed in gasoline multi-hole injectors. More specifically, a six-hole nozzle with an L/D ratio of 2.14 produced jets with larger individual cone angle than a 12-hole nozzle with an L/D ratio of 4.28. The most important characteristic of nozzles with high L/D ratios is their performance in atomisation that is reflected in the smaller droplet size distributions compared to lower L/D ratio nozzles. Furthermore, reduced size droplets appear to decelerate fast enough so that the overall spray tip penetration length is reduced. In addition, the increased fuel mass distribution achieved by 12-hole nozzles, results in quick and efficient evaporation at elevated chamber temperatures.

Finally, the sprays from high-pressure multi-hole gasoline injectors have been completely characterised through experiments, which confirmed the ability of these injectors to operate in a multiple injection mode. Double injection does not seem to affect the aforementioned spray characteristics, unless dwell time settings violate the needle-driving coil performance. Following the collection of all vital information regarding multi-hole high-pressure sprays, it can be argued that the second-generation injectors are very promising fuel injection equipment candidates for future passenger car engines. By maintaining base injection pressures at the low energy level of 80 to 120bar and preferably selecting six and twelve holes nozzles, it is expected that engine tests will eventually demonstrate whether multi-hole injectors are capable of delivering consistently an ignitable air/fuel mixture around the spark plug under stratified overall lean mixture operating conditions, thus extending the efficiency and range of emerging direct-injection gasoline engines.

## *Chapter 5*

### *Mixture Distribution*

The in-cylinder flow and thermodynamic conditions exert a substantial influence on the spray structure [122], fuel atomisation and dispersion, air entrainment inside the fuel cloud and the subsequent fuel/air mixing process. Interaction of the high-pressure spray with the in-cylinder airflow is an extremely transient process that determines the spatial characteristics of the air/fuel mixture prior to ignition and, depending upon the injection strategy, its homogeneity or various levels of charge stratification. In general, the operation of the direct-injection spark-ignition engine is classified in three distinct modes: (i) homogeneous stoichiometric, (ii) homogeneous lean and (iii) stratified overall lean. The first mixture mode exploits the full potential of an internal combustion engine, by operating at full engine load. In addition to that, homogeneous stoichiometric operation is widely used in engine cold start, optimising warm-up periods and exhaust gas emissions. Furthermore, full engine power output is required at engine load transitions, i.e. during vehicle acceleration, forcing the engine to operate at the homogeneous stoichiometric mode featuring maximum air utilisation. Finally, this mode is the only one that allows the use of the existing technology 3-way catalysts for reduced exhaust gas emissions at all times. The homogeneous lean operation does not differ significantly from the aforementioned mode, since it requires homogeneous fuel distribution inside the engine cylinder, although the fuel quantity is kept at the minimum possible within the ignition limits for successful combustion. The second operating mode is widely used at medium engine loads, where maximum power output is not required and elementary fuel economy coupled with NO<sub>x</sub> trade-off set the engine operating characteristics. Finally, for idle and low load engine operation where maximum fuel economy is the target, power output demands are very low. Stratified overall lean operation is achieved by injection of a relatively small fuel quantity in the vicinity of the spark plug electrodes, while the rest of the engine cylinder is filled with air or much leaner mixture. The charge is then highly stratified and combustion is maintained by the minimum possible fuel quantity, thus minimising fuel consumption and CO<sub>2</sub> emissions. The objective of charge stratification in the DISI engine is to operate the engine unthrottled at part load at an

overall air-fuel ratio that is leaner than conventional lean-burn or homogeneous mixture engines.

The aforementioned engine operating conditions are realised by distinct fuel injection strategies. Injection of fuel during the induction stroke aims at homogeneous stoichiometric operation. The increased fuel quantity required for full load operation should exhibit maximum air utilisation. In addition to that, the maximum possible time for effective fuel evaporation should be provided. These two conditions can only be realised when injecting early during the induction stroke, where in-cylinder flow fields are at maximum levels and the time to the ignition point is sufficient for fuel evaporation and mixing. Furthermore, homogeneous stoichiometric operation is also required at engine start up, where engine warm-up periods should be minimised, for exhaust gas emissions to be kept at minimum possible levels. It has been found [4, 17, 26, 34, 74] that multiple injections during the induction stroke, or a combination of injections during induction and early compression strokes, contributes in quick and effective engine warm-up, minimising start-up emissions that cannot be avoided. Immediately, it becomes evident that injection timing is a crucial parameter determining the severity of wall wetting, the liquid fuel distribution and the degree of charge cooling, which affects the volumetric efficiency and knock sensitivity of the engine.

On the other hand, air/fuel mixture stratification is realised by fuel injection during the compression stroke. The use of charge stratification near the spark plug in an overall lean mixture provides significant improvements in BSFC. This is achieved primarily through reduction of the throttling-associated pumping losses as well as the heat losses, the chemical dissociation from the lower cycle temperatures and by the increase of the specific heat ratio of the cycle. During the stratified mode operation, injection timing is an important parameter as the time available for evaporation and mixing is limited. In addition to that, the end of injection (EOI) timing should be carefully selected, since the fuel cloud should remain close to the spark plug and be vaporised as well. It should be noted that the second generation high-pressure gasoline injectors require approximately 0.6ms to start injecting and 0.3ms to seal fuel from exiting the nozzle, thus fuel will continue to enter the combustion chamber after the end of injection signal.

The inter-relationships of injector location, spray characteristics, combustion chamber geometry, injection timing and spark timing are quite complex and must be optimised for each system and each operating mode. Therefore, fuel liquid and vapour distributions, within a motored single cylinder DISI optical research engine, are investigated with the aid of planar Laser Induced Fluorescence (LIF) measurements over a range of different injection strategies aiming to gain insight of the trends of in-cylinder mixture distribution phenomena. Following the investigations of spray characteristics of gasoline multi-hole injectors, two multi-hole nozzles have been selected for engine experiments; a 12-hole (10(12-2) + 1 central holes) and a six-hole nozzles featuring 90° and 40° overall spray cone angles, respectively. All injectors operate in a range of 60-120bar injection pressures. The selection of different spray cone angle nozzles is based on the fact that the single cylinder research engine features a cylinder bore of 73mm, a value that is expected to be small for a wide spray from 90° nozzles.

## **5.1 OPTICAL ENGINE TEST RIG**

The study of fuel vapour distribution in an engine's cylinder is mainly performed with the use of well-established non-intrusive laser techniques in conjunction with pressure measurements and other advanced optical diagnostics. In utilising these techniques, either individually or simultaneously, advanced optical and electronic equipment has to be employed for the measurement, synchronisation and data processing procedures. Improved understanding of the fundamental operating principles of the various measuring equipment is vital for the successful outcome of these sophisticated experiments and the elimination of any systematic error sources.

### **5.1.1 Research engine**

Due to the need to apply laser, as well as other optical techniques, in order to characterise the mixture distribution, research engines are expected to allow optical access into the cylinder throughout the whole engine cycle. The research engine employed throughout the research programme, incorporated a prototype five-valve cylinder head designed to allow close-spacing piston-guided operation combined with twin spark plugs; it was provided by Yamaha Motor Corporation as part of a collaboration contract. The innovative design of this engine is the centrally located

high-pressure injector and the twin spark plugs. The optical engine, as illustrated in Figure 5.1, is a 250cc single cylinder engine featuring 73mm bore times 59.6mm stroke. The valvetrain is a five-valve, double overhead camshafts system and the maximum speed is up to 3,000rpm. The cylinder's compression ratio is almost 10:1 (exact value is not given because the combustion chamber is hand-curved).

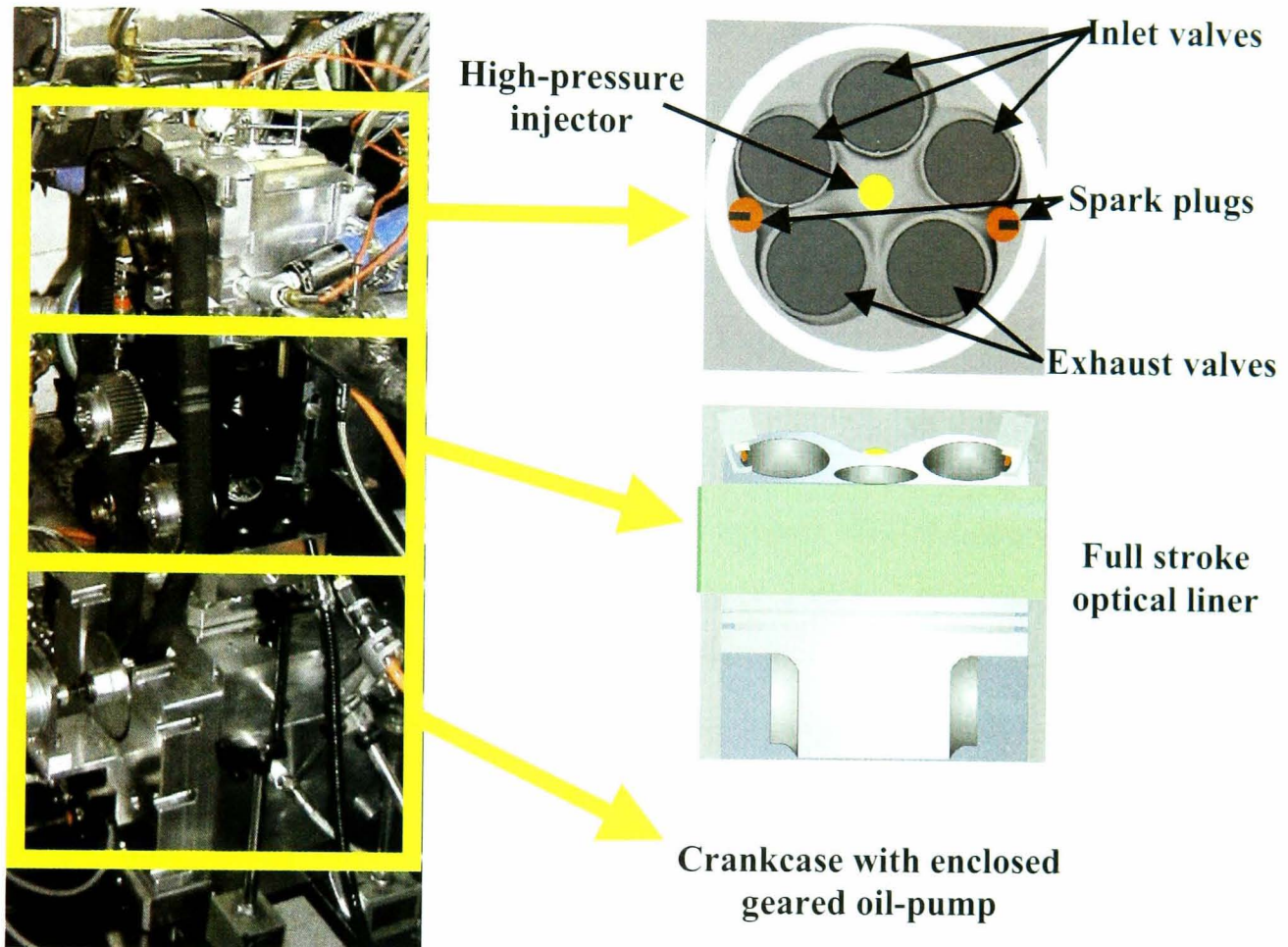


**Figure 5.1: Schematic representation of the key elements of the 5-valve, twin-spark ignition optical engine.**

The cylinder-head inlet ports generate in-cylinder low-tumble and variable swirl air motion. The latter is achieved by a second valve installed downstream the throttle valve, which is mainly not used in this investigation. This second valve is named Swirl Control Valve (SCV) and it controls the desired in-cylinder swirling motion. This valve, when closed, covers two-thirds ( $2/3$ ) of the inlet port, which effectively blocks the flow of two inlet valves and directs the whole intake flow to the third valve (Figure 5.2). In this way, maximum in-cylinder swirling flow is achieved. The angle of this valve is variable and controlled automatically; so it is possible to achieve any desired swirl ratio in the cylinder by varying the SCV angle. From this point forward the statement “SCV open” or “SCV90” means no swirl (valve fully open), while “SCV closed” or “SCV0” means maximum in-cylinder swirl (valve closed).

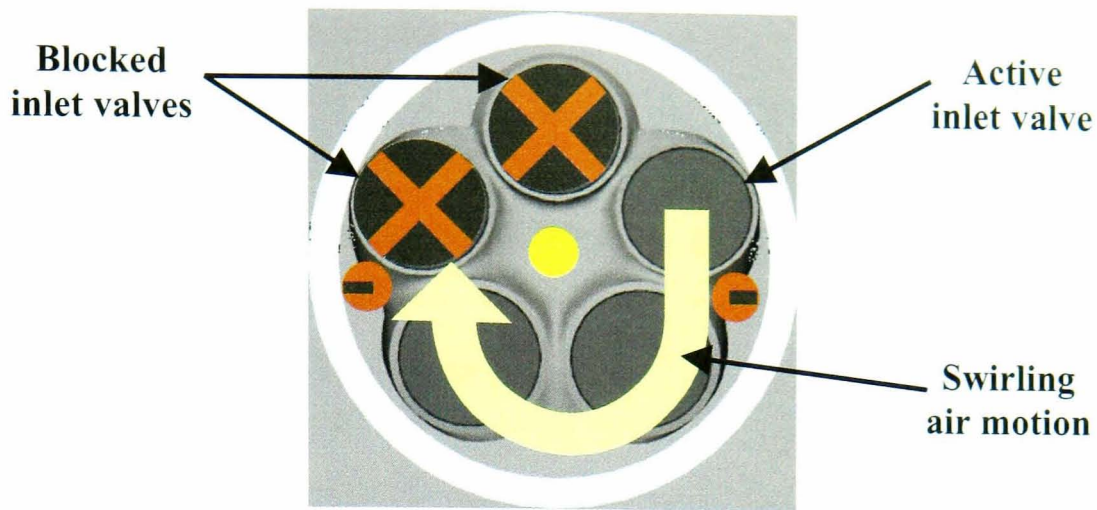


**Figure 5.2: Schematic diagram of the Swirl Control Valve operation.**

The engine's cylinder features a full stroke length optical quartz liner, an elongated Bowditch piston with flat shaped crown and a pent-roof style combustion chamber. The cylinder-head utilises a 5-valve configuration, 3 inlet valves and 2 exhaust valves. The injector is located centrally, with a 1mm offset to the geometrical centre of the cylinder. In order to overcome known issues of cocking and injector deposits the initial closed-spacing configuration has been replaced with a twin-spark arrangement, employing 2 spark-plugs at the two sides of the cylinder, installed one opposite to the other (Figure 5.1). This is believed to be the best solution for reducing injector's tip temperature during engine firing operation, which is the main source for cocking. Although this engine is not fired, but only motored, the aforementioned configuration has been followed for the closest representation of a realistic combustion system employing multi-hole injectors. The proposed configuration shares features from a close-spacing, spray-guided concept as well as from wide-spacing, wall-guided designs. Thus, it is named twin spark plug, piston-guided engine. The optical engine is coupled to a shunt dynamometer, and it could be motored up to 3000rpm for realistic results on the preparation of the desired mixture prior to the combustion event.

### 5.1.2 Optical engine experimental set-up

A complete and fully functional research engine test rig should be equipped with various instrumentation providing information for almost all engine operating parameters. As mentioned in previous sections of this chapter, the air intake system is equipped with a throttle valve, although it is not used. In direct-injection spark-ignition engines, the basic target is to transfer the fully unthrottled operation of the

diesel engine in order to minimise the pumping losses of the Otto operating cycle. Then, the load of the engine is directly controlled by the injected fuel quantity. In such cases, the main indication of engine load is provided by the volumetric efficiency. A laminar flow meter, installed well upstream the intake ports, determines the air consumption of the engine and according to the engine speed signal, the volumetric efficiency is calculated. Based on the cylinder inducted air and the desired final air to fuel ratio (AFR), the fuel quantity is controlled accordingly by the injection duration. The engine's intake system features extra equipment when intended for LIF measurements. As it will be analytically described in following paragraphs, LIF measurements require insitu calibration. The latter is achieved by engine operation at homogeneous stoichiometric conditions. More specifically, induction of pre-mixed charge is required for accurate fuel vapour distribution results. Therefore, a mixing chamber is installed upstream the intake valves that consists of a high-pressure injector and a heated honeycomb. As fuel is injected onto the heated honeycomb, it is quickly vaporised and enters the cylinder with the best possible mixing and homogeneity. A schematic of the aforementioned instrumentation is illustrated in Figure 5.3.

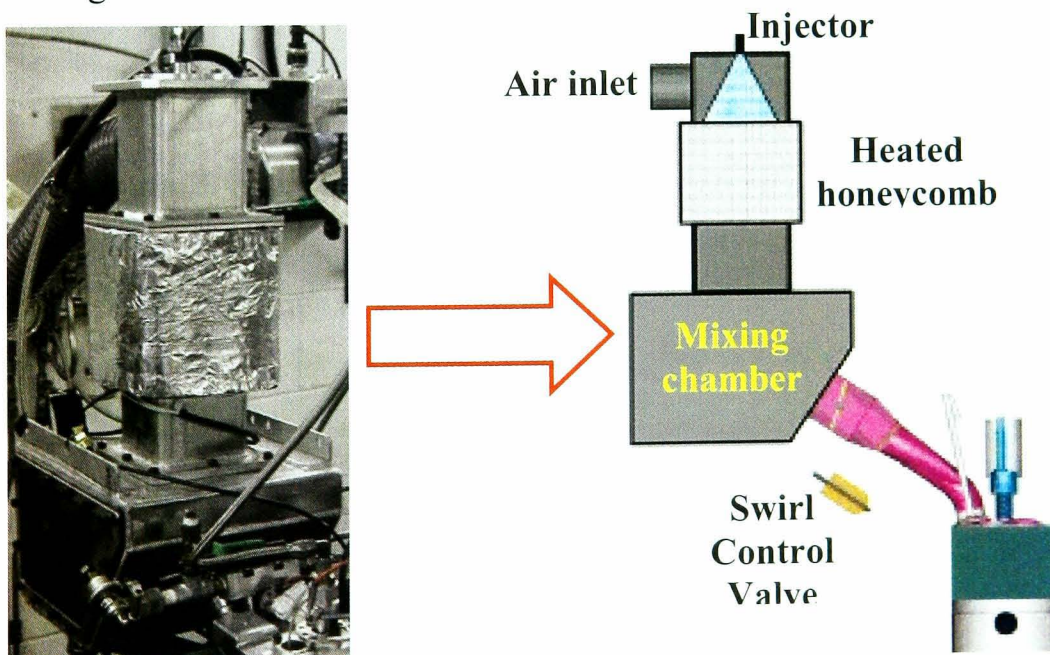


**Figure 5.3:** Schematic representation of the inlet pre-mixing chamber.

The high-pressure fuel system is completely isolated from the engine operation, as a stand-alone high-pressure instalment. A three-piston-type pump, coupled to an electric motor, is responsible for delivering high-pressure fuel (up to 120bar) to the common rail, which has been specifically built with two injector outlets. This common rail is connected to the injector via a pipe with specific diameter and length.

A fuel pressure regulator is attached on the common rail and it automatically regulates fuel pressure by throttling the return fuel line. A fuel cell is installed inline with the injector and provides the fuel consumption under any operating conditions.

The engine cooling / heating system consists of a water tank, a high-power heater, a heat exchanger and a flow meter. The dual operation of the engine's water system is essential for both possible engine-operating modes, firing and motoring. In any case, engine temperature should be kept constant at around 90°C; when fired the heat exchanger takes away the combustion-generated heat, while in motoring mode, the heater in conjunction with the temperature control unit, rises engine temperature at desired levels. Final engine temperature is monitored by two thermocouples installed in engine's water inlet and outlet.

Finally, three pressure transducers are responsible for monitoring cylinder, inlet and exhaust pressures. Signals from the aforementioned instrumentation and two thermocouples installed in the inlet and exhaust pipes are gathered and saved in the monitoring PC, where further processing provides information on engine's operating conditions.

### **5.1.3 Engine management**

The optical direct injection twin-spark engine is a purpose designed and built unit. At an early stage in order to develop confidence on the results and the measurement procedure, it is necessary to have full control of each engine parameter from fuel injection to data acquisition. For this reason, computer-based versatile management systems that could be customised according to the needs of various experiments are built. Vital equipment of the control and acquisition software is an optical encoder, a pickup sensor and two National Instruments PC cards, a timer and a data-logging card. The optical encoder is directly mounted on the engine crankshaft and provides the time-base to the two PC cards that is 1,000 pulses per engine revolution (2,000 pulses per cycle). The pickup sensor is installed in the exhaust camshaft and produces a marker pulse of the engine cycle; in this way, identification of induction or expansion stroke is secured. The engine cycle marker and one pulse per crankshaft revolution are feed to the PC cards, thus the zero point of induction top dead centre and engine speed could be measured. The potential of the eight available counter /

timers of the advanced timer card (NI PCI-6602) is exploited by a custom made software written in the LabView compiler [115]. A screenshot of the engine control software graphical user interface is illustrated in Figure 5.4. After processing of the input pulses, the control software creates four fully independent and totally synchronised TTL pulses, which are used as injection, ignition (where applicable) and two general-purpose triggering signals. These counters could be reprogrammed “on the fly” allowing updating of the time dependent variables accounting for the speed variations of the engine.

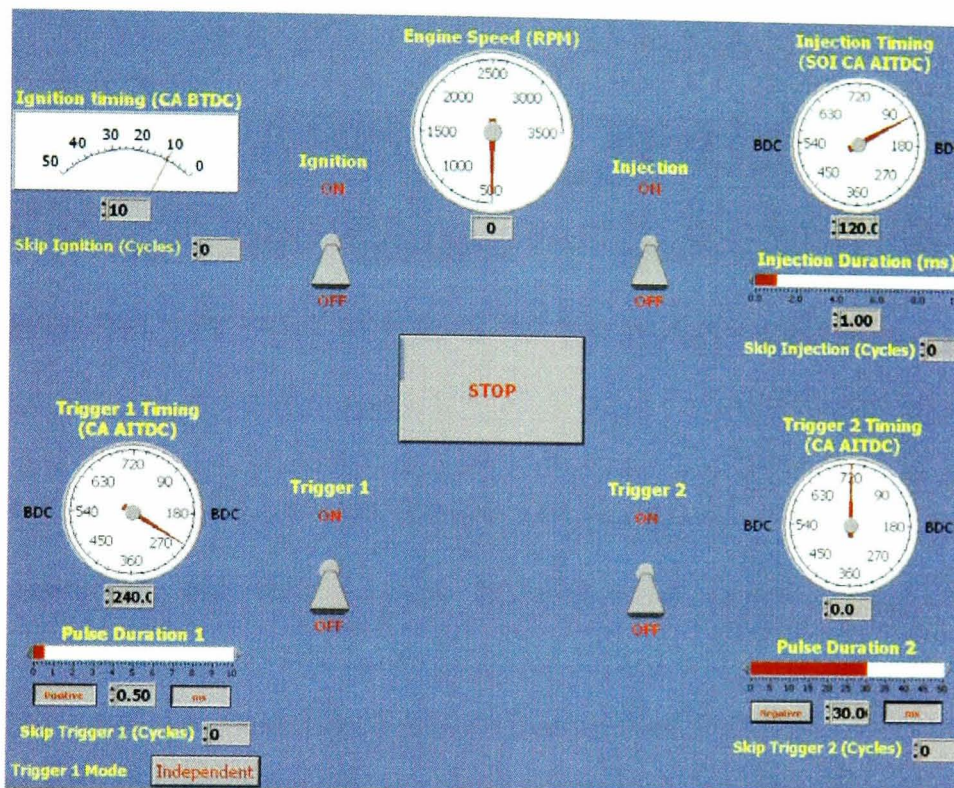


**Figure 5.4:** Screen shot of the engine control software.

The second PC card, a data acquisition card, is responsible for collecting all the important signals from the installed sensors. Sharing the same time base as the engine control software, the data acquisition program is written in Microsoft Visual Studio .NET. Among its capabilities is the graphical representation of all important engine operating parameters and, necessary data processing. The latter is being done in real time, thus, parameters like volumetric efficiency, air to fuel ratio (AFR), indicated mean effective pressure (IMEP) and coefficient of variance of IMEP are monitored in real time. Furthermore, all calculated and measured parameters can be recorded on the hard drive for further processing. The graphical user interface of the aforementioned data logging software is illustrated in Figure 5.5.

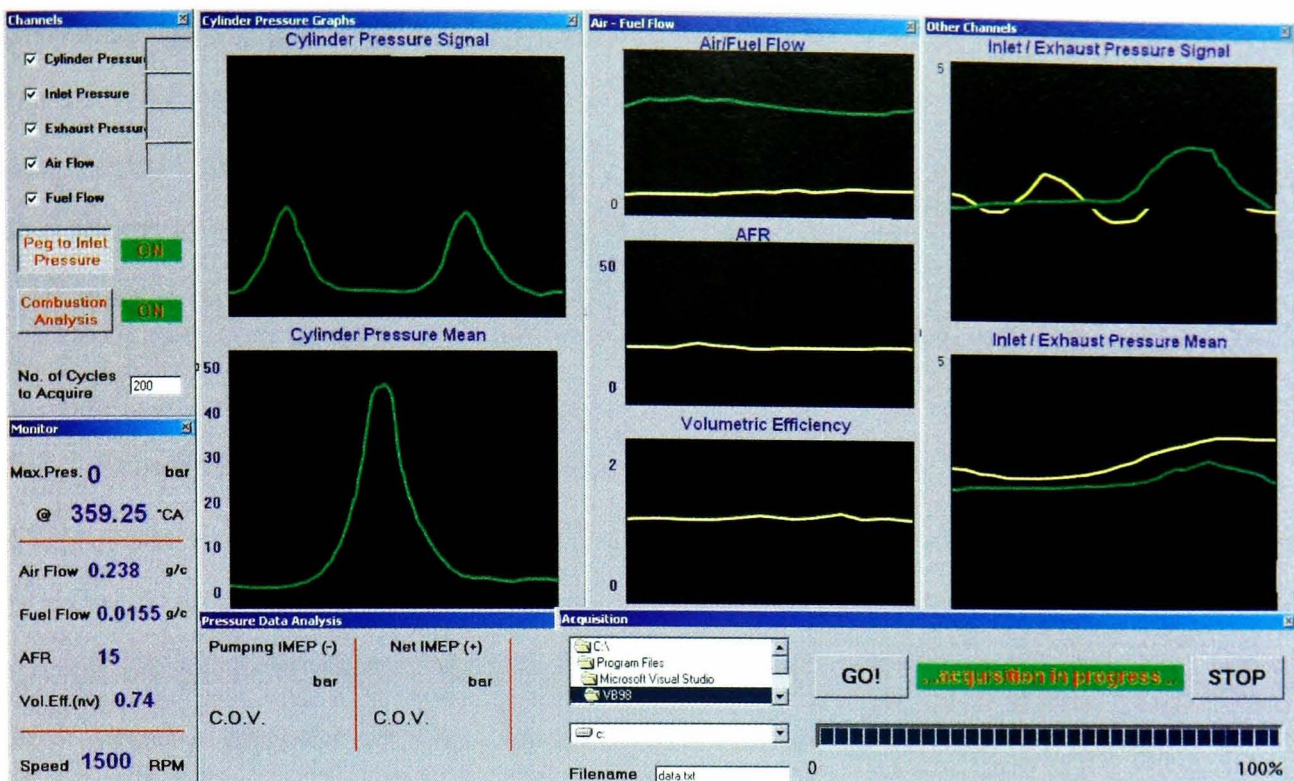


Figure 5.5: Screen shot of the engine monitoring and data acquisition software.

## 5.2 LASER INDUCED FLUORESCENCE TECHNIQUE

The most common and widely used technique for engine in-cylinder mixture distribution investigations is the Laser Induced Fluorescence (LIF) technique. LIF is an optical non-intrusive, laser diagnostic technique that is used to detect qualitatively and quantitatively the presence and the local concentration of molecular species under examination, such as liquid or vapour fuel [72, 76, 78, 123-125],  $O_2$  [126],  $SO_2$  [127], OH [128], NO [123] as well as to measure spatial variations of temperature [71, 72, 110, 129]. In the last two decades, the urge in understanding the mixture preparation processes in internal combustion engines, during the induction and compression strokes, has rendered this technique very attractive as it provides a two-dimensional impression of liquid and/or vapour distribution with a single measurement.

Certain difficulties in associating the fluorescence signal levels to absolute in-cylinder fuel concentration, the LIF technique is frequently used to visualize qualitatively the 2-D fuel distribution. However, in the present study the in-cylinder mixture distribution has been analysed quantitatively by referencing the LIF signal with the aid of an insitu calibration method, which accounts for the signal temperature and pressure dependences, any quenching effects as well as laser sheet heterogeneities. A specifically designed air / fuel mixing device, as described in previous paragraphs,

provides the engine with a homogeneous mixture of known equivalence ratio ( $\phi=14.7/AFR$ ). In this way, acquisition of calibration images is possible sharing the same optics and operating conditions to the data images. Consequently, a molecular and thermodynamic analysis in conjunction with some image processing converts the LIF images to contour plots of local air to fuel ratio (AFR).

### 5.2.1 Principles of the LIF technique

Fluorescence is the spontaneous emission of photons by a molecule caused by the relaxation of a molecule from an excited high energy level to its ground state. The excitation can have various forms but specifically in the LIF technique it is caused by high energy photons emitted by a laser while the subsequent relaxation of the electrons generates light, which is one of many forms of “Stokes shifted” radiation emission with others being phosphorescence and chemiluminescence. More specifically, the electrons of the investigated molecule are initially in a ground state denoted as 1 in the energy diagram of Figure 5.6. The incident laser light elevates the electrons to a higher energy level (2), through the fractional rate of stimulated absorption  $B_{21}I_0$ , from where five processes are possible to occur, in the electrons effort to return to their initial ground state. The first two usually occur during the excitation by the laser pulse. In the first one, the molecule returns to its original ground state ( $B_{12}I_0$ ) by laser induced stimulated emission (fractional rate of stimulated emission – internal conversion), while in the second process, with the addition of a further photon, an even higher energy level is reached ( $B_{i2}I_0$ ) that could trigger the ionisation of the molecule. Intermolecular collisions result in inelastic energy transfer by changing the electron vibration and rotational energy ( $Q_{rot,vib}$ ). In many cases, the inelastic collisions with other molecules result in electronic energy transfer ( $Q_{elec}$ ), which is often referred to as quenching effect. The latter processes lead to radiationless transitions and are more pronounced in high-pressure conditions, where the probability of molecule-to-molecule collisions is higher. Intra-molecular energy transfer between atoms of the molecule lead to its dissociation (intersystem crossing) as it now contains electrons in an unstable (repulsive) state ( $Q_{pre}$ ). Finally, the fluorescent emission ( $A_{12}$  – elastic spontaneous emission) is a result of transitions from various excited energy levels, caused by the molecular energy transfers. These different energy level transfers result in the fluorescent light emission having a broadband range of wavelengths.

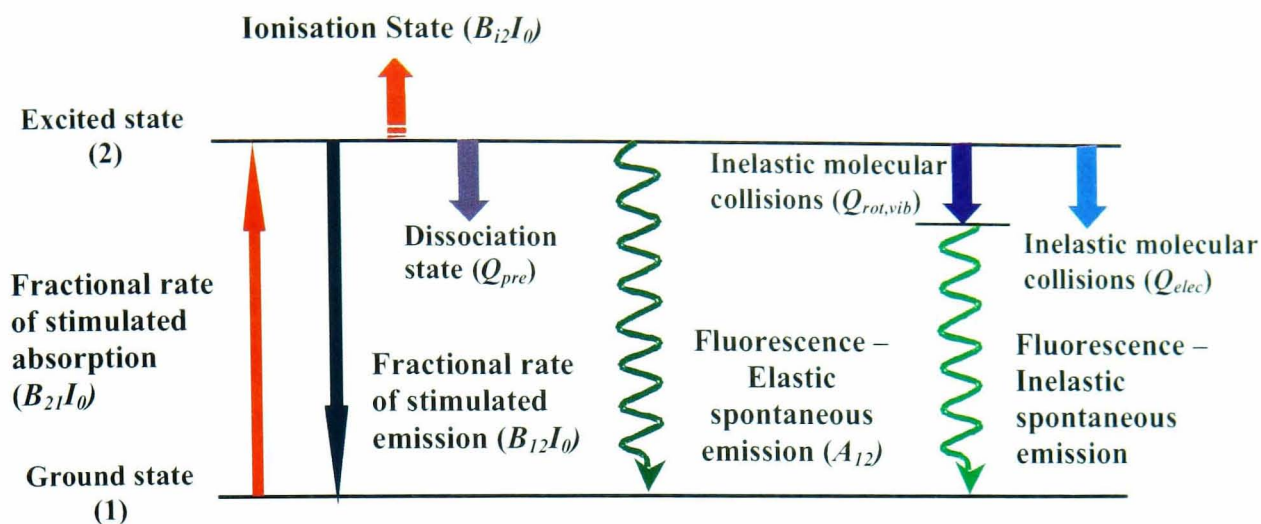


Figure 5.6: Electron energy transfer diagram.

If the fluorescence effect is to be used for concentration measurements of a species, a relationship has to be found between the emitted light intensity and the concentration. The number of emitted photons per  $\text{cm}^3$  is given by equation 5-1,

$$R_p = n_1^0 \cdot B_{21} \cdot I_0 \cdot \frac{A_{12}}{A_{12} + Q_{12}} \cdot \frac{1}{1 + \frac{I_0}{I_{sat}}} \quad [5-1]$$

where  $n_1^0$  is the initial ground state population,  $A_{12}$  the Einstein coefficient of spontaneous emission (fluorescence),  $B_{21}$  the Einstein coefficient of stimulated absorption,  $I_0$  the laser spectral flux density,  $Q_{12}$  the collisional transfer coefficient or collisional quenching rate constant and  $I_{sat}$  the saturation laser spectral flux density, expressed as:

$$I_{sat} = \frac{A_{12} + Q_{12}}{B_{21} + B_{12}} \quad [5-2]$$

where  $B_{12}$  the Einstein coefficient for stimulated emission. As the laser intensity used during the experiments is much lower than the saturation intensity ( $I_0 \ll I_{sat}$ ), the total number of photons can be shown to be proportional to the number density  $n$  of the species, the incident radiation energy  $\mathcal{G}$  ( $B_{21}I_0$ ) and molecule dependent constants ( $A_{12}$ ,  $Q_{12}$ ) (equation 5-3).

$$N_p = \mathcal{G} \cdot n \cdot \frac{A_{12}}{A_{12} + Q_{12}} \quad [5-3]$$

As  $Q_{12}$  is usually much greater than  $A_{12}$ , the ratio on the right hand side becomes very small and is usually denoted as the fluorescence efficiency. This is a very important parameter as it will ultimately determine the signal to noise ratio of the measurement.

### 5.2.2 Choice of dopant

Commercial grade gasoline fluoresces strongly in the presence of ultraviolet illumination, especially when excited at 308nm [123], and would be most preferable for internal combustion engine diagnostics, as it would provide a realistic impression of the in-cylinder mixture distribution and the formation of possible fuel films. However, although at first sight appears to be attractive for LIF measurements, it does bring several disadvantages in terms of signal interpretation for quantitative measurements. This is due to the fact that gasoline is a multi-component fuel and its composition is batch dependent, resulting in calibration uncertainties. In addition to that, discerning the fluorescent components is not always possible and therefore, their dependencies on pressure and temperature cannot be quantified. The fluorescence signal is a consequence of the presence of some compounds in the fuel, which are more likely to be aromatics with high boiling points; hence they may not provide a complete picture of the mixture distribution. Although these problems exist in terms of fluorescence limitations, fluorescence from commercial grade fuels has been effectively used for obtaining qualitative information regarding fuel films on intake ports [130, 131] and combustion chamber surfaces [3, 132].

Finally, for the aforementioned reasons, a single component fuel is preferable for LIF investigations. Therefore, isooctane (2,2,4-trimethylpentane) is selected to be the base fuel for in-cylinder mixture distribution measurements. However, it has been found experimentally that isooctane exhibits negligible fluorescence when excited by a 266nm wavelength laser light. Hence, a suitable tracer has to be added in the fuel to increase its quantum yield, featuring some of the requirements presented below:

Ideally, the selected tracer should

- Be soluble in isooctane.
- Have similar evaporation and mass diffusion characteristics to isooctane.
- Have high fluorescence quantum yield at the excitation wavelength of the available lasers.
- Have low pressure and temperature dependencies.
- Be non toxic for the user.
- Be compatible for the materials of the fuel system.

Based on the above requirements, tracers that have seen most frequent use in similar

studies [123, 124, 133-135] are Acetone ( $\text{CH}_3\text{COCH}_3$ ) and 3-Pentanone ( $\text{C}_2\text{H}_5\text{COC}_2\text{H}_5$ ), which are both ketones. They both share similar spectral characteristics owing to their similar chemical structure and their fluorescence show modest pressure dependence at some excitation wavelengths. This is due to the fact that ketones present rapid intersystem crossing transitions (within 5ns) and therefore a reduced probability for inelastic molecular energy transfers (quenching) [106, 125]. As a result, the dependency of the fluorescence yield upon ambient pressure is diminished although the severe dissociative consumption of the excited molecules result in lower signal levels. This dependency varies with the incident radiation wavelength and collision partners. Under real engine conditions various researchers have shown that with the use of 266 nm wavelength light, the variation is minimum and ranges between +3%/MPa [124] and -3%/MPa [134]. Temperature dependence for the same wavelength can be more significant though (-10% / 100°K) within the range of 300-900°K [124] as the elevated temperature leads to the population of higher vibration levels of the singlet state where faster intersystem crossing occurs resulting in reduced fluorescent yield [125, 129]. In the present study, 3-Pentanone has been chosen as a tracer, since it presents more favourable evaporation characteristics compared to Acetone. Its boiling point is 101.7°C (Acetone b.p.: 56°C), which is almost the same to that of isooctane (99.7°C). Although according to [136] this is not a prerequisite for similar evaporation rates it is certainly a better choice compared to Acetone. After some trial and error, a 20% 3-Pentanone in isooctane mixture was found to be the best compromise as it combined good signal to noise ratio and an acceptably optically thin medium.

### 5.2.3 LIF optical arrangement

The excitation of electrons to a higher energy state, than their ground energy, so that the resulting relaxation provides fluorescence emission with a high quantum yield, has to be promoted by incident laser radiation. The energy present within each photon of light is inversely proportional to the light wavelength produced and is represented by equation 5-4, i.e.

$$\varepsilon = \frac{h \cdot c}{\lambda} \quad [5-4]$$

where  $\varepsilon$  is the photon energy,  $h$  the Plank's constant ( $6.63 \times 10^{-34}$  Js),  $c$  the speed of light ( $2.998 \times 10^8$  m/s) and  $\lambda$  the radiated light wavelength (nm). Therefore, the laser

incident light should be of a short wavelength (ultraviolet) and must contain a large number of photons per pulse. For the present study the fourth harmonic of a Spectra Physics GCR170 Nd:YAG laser is used and emission of ultraviolet light at 266 nm wavelength featuring 60mJ energy per pulse is achieved.

The Nd:YAG laser is a solid state laser where flash-lamps excite Nd:YAG rods and the emitted light is amplified within a cavity. The output energy of the laser pulse is determined from an electro-optical switch (Q switch). The aforementioned switch operates as a diaphragm within the light amplification cavity and its operation is summarised as a very short opening by the time the lamp energy has reached a maximum value. The frequency of the lamp Q-switch pulses determines the thermal loading of the cavity mirrors. This frequency must lie in a narrow band window, since any substantial deviation from this operating frequency results in changes to the divergence of the beam or in a potentially hazardous convergent beam, for lower and higher frequencies, respectively. The laser's nominal frequency setting is at 10Hz, and for the purposes of the present study, it is set to operate at a frequency of 12.5Hz, as it is dictated by the engine's speed (1,500 / 3,000rpm).

The fundamental wavelength of this type of laser is 1,064 nm that is in the infrared region of the light spectrum. Therefore, the required wavelength of 266 nm is achieved by a harmonic generator with frequency doubling crystals that ensure the transition from 1,064 to 532 nm (2nd harmonic) and consequently to 266 nm (4th harmonic) beam. The second and fourth harmonic conversion crystals are found to be strongly influenced by the thermal loading, thus exhibiting a steep change in behaviour during the warm-up period before thermal equilibrium is achieved. To overcome the aforementioned problem, during the first 5-10 minutes of operation, the crystals are constantly realigned for efficient warm-up.

The mean laser power is monitored regularly, during testing, with the aid of a power meter (Powermax 500A). Although shot-to-shot energy fluctuations could be up to 8%, thus introducing an equivalent uncertainty in the calibration of individual images, this study is focused on mean fuel vapour concentration distribution and the laser power associated error is expected to be much smaller following averaging over 50 consecutive cycles.

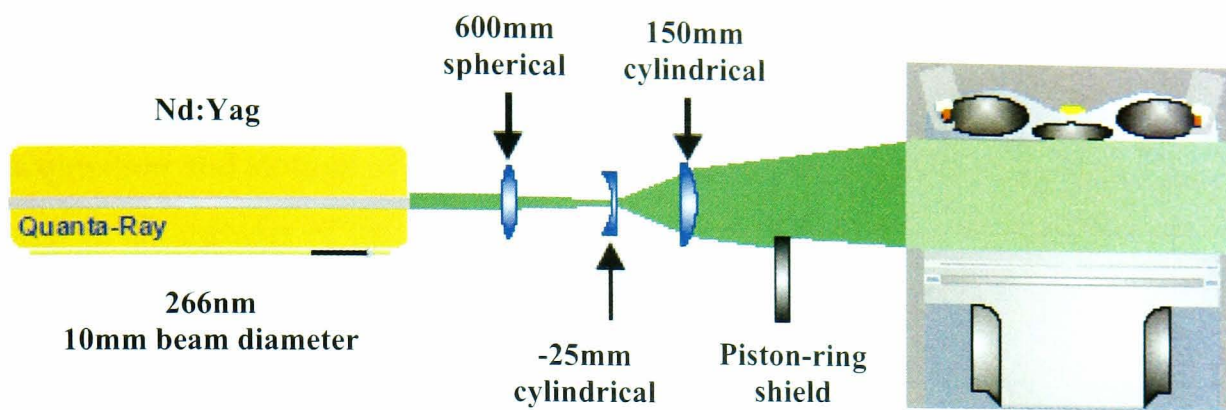


**Figure 5.7: Schematic of LIF optical set up.**

A schematic representation of the LIF optical set up is illustrated in Figure 5.7. The laser is mounted on a three-dimensional traverse mechanism of a milling machine with a positional sensitivity of 0.1mm. The 266nm laser beam, after exiting the Nd:YAG laser, is redirected, with the aid of three dichroic mirrors, to the optical lenses, which are mounted on a specially made traverse allowing their accurate alignment with respect to the laser tube and the engine. A collimated laser sheet of 50mm width and 0.5mm waist thickness is produced using a 600mm biconvex spherical lens, a  $-25\text{mm}$  planoconcave cylindrical lens and a 150mm planoconvex cylindrical lens. The resulted laser sheet enters the cylinder through the optical liner, having its plane almost aligned to the plane of the injector with a 6.5mm offset to the plane of the two spark plugs (Figure 5.8).

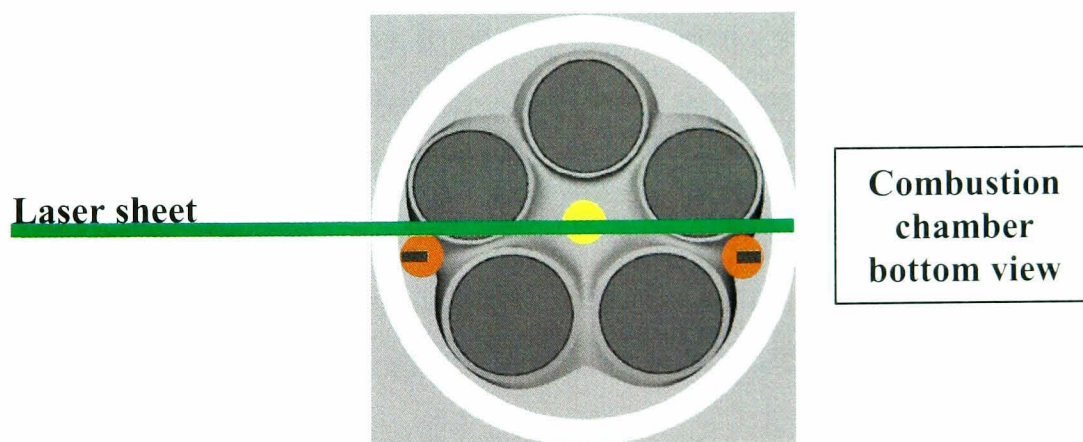


**Figure 5.8: Schematic representation of the laser sheet position relative to the spark plugs.**

A PCO DiCam intensified CCD camera is utilized for in-cylinder LIF experiments. The intensifier featured a last generation micro-channel plate that, in conjunction with the Super VGA CCD chip, offered a high spatial resolution and dynamic range. The input optical window and the photo-cathode materials (S20Q) are specially selected to suit the requirements of a LIF experiment, offering peak intensifier sensitivity towards the low end of the optical spectrum. The CCD chip features a spatial resolution of  $1,280 \times 1,024$  with a pixel size of  $6.5 \times 6.5\mu\text{m}$ . A CCD chip cooler suppresses thermal

noise and is able to maintain the chip temperature at  $-12^{\circ}\text{C}$ . The camera is fully controlled by a PC with the aid of a dedicated PCO software through which the set up, acquisition and storage of the images is performed. The management of the camera as well as the transfer of the images to the PC hard drive is done through an optical fibre cable.

As mentioned in previous sections of the chapter, induced fluorescence light is emitted at a wide range of wavelengths. This implies that the emitted fluorescent light is of a higher wavelength than that of the incident laser light. Therefore, band-pass filters are introduced in front of the camera lens that allow the appropriate wavelengths, depending on the tracer used, to be captured by the camera. More specifically, these filters eliminate any elastically scattered light and background noise due to light reflections on shiny metal surfaces. Tracer 3-pentanone yields a peak signal at around 420 nm, therefore a band-pass filter of 375-435nm operating wavelengths is utilised.

#### **5.2.4 Calibration of images**

The difficulty behind the task of producing quantitative LIF results is the calibration of the signal. The LIF signal is sensitive to various parameters such as the tracer concentration, ambient chamber temperature and pressure, oxygen concentration and laser fluency. Furthermore, there are various sources of noise such as shot-to-shot intensifier noise, thermal noise from the CCD chip and most importantly background fluorescence and Mie scattered light. Finally, the effective gain of the detection system may vary spatially due to contamination of the optics requiring different calibration constants from pixel to pixel. Therefore, the raw data images have to be normalised against a calibration image, which has been acquired under very similar operating conditions, exactly the same optical set-up and with a minimum time interval intervening between the two acquisitions.

For these reasons, an insitu calibration procedure is followed where images are acquired while the motored engine is fed with a premixed charge of known constitution (see 5.1.2) providing therefore, a reference for the greyscale at each pixel of the image and accounting for any heterogeneities in the laser sheet profile and the contamination of the optical liner. Furthermore, by being able to calibrate during

normal engine operation, calibration images are acquired at very similar conditions of pressure, temperature and mixture constitution to those of the data images, thus reducing the uncertainties due to oxygen quenching and temperature dependency of the LIF signal. As aforementioned within the acquired signal whose intensity should be mainly proportional to the tracer concentration, background noise exists, which originates from the grey-scale offset of the CCD chip, the fluorescence of oil/fuel deposits on surfaces or from Mie scattered light reflections from the incident radiation. Although a band pass filter was used to eliminate the latter, a small proportion still remained in the data and the calibration images. Therefore, an image set was acquired with the engine being motored but without any fuel injection, which could be later subtracted from the data and calibration images. In cases where the background noise was not strong enough to reduce the effective local dynamic resolution the subtraction of the background image completely removed its effects on the data.

In an effort to reduce the shot-to-shot and thermal noise of the camera a set of 50 images is acquired for the three image types, the data, the calibration and the background images. The average calibration and background images are then calculated and each of the data images is calibrated in a pixel-to-pixel basis according to the following formula:

$$I_{final} = \frac{I_{data} - \bar{I}_{back}}{\bar{I}_{calib} - \bar{I}_{back}} \quad [5-5]$$

where  $I_{final}$  is the corrected ratio of the local greyscale level of the data image to that of the calibration image,  $I_{data}$ ,  $I_{calib}$ ,  $I_{back}$  the raw data, calibration and background level respectively. The result of equation 5-5 is an array of numbers representing the relative concentration of the data to the calibration conditions. A graphical representation of equation 5-5 is illustrated in Figure 5.9.

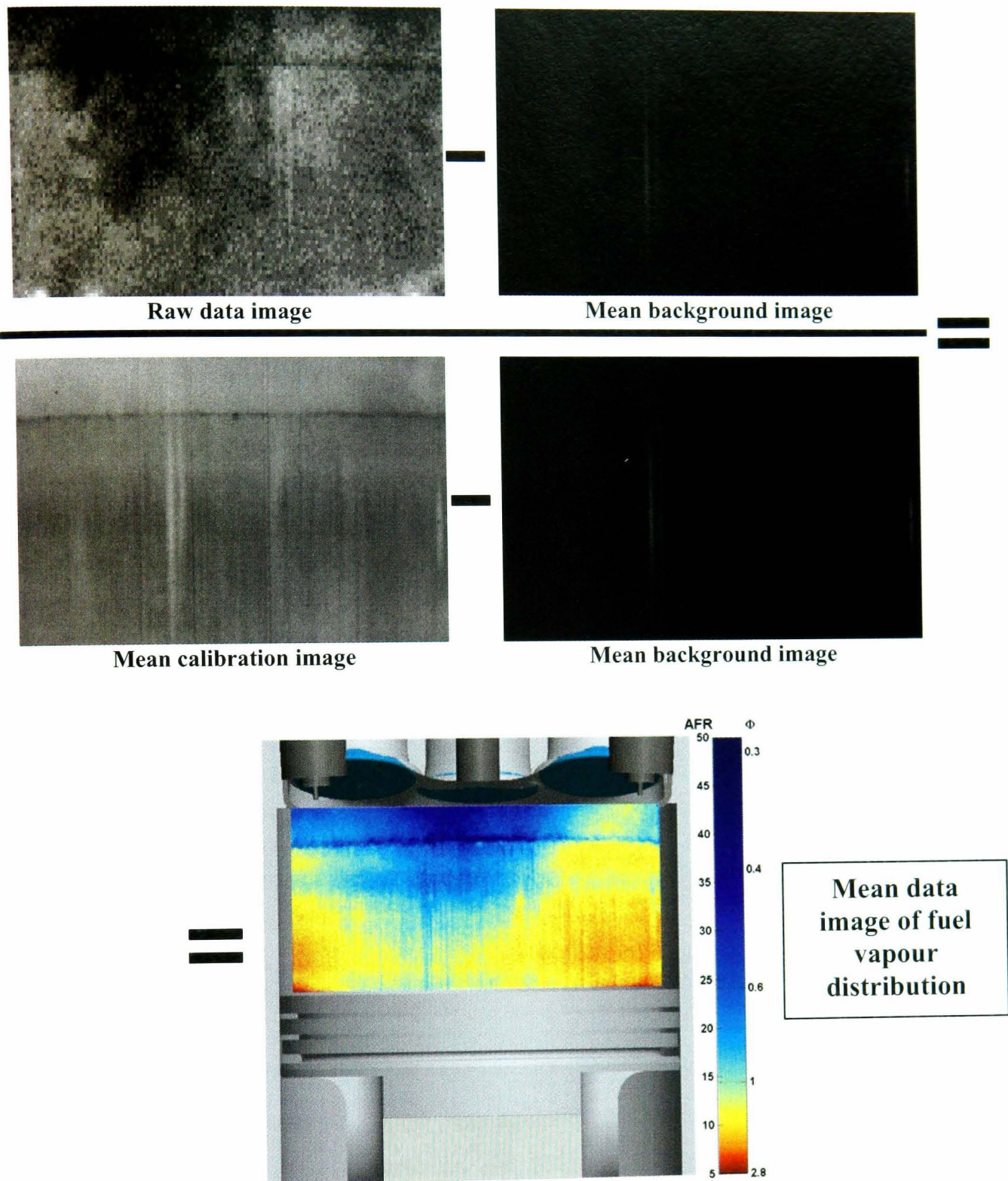


Figure 5.9: Graphical representation of image calibration.

### Tracer concentration in fluorescence images

Following the initial post processing, images representing the relative fuel vapour concentration distribution can be converted into absolute equivalence ratio images

$\left( \phi = \frac{1}{\lambda} = \frac{AFR_{stoichiometric}}{AFR_{local}} \right)$  with a procedure resembling the one followed in [123, 135].

As both calibration and data images are acquired under the same pressure and temperature conditions, fluorescence intensity (LIF signal) is proportional to the

concentration of the species in the measurement volume, or in other words, to the number density of tracer molecules at a given point (see equation 5-3), therefore it is safe to assume that:

$$I_{final,pent} = \frac{I_{data}}{I_{calib}} = \frac{X_{data,pent}}{X_{calib,pent}} \quad [5-6]$$

where  $I_{data}$ ,  $I_{calib}$  are the data and calibration greyscale intensities and  $X_{data,pent}$ ,  $X_{calib,pent}$  are the data and calibration concentrations (or number densities that is defined as the number of moles per unit volume) respectively. Thus, the number density in a data image is given by the following equation:

$$X_{data,pent} = \frac{I_{data}}{I_{calib}} \cdot X_{calib,pent} \quad [5-7]$$

On the right hand side of this equation,  $I_{data}$  and  $I_{calib}$  are intensities taken from the LIF images while the calibration concentration ( $X_{calib,pent}$ ) has to be calculated from the overall air to fuel ratio at which the engine is running during the calibration. As the LIF signal is mainly attributed to the 3-Pentanone tracer (isooctane exhibits minimal fluorescence) it can be inferred that the concentrations calculated above are solely tracer concentrations and hence in the following sections the parameter  $X_{data,pent}$  is denoted as  $X_{pent}$ .

### Fuel concentration

Having related the tracer concentration in the data images to the ratio of the data to calibration image intensities and the calibration tracer concentration, it is now necessary to find a relation between the tracer and the fuel number density. The starting point for this calculation is the concentration of 3-Pentanone in the isooctane-based fuel mixture, which throughout the experiments has been 20% by volume. By expressing the volume in terms of the number of moles, the molecular weight and density the expression of 3-pentanone in the fuel mixture can be written as:

$$\frac{V_{iso}}{V_{pent}} = \frac{n_{iso} \cdot M_{iso} \cdot \rho_{pent}}{n_{pent} \cdot M_{pent} \cdot \rho_{iso}} = \frac{4}{1} \quad [5-8]$$

Hence, the number of isooctane moles can be expressed in terms of the tracer moles:

$$n_{iso} = 4 \cdot \frac{M_{pent} \cdot \rho_{iso}}{M_{iso} \cdot \rho_{pent}} \cdot n_{pent} = 4 \cdot \frac{86 \cdot 7025}{114 \cdot 8103} n_{pent} = 2.616 \cdot n_{pent} \quad [5-9]$$

Therefore, the number of fuel moles in terms of 3-pentanone moles is given by:

$$n_{fuel} = n_{iso} + n_{pent} = 2.616 \cdot n_{pent} + n_{pent} = 3.616 \cdot n_{pent} \quad [5-10]$$

Normalising the above relation by the volume reveals the following expression:

$$X_{fuel} = 3.616 \cdot X_{pent} \quad [5-11]$$

where  $X_{fuel}$  is the number density of the fuel.

### Air concentration

The total number of moles inside the cylinder volume is

$$X_{total} = X_{air} + X_{fuel} + X_{residual} \quad [5-12]$$

where  $X_{residual}$  is the concentration of the residual exhaust gasses in the cylinder. In this particular case however, the experiments are conducted with the engine being motored and hence no residual burned gasses are expected to exist inside the cylinder.

Using the equation of state, the total concentration is expressed as:

$$X_{total} = \frac{P_{total}}{R \cdot T} \quad [5-13]$$

where  $P_{total}$  is the total pressure in the cylinder and T is the bulk temperature. Although the pressure is relatively straightforward to measure with the aid of a piezoelectric transducer, measuring the transient temperature inside the cylinder is not an easy task. Hence, it has to be calculated with the aid of a simple thermodynamic analysis, which is illustrated in a following section. Substituting equation 5-13 in 5-12 and solving for the air number density:

$$X_{air} = \frac{P_{total}}{R \cdot T} - 3.616 \cdot X_{pent} \quad [5-14]$$

### Air / fuel ratio calculation

Having assessed the fuel and air concentrations from the LIF images and other measurements, it is now possible to compute the local air to fuel ratio (AFR).

According to its definition:

$$AFR = \frac{m_{air}}{m_{fuel}} = \frac{n_{air} \cdot M_{air}}{n_{fuel} \cdot M_{fuel}} \quad [5-15]$$

where  $M_{air}$  and  $M_{fuel}$  are the molecular weights of the air and fuel respectively. As temperature and pressure are the same for the two constituents of the mixture, the above relation can be written as:

$$AFR = \frac{X_{air} \cdot M_{air}}{X_{fuel} \cdot M_{fuel}} = \frac{\left( \frac{P_{total}}{R \cdot T} - 3.616 \cdot X_{pent} \right) \cdot M_{air}}{3.616 \cdot X_{pent} \cdot M_{fuel}} \quad [5-16]$$

where  $M_{fuel}$  is the molecular weight of the fuel and for a mixture of 80% isooctane and 20% 3-pentanone is calculated as follows:

$$m_{fuel} = m_{iso} + m_{pent} \Rightarrow n_{fuel} \cdot M_{fuel} = n_{iso} \cdot M_{iso} + n_{pent} \cdot M_{pent} \Rightarrow$$

$$M_{fuel} = \frac{n_{iso}}{n_{fuel}} \cdot M_{iso} + \frac{n_{pent}}{n_{fuel}} \cdot M_{pent} = \frac{2.616 \cdot n_{pent}}{3.616 \cdot n_{pent}} \cdot 114 + \frac{n_{pent}}{3.616 \cdot n_{pent}} \cdot 86 \Rightarrow \quad [5-17]$$

$$M_{fuel} = 106.257$$

For similar compression temperature and pressure conditions between the calibration and data cases equation 5-16 could be rearranged to give the following expression:

$$AFR = \frac{I_{calib}}{I_{data}} \cdot AFR_{calib} + \frac{M_{air}}{M_{fuel}} \cdot \left( \frac{I_{calib}}{I_{data}} - 1 \right) \quad [5-18]$$

Using this expression, only image acquisition and the calibration AFR are necessary for the calibration of the LIF images. However, in such case no variations in air and fuel mass flow rates are accounted for, between the two cases, which can be of the order of 2-5% in a DI engine and hence the more elaborate method was preferred.

### Calibration tracer concentration

In the previous section the local air to fuel ratio is calculated as a function of the tracer concentration, pressure and temperature. However, the tracer concentration, which is given by equation 5-14, is in turn a function of the tracer concentration in the calibration images. Following the assumption that the air and fuel are fully mixed in the premixing chamber during the calibration procedure and that there is no loss of fuel in its path towards the engine (retention can often occur if the air temperature is not high enough), the tracer concentration can be easily related to the overall air to fuel ratio, as follows:

$$X_{calib,pent} = \frac{\frac{P_{total}}{R \cdot T} \cdot M_{air}}{3.616 \cdot (AFR_{calib} \cdot M_{fuel} + M_{air})} \quad [5-19]$$

Therefore, having measured the overall air to fuel ratio, acquired the cylinder pressure

trace during the calibration and calculated the bulk temperature following the aforementioned procedure the tracer concentration can be found.

### **Temperature calculation**

As seen in previous sections, the bulk cylinder temperature is essential for the calculation of the local AFR. Until today no reliable and straightforward method has been devised that can measure the temperature profile inside the engine cylinder. Some researchers [137] have demonstrated the ability of special thermocouples to respond to the highly transient temperature variations inside a diesel engine in order to calculate the heat release rate. However, the reliability of such a system is poor, as the thermocouple junction only lasted for a few tests. Optical techniques such as CARS have shown good results in the past but require excessive complication in the instrumentation, which would render the experiment too expensive and difficult to accomplish. Furthermore, CARS is a point measuring technique and thus scanning of the cylinder would be required in order to acquire an impression of the mean bulk cylinder temperature, rendering this a separate investigation on its own. For these reasons, the bulk temperature was calculated using thermodynamic assumptions the cylinder pressure trace, and air/fuel mass flow measurements.

In order to calculate the temperature during the induction stroke, a simple thermodynamic model has to be assumed, which cannot account for the complex processes that take place and often lead to ambiguous results. Therefore, for the period between the start of compression stroke (bottom dead centre) and the inlet valves closing time the charge pressure and temperature inside the cylinder are assumed to be equal to the values measured at the time of inlet valves closure. Effectively, the charge compression starts the moment intake valves close (IVC) and cylinder pressure starts raising, hence charge temperature calculations are more accurate. During the calculations the following assumptions were made:

- There is no mass flux towards or out of the cylinder originating from the inlet valves.
- No loss of air and fuel has occurred during the valve overlap period towards the exhaust manifold.
- The mass inside the cylinder is equal to the mass per cycle calculated by the measured mass flow rate (air and fuel) and the trapped mass filling the

combustion chamber volume.

- The measured mass from the mass flow rate covers only the swept volume of the cylinder.
- The trapped mass has the same density and constitution to the rest of the mass in the cylinder.
- Fuel and air are fully mixed, the fuel vaporised and the temperature is uniform.

The second assumption is very critical for the validity of this calculation. The engine being designed to operate at high engine speeds, features a large valve overlap period (62°CA). In cases where a rarefaction wave in the exhaust coincides with this period, short-circuiting may occur, which at the investigated engine speeds, is able of increasing the measured mass flow rate by more than 20%. If this is not accounted for, the errors in the calculations will be significant. The only way of avoiding this problem without changing the timing of the exhaust valves is to suppress the exhaust gas dynamics by shortening the track length of the exhaust significantly. Hence, whenever air mass flow measurements are conducted the exhaust pipe is removed leaving an exhaust track of only a few centimetres in length. All the image acquisition however, is done with the exhaust pipe installed so that the flow characteristics are simulated more closely. Although no pressure measurements in the exhaust pipe are feasible any more (the exhaust pressure transducer is mounted on the exhaust pipe), the cylinder pressure diagram exhibits no suction effects during the overlap period throughout the operating speed regime investigated leading to the conclusion that no significant short-circuiting occurs.

In general, it could be assumed that the charge behaves as a perfect gas. Therefore, temperature is calculated at any point of the compression curve as a function of pressure and the local polytropic coefficient. More specifically, using the equation of state, it is given that:

$$\frac{P_i}{P_y} = \left( \frac{v_y}{v_i} \right)^{n_i} \quad [5-20]$$

where  $P$  is the measured pressure,  $v$  the specific volume and index  $i$  refers to any point on the compression curve and index  $y$  to the end of compression that is effectively the start of combustion or the ignition timing. The calculation of the mean polytropic coefficient,  $n_i$ , is done by the least square method after converting equation

5-20 to a linear logarithmic equation:

$$\ln\left(\frac{P_i}{P_y}\right) = n_1 \cdot \ln\left(\frac{v_y}{v_i}\right) \quad [5-21]$$

Following the polytropic coefficient calculation, it is vital for the compression initial pressure value to be calculated again, based on the polytropic coefficient and the pressure at the end of compression. This is done due to significant errors that the initial part of the pressure curve may contain because of low-pressure values and the electronic noise that cannot be rejected. Thus, the pressure at the start of compression is given by:

$$P_a = P_y \cdot \left(\frac{v_y}{v_a}\right)^{n_1} \quad [5-22]$$

where index  $a$  refers to the start of compression.

After an accurate calculation of the compression initial pressure value, the initial compression temperature should be calculated. According to an empirical rule, the initial compression stroke temperature is given by:

$$T_a = \frac{T_0 + \Delta T + r \cdot T_R}{1 + r} \quad [5-23]$$

where  $T_0$  is the inducted air temperature,  $\Delta T$  the inducted air temperature rise due to heat exchange between the air and the hot inlet manifold walls,  $r$  a coefficient connected to residual gasses and  $T_R$  the temperature of the residual gasses in the cylinder.  $\Delta T$  and  $r$  are given from the following empirical equations:

$$\Delta T = \left( \frac{P_y}{P_a} + \frac{P_y - P_r}{P_a} \cdot \frac{1}{\varepsilon - 1} \right) \cdot \frac{T_a}{n_L} - T_a \quad [5-24]$$

$$r = \frac{P_r \cdot T_a}{(\varepsilon - 1) \cdot n_L \cdot P_a \cdot T_r}$$

where  $n_L$  is the volumetric efficiency,  $P_r$  the exhaust gasses pressure and  $T_r$  the temperature of the exhaust gases. Finally, the compression temperature is calculated for every time-step (being the resolution of the shaft encoder  $0.36^\circ\text{CA}$ ) from the following equation:

$$T_{i+1} = T_i \cdot \left( \frac{P_i}{P_{i+1}} \right)^{\frac{1-n_1}{n_1}} \quad [5-25]$$

### Calibration results

Prior to the tests the validity of the assumptions concerning the calibration system has to be checked. Checking procedures dictates that the engine should operate at constant conditions, and these are 1,500 rpm and wide-open throttle (WOT). The engine is then fed with uniform mixture prepared in the mixing chamber, and 50 (flat-field) images are acquired at 250°CA ATDC (after Top Dead Centre or 110°CA Before Top Dead Centre @1bar, 355°K) with the cylinder illuminated with a constant incident laser sheet of 70mJ/pulse power. Acquisition is repeated for various tracer concentrations, which ranged from zero to 1.5 times of the maximum used during the experiments (0.28 mole/m<sup>3</sup>). The average greyscale values of the illuminated image region are then plot against the calculated tracer number density after being normalised against maximum values. The above-described procedure had been previously followed by researchers in the same engine utilising the existing setup [115, 138]. Their findings are illustrated in Figure 5.10a and can be used in the present study since the research engine and experimental arrangement are kept identical. The results follow a linear trend with small deviations from the trend line throughout the investigated range, which is in agreement with [124] and furthermore demonstrates that the pre-mixing chamber is functioning satisfactorily. Finally, it is also evident that self-quenching of 3-pentanone is insignificant.

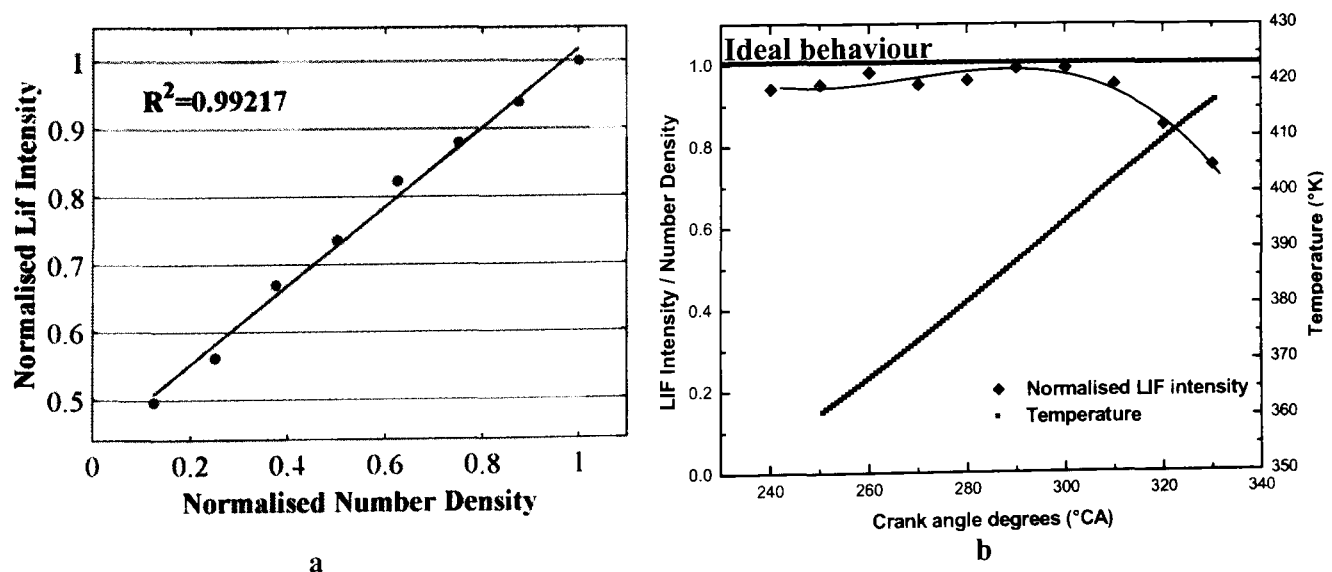


Figure 5.10: Calibration results. (a). [115]

The combined effect of temperature and pressure upon the signal behaviour is also investigated. The engine is once more fed with a homogeneous mixture at constant tracer concentration and images are acquired at ten different crank angles ranging from IVC position ( $120^\circ$  BTDC) to  $30^\circ$  BTDC. The laser output is kept constant at 70mJ/pulse as well as the camera and intensifier settings. Only the illuminated region of the last crank angle is used for the calculation of the average level in all of the images in order to avoid biasing effects owing to laser profile heterogeneities. The results divided to the corresponding number density and normalised to the maximum value are plotted against crank angle along with the compression temperature in Figure 5.10b. Assuming no sensitivity of the fluorescence yield upon thermodynamic in-cylinder properties, the LIF to concentration ratio should be constant and close to 1 (normalised). Observing the plot (black line), it is evident this is true up to  $60^\circ$  BTDC (within 5%). As the piston approaches TDC though the relative signal level progressively drops and by  $30^\circ$  BTDC a 25% drop is encountered. Similar behaviour has been reported in [124] and is attributed to the temperature dependence of the signal at the high temperature region. Considering that the blow-by of the engine is insignificant and that the signal loss is of the order of 12%/100°K a value close to the quoted temperature dependence of 3-pentanone, it can be inferred that this is also true in this particular case. Although the determination of the temperature dependence under various pressure conditions would be otherwise necessary, the insitu calibration technique used reduces its significance considerably as signal referencing is performed under the same thermodynamic conditions to those during data acquisition. Furthermore, although the relative signal loss is considerable towards TDC, the higher absolute light levels recorded owing to the increased number density lead to improved signal to noise ratio at these crank angles. On the other hand, temperature dependence can still introduce uncertainties in the measurement owing to non-uniform temperature distribution within the cylinder.

### 5.3 EXPERIMENTAL RESULTS

Until now the injector internal flow and multi-hole spray characteristics have been investigated under various operating conditions. As mentioned previously, the high-pressure spray interaction with the in-cylinder airflow is quite complicated in DISI engines and therefore, fuel vapour distribution measurements should be performed.

Due to the direct dependence of the latter on the in-cylinder spray development, both, liquid and vapour phases of the fuel have been acquired. In addition to that, this investigation focuses on homogeneous as well as stratified engine operating modes, since a single injector configuration should be able of performing adequately in both cases.

Two multi-hole injector geometries have been chosen to demonstrate their ability in creating a combustible mixture, according to engine's operating conditions. More specifically, these are the thoroughly investigated 12-hole nozzle that features an overall spray cone angle of  $90^\circ$  and a six-hole nozzle featuring a  $40^\circ$  overall spray cone angle. The reason of employing a narrow angle injector, which has not been previously investigated, is the extensive cylinder walls wetting resulting from a  $90^\circ$  nozzle. More specifically, the engine's bore is 73mm and a wide spray cone angle of  $90^\circ$  combined with the increased spray tip penetration length of the six-hole injector, relative to the 12-hole nozzle, cause severe liner wetting. The latter is undesirable, since it is a potential source of increased unburned hydrocarbon emissions. Finally, extensive investigations on several multi-hole nozzle designs have increased the knowledge on spray development mechanisms and grouped multi-hole injectors mainly according to the number of holes. Thus, it is safe to assume that sprays from  $90^\circ$  and  $40^\circ$  six-hole nozzles share similar spray development characteristics and the only difference could be located in the narrower fuel liquid distribution and the slightly weaker air-entrainment intensity present in the case of the  $40^\circ$  spray cone angle nozzle.

This chapter is divided in two major sections according to engine operation, which are homogeneous and stratified. In homogeneous engine operation, injection timings are set to be during the induction stroke of the engine, for achieving the best possible air / fuel mixing and improving the volumetric efficiency due to charge cooling. In all homogeneous test cases, the global engine AFR is kept constant at the stoichiometric level that is around 15. On the other hand, stratified engine operation is achieved by injecting fuel during the compression stroke and after the inlet valves have closed. Elevated in-cylinder temperature and pressure conditions contribute in efficient fuel evaporation and the desired combustible air/fuel mixture is transported towards the two spark plugs by the weak in-cylinder flow, induced, mainly, by the piston movement. During stratified engine operation, the amount of fuel injected is less than

the stoichiometric level, resulting in a global AFR of 30, or, in some cases, as high as 40. The effectiveness of single, double and triple injection strategies have been investigated in both operating conditions. In addition to that, the effects of various levels of in-cylinder swirl flow and injection pressure on fuel vapour distribution have been quantified.

Throughout this chapter, the time-base for all experiments is referred to crankshaft angle degrees. The zero point is set to be the induction top-dead-centre (TDC), or, in other words, the start of induction stroke. More specifically, a timing of i.e.  $50^{\circ}\text{CA}$  effectively means  $50^{\circ}\text{CA}$  after induction top dead centre (AITDC). Following the same numbering rule,  $360^{\circ}\text{CA}$  is referred to compression TDC, or end of compression stroke. For example,  $300^{\circ}\text{CA}$  is translated to  $60^{\circ}\text{CA}$  before compression top dead centre. Fuel vapour distribution inside the engine's cylinder starts becoming critical at angles where the spark plug discharge should occur. These angles could vary from  $60^{\circ}\text{CA}$  before compression TDC to  $10^{\circ}\text{CA}$  after compression TDC, or, according to the numbering followed, from  $300^{\circ}\text{CA}$  to  $370^{\circ}\text{CA}$ . For visualisation purposes, the last clearly visible data image is taken at  $340^{\circ}\text{CA}$ ; later timings do not produce any valuable results.

### 5.3.1 Homogeneous stoichiometric engine operation

Homogeneous stoichiometric engine operation dictates a highly uniform vapour distribution in the combustion chamber. The injected fuel should be fully vaporised and very well mixed with the air present in the combustion chamber. The air / fuel mixture should then occupy the entire chamber without any local AFR abnormalities. More specifically, there should not be regions inside the combustion chamber featuring local AFR values significantly different than the stoichiometric value of 15. Although fuel vapour distribution images are mapped quantitatively according to the AFR values, it is really difficult to judge on homogeneity since a data image could never be characterised by a single colour value. The reason is that, in direct-injection spark-ignition engines, the level of homogeneity is never comparable to the one achieved by port-fuelled engines, where the air / fuel mixing starts in the inlet ports. Therefore, for homogeneous engine operation, it is decided to convert the image mapping from AFR values to normalised deviation of AFR value, as follows

$$Dev(AFR)_{ij} = \frac{\overline{AFR_{ij}} - AFR_{ij}}{\overline{AFR_{ij}}} \quad [5-26]$$

where

$$\overline{AFR_{ij}} = \frac{\sum_{i,j=1}^n AFR_{ij}}{n} \quad [5-27]$$

and  $AFR_{ij}$  is the air to fuel ratio at each pixel of the data image. Based on the previous formulas, the coefficient of variation of AFR in an image gives a clear indication on the “level of homogeneity” achieved. According to

$$C.O.V.(AFR) = \frac{\sqrt{\sum_{i,j=1}^n (AFR_{ij} - \overline{AFR_{ij}})^2}}{\overline{AFR_{ij}}} \quad [5-28]$$

the smaller the value of  $C.O.V.(AFR)$  for an image, the more homogeneous the mixture distribution in that image.

The test cases for homogeneous stoichiometric engine operation have been chosen according to injection timings. Four distinct groups of injection timings have been created, starting from 50°, 70°, 90° and finally, 120°CA. At each one of the four groups, single, double and triple injection strategies have been applied, by setting the first injection timing constant at the group’s characteristic timing and varying the timing of the subsequent injection events. At all cases, several injection pressures and in-cylinder airflows have been tested for two different engine speeds at engine full load (wide open throttle – WOT). Summaries of the investigated conditions at both engine speeds are presented in Table 5-1 and Table 5-2.

Engine Speed = 1500RPM				
Injection Timing [°CA]	10(12-2) + 1 central holes (90°)		6-holes (40°)	
	80bar	120bar	80bar	120bar
30	SCV90	-	-	-
30-54	SCV90	-	-	-
50	SCV90/60/0	SCV90/60/0	SCV90	-
50-80	SCV90/60/0	SCV90/60/0	SCV90	-
50-180	SCV90/0	-	-	-
50-220	SCV90/60/0	SCV60/0	SCV90	-
50-70-90	SCV90/60/0	SCV90/60/0	-	-
50-70-180	SCV60	-	-	-
50-70-220	SCV90/60/0	SCV90/60/0	-	-
50-180-220	SCV90/0	SCV90	-	-
70	SCV90	-	SCV90	-
70-100	SCV90	-	SCV90	-
70-180	SCV90	-	SCV90	-
70-220	SCV90	-	SCV90	-
70-90-110	-	-	SCV90	-
70-90-180	-	-	SCV90/0	SCV90
70-90-220	-	-	SCV90	-
90	SCV90	-	SCV90/0	SCV90
90-120	SCV90	-	SCV90/0	SCV90
90-180	SCV90	-	SCV90/0	SCV90
90-220	SCV90	-	SCV90	-
90-110-130	-	-	SCV90	-
90-110-180	-	-	SCV90/0	SCV90
90-110-220	-	-	SCV90	-
120	-	-	SCV90/0	SCV90
120-150	-	-	SCV90/0	SCV90
120-180	-	-	SCV90/0	SCV90
120-220	-	-	SCV90	-
120-140-160	-	-	SCV90	-
120-140-180	-	-	SCV90/0	SCV90
120-140-220	-	-	SCV90	-

Table 5-1: Experimental cases for the in-cylinder LIF investigation at 1500rpm engine speed. – SCV90 stands for swirl control valve fully open (no swirl), SCV60 for 60degrees opening (medium swirl) and SCV0 for fully closed (high swirl).

Engine Speed = 3000RPM					
Injection Timing [°CA]	10(12-2) + 1 central holes (90°)			6-holes (40°)	
	60bar	80bar	120bar	80bar	120bar
50	-	SCV90/0	SCV90	SCV90/0	SCV90
50-90	-	SCV90/0	SCV90	SCV90/0	SCV90
50-220	-	SCV90	-	SCV90/0	SCV90
50-90-120	-	SCV90/0	-	SCV90/0	SCV90
70	SCV90	SCV90/0	SCV90	SCV90/0	SCV90
70-110	-	SCV90/0	SCV90	SCV90/0	SCV90
70-140	-	-	-	SCV90	-
70-180	-	-	-	SCV90	-
70-220	-	SCV90/0	SCV90	SCV90/0	SCV90
70-110-140	-	SCV90/0	SCV90	SCV90/0	SCV90
70-110-180	-	-	-	SCV90	-
70-110-220	-	-	-	SCV90	-
90	-	SCV90/0	SCV90	SCV90/0	SCV90
90-130	-	SCV90	SCV90	SCV90/0	SCV90
90-180	-	-	-	SCV90	-
90-220	-	SCV90	-	SCV90/0	SCV90
90-130-160	-	SCV90/0	-	SCV90/0	SCV90
90-130-180	-	-	-	SCV90	-
90-130-220	-	-	-	SCV90	-
120	SCV90	SCV90/0	-	SCV90/0	SCV90
120-160	-	-	-	SCV90/0	SCV90
120-180	-	-	-	SCV90	-
120-220	-	-	-	SCV90/0	SCV90
120-160-190	-	-	-	SCV90/0	SCV90
120-140-220	-	-	-	SCV90	-

Table 5-2: Experimental cases for the in-cylinder LIF investigation at 3000rpm engine speed. – SCV90 stands for swirl control valve fully open (no swirl), SCV60 for 60degrees opening (medium swirl) and SCV0 for fully closed (high swirl).

Careful observation of the above table reveals the philosophy hidden behind the LIF experimental design. At first, the majority of test cases are done at 80bar injection pressure. Following the spray characterisation of the multi-hole nozzle injector, it is decided to focus on 80bar injection pressure, since the improvements in atomisation gained at 120bar do not justify such an energy loss. Secondly, experimental cases of the 12-hole nozzle are found to be at early injection timings (30-70°CA), while almost the opposite trend is observed for the 6-hole injector. This happens because of the difference in the overall spray cone angle. More specifically, wide cone angles (i.e. 90° of the 12-hole nozzle) lead to extensive liner wetting when injection timing is retarded towards values greater than 70°. At earlier injection timings, liner wetting is

avoided due to the piston position that acts as a shield! On the other hand, narrow spray cone angles, i.e.  $40^\circ$  of the 6-hole nozzle, favour late injection timings because liner wetting is by default avoided and piston wetting is minimised. In general, fuel impingement on the piston crown is less harmful than fuel impingement on the cylinder walls. The latter causes increased hydrocarbon emissions and affects, in the long term, engine lubrication [3, 17, 27, 96].

### Injection timing

Multi-hole injectors are known to have stable spray structure under various operating conditions. As discussed in previous chapters, overall spray cone angle remains close to the nominal design value with increasing chamber pressure; thus early and late injection during an engine's cycle appear to have almost identical spray shape, affecting only spray's penetration in the combustion chamber. Therefore, injection timing mainly controls wall-impingement. As illustrated in Figure 5.11, for the 12-hole injector, early injection timings lead to fuel impingement on the piston, while later injection timings result in liner wetting. The fuel liquid concentration images presented are taken at 1,500rpm engine speed and the mapping is done according to light intensity. In a similar manner, Figure 5.12 illustrates fuel liquid concentration for the 6-hole nozzle. It is obvious that there is not any fuel in contact with the cylinder walls and piston impingement is avoided when injection timings are set at values later than  $70^\circ\text{CA}$ .

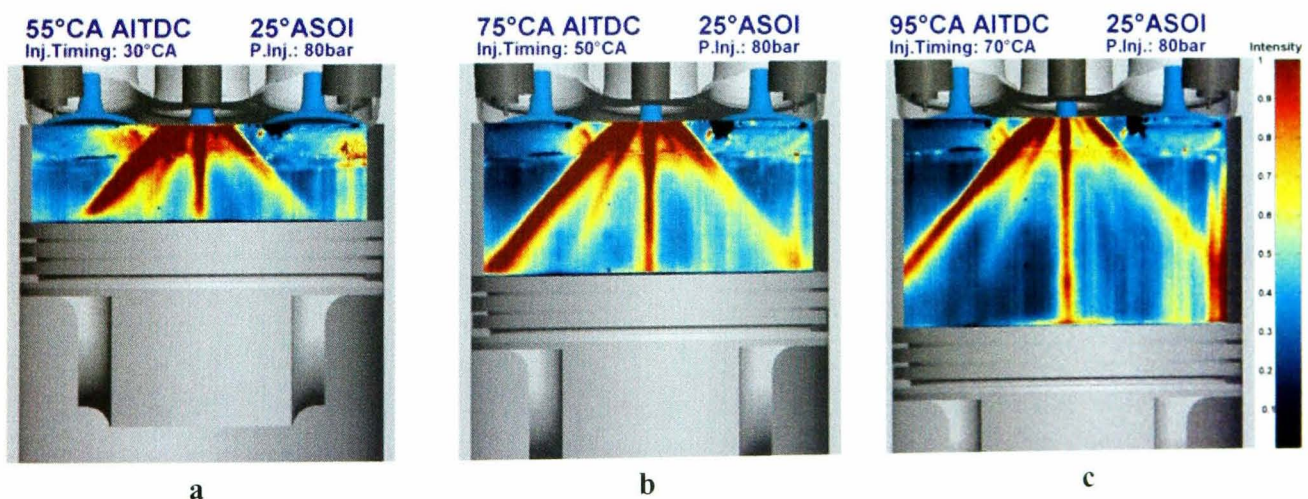


**Figure 5.11: Fuel liquid concentration at  $25^\circ\text{CA}$  ASOI for the 12-hole nozzle at injection timings of (a).  $30^\circ$ , (b).  $50^\circ$  and (c).  $70^\circ\text{CA}$ .**

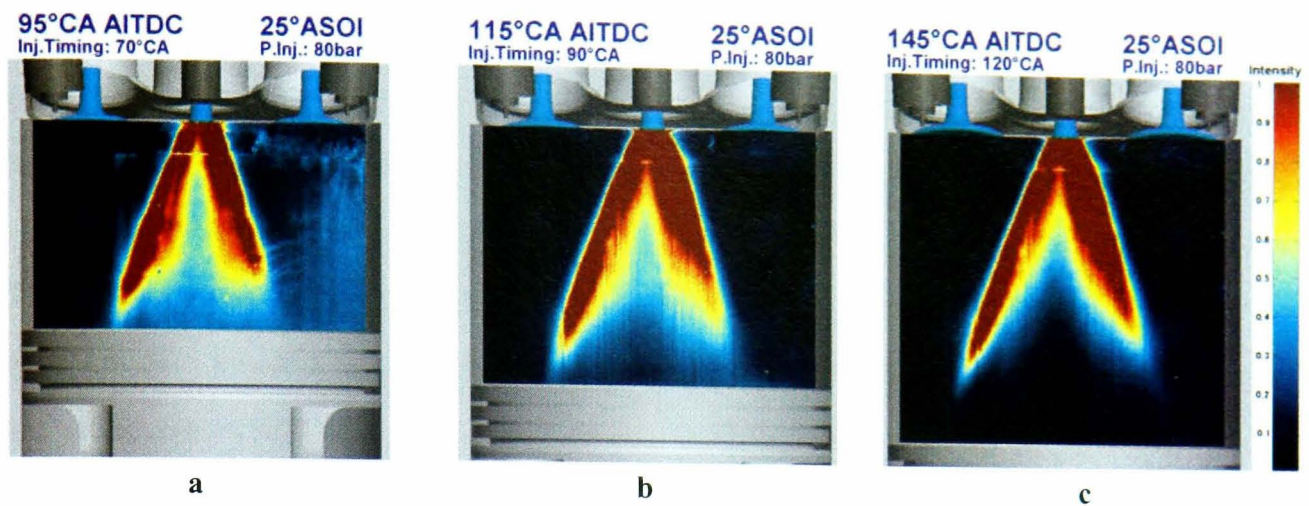


Figure 5.12: Fuel liquid concentration at 25°CA ASOI for the 6-hole nozzle at injection timings of (a). 70°, (b). 90° and (c). 120°CA.

The aforementioned effect of injection timing, on fuel impingement on piston and cylinder surfaces, is immediately mirrored on the vapour distribution images at, or near, the time of ignition. More specifically, at 1,500rpm engine speed the most uniform fuel vapour distribution is achieved at 30°CA injection timing for the 12-hole and at 120°CA for the 6-hole injectors. As illustrated in Figure 5.13, the homogeneity becomes worse as injection timing is retarded (from left to right), for the 12-hole nozzle. The injection duration for achieving stoichiometric charge is roughly 35°CA (including injector opening delay) at 1,500rpm engine speed, considering the flow rate of the 12-hole injector. This fact leads to an end of injection (EOI) timing around 65°CA after TDC. As a result, there is enough time left for the fuel to vaporise completely of the piston surface and form a uniform ignitable mixture cloud around the vicinity of the spark-plug locations at the time of ignition (~330-360°CA).



Figure 5.13: Two-dimensional deviation of air/fuel ratio (AFR) distribution at 340°CA (20° before compression TDC) of the 12-hole injector at injection timings of (a). 30°, (b). 50° and (c). 70°CA.

As the injection timing is retarded at  $50^\circ\text{CA}$  after TDC, always having the SCV fully open (no swirl), liner wetting appears towards the end of injection, it is minimum though. The effective time for mixing is reduced at this case and it can be seen in the 2-D AFR distribution image taken at  $340^\circ\text{CA}$ , otherwise  $20^\circ\text{CA}$  before compression TDC. There is an AFR gradient along the laser path; mixture distribution, from left to right, appears slightly lean in fuel in the beginning and passed the centre line of the liner, it becomes richer.

The opposite trend is recorded for the 6-hole nozzle. According to Figure 5.14, fuel vapour distribution in the combustion chamber becomes more uniform as injection timings become retarded. Although liner wall wetting is not an issue with the narrow spray from the 6-hole injector, fuel impinging on the flat piston crown is evident. Starting from  $70^\circ$ ,  $90^\circ$  and finally  $120^\circ\text{CA}$  injection timings, the effect of fuel impinging on the piston is evident on AFR distribution across the centre plane of the cylinder. At early timings, such as  $70^\circ\text{CA}$  after TDC, piston impingement rules the final fuel vapour distribution. More specifically, most of the fuel injected lies on the piston and evaporation starts from the hot piston surface as compression temperature rises; a very similar mechanism to what was mentioned before, for the case of early injection of the 12-hole injector. As a result, fuel vapour distribution between the two nozzle designs is comparable and features areas rich in fuel and steep AFR gradients across the plane of the image. Although the 6-hole nozzle produces a more compact and narrow spray shape, compared to that of the 12-hole injector, areas rich in fuel, at the time of ignition, can be found at the sides of the cylinder. Airflow does not



**Figure 5.14:** Two-dimensional deviation of air/fuel ratio (AFR) distribution at  $340^\circ\text{CA}$  ( $20^\circ$  before compression TDC) of the 6-hole injector at injection timings of (a).  $70^\circ$ , (b).  $90^\circ$  and (c).  $120^\circ\text{CA}$ .

enhance atomisation and ultimately evaporation at 1,500rpm, as mentioned before, due to the weak inlet flow imposed by the three-valve configuration of the cylinder-head and increased penetration momentum of the individual fuel jet plumes. Therefore, the mechanism that justifies transportation of vapour clouds to the sides of the cylinder can be found in the spray itself. The last two cases in Figure 5.14 stand for 90° and 120°CA injection timings. Deviation of AFR is not as uniform as expected, but the contrast between too rich and too lean, in fuel areas, is missing. This happens mainly due to the fact that there is no fuel impinging on the piston in both cases.

At higher engine speeds, the stronger airflow present inside the cylinder, even with the three-valve configuration, makes the differences in mixture distribution much smaller. The large-scale bulk in-cylinder airflow, at 3,000rpm, maximises air / fuel mixing significantly. As illustrated in Figure 5.15, for the 12-hole nozzle (top row), the strong airflow reduces spray tip penetration by increasing air-entrainment. Similarly, for the compact spray of the 6-hole nozzle, air-entrainment is efficient as injection timing approaches the timing of the inlet valves maximum lift (~100°CA).

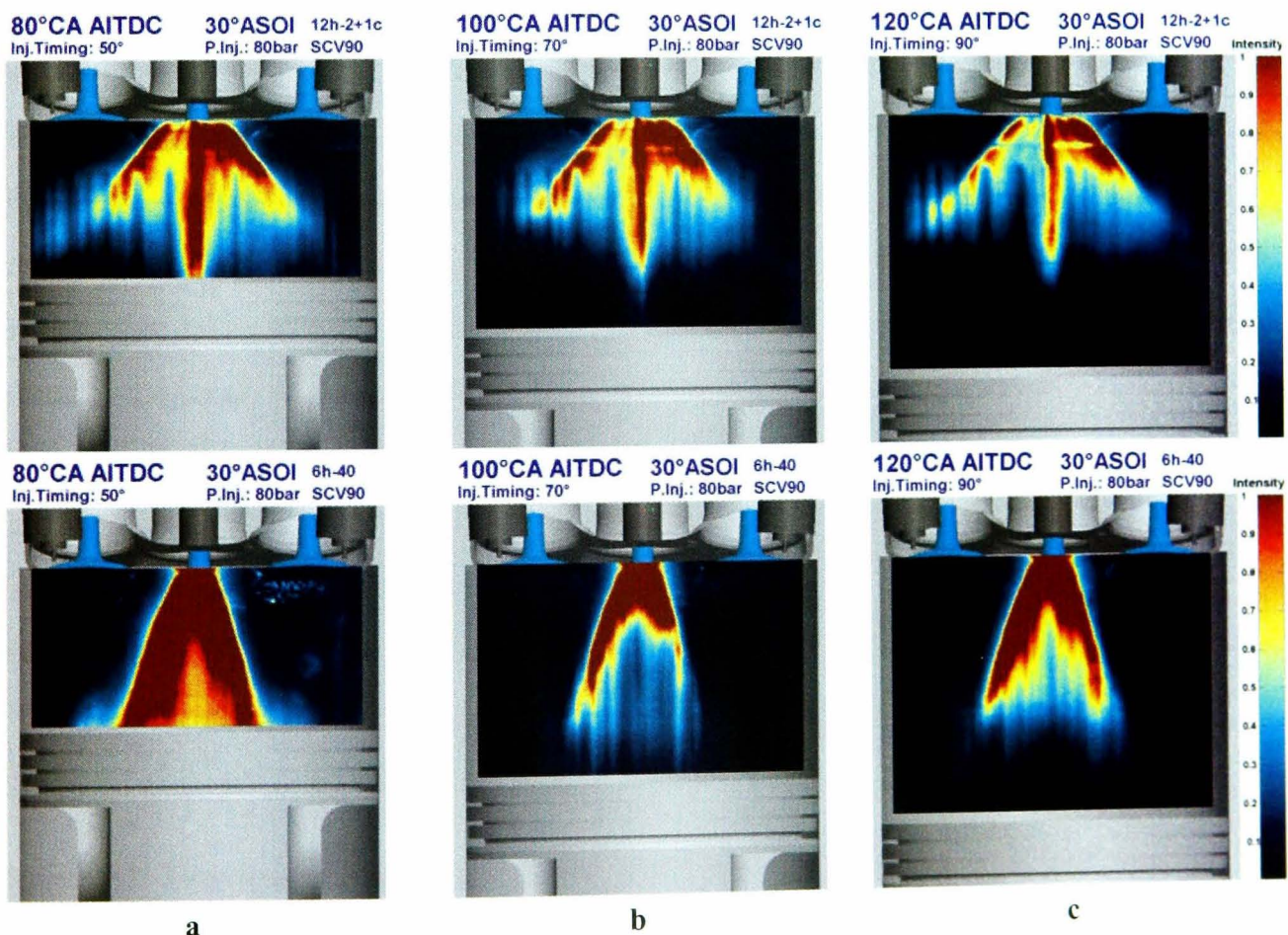


Figure 5.15: Fuel liquid concentration at 30°CA ASOI for the 12- (top row) and the 6-hole (bottom row) nozzles at injection timings of (a). 50°, (b). 70° and (c). 90°CA.

The minimum spray impingement on combustion chamber surfaces is immediately visible on fuel vapour distribution. More specifically, for the 12-hole injector, the best injection timing for achieving homogeneous charge is still  $50^{\circ}\text{CA}$ , although the differences among the various injection timings are minimised, as illustrated in Figure 5.16.



Figure 5.16: Two-dimensional deviation of air/fuel ratio (AFR) distribution at  $340^{\circ}\text{CA}$  ( $20^{\circ}$  before compression TDC) of the 12-hole injector at injection timings of (a).  $50^{\circ}$ , (b).  $70^{\circ}$  and (c).  $90^{\circ}\text{CA}$ .

The aforementioned minimisation of the effect of injection timing on mixture distribution at high engine speeds is clearly evident for the 6-hole nozzle. The differences in homogeneity among  $50^{\circ}$ ,  $70^{\circ}$ ,  $90^{\circ}$  and  $120^{\circ}\text{CA}$  injection timings are negligible, as illustrated in Figure 5.17. Although  $90^{\circ}\text{CA}$  remains the best injection timing, as far as homogeneity is concerned, all other timings present comparable results. The latter is an important finding that renders the 6-hole nozzle the injector, which can operate in a significantly wide injection-timing window.



Figure 5.17: Two-dimensional deviation of air/fuel ratio (AFR) distribution at  $340^{\circ}\text{CA}$  ( $20^{\circ}$  before compression TDC) of the 6-hole injector at injection timings of (a).  $70^{\circ}$ , (b).  $90^{\circ}$  and (c).  $120^{\circ}\text{CA}$ .

## Multiple-injection

Multiple-injection is believed to be a powerful tool in the hands of engine manufacturers contributing to quick and efficient engine warm-up, as well as to reduced exhaust gas emissions during that period. Research groups worldwide have investigated double injection and the latter has been confirmed [17, 26, 34, 74, 97]. Apart from reduced warm-up emissions, multiple injection strategy can be seen as a way of reducing spray tip penetration lengths from high-pressure sprays. More specifically, the same amount of fuel injected by a single injection could be split into two or three smaller duration injection events, and as a result, the total spray penetration length is significantly reduced. Multiple-injection strategy is effectively the combined effect of injection timing and duration on final in-cylinder mixture distribution. Therefore, the benchmark for double or triple injection strategies investigated should be the corresponding single injection performance. The corresponding single injection event is defined as if multiple injections are replaced by a single injection that delivers the same amount of fuel and starts on the first injection timing.

Experiments at 1,500rpm engine speed showed that fuel impingement on cylinder and piston crown surfaces is not completely avoided, however it is significantly reduced, for both nozzles. More specifically, for the 12-hole nozzle, although double injection reduces wall wetting, the final fuel vapour distribution maps appear to be less uniform than the single injection event. This is believed to happen mainly due to the lack of airflow inside the engine cylinder. Multiple injections feature short spray tip penetration lengths, but air-entrainment process is interrupted. The repeated short-duration injections induce a weak airflow instead, which is not in favour of mixing for the double-pulsed injection. A better result is achieved when triple injection is employed. In the case of three injection pulses, the final air / fuel mixing appears to be similar to the one achieved by the single injection strategy. Finally, the presented AFR deviation images do not justify the use of multiple injection strategy in the case of a 12-hole nozzle. According to data images illustrated in Figure 5.18, there is not any improvement gained by double-injection in fuel vapour distribution relative to single injection at 30°CA with the 12-hole nozzle, which presented the best homogeneity of all tested conditions at 1,500rpm engine speed.



**Figure 5.18:** Two-dimensional deviation of air/fuel ratio (AFR) distribution at 340°C AITDC (20° before compression TDC) of the 12-hole injector at double-injection strategy. The timing of the first injection in the sequence is set at 50°C CA (top row), at 70°C CA (middle row) and at 90°C CA (bottom row). The second injection timing is placed at (a). 30°CA after the start of the first injection event, (b). 180°CA, or bottom dead centre and (c). 220°CA, timing at which inlet valves have closed.

As mentioned before, triple injection strategy appears to assist the mixing procedure, presenting better results than the double-injection. As illustrated in Figure 5.19, two-dimensional AFR distribution of triple-injection, starting at 50°C CA, appears more homogeneous than double-injection, but there is not any improvement relative to single injection at the same timing.



**Figure 5.19:** Two-dimensional deviation of air/fuel ratio (AFR) distribution at 340°C AITDC (20° before compression TDC) of the 12-hole injector at triple-injection strategy. The timing of the first injection in the sequence is set at 50°C A, the second at 70°C A and the third injection timing is placed at (a). 90°C A and (b). 220°C A, timing at which inlet valves have closed.

The second tested multi-hole nozzle appears to be more tolerant to multiple injection strategy than the 12-hole design. More specifically, double-injection does not improve homogeneity, however it does not create significant abnormalities in mixture distribution. As illustrated in Figure 5.20, column a presents more homogeneous AFR distributions than columns b and c. In addition to that, top and bottom rows (group of 70°C A and 120°C A) appear to be in a better shape, as far as homogeneity is concerned. The aforementioned observation, coupled with the fact that at 1,500rpm engine speed the best AFR distribution for the 6-hole nozzle is achieved at 90°C A injection timing by single injection, draws the conclusion that double-injection strategy increased homogeneity in cases, where there was room for improvements. In other words, double-injection assisted in blunting the differences among that three injection timings. Finally, by careful observation of the 6-hole nozzle double-injection fuel vapour distribution images, a second conclusion is being drawn in terms of the relative timing of the two injection pulses and to what extent the final AFR distribution is affected. In Figure 5.20a the dwell time between the two injection pulses is set to minimum possible value, according to the needle driving mechanism, thus the total injection event is finished as early as possible during the induction stroke. Early end-of-injection timings, by default, provide sufficient mixing time therefore increased homogeneity is expected.



**Figure 5.20:** Two-dimensional deviation of air/fuel ratio (AFR) distribution at 340°C AITDC (20° before compression TDC) of the 6-hole injector at double-injection strategy. The timing of the first injection in the sequence is set at 70°C A (top row), at 90°C B (middle row) and at 120°C C (bottom row). The second injection timing is placed at (a). 30°CA after the start of the first injection event, (b). 180°CA, or bottom dead centre and (c). 220°CA, timing at which inlet valves have closed.

A slightly different action is observed in triple-injection strategy, compared to double-injection. More specifically, as illustrated in Figure 5.21, triple-injection does not promote mixing at cases where the 6-hole nozzle traditionally does not perform well, i.e. 70°C A injection timing. On the contrary, by triple-injection, injection timings with acceptable homogeneity, as 90°C B and 120°C C, are further optimised. In general, a tendency of smoothing already homogeneous mixture distributions has been observed by triple-injection. Middle and bottom rows of Figure 5.21 illustrate

injection timings that start from  $90^\circ\text{CA}$  and  $120^\circ\text{CA}$  respectively. Single injection with the 6-hole nozzle has previously demonstrated acceptable homogeneity for the aforementioned cases. Triple-injection strategy has only managed to eliminate any steep AFR gradients present on the plane of the image, and transitions from slightly rich to slightly lean in fuel areas are done smoothly.

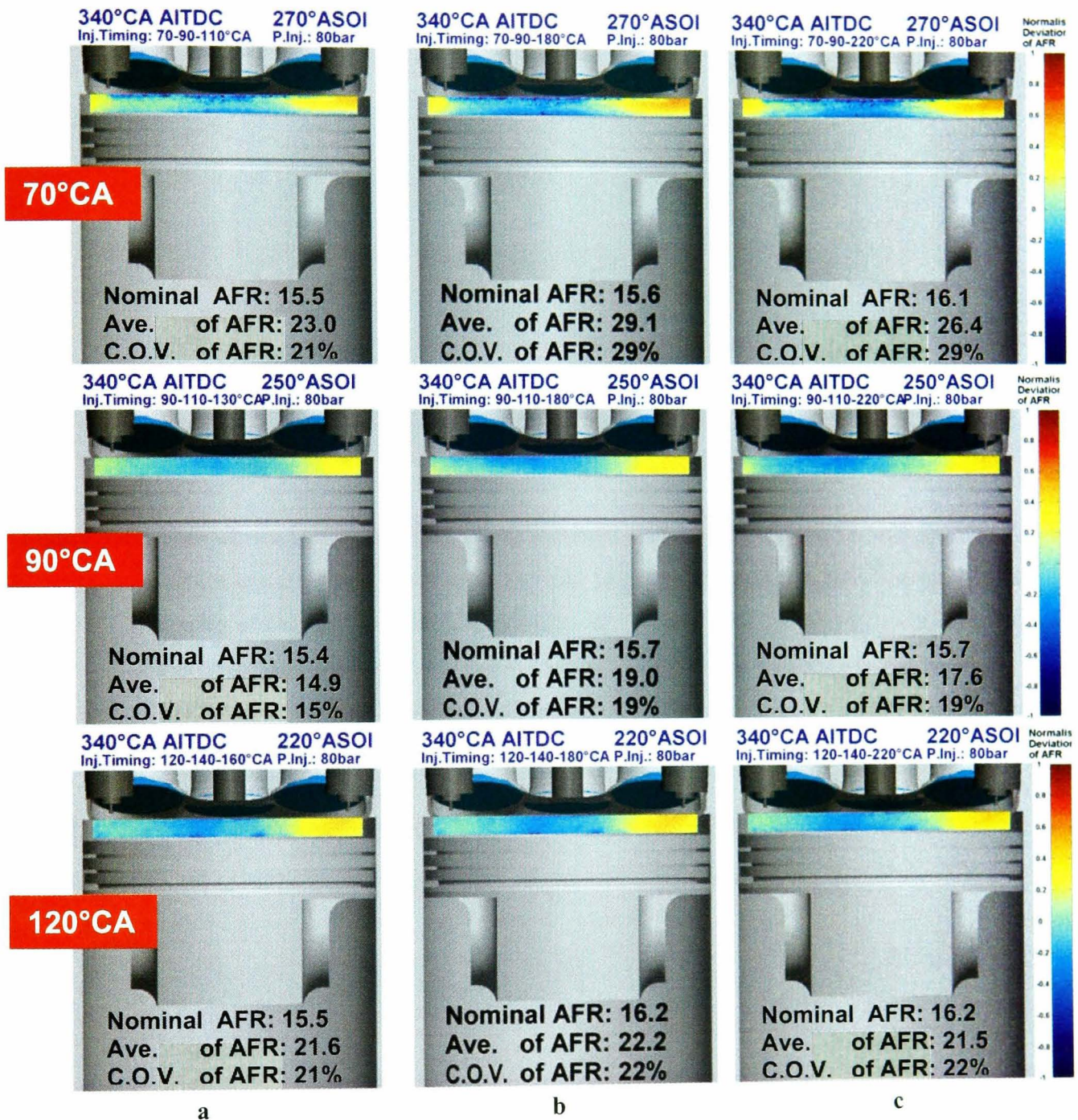


**Figure 5.21:** Two-dimensional deviation of air/fuel ratio (AFR) distribution at  $340^\circ\text{CA}$  ( $20^\circ$  before compression TDC) of the 6-hole injector at triple-injection strategy. The timing of the first injection in the sequence is set at  $70^\circ\text{CA}$  (top row), at  $90^\circ\text{CA}$  (middle row) and at  $120^\circ\text{CA}$  (bottom row). The second at  $20^\circ\text{CA}$  after the start of the first pulse and the third injection timing is placed at (a),  $20^\circ\text{CA}$  after the start of the second pulse, (b),  $180^\circ\text{CA}$  or bottom dead centre and (c),  $220^\circ\text{CA}$ , timing at which inlet valves have closed.

At higher engine speeds the previously observed situation is at a certain extent smoothed out. More specifically, at 3,000rpm, mixture distribution achieved with the 12-hole nozzle is fairly independent on injection timing. The high intensity bulk in-cylinder flow, induced by high-speed operation, produces mixture distribution of similar quality for timings of  $50^{\circ}\text{CA}$  to  $90^{\circ}\text{CA}$ . All double-injection tested cases appear moderate homogeneity, as illustrated in Figure 5.22 for the case of  $70^{\circ}\text{CA}$ .

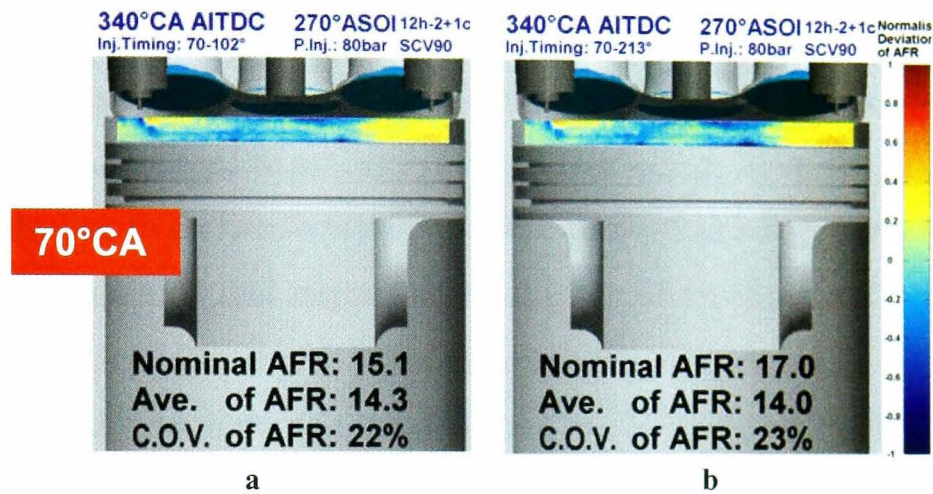


**Figure 5.22:** Two-dimensional deviation of air/fuel ratio (AFR) distribution at  $340^{\circ}\text{CA}$  ( $20^{\circ}$  before compression TDC) of the 12-hole injector at double-injection strategy. The timing of the first injection in the sequence is set at  $70^{\circ}\text{CA}$ , the second injection timing is placed at (a).  $30^{\circ}\text{CA}$  after the start of the first injection event and (b).  $213^{\circ}\text{CA}$ , timing at which inlet valves have closed.

Similar results are observed with triple-injection, as illustrated in Figure 5.23. All three groups of injection timing present comparable and moderate homogeneity.



**Figure 5.23:** Two-dimensional deviation of air/fuel ratio (AFR) distribution at  $340^{\circ}\text{CA}$  ( $20^{\circ}$  before compression TDC) of the 12-hole injector at triple-injection strategy. Injection timings of (a).  $50\text{-}90\text{-}120^{\circ}\text{CA}$ , (b).  $70\text{-}110\text{-}140^{\circ}\text{CA}$  and (c).  $90\text{-}130\text{-}160^{\circ}\text{CA}$ .

The 6-hole injector presented better homogeneity in 3,000rpm engine speed than in 1,500rpm. Both, double- and triple-injection strategies, coupled with the increased airflow of high engine speed, demonstrated acceptable 2-D AFR distribution maps. The achieved homogeneity proved to be independent of the relative timing of the multiple injection events. The preference of the 6-hole nozzle towards retarded injection timings is once more confirmed and the 6-hole injector has achieved, at 3,000rpm and 120° CA injection timing, the best possible homogeneity. As illustrated in Figure 5.24, the deviation of AFR in the centre plane of the cylinder is really stable and very close to stoichiometric. The two consistent rich in fuel spots observed do not represent real measured AFR ratios, but foreground noise. More specifically, at high engine speeds, due to high-velocity flow-fields, during induction and exhaust strokes there is a percentage of fuel impinging on the top of the liner, next to the valves. These two spots are located in a plane between the imaging plane and the camera, thus any scattered laser light could cause the small liquid pockets to fluoresce. The same effect is not visible during the background image acquisition since there is not fuel injection happening during that stage. Results from triple-injection strategy are not presented here, since the two-dimensional deviation of AFR is almost identical to the presented double-injection cases.



**Figure 5.24:** Two-dimensional deviation of air/fuel ratio (AFR) distribution at 340°C A (20° before compression TDC) of the 6-hole injector at double-injection strategy. Injection timings of (a). 70-213°C A, (b). 90-213°C A and (c). 120-213°C A.

## In-cylinder charge motion

So far, it has been proven that the lack of strong airflow is partly responsible for the poor mixing at low engine speeds, presented in previous sections of this paragraph. Given the fact that the five-valve engine features low tumble intake ports, an intake flow enhancement device has been installed that increases swirl levels in the cylinder. An interesting piece of equipment, offering the possibility of fully customisable swirl levels by varying the angle of a Swirl Control Valve (SCV). Introduction of moderate swirl (swirl control valve at an angle of  $60^\circ$ , relative to fully open position and zero swirl) immediately improved mixing and fuel vapour distribution. At low engine speeds (1,500rpm), where weak airflow rules mixture distribution, in-cylinder swirl improves mixing significantly, as illustrated in Figure 5.25. More specifically, in cases where acceptable homogeneity is achieved without in-cylinder swirl, the improvement in AFR distribution maps due to added swirl is minor. On the contrary, in cases similar to the one presented in bottom row of Figure 5.25, the improvement is significant.

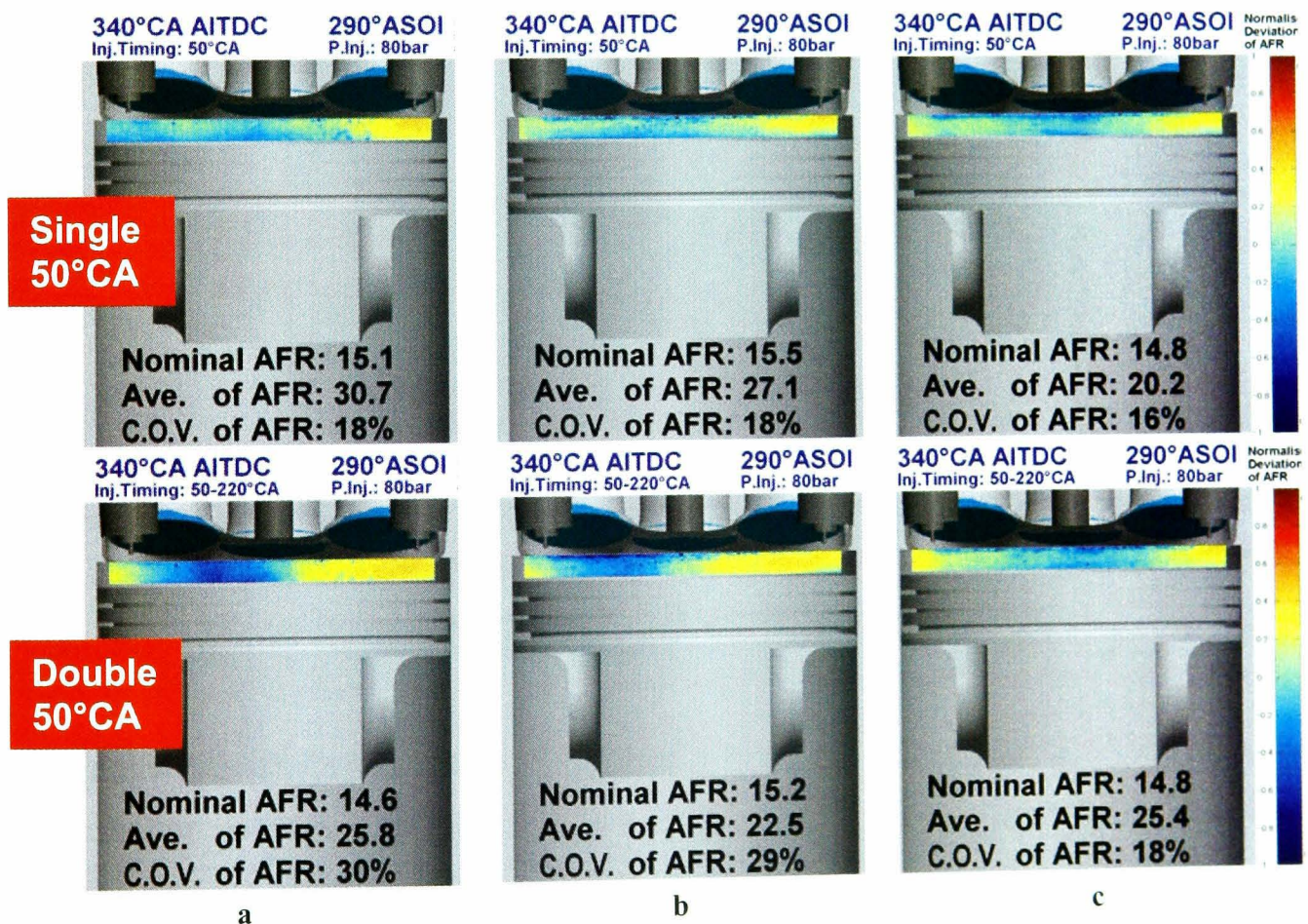
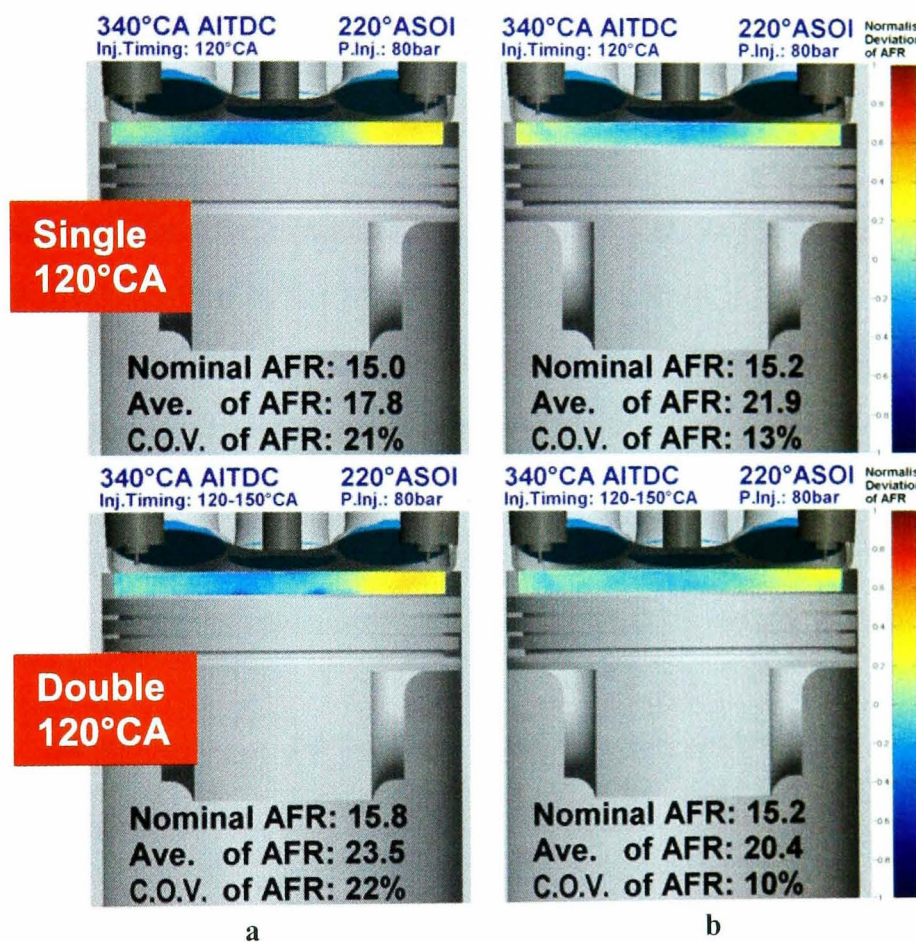


Figure 5.25: Comparison of three different in-cylinder swirl levels for the 12-hole nozzle operating at single- (top row) and double-injection (bottom row) conditions. (a). No swirl (SCV  $90^\circ$ ), (b). Medium swirl (SCV  $60^\circ$ ) and (c). Maximum swirl (SCV  $0^\circ$ ) at  $50^\circ\text{CA}$  injection timing.

The 6-hole injector demonstrates similar dependencies on in-cylinder swirl motion to that of the 12-hole nozzle. Increased swirl levels tend to eliminate the effect of injection timing on the final AFR distribution and all timings and injection strategies feature almost identical fuel vapour distribution under maximum in-cylinder swirl flow. The only difference, compared to the 12-hole nozzle, is the level of homogeneity achieved. As illustrated in Figure 5.26b, for both single and double-injection strategies the AFR distribution is extremely smooth and the level of homogeneity is close to port-fuelled injection standards.



**Figure 5.26:** Comparison of two different in-cylinder swirl levels for the 6-hole nozzle operating at single- (top row) and double-injection (bottom row) conditions. (a). No swirl (SCV 90°) and (b). Maximum swirl (SCV 0°) at 120°CA injection timing.

At higher engine speeds, similar behaviour is observed. More specifically, final AFR distribution maps present increased homogeneity when swirl is introduced. Injection timing appears to have no apparent effect on mixing, since in-cylinder swirl is so intense that overshadows all other parameters, apart from the nozzle design. Similar to 1,500rpm engine speed, the 6-hole nozzle performs better than the 12-hole design, demonstrating better homogeneity, although the differences between the two nozzle designs are not quite significant.

## Injection pressure

According to findings presented in previous chapter, injection pressure increases atomisation quality and spray tip penetration for multi-hole nozzles. The latter is rather a disadvantage for successful implementation of multi-hole injectors in DISI engines, however increased atomisation quality has always been in favour of mixing. Based on previously presented data, it has been confirmed that an increase in injection pressure from 80 to 120bar improves atomisation, although that improvement is minor and does not justify the extra energy spent from the high-pressure fuel pump. The latter conclusion is drawn by spray characterisation experiments; therefore engine experiments are needed to promote that conclusion to a solid fact.

As aforementioned, the main injection pressure for LIF experiments is set to 80bar. However, the investigation of the effect of injection pressure on fuel / air mixing in an engine's cylinder involved pressures from 60 up to 120bar. The results confirm the expected trends, and increasing injection pressure contributes to a more homogeneous mixture distribution at the time of ignition under all tested nozzle designs. Figure 5.27 confirms the aforementioned observation and from left to right hand image the deviation of AFR becomes more uniform in the cylinder's centre plane.

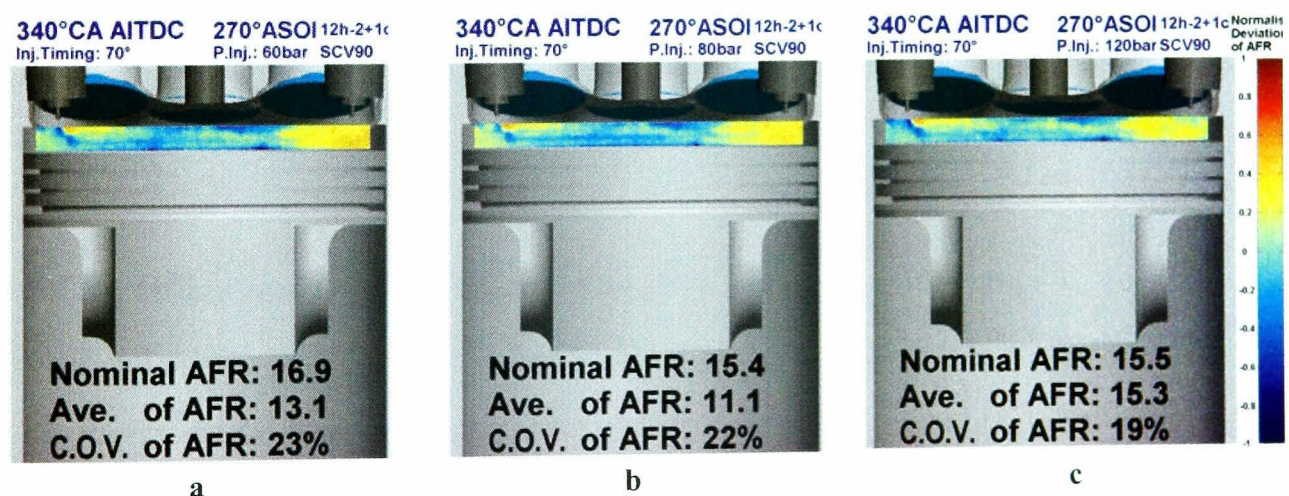


**Figure 5.27:** Two-dimensional deviation of air/fuel ratio (AFR) distribution at 340°C AITDC (20° before compression TDC) of the 12-hole injector injecting at 70°C A at (a). 60, (b). 80 and (c). 120bar injection pressure.

This slight improvement in homogeneity, with increasing injection pressure, becomes more pronounced at engine speeds where the bulk in-cylinder flow field is weak and the mixing is by default poor. More specifically, at 1,500rpm engine speed, the difference in air / fuel ratio distribution between 80 and 120bar injection pressure is

more evident than at 3,000rpm. As illustrated in Figure 5.28, at low engine speed higher injection pressure produces increased homogeneity, although this is not always valid for higher engine speeds.

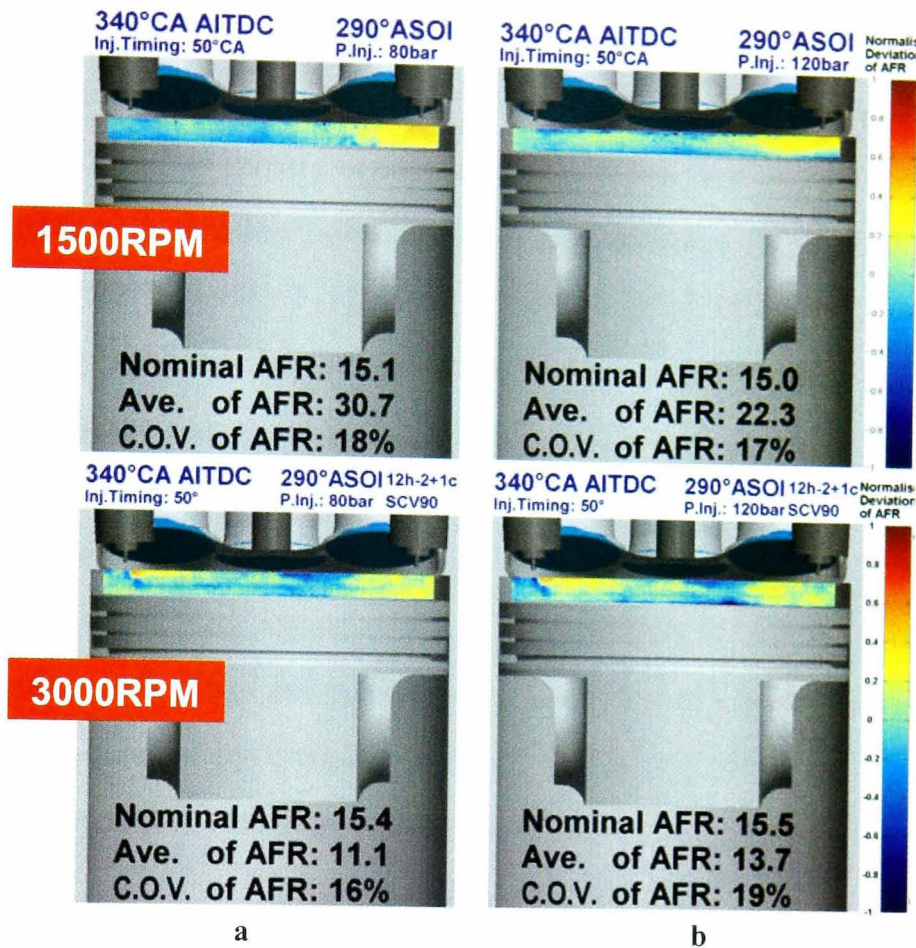


**Figure 5.28:** Two-dimensional deviation of air/fuel ratio (AFR) distribution at 340°C (20° before compression TDC) of the 12-hole injector at 1,500rpm (top row) and 3,000rpm (bottom row) engine speed. Injection timing is kept constant at 50°C and injection pressure is set to (a). 80 and (b). 120bar.

### 5.3.2 Stratified lean-in-fuel engine operation

Direct-injection spark-ignition engines are believed to be the way forward together with diesel engines, as far as vehicle power plants are concerned, due to the fuel consumption advantages these engines offer. Diesel powered engines alter their load by accurate controlling of the fuel quantity injected. Thus, fuel consuming intake throttling is not necessary. This technology is partly transferred to gasoline engines in an attempt to increase the low efficiency of spark-ignition engines. The advantages of such a technological upgrade in the conventional port-fuelled injection engines are vital for the environment and human health. More specifically, by direct injection of fuel into the cylinder of a spark-ignition engine, the accurate control of the injected fuel quantity and the ability of creating stratified charge in the combustion chamber

enable the realisation of combustion at AFRs higher than stoichiometric. Therefore, less fuel burnt leads to less  $\text{CO}_2$  produced, followed by reduction in all emitted pollutants in general. As aforementioned, stable combustion at AFR values higher than stoichiometric can only be achieved if the cylinder charge is highly stratified. The latter effectively means local AFR values richer than 15 ( $\text{AFR}_{\text{locally}} < 15$ ), while the rest of the cylinder is mostly occupied by air. Areas rich in fuel should be located around the spark plug area for the initiation of combustion.

It is immediately realised that stratification is highly dependent on the engine and combustion chamber design. It is the relative position of the injector and the spark plug that set the requirements for rich and lean in fuel areas. The five-valve, twin-spark engine design used in this study presents certain particularities in stratification due to the twin spark plug arrangement. As mentioned in previous sections, of this chapter, the two spark plugs are positioned at the two sides of the cylinder, thus good stratification is achieved by creating two rich in fuel regions at the two sides of the cylinder while the rest is very lean in fuel, as illustrated in Figure 5.29.

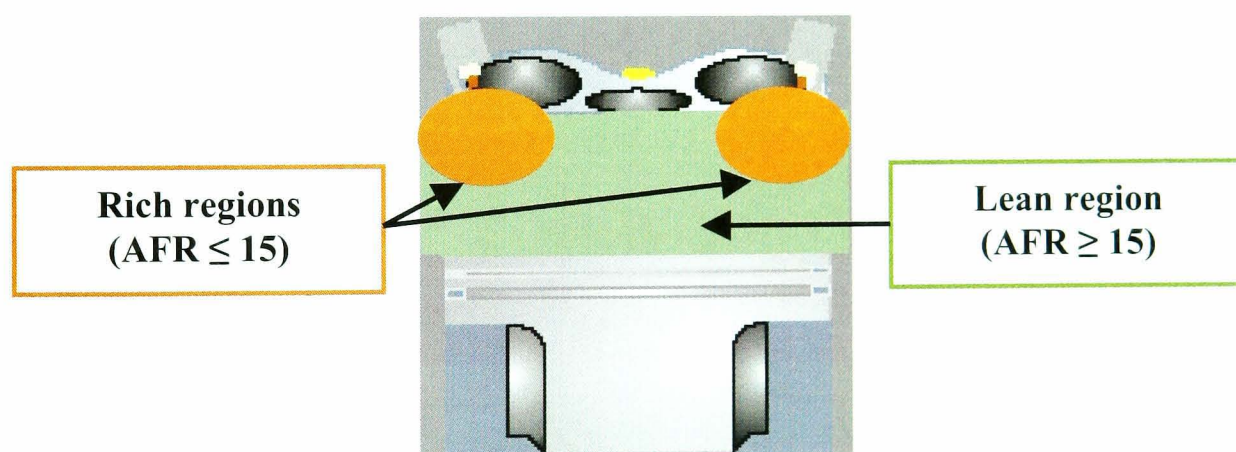


**Figure 5.29:** Schematic representation of the stratification concept for the five-valve twin-spark direct-injection gasoline engine.

In a direct-injection gasoline engine stratification is achieved by injection of fuel during the compression stroke. Under high-temperature and weak airflow conditions the fuel is vaporised but not mixed with the available air in the cylinder, instead it forms the required fuel vapour clouds. The parameters affecting the final vapour distribution inside the cylinder is the timing of injection event, injection strategy and pressure, as well as, in-cylinder airflow. Thus, the experimental study carried out included investigation of all the aforementioned parameters at two different engine speeds for two multi-hole nozzle designs. All experimental cases are presented in

Table 5-3 and Table 5-4. More specifically, for the low engine speed (1,500rpm) cases, the AFR is set constant at 35 for the case of 80bar injection pressure for two in-cylinder swirl levels (SCV90 – no swirl and SCV0 – swirl), while in the case of 120bar injection pressure the SCV is set to fully open position (no swirl) and the AFR is varied from 35 to 45. At higher engine speeds (3,000rpm), for 80bar injection pressure the investigation includes two swirl levels and two AFR values, while for the 120bar injection pressure there is no swirl and the AFR is set to 35.

<b>Engine Speed = 1500RPM</b>				
<b>Injection Timing [°CA]</b>	<b>10(12-2) + 1 central holes (90°)</b>		<b>6-holes (40°)</b>	
	<b>80bar</b>	<b>120bar</b>	<b>80bar</b>	<b>120bar</b>
<b>240</b>	SCV90	-	-	-
<b>240-255</b>	SCV90	-	-	-
<b>240-251-261</b>	SCV90	-	SCV90	-
<b>250</b>	SCV90/0	-	-	-
<b>250-265</b>	SCV90/0	-	-	-
<b>250-261-271</b>	-	-	SCV90	-
<b>260</b>	SCV90	-	-	-
<b>260-275</b>	SCV90	-	-	-
<b>270</b>	SCV90/0	AFR 35 / 45	SCV90/0	AFR 35 / 45
<b>270-285</b>	SCV90	AFR 35 / 45	SCV90/0	AFR 35 / 45
<b>270-289</b>	SCV90	AFR 35 / 45	SCV90/0	AFR 35 / 45
<b>270-306</b>	SCV90/0	AFR 45	SCV90/0	AFR 45
<b>270-281-291</b>	SCV90	-	SCV90	-
<b>280</b>	SCV90	AFR 35 / 45	SCV90	AFR 35 / 45
<b>280-295</b>	SCV90	AFR 35 / 45	SCV90	AFR 35 / 45
<b>280-299</b>	SCV90	AFR 35	SCV90	AFR 35
<b>280-306</b>	-	-	SCV90	-
<b>290</b>	SCV90/0	AFR 35 / 45	SCV90/0	AFR 35 / 45
<b>290-306</b>	SCV90/0	AFR 35 / 45	SCV90/0	AFR 35 / 45
<b>290-309</b>	SCV90/0	AFR 35 / 45	SCV90/0	AFR 35 / 45
<b>300</b>	SCV90/0	AFR 35 / 45	SCV90/0	AFR 35 / 45
<b>300-315</b>	-	-	SCV90	-
<b>310</b>	SCV90	AFR 35 / 45	SCV90/0	AFR 35 / 45

Table 5-3: Experimental cases for the in-cylinder LIF investigation at 1500rpm engine speed. –

SCV90 stands for swirl control valve fully open (no swirl), SCV0 for fully closed (high swirl) and AFR 35 / 45 stands for two different AFR values.

Engine Speed = 3000RPM						
Injection Timing [°CA]	10(12-2) + 1 central holes (90°)			6-holes (40°)		
	80bar		120bar	80bar		120bar
	SCV90	SCV0	SCV90	SCV90	SCV0	SCV90
220-240-260	AFR35	-	-	AFR35	-	-
240	AFR35/45	-	-	AFR35/45	-	-
240-261-280	AFR35	-	-	AFR35	-	-
250	AFR35/45	AFR35	AFR35	AFR35/45	AFR35	AFR35
250-275	AFR35/45	-	AFR35	AFR35/45	-	AFR35
250-285	AFR35/45	AFR35	AFR35	AFR35/45	AFR35	AFR35
250-302	AFR35	AFR35	-	AFR35	AFR35	-
250-271-290	-	-	-	AFR35	-	-
260	AFR35/45	AFR35	AFR35	AFR35/45	AFR35	AFR35
260-285	AFR35/45	-	-	AFR35/45	-	-
260-295	AFR35/45	-	-	AFR35/45	-	-
270	AFR35/45	AFR35	AFR35	AFR35/45	AFR35	AFR35
270-295	AFR35/45	-	AFR35	AFR35/45	-	AFR35
270-302	AFR35/45	AFR35	AFR35	AFR35/45	AFR35	AFR35
280	AFR35/45	AFR35	AFR35	AFR35/45	AFR35	AFR35
280-305	AFR35/45	AFR35	AFR35	AFR35/45	AFR35	AFR35
290	AFR35/45	AFR35	AFR35	AFR35/45	AFR35	AFR35
300	AFR45	-	AFR35	AFR45	-	AFR35

Table 5-4: Experimental cases for the in-cylinder LIF investigation at 3000rpm engine speed. –

SCV90 stands for swirl control valve fully open (no swirl), SCV0 for fully closed (high swirl) and AFR 35 / 45 stands for two different AFR values.

As presented in the previous tables, experimental cases include injection timings from 220°CA to 310°CA. Therefore, for better interpretation of the results, injection timings are grouped into early, medium and late compression timings. The first group involves injection from 220°CA to 250°CA, or during the early stages of the compression stroke. The second group features injection at timings from 260°CA to 280°CA and finally, late injection refers to timings beyond 290°CA. Vapour distribution images presented in this section have undergone certain port-processing and the local AFR ratio of each pixel is presented. The reason for not presenting the normalised deviation of AFR is the need to know local AFR values at the spark plug regions in order to be able to judge whether the mixture is ignitable or not.

### Injection timing

Early and late injection timings and single injection during compression stroke did not provide the expected results for both multi-hole injectors at 1,500rpm engine speed. In

turn, liner wetting and extensive piston impingement for early and late timings, respectively, caused undesired stratification. More specifically, for the late injection case, the lack of time available for vaporisation is evident, and causes the fuel to stick on the piston. Unlike early and late injection, very good results are obtained at medium injection timings. The relative position of the piston to the fuel spray is such that directs the mixture cloud towards the spark plugs. The time available for vaporisation is sufficient for both, free fuel spray and spray previously impinged on the piston. Figure 5.30 illustrates the AFR distribution images for the 12-hole nozzle and Figure 5.31 for the 6-hole.



Figure 5.30: Two-dimensional AFR distribution for the 12-hole injector at injection timing of (a). 240°CA, (b).270°CA and (c). 300°CA at 80bar injection pressure and 1,500rpm.



Figure 5.31: Two-dimensional AFR distribution for the 6-hole injector at injection timing of (a). 270°CA and (b). 300°CA at 80bar injection pressure and 1,500rpm.

It is evident from the above images that single injection at the late stages of the compression stroke is not in favour of stratification. Liquid fuel impinges on the piston and since the time available for vaporisation is not enough, fuel remains on the flat piston surface. In the case of the 12-hole nozzle, all the injected fuel seems to be

lying on the piston, while, in the case of the 6-hole nozzle, the poor liquid mass distribution and the almost non-existent air-entrainment result in a not fully vaporised fuel spray at the time of ignition. Early injection timing during the compression stroke is tested only for the 12-hole injector. The achieved stratification is better than that of late injection, but still there is a vapour cloud almost in the middle of the cylinder that will cause increased soot emissions, since it is away from the ignition source. Finally, medium injection timings appear to be promising, as far as stratification in a twin-spark engine is concerned. Both sides of the cylinder feature richer in fuel areas than the rest of the image area. Right-hand side spark plug appears to have always an ignitable mixture surrounding it, while the other side of the cylinder presents lean AFR distributions. Six-hole nozzle performs better than the 12-hole at medium injection timings due to the right delivery of an ignitable mixture cloud at both spark plugs.

At higher engine speeds, the performance of single injection, as far as stratification is concerned, does not change significantly for both nozzles. As illustrated in Figure 5.32, the most promising cases involve injection at medium timings during the compression stroke. Both nozzle designs manage to ensure slightly rich in fuel areas right at the two spark plug positions. More specifically, in the case of the 12-hole injector (top row), early injection timings tend to gather an ignitable fuel vapour cloud (AFR around 15) towards the right side of the cylinder, while the left-hand side remains lean in fuel. As injection timing is retarded towards  $260^\circ\text{CA}$ , a fuel vapour cloud of AFR around 16 is concentrated at the left spark plug ensuring that ignition will take place at both ignition sources. Late injection timings proved to be inefficient also at high engine speeds, since the fuel is not fully vaporised and remains on the piston surface. The 6-hole nozzle shows similar behaviour with the best stratification to be achieved at medium injection timings.



**Figure 5.32:** Two-dimensional AFR distribution for the 12-hole (top row) and the 6-hole (bottom row) injectors at injection timings of (a). 240°CA, (b).260°CA and (c). 300°CA at 80bar injection pressure and 3,000rpm.

### Multiple-injection

Double- and triple-injection strategies have also been investigated for both nozzle designs at low and high engine speeds. Double-injection is extensively tested in early and medium timings and triple mainly at early timings during the compression stroke. The reason is that multiple-injection generally delays the end of injection timing (EOI) leaving no time for evaporation when the EOI is placed at late crank angle degrees. The latter observation is confirmed in Figure 5.33, where AFR distribution images of double-injection of the 12-hole nozzle at 1,500rpm engine speed show that at late timings the resulted stratification is totally inappropriate for this particular engine design. Similarly to late timings, early double-injection during the compression stroke does not produce the required AFR distribution. On the contrary, 12- and 6-hole nozzles achieve acceptable stratification with double-injection at medium timings, as Figure 5.33b and Figure 5.34b illustrate. More specifically, both nozzles manage to transport the required fuel vapour clouds at the positions of the spark plugs. The 6-hole nozzle appears to be more efficient and it features ignitable mixture clouds (AFR: 14-16) below both spark plugs.



**Figure 5.33:** Two-dimensional AFR distribution for the 12-hole injector at double-injection strategy. Injection timings of (a). 240-255°CA, (b).270-285°CA and (c). 290-306°CA at 80bar injection pressure and 1,500rpm.



**Figure 5.34:** Two-dimensional AFR distribution for the 6-hole injector at double-injection strategy. Injection timings of (a). 270-285°CA and (b). 290-306°CA at 80bar injection pressure and 1,500rpm.

Due to the limited time available for the processes of injection, evaporation and ignition, the timing of the second injection in a double-injection sequence did not show any improved results. The AFR distribution maps presented above demonstrate that the best possible stratification for this engine design is achieved when the dwell time between the two injection pulses is set to minimum possible time dictated by the needle driving mechanism. Similar method is followed also at triple-injection strategy, where both dwell times are set to minimum possible and injection could only start at early and medium injection timings during the compression stroke. The 12-hole nozzle did not show any difference between double and triple-injection modes at the low engine speed and stratification does not help the twin-spark concept.

However, significant improvements are achieved with triple-injection and the 6-hole nozzle. As illustrated in Figure 5.35, both presented early triple-injection timings appear to create the desirable stratification at the time of ignition. In both cases vapour clouds of local AFR of 17 are created right at the spark plug locations. On the contrary, triple injection at medium timings during the compression stroke confirms that the later the EOI timing, the worse the stratification. The latter happens due to the limited time available for vaporisation and transportation of the vapour cloud towards the spark plugs. As it is presented in Figure 5.35c, most of the fuel lies on the piston surface and probably it has not vaporised completely.



**Figure 5.35:** Two-dimensional AFR distribution for the 6-hole injector at triple-injection strategy. Injection timings of (a). 240-252-263°C AITDC, (b).250-262-273°C AITDC and (c). 270-282-293°C AITDC at 80bar injection pressure and 1,500rpm.

At higher engine speeds the situation is not remarkably reversed. More specifically, at 3,000rpm, the 12-hole nozzle does not manage to create stable and ignitable vapour clouds at the vicinity of the spark plugs at either injection strategies, double and triple. A reasonable explanation for this behaviour could be the spray induced airflow that possibly forces the vapour clouds to off imaging plane positions that the imaging system cannot visualise. In addition to that, the very well distributed fuel spray mass achieved by the 12-hole injector initiates certain recirculation zones in the entire volume of the cylinder, which in turn, tends to transport the vaporised fuel at areas, which are out of interest. In all the images illustrated in Figure 5.36 and Figure 5.37, for double and triple-injection respectively, an ignitable mixture cloud is found only on side of the cylinder.



**Figure 5.36:** Two-dimensional AFR distribution for the 12-hole injector at double-injection strategy. Injection timings of (a). 250-275°CA, (b).260-285°CA and (c). 280-305°CA at 80bar injection pressure and 3,000rpm.



**Figure 5.37:** Two-dimensional AFR distribution for the 12-hole injector at triple-injection strategy. Injection timings of (a). 220-240-260°CA and (b).240-260-279°CA at 80bar injection pressure and 3,000rpm.

Unlike the 12-hole nozzle, the 6-hole design offers better stratification potential also at 3,000rpm engine speed. As illustrated in Figure 5.38, double injection at timings of 250° to 260°CA present the best stratification ever recorded in the five-valve twin-spark engine. These timings correspond to almost early injection timings during the compression stroke and feature two distinct vapour clouds of AFR values of around 14. At later injection timings of 270°, similar stratification cannot be achieved, as presented in Figure 5.38c. Careful observation of all three images presented concludes that the major part in achieving such stratification is contributed by the second injection timing in the sequence. When the latter is set at around 280°CA, the relative position of the piston combined with the spray-induced airflow contribute to the formation of the two ignitable mixture clouds at the regions of the two spark plugs.

Position of the second injection timing at crank angle degrees later than  $290^\circ$  does not provide the appropriate evaporation time and there is a cloud rich in fuel in the centre of the cylinder.



**Figure 5.38:** Two-dimensional AFR distribution for the 6-hole injector at double-injection strategy. Injection timings of (a). 250-285°CA, (b).260-285°CA and (c). 270-295°CA at 80bar injection pressure and 3,000rpm.

Similar results cannot be achieved with triple-injection. More specifically, Figure 5.39 illustrates that at triple injection there is not enough time for effective evaporation and transportation of the mixture clouds to the desired locations. The latter is concluded from the fact that the richer areas in the cylinder are appeared to be close or on the piston crown surface. A useful conclusion out of the triple-injection data is that the closer the injection timing to the 250-260°CA band, the more the vapour clouds tend to occupy the two sides of the cylinder. Although the available time for evaporation is still not sufficient and fuel is found on the piston surface, the already vaporised fuel has formed two rich areas at the spark plug positions (Figure 5.39c).



**Figure 5.39:** Two-dimensional AFR distribution for the 6-hole injector at triple-injection strategy. Injection timings of (a). 220-243-257°CA, (b).240-253-287°CA and (c). 250-273-297°CA at 80bar injection pressure and 3,000rpm.

Finally, it could be safely concluded that the six-hole nozzle is able of forming the desired stratification levels inside the cylinder of the five-valve, twin-spark ignition engine. This rather strange requirement of the two ignitable mixture clouds at the two sides of the cylinder is greatly accomplished with the help of double-injection. There have also been identified certain dependencies between the timing of the second injection event and the final AFR distribution maps.

### Injection pressure

As the results from spray characterisation experiments showed, an increase of injection pressure to 120bar does not improve spray atomisation significantly. Similar conclusion is also drawn by the LIF experiments. As illustrated in Figure 5.40, at both engine speeds, injection at 120bar does not improve the AFR distribution maps. Top row in the figure stands for injection at 270°CA at 1,500rpm engine speed and bottom row for injection at 260°CA at 3,000rpm. At both engine speeds increased injection pressure does not improve mixture distribution at the time of ignition. Therefore the effect of injection pressure on stratification is rather insignificant.

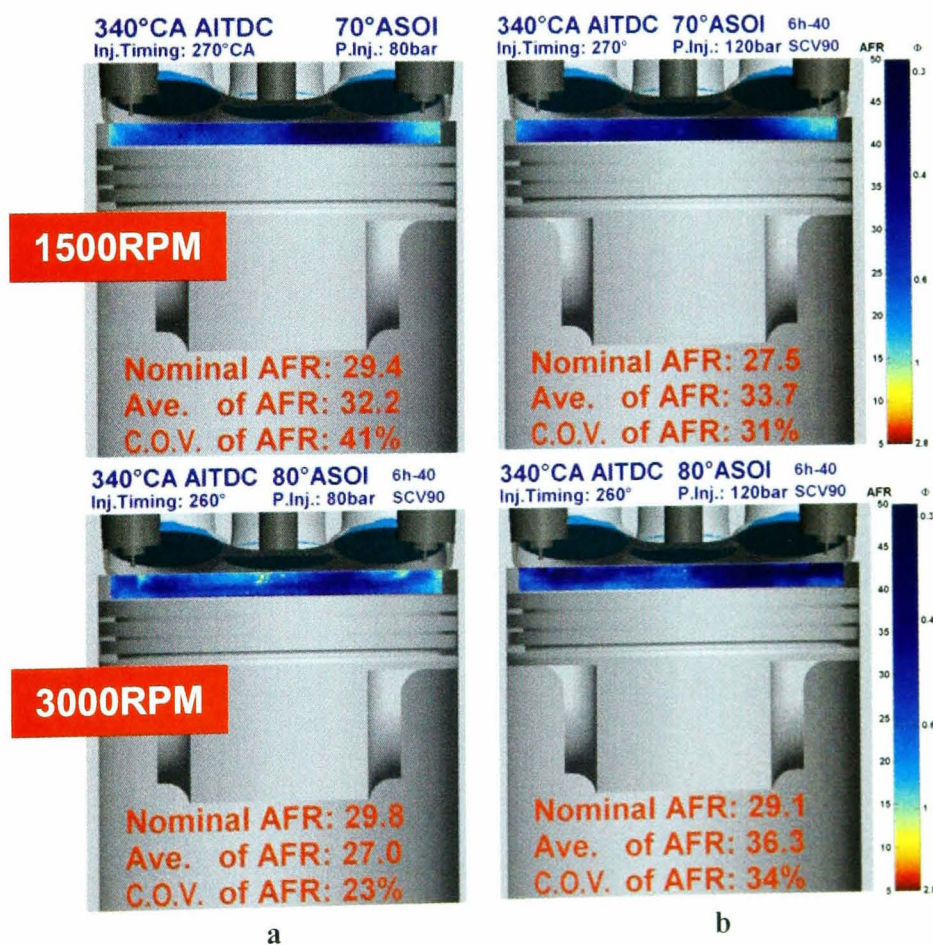


**Figure 5.40:** Two-dimensional AFR distribution for the 6-hole injector at low (1,500rpm – top row) and high (3,000rpm – bottom row) engine speed. Injection pressure of (a) 80bar and (b) 120bar at two different injection timings.

### In-cylinder charge motion

According to data presented in section 5.3.1, elevated swirl levels tend to distribute fuel vapour uniformly inside the cylinder. Therefore, increased in-cylinder swirl is expected to homogenise the mixture rather than to produce the desired stratification. This behaviour has been confirmed from the LIF results for both injectors. As mentioned before, stratification is achieved by injecting fuel during the compression stroke and after the closure of the intake valves. Even though the valves are closed, swirling motion is preserved in the cylinder losing some of its strength. Additionally, it has been proven that sprays from multi-hole injectors are rather insensitive to in-cylinder air motion due to their increased penetration momentum. Therefore, in-cylinder swirl under these conditions is not strong enough to affect the spray development. Moving one step forward, after the fuel has been completely vaporised, with swirling motion still present in the cylinder, the result would be homogenisation of the charge rather than stratification. The latter is observed at both engine speeds as illustrated in Figure 5.41. The weak swirl present in the cylinder during compression tends to gather vapour clouds in the centre, in the low-pressure region.

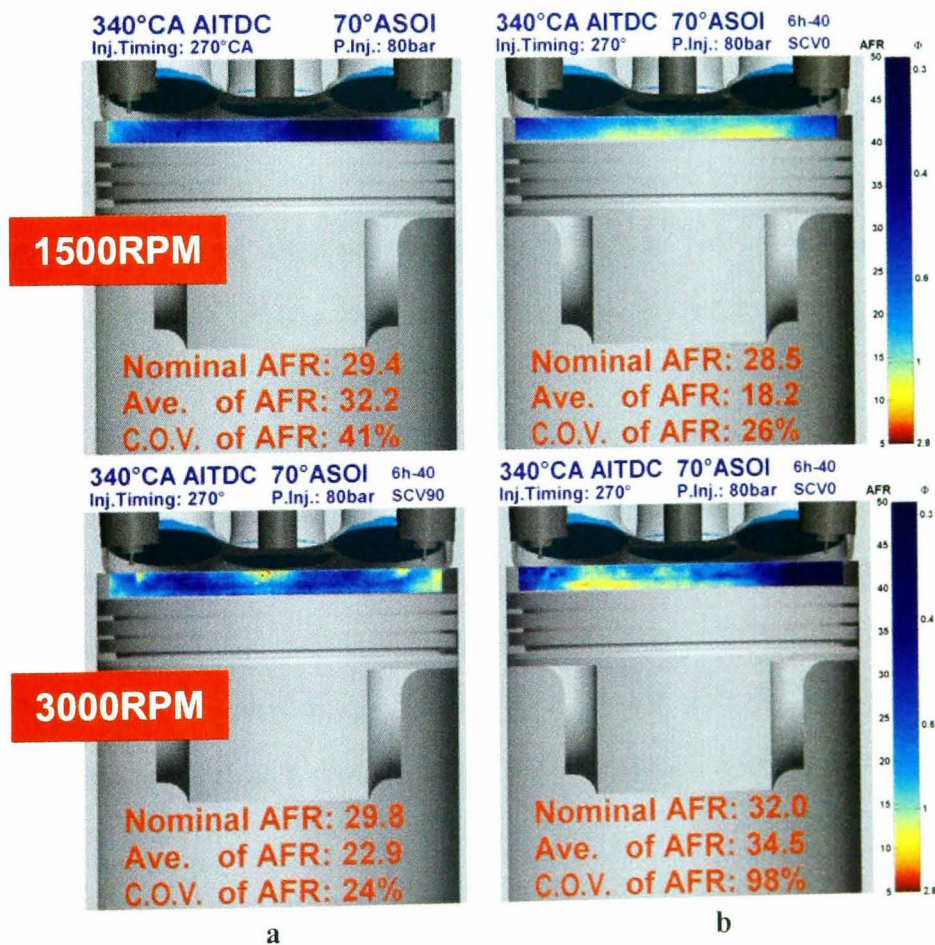


**Figure 5.41:** Two-dimensional AFR distribution for the 6-hole injector at low (1,500rpm – top row) and high (3,000rpm – bottom row) engine speed. Injection at 270°CA at 80bar for (a). SCV open (no swirl) and (b). SCV closed (high swirl).

## 5.4 SUMMARY

Laser induced fluorescence measurements proved to be a useful tool for detailed investigation of the potential of high-pressure multi-hole injectors in creating homogeneous as well as stratified mixture distributions in a five-valve twin-spark ignition engine. The motored single-cylinder optical engine used features a centrally mounted injector and two spark plugs located at opposite sides of the cylinder. Laser induced fluorescence quantified the fuel concentration and local air/fuel ratio along a central plane of the cylinder which was 6.5mm offset relative to the spark-plug plane.

The twin-spark combustion concept featuring central injection is generally offering advantages in HC and smoke emissions relative to its side-injection, wall-guided counterpart. Additionally, the previously observed problem of cocking in multi-hole injectors can be minimised due to reduced injector tip temperatures, as a result of twin-spark combustion. A second advantage of having two spark plugs installed is the reduced danger of spark plug fouling present in most spray-guided configurations. This is also ensured by the stable spray structure of multi-hole injectors and the flexibility they offer in nozzle design, which helps in matching closely the spray shape to engine specifications. The characteristics of multi-hole sprays, carefully evaluated recently, are the increased spray tip penetration relative to the swirl or hollow cone sprays from outwards opening nozzles. This can, unfortunately, lead to extensive impingement of the fuel on cylinder walls and piston. Although there are ways for controlling this characteristic; such as careful selection of injection timing, there will always be a small percentage of fuel impinging on the piston. On the other hand, the increased penetration momentum can make multi-hole sprays less sensitive to the in-cylinder air motion. This leads to simpler engine management system eliminating the need for accurate control of the airflow. Nevertheless, results presented here have shown that airflow is vital for effective mixing and improved homogeneity implying that a compromise may be needed for complete combustion.

Overall, multi-hole injectors have demonstrated their ability to produce homogeneous and stratified charge in a multi-valve twin-spark ignition engine. More specifically, it has been confirmed that injection timing controls wall impingement, resulting in quick and efficient evaporation for homogeneous engine operation. At low and high engine speeds, the 12-hole nozzle demonstrated increased homogeneity at injection

timings early in the induction stroke. This is mainly due to the fact that the increased spray cone angle ( $90^\circ$ ) of that injector resulted in extensive liner wetting at timings later than  $50^\circ\text{CA}$ . Therefore, early injection timings and the sufficient time they offer for evaporation and mixing, resulted in effective evaporation of the fuel previously impinged on the piston. On the contrary, the 6-hole injector that features a spray cone angle of  $40^\circ$  performed better at later timings of  $90^\circ$  and  $120^\circ\text{CA}$ . Since the possibility of fuel impinging on the cylinder walls is avoided, late injection during the induction stroke ensured that minimum quantity of fuel impinges on the piston surface.

Multiple-injection has also been tested. Double and triple-injection events have been found to reduce exhaust gas emissions during the engine warm-up period and assist the mixture formation process. However, double injection did not improve homogeneity at any tested conditions, unless at the high engine speed of 3,000rpm and 6-hole injector. The latter combination proved to be very effective and from early to late injection timings, the achieved homogeneity with double injection was slightly improved, compared to single injection cases. On the other hand, triple-injection appeared to be effective at low engine speeds. At 1,500rpm, triple-injection produced acceptable homogeneity for the 12-hole nozzle, while the most uniform mixture distribution is recorded for the 6-hole nozzle at the low engine speed and triple-injection. Finally, a summary of the effect of multiple-injection on homogeneity would rather conclude that double-injection is in favour of uniform mixture distribution at high engine speeds, while triple-injection performs better at low engine speeds.

Another factor affecting homogeneity is internal cylinder airflow. The five-valve cylinder-head configuration used in this study featured weak airflow at all engine speeds. Therefore, a swirl control valve is installed upstream the throttle valve, which effectively blocks the flow of two intake valves and redirects the entire intake flow through the third valve. The achieved in-cylinder swirl levels with this mechanism are high and in favour of mixing. Increased swirl assisted air / fuel mixing and resulted in a uniform AFR distribution at the time of ignition. The latter conclusion is valid for both multi-hole nozzle designs, at all tested engine speeds and injection timings. On the contrary, injection pressure did not produce significant improvements in

homogeneity. Comparison of the AFR distribution maps of 80 and 120bar concluded that the minor improvements in homogeneity do not justify the energy cost for increasing injection pressure to levels more than 80bar.

Following the investigation on homogeneous mixture distribution, the ability of multi-hole nozzles in creating stratification for lean in fuel combustion had to be explored. Overall, it has been confirmed that both multi-hole nozzles are able in achieving the desired stratification levels inside the twin-spark engine cylinder. The major parameter towards that direction is injection timing. As mentioned in previous sections of this chapter, the direct-injection twin-spark engine shares operating principles from spray-, as well as, wall-guided configurations, thus it is named piston-guided. Therefore, stratification is mainly controlled by the time the fuel spray impinges on the piston, which directs the mixture cloud towards the spark plugs. This timing is determined mainly by the injection timing. The latter plays the major role in achieving the desired stratification for both nozzle designs. The best timing for low and high engine speeds is located around  $260^{\circ}\text{CA}$ , or  $100^{\circ}\text{CA}$  before compression top dead centre. Earlier timings lead to false exploitation of the internal airflow, resulting in undesired stratification, and later timings do not provide sufficient time for fuel evaporation. Multiple-injection also demonstrated increased stratification potential. More specifically, triple-injection did not perform well due to the short time scales between injection and combustion. On the other hand, double-injection proved to be a useful tool in producing stratification and more specifically, in transportation of the required ignitable mixture clouds ( $14 \leq \text{AFR} \leq 16$ ) towards the spark plug locations. However, careful selection of the second injection timing is required. Finally, in-cylinder swirl was shown to improve homogeneity significantly but to be an obstacle to any attempts for creating charge stratification. Similarly, injection pressure did not improve stratification. In concluding, it should be stated that combustion tests will conclusively determine whether the proposed combustion concept stand a chance to reach production.

## *Chapter 6*

### *Conclusions & Recommendations*

The most important conclusions drawn from the results of the conducted work during this research programme are presented in the following sections. The internal nozzle flow, spray characteristics and the potential of gasoline multi-hole injectors in creating homogeneous as well as stratified mixture distributions in a multi-valve, direct-injection, twin-spark engine were investigated experimentally. Initially, the structures and patterns of the cavitating flow through the nozzle holes and sac volume were observed and correlations between the investigated conditions (e.g. cavitation number and needle lift) and the flow development (e.g. film cavitation and strings) have been identified (Section 6.1).

Following the internal nozzle flow investigation, the sprays from high-pressure multi-hole gasoline injectors have been characterised. Various nozzle designs have been considered and the dependencies of spray structure, penetration length and atomisation quality on injection and chamber pressures, as well as ambient temperature, have been quantified. The ability of multi-hole injectors to adapt to the updated technological demands of direct-injection engines, such as multiple-injection operation, has been also investigated. The conclusions from the spray characterisation experiments are presented in Section 6.2.

Finally, the ability of multi-hole injectors to generate homogeneous stoichiometric and stratified-lean mixture distribution inside a direct-injection gasoline engine has been investigated. Two-dimensional fuel vapour distributions inside a single cylinder, multi-valve, twin-spark ignition research engine have been characterised by means of the laser induced fluorescence technique. The latter revealed useful information on the dependencies of mixture distribution and fuel evaporation time-scales on injection timing and pressure, in-cylinder flow fields and nozzle design characteristics. The main findings of the engine-related investigations are summarised in Section 6.3.

For reasons of completeness, some additional experiments are required for robust conclusions to be drawn. Moreover, technological advances in the field of direct-

injection spark-ignition engines require continuous research on present and future injection equipment capabilities and designs. In addition to that, recommended alternative injection and engine management strategies necessitate the development of more accurate experimental techniques. In this respect, some recommendations for future work are given in Section 6.4.

## **6.1 INTERNAL NOZZLE FLOW**

The experimental investigation of the cavitating flow through gasoline multi-hole injector nozzles has provided qualitative results by means of flow visualisation inside an enlarged three-dimensional model nozzle. High-speed video imaging proved to be a useful tool in terms of identification of internal nozzle flow patterns, visualisation of incipient cavitation structures and, finally, classification of pre-film and film stage cavitation as a function of cavitation and Reynolds number. The most important conclusions from this work are presented here.

An enlarged (29x) transparent model of a vertical six-hole nozzle for direct injection gasoline engines was used in order to investigate the onset and development of cavitation in the nozzle sac volume and injection holes. Simultaneous matching of the Reynolds and cavitation numbers was attempted in order to simulate flow conditions similar to those in real-size nozzles, while the needle lift was set to different values between 0.51 and 2.04mm, which correspond to those in production nozzles. The cavitating flow structures were visualised with a dual high-speed CCD camera system, equipped with appropriate lenses, which allowed details of the flow previously unresolved to be identified. The dynamic development of cavitation inside the nozzles for a wide range of operating conditions was then captured and analysed.

### **6.1.1 Internal nozzle flow patterns**

The internal nozzle flow in multi-hole injectors was found to be highly transient and unstable. For representative visualisation of such flow field, fine air bubbles were introduced for effective flow seeding. The results presented have increased complexity, mainly in the transitional phase, where the incoming annular flow was forced to enter the injection holes or to be directed into the sac volume. More specifically, the parts of the annular flow that were located above the six injection

holes were directed towards the holes by experiencing a steep turning angle. For the annular flow in-between two adjacent injection holes, the flow experienced a pressure gradient along the distance between the two injection holes that resulted in the formation of vortices in the volume formed between the needle face and the two adjacent injection holes. These vortices contributed to the formation of hole interconnecting strings that are described in a subsequent paragraph.

Finally, the flow dynamics inside the sac volume were characterised by slow moving, almost stagnant flow. The fluid trapped in that region of the nozzle was eventually convected, by newly arrived liquid parcels towards random injection holes, where it entered from the bottom side of the hole. However, in general, the injection hole incoming flow was entering mainly from the top of the hole with the contribution of the side incoming flow being rather low, although it increased with increasing flow rate and cavitation number.

### 6.1.2 Incipient cavitation

The onset of cavitation was investigated for various flow rates, cavitation numbers and needle lifts. Interestingly enough, results showed that prior to any cavitation hole structures needle strings appeared in the multi-hole gasoline injector, resembling the nozzle flow behaviour of multi-hole diesel injectors. More specifically, cavitation strings were initiated on the needle face and their formation has been attributed to a strong vortex flow around the hole axis. Once a needle string was created, the low-pressure region in its core was extended well inside the injection hole. The frequency of appearance of needle strings has increased as needle lift decreased. In addition to that, low needle lifts resulted in more stable needle string structures.

At higher cavitation numbers, the first sign of geometric cavitation appeared at the top entrance of the hole while needle strings were still visible. Incipient geometric cavitation structures were very unstable and significantly affected by needle strings. More specifically, as needle strings moved randomly inside the injection hole, once they approached the inlet hole boundary, the low pressure of the string's core was able to initiate geometric cavitation. In some cases, geometric cavitation in the hole inlet could occupy half of the hole's inlet perimeter by forming a canopy-shaped vapour pocket. Although the aforementioned cavitation structures were highly

unstable, they were able to verify the onset of cavitation in multi-hole gasoline injectors and the ensuing interaction between needle strings and geometrically induced cavitation structures.

### 6.1.3 Developed cavitation

The first structures of developed cavitation appeared at cavitation numbers greater than 1. The first important observation is related to needle strings as they began to disappear with increasing cavitation number. At the same time, bubble clouds from geometric cavitation started becoming more opaque and bubble coalescence was evident, which led to formation of larger voids and ultimately local vapour films. In addition to that, and following the complete disappearance of needle strings, another type of string was captured that initiated inside the injection hole. The latter was a cavitation string and its creation mechanism was not different than the one of needle strings. A strong vortex around the hole axis that was enhanced by the dense bubble vapour clouds in the hole inlet, which effectively reduced the hole flow area and increased flow velocities, contributed to the formation of cavitation strings inside the injection hole. Cavitation strings, which were possible to extend towards the hole inlet, triggered a bubble creation mechanism at the core of the vortex existing between two adjacent holes. The latter was the result of the interaction between the high momentum annular flow and the cross flow initiated by two neighbouring injection holes, as discussed in Section 6.1.1. Finally, the bubble creation mechanism at the core of that vortex resulted in formation of hole interconnecting strings. Cavitation strings shared similar effects with needle strings. More specifically, they considerably affect geometric cavitation structures at the hole inlet by increasing turbulence levels. In addition to that, it has been confirmed that the existence of cavitation strings stabilises geometric cavitation structures inside the injection hole. Finally, Reynolds number did not have a profound effect on the formation of cavitation strings, unlike the cavitation number, which enhanced the stability of these strings.

At cavitation numbers greater than two ( $CN \geq 2$ ), the previously observed pre-film stage cavitation structures were gradually replaced by film cavitation that featured separation of the flow from the hole boundaries. Although there was a highly transient behaviour between pre-film and film cavitation structures, the latter did not show any correlation to Reynolds number. Instead, the transition from bubbly cavitation films to

fully separated two-phase flow showed great dependence on needle lift. More specifically, low needle lifts were associated with a highly turbulent behaviour that resulted in more bubbly cavitation structures. Further increase in cavitation number ( $CN \geq 2.5$ ) caused a definite establishment of a two-phase flow and clearly identifiable film stage cavitation structures. As aforementioned, the flow rate through the nozzle did not have any effect on the development of the separated flow inside the hole, unlike the needle lift settings, which appeared to dictate the formation of well-established gaseous pockets around the hole entrance. As needle lift was decreased, the appearance of the fully separated two-phase flow was effectively delayed.

## 6.2 SPRAY CHARACTERISATION

The sprays generated from the multi-hole injectors introduced recently in spray-guided direct injection gasoline engines, have been characterised in terms of droplet velocities/diameters at injection pressures of 80, 120 and 200bar, chamber pressures varying from atmospheric to 12bar and chamber temperatures up to 120°C. Several multi-hole injector nozzle designs have been employed in this study featuring different arrangement in hole positioning (symmetric and asymmetric nozzles) and different number of holes corresponding to different L/D ratios. The sprays from these injectors have been visualised inside a high-pressure / temperature constant volume chamber under various operating conditions employing the Mie scattering technique with a fast-shutter CCD camera and a high-speed imaging system. Spray visualisation has confirmed that the spray angle remains constant and is almost independent of injection and chamber pressure, a significant advantage relative to pressure-swirl atomisers used in the first-generation, wall-guided gasoline engines. For complete spray characterisation results, droplet velocities and diameters of the aforementioned nozzle designs have been measured with a two-dimensional PDA system.

Among the several multi-hole nozzle designs tested, the twelve-holes nozzle that featured two blocked side holes and one central hole, presented the highest volumetric capacity of all the other six-hole configured nozzles. At first sight, a 12-hole nozzle is expected to have larger pressure drop across the injection holes due to their smaller diameter relative to six-hole nozzle holes. However, 12-holes nozzle demonstrated reduced pressure drop across the nozzle due to their larger radius of curvature in the hole inlet to diameter ratio ( $r/D$ ) value that is the result of their reduced hole diameter

while the hole inlet radius of curvature remained unchanged. Geometric cavitation structures are more pronounced in the case of small  $r/D$  values (6-hole nozzle), associated with reduced flow area inside each hole.

### 6.2.1 Spray visualisation

Still and high-speed imaging have improved the understanding of multi-hole sprays' structure and the injector's behaviour under various operating conditions. High-magnification images provided the actual delay time for the needle to fully open, following the triggering pulse. Increasing the injection pressure from 80-120bar resulted in the largest recorded delay time; this shows that injection pressure is not necessarily leading to fast needle opening, as observed in diesel injectors, but it rather slows down the opening event.

The main mechanism of air-entrainment in multi-hole sprays has also been identified. The air motion induced by the high-pressure spray created counter rotating vortices around each liquid jet that forced the smaller droplets to be transferred away from the liquid core. The images revealed a fishbone structure of each jet, similarly to diesel sprays, a structure that enhances air-entrainment, thus improving fuel atomisation and evaporation. The above-described mechanism proved to be a characteristic of all investigated multi-hole nozzle designs, although certain differences were observed between 6- and 12-hole nozzles. Large  $L/D$  values resulted in thin individual jet shapes. Further parametric investigation on the  $L/D$  design characteristics revealed that sprays from 12-hole nozzles penetrate less in the constant-volume chamber compared to the 6-hole generated jets. Furthermore, an increase in injection pressure was much likely to increase penetration of the 6-hole sprays relative to the 12-hole ones.

Injection and chamber pressure dependencies of all tested multi-hole nozzle sprays were found to be similar. More specifically, an increase in injection pressure resulted in a marginal increase in the spray tip penetration for all investigated injectors. Injection pressure also increased spray atomisation, but not indefinitely, although the full quantitative investigation of the effect of injection pressure on spray atomisation was conducted with PDA measurements and is presented in a subsequent section. The inverse effect of injection pressure on spray tip penetration length and fuel atomisation was observed with increasing chamber pressure, which resulted in sprays

with reduced penetration lengths and compact jet shapes. Finally, the effect of chamber temperature was also investigated; injection into ambient temperatures of 50°, 90° and 120°C was realised and the increased evaporation rates expected in 120°C were confirmed. An important observation was made concerning the hole L/D value; the thin sprays produced by large L/D ratios demonstrated higher evaporation rates compared to sprays generated from nozzles with smaller L/D.

Some of the Mie scattering experiments involved investigation of injection duration on spray behaviour and the ability of multi-hole injectors to perform under multiple (double)-injection pulses. The results demonstrated some limitations of the multi-hole injectors driving system concerning minimum injection duration and dwell time. More specifically, the minimum injection duration of multi-hole injectors showed a dependency on injection pressure. Finally, multi-hole injectors demonstrated their ability to operate under double-pulsed conditions. Both injection events appeared to follow the trend of the single injection dependency on injection and chamber pressure, although the overall stability of the double-injection sequence was found to be greatly dependent on the selected dwell time; dwell times smaller than 0.7ms resulted in the formation of a pre-spray between the two main injection events.

### **6.2.2 Phase-Doppler anemometry**

Although spray visualisation produced important qualitative results, quantitative droplet information was essential in completing the spray characterisation investigation. Droplet velocity field and size distribution information, as well as their behaviour under various thermodynamic ambient chamber conditions, has confirmed that multi-hole injectors are very promising fuel injection equipment candidates. Droplet velocity and size distribution data was acquired using a two-dimensional phase – Doppler anemometry system.

Injection and chamber pressure appeared to have quite predictable effects on spray droplet velocities and size distributions. More specifically, injection pressure resulted in increased droplet velocities, for all tested nozzles, and slightly decreased droplet diameters. On the other hand, increasing chamber pressure resulted in reduction of droplet velocities. Additionally, an increase in droplet sizes of up to 55% was observed when chamber pressure increased from atmospheric to 12bar. The stability of the overall multi-hole spray cone angle was also confirmed by the PDA results.

Simultaneous measurements of the axial and radial velocity components showed that the overall cone angle is not dependent on chamber pressure, in agreement with the results deduced from the Mie scattering images. Finally, the ambient chamber temperature had no apparent effect on droplet velocities, while the droplet size distributions as expected were significantly affected.

Injector operating parameters such as injection duration and a multiple-injection pattern showed no apparent effect on droplet velocities; however, droplet size distribution was affected in certain ways. Long injection durations resulted in larger droplet sizes. Furthermore, the effect of dwell time on droplet size characteristics was quantified and the observed pre-spray at short dwell times was found to have larger droplet diameters due to poorer atomisation. In addition, the differences between sprays from 6- and 12-hole nozzles were quantified. The reduced spray droplet sizes produced at larger L/D values also affected droplet velocities. As a result, 12-hole nozzle sprays exhibited smaller droplet velocities and sizes (up to 20%) compared to 6-hole nozzles, which could be an advantage in both stratified and homogeneous engine operation.

Overall, the obtained results have confirmed the advantages and flexibility offered by new generation high-pressure multi-hole injectors for gasoline direct-injection engines, compared to the swirl pressure atomisers, in terms of spray structure stability under varying chamber thermodynamic and injector operating conditions. Nevertheless, their ability to generate the desired air/fuel mixture at the spark plug at the time of ignition under stratified operating conditions with minimum nozzle cocking remains to be confirmed in production engines.

### **6.3 MIXTURE DISTRIBUTION**

The last stage of the present work has been the investigation of the generated mixture distributions by the multi-hole injector inside a direct-injection twin-spark-ignition engine. Two multi-hole nozzle designs have been selected to demonstrate their ability in creating homogeneous as well as stratified mixture distribution inside the single-cylinder optical research engine. A 12-hole and a 6-hole nozzle, featuring an overall spray cone angle of  $90^\circ$  and  $40^\circ$ , respectively, were tested by means of the laser

induced fluorescence technique. The motored single-cylinder optical engine featured a centrally located injector and two spark plugs installed at opposite sides of the cylinder. Laser induced fluorescence quantified the 2-D fuel concentration and local air/fuel ratio along a central plane of the cylinder, with a 6.5mm offset relative to the spark-plug plane for homogeneous stoichiometric and stratified overall lean engine operation.

The twin-spark combustion concept featuring central injection is, in principle, offering advantages in HC and smoke emissions relative to its side-injection, wall-guided counterpart. Additionally, the previously observed problems of cocking in multi-hole injectors and spark plug fouling present in most spray-guided configurations, could be minimised due to the reduced injector tip temperatures. Protection against spark plug fouling is also provided by the stable spray structure of multi-hole injectors and the flexibility they offer in nozzle design and, thus, spray configuration.

### **6.3.1 Homogeneous stoichiometric engine operation**

Overall, multi-hole injectors have demonstrated their ability to produce a homogeneous stoichiometric charge in a multi-valve twin-spark ignition engine. More specifically, it has been confirmed that injection timing controls wall impingement. At low and high engine speeds, the 12-hole nozzle resulted in increased mixture homogeneity at injection timings early in the induction stroke. This is mainly attributed to the fact that the increased spray cone angle ( $90^\circ$ ) of that injector resulted in extensive liner wetting at late injection timings and, at the same time, the crank angle window available for evaporation and mixing was not sufficient. On the contrary, the 6-hole injector that featured a spray cone angle of  $40^\circ$  performed better at later timings of  $90^\circ$  and  $120^\circ\text{CA}$ . Late injection timing ensured minimum impingement on the piston surface and the possibility of fuel impinging on the cylinder walls almost diminished by the narrow spray cone angle. In general, injection timing demonstrated significant effect on homogeneous mixture distribution at low engine speeds (1,500rpm). At higher engine speeds (3,000rpm), however, the effect of injection timing was rather overshadowed by the increased in-cylinder turbulent airflow and the differences between several injection timings relative to mixture uniformity were rather small.

A multiple-injection strategy has also been tested. Double and triple-injection events have been found to reduce spray tip penetration lengths by sub-dividing the actual single injection duration into two or three shorter events. However, at low engine speeds with the 12-hole nozzle, double- and triple-injection did not improve homogeneity. More specifically, double-injection produced a highly non-uniform AFR distribution while triple-injection performed similar to the single injection strategy. Overall, the multiple-injection strategy demonstrated better results with the 6-hole nozzle. Double-injection presented similar results to single injection, although, the timing of the second injection pulse was found to have an effect on the final AFR distribution; homogeneity at early injection timings where single injection did not perform well, was slightly improved. In a similar manner, triple-injection optimised further the homogeneity of single injection and allowed smooth transition from rich to lean areas without steep AFR gradients. At the higher engine speed of 3,000rpm, both double and triple injection strategies demonstrated moderate homogeneity for the 12-hole nozzle. However, the combination of multiple-injection and 6-hole injector at the higher engine speeds proved to be very effective over a wide range of injection timings, with the achieved homogeneity slightly improved compared to the single injection cases. In concluding, the effect of multiple-injection on homogeneity is advantageous in that double-injection provides uniform mixture distribution at high engine speeds, while triple-injection performs better at lower engine speeds.

Another factor affecting mixture homogeneity is in-cylinder airflow. Increased swirl assisted air/fuel mixing and resulted in more uniform AFR distribution at the time of ignition. The latter conclusion is valid for both multi-hole nozzle designs, and for all engine speeds and injection timings. On the contrary, injection pressure did not produce significant improvements in mixture homogeneity. Comparison of the AFR distribution maps of 80 and 120bar revealed that these minor improvements in homogeneity do not seem to justify the energy cost for increasing the injection pressure to levels beyond 80bar.

### **6.3.2 Stratified overall lean engine operation**

Following the investigation on homogeneous mixture distribution, the ability of multi-hole nozzles in creating mixture stratification at the time of ignition had to be

explored. Overall, it has been confirmed that both multi-hole nozzles are able to produce the desired stratification levels inside the twin-spark engine cylinder, with the major parameter affecting stratification being the injection timing. It is useful to note that the direct-injection twin-spark engine shares operating principles from both the spray- as well as the wall-guided configurations, in that it is piston-guided. Therefore, mixture stratification is mainly controlled by the time the fuel spray impinges on the piston, which directs the mixture cloud towards the two spark plugs. Injection timing has, thus, played a major role in achieving the desired stratification for both nozzle designs. The best timing for low and high engine speeds seemed to be around  $260^{\circ}\text{CA}$ , or  $100^{\circ}\text{CA}$  before compression top-dead-centre. Earlier timings led to poor exploitation of the internal airflow, resulting in undesired stratification, while later timings did not provide sufficient time for fuel evaporation. Finally, as far as the single injection strategy is concerned, the 6-hole nozzle presented slightly better stratification potential than the 12-hole one, mainly due to the on-time delivery of fuel to the ignition sources. Multiple-injection also demonstrated increased stratification potential. More specifically, triple-injection achieved the desired stratification levels at early injection timings and low engine speeds for both multi-hole nozzles since, the more the end of injection timing was retarded, the shorter the time available for evaporation and mixing. Furthermore, double-injection proved to be a useful tool in producing stratification and more specifically, in transporting the required ignitable mixture clouds ( $14 \leq \text{AFR} \leq 16$ ) towards the spark plug locations when injection started at around  $250\text{-}260^{\circ}\text{CA}$ . In general, multiple-injection assisted greatly the 6-hole nozzle to produce the desired stratification at all tested engine speeds, while the 12-hole injector did not appear capable of creating stratification at higher engine speeds. Finally, in-cylinder swirl was shown to improve homogeneity significantly but to be an obstacle to any attempts for creating charge stratification, similarly to injection pressure.

#### **6.4 RECOMMENDATIONS FOR FUTURE WORK**

It can be argued that the presented work provided useful information about gasoline multi-hole high-pressure injector nozzle flow, spray characterisation and mixture distribution of relevance to direct-injection spark ignition engines. Nevertheless, in the course of this experimental investigation it became apparent that some further

research on the discussed topics could be valuable. The focus of this proposed work lies on the internal flow in fully transparent real-size multi-hole nozzles, the spray vaporisation characteristics inside a heated constant-volume chamber and combustion development in the single-cylinder twin-spark direct-injection research engine.

#### **6.4.1 Internal nozzle flow investigations**

The suggested future work comprises the manufacturing of both real-size and large-scale transparent model nozzles, for a detailed parametric study of two important geometric factors, hole length to diameter ( $L/D$ ) and radius of curvature to diameter ( $r/D$ ) ratios, which affect directly the cavitation development inside multi-hole nozzles. More specifically, the manufacturing (from plexiglass or glass) of 6- and 12-hole real size transparent model nozzles is proposed for a detailed investigation of the  $L/D$  ratio effect on in-hole cavitation structures. Additionally, simultaneous fully-synchronised imaging of the in-hole cavitation development and the emerging spray structure will provide the link between cavitation onset and type of cavitation with spray atomisation mechanisms in multi-hole injectors. Finally, the application of micro PIV (Particle Image Velocimetry) to real size transparent multi-hole nozzles although it represents a major experimental challenge it may provide valuable and unique information on the velocity flow field inside multi-hole nozzle.

The second parameter that was identified to have an effect on in-hole geometric cavitation inception and development is the  $r/D$  ratio. Therefore, the manufacturing of large-scale transparent nozzles that feature different  $r/D$  ratios is proposed. More specifically, these nozzles should feature a constant number of holes with each nozzle being slightly different in terms of the  $r/D$  ratio. Application of high-speed imaging to in-hole cavitation structures of various manufactured models could provide very useful information on cavitation inception and development.

#### **6.4.2 Spray investigations**

As expected, the spray dependence on ambient temperature was found to be significant. However, these observations are based on Mie scattered light, which is representing only liquid concentration. A direct and simultaneous acquisition of liquid and vapour phase images in evaporating high-pressure gasoline multi-hole sprays

would provide much improved understanding of the effect of ambient temperature on spray propagation and evaporation. More specifically, evaporating high-pressure gasoline sprays inside a high-pressure/temperature constant-volume chamber would render ideal the application of the Laser Sheet Drop-sizing technique (LSD) using Laser Induced Exciplex Fluorescence (LIEF) [58, 59, 61, 69, 71]. According to the theoretical description of this technique, a dual imaging optical system enables simultaneous imaging of the liquid (Mie) and vapour (LIF) phases under the same laser and camera operating conditions. Thus, quantitative information of the effect of ambient temperature on spray evaporation can be made possible at conditions simulating closely those during the compression stroke in direct-injection gasoline engines.

#### **6.4.3 Engine investigations**

The potential of multi-hole injectors in creating homogeneous stoichiometric as well as stratified overall lean mixture distribution inside a direct-injection gasoline engine has been investigated by the LIF technique. The results were promising, and certain operating conditions were considered to be appropriate for combustion experiments. Therefore, the next phase in the engine investigations should focus on combustion experiments. More specifically, combustion stability in terms of misfires and blockage-free injector operation are considered to be key parameters that will determine the future of multi-hole gasoline injectors as promising FIE candidates. In addition, exhaust gas emission measurements are vital in supporting the flame development investigation since the final judgement on multi-hole injector efficiency will be based on their ability to provide fuel economy approaching that of diesels and exhaust emissions comparable to the best of today's port injection gasoline engines equipped with the most sophisticated catalyst systems.

## Chapter 7

### References

1. Agency, E.E., *Climate change and a European low-carbon energy system*. EEA Report, 2005(1/2005).
2. Geiger, J., M. Grigo, O. Lang, P. Wolters and P. Hupperich, *Direct Injection Gasoline Engines - Combustion and Design*. SAE 1999-01-0170, 1999.
3. Ortmann, R., S. Arndt, J. Raimann, R. Grzeszik and G. Wuerfel, *Methods and Analysis of Fuel Injection, Mixture Preparation and Charge Stratification in Different Direct Injected SI Engines*. SAE 2001-01-0970, 2001.
4. Ando, H., *Mitsubishi GDI Engine - Strategies to Meet the European Requirements*. AVL Conference, 4-5 Sep. 1997, 1997.
5. Ando, H., *Combustion Control Technologies for Gasoline Engines*. IMechE International Seminar on Lean Burn Engines.
6. Arcoumanis, C., M.R. Gold, J.H. Whitelaw and H.M. Xu, *Local Mixture Injection to Extend the Lean Limit of Spark-Ignition Engines*. *Experiments in Fluids*, 1999. **26**: p. 126-135.
7. Mitroglou, N., C. Arcoumanis, K. Mori and Y. Motoyama, *Mixture distribution in a multi-valve twin-spark ignition engine equipped with high-pressure multi-hole injectors*. International Conference on Optical and Laser Diagnostics, 2005.
8. Zhao, F., M.-C. Lai and D.L. Harrington, *Automotive spark-ignited direct-injection gasoline engines*. *Progress in Energy and Combustion Science*, 1999. **25**: p. 437-562.
9. Skogsberg, M., P. Dahlander, R. Lindgren and I. Denbratt, *Effects of Injector Parameters on Mixture Formation for Multi-Hole Nozzles in a Spray-Guided Gasoline DI Engine*. SAE 2005-01-0097, 2005.
10. Pontoppidan, M., G. Gaviani, R. Rotondi and A. DeMaio, *Reduction of Spray Momentum for GDI High-Pressure Injectors - A Necessary Step to Accomplish Series Production of Super-Charged DI-Engines*. SAE 2005-01-0104, 2005.
11. Cathcart, G. and C. Zavier, *Fundamental Characteristics of an Air-Assisted Direct Injection Combustion System as Applied to 4 Stroke Automotive Gasoline Engines*. SAE 2000-01-0256, 2000.
12. Sczomak, D.P. and G.J. Patterson, *Overview of Central-Injection Air-Assisted SIDI Technology Emissions and Fuel Consumption*. SAE 2003-01-0545, 2003.

13. Duret, P., J.-C. Dabadie, J. Lavy, J. Allen, D. Blundell, J. Oscarsson, G. Emanuelsson and M. Perotti, *The Air Assisted Direct Injection ELEVATE Automotive Engine Combustion System*. SAE 2000-01-1899, 2000.
14. Nouri, J.M., E. Abo-Serie, A. Marchi, N. Mitroglou and C. Arcoumanis, *Internal and near nozzle flow characteristics from an enlarged model of an outward opening gasoline direct injector*. International Conference on Optical and Laser Diagnostics, 2005.
15. Yan, Y., S. Gashi, J.M. Nouri, R.D. Lockett and C. Arcoumanis, *Investigation of spray characteristics in a spray guided DISI engine using PLIF and LDV*. International Conference on Optical and Laser Diagnostics, 2005.
16. Seibel, C., K. Gartung, S. Arndt and B. Weigand, *Detailed analysis of spray structure and air entrainment in GDI sprays using a tomographic approach*. ICLASS 2003, 2003.
17. Szekely, G.A. and A.C. Alkidas, *Combustion Characteristics of a Spray-Guided Direct-Injection Stratified-Charge Engine with a High-Squish Piston*. SAE 2005-01-1937, 2005.
18. Shelby, M.H., B.A. VanDerWege and S. Hochgreb, *Early Spray Development in Gasoline Direct-Injected Spark Ignition Engines*. SAE 980160, 1998.
19. Wigley, G., G.K. Hargrave and J. Heath, *A high power, high resolution LDA/PDA system applied to dense gasoline direct injection sprays*. 9th International Symposium of Applied Laser Techniques to Fluid Mechanics - Lisbon, 1998. **1**.
20. Abo-Serie, E., C. Arcoumanis, M. Gavaises, B. Argueyrolles and F. Galzin, *Structure of Sprays Generated by Pressure Swirl Injectors for Direct-Injection Gasoline Engines*. ILASS-Europe, 1999.
21. Ipp, W., V. Wagner, H. Kraemer, M. Wensing, A. Leipertz, S. Arndt and A.K. Jain, *Spray Formation of High Pressure Swirl Gasoline Injectors Investigated by Two-Dimensional Mie and LIEF Techniques*. SAE 1999-01-0498, 1999.
22. Nouri, J.M. and J.H. Whitelaw, *Spray Characteristics of a Gasoline Direct Injection Injector with Short Duration of Injection*. Experiments in Fluids, 2001. **vol.31**: p. 377-383.
23. Nouri, J.M., C. Brehm and J.H. Whitelaw, *The Spray form a Gasoline Direct Injector*. ILASS-Europe 1999, 1999.
24. Gavaises, M. and C. Arcoumanis, *Modelling of sprays from high-pressure swirl atomisers*. International Journal of Engine Research, 2001. **vol.2**(No.2): p. p.95-118.
25. Wigley, G., M. Goodwin, G. Pitcher and D. Blondell, *Near nozzle LDA/PDA measurements of a GDI spray and their analysis to quantify liquid breakup and atomisation mechanisms*. ICLASS 2003, 2003.

26. Lippert, A.M., S.H. El Tahry, M.S. Huebler, S.E. Parrish, H. Inoue and T. Noyori, *Development and Optimisation of a Small-Displacement Spark-Ignition Direct-Injection Engine - Full-Load Operation*. SAE 2004-01-0033, 2004.
27. Lippert, A.M., S.H. El Tahry, M.S. Huebler, S.E. Parrish, H. Inoue, T. Noyori, K. Nakama and T. Abe, *Development and Optimisation of a Small-Displacement Spark-Ignition Direct-Injection Engine - Stratified Operation*. SAE 2004-01-0033, 2004.
28. Pontoppidan, M., G. Gaviani, G. Bella and A. De Maio, *Study of the Benefits and Drawbacks of a Substantial Increase of Rail-Pressure in GDI-Injector Assemblies*. SAE 2002-01-1132, 2002.
29. Moon, S., J. Choi, E. Abo-Serie and C. Bae, *The Effects of Injector Temperature on Spray and Combustion Characteristics in a Single Cylinder DISI Engine*. SAE 2005-01-0101, 2005.
30. Koike, M., A. Saito, T. Tomoda and Y. Yamamoto, *Research and Development of a New Direct Injection Gasoline Engine*. SAE 2000-01-0530, 2000.
31. Kanda, M., T. Baika, S. Kato, M. Iwamuro, M. Koike and A. Saito, *Application of a New Combustion Concept to Direct Injection Gasoline Engine*. SAE 2000-01-0531, 2000.
32. Takeda, K., T. Sugimoto, T. Tsuchiya and M. Ogawa, *Slit Nozzle Injector for a New Concept of Direct Injection SI Gasoline Engine*. SAE 2000-01-1902, 2000.
33. Arndt, S., K. Gartung and D. Brueggemann, *Spray Structure of High Pressure Gasoline Injectors : Analysis of Transient Spray Propagation and Spray-Gas Momentum Transfer*. ILASS Europe, Zurich 2-6 Sep. 2001, 2001.
34. Landenfeld, T., A. Kufferath and J. Gerhardt, *Gasoline Direct Injection - SULEV Emission Concept*. SAE 2004-01-0041, 2004.
35. Honda, T., M. Kawamoto, H. Katashiba, M. Sumida, M. Fukutomi and K. Kawajiri, *A Study of Mixture Formation and Combustion for Spray Guided DISI*. SAE 2004-01-0046, 2004.
36. Nouri, J.M., N. Mitroglou, Y. Yan and C. Arcoumanis, *Internal flow and cavitation in a multi-hole injector for gasoline direct injection engines*. sent for publication in SAE 2007, 2007.
37. Mitroglou, N., J.M. Nouri, M. Gavaises and C. Arcoumanis, *Spray structure generated by multi-hole injectors for gasoline direct-injection engines*. sent for publication in SAE 2007, 2007.
38. Mitroglou, N., J.M. Nouri, M. Gavaises and C. Arcoumanis, *Spray Characteristics of a multi-hole Injector for Direct-Injection Spark-Ignition*

- Engines*. International Journal of Engine Research, 2006. vol.7(issue 3).
39. Gashi, S., Y.-Y. Yan, R.D. Lockett and C. Arcoumanis, *Mixture Distribution in a Spray-Guided Direct Injection Spark Ignition (DISI) Engine using Planar Laser Induced Fluorescence (PLIF)*. to be published in International Journal of Engine Research, 2006.
  40. Karaiskos, E., *Spray Structure and Mixture Distribution in Direct-Injection Gasoline Engines*. Imperial College, 2005. **PhD Thesis**.
  41. Roth, H., E. Giannadakis, M. Gavaises, C. Arcoumanis, H. Yanagihara and I. Sakata, *Effect of Multi-injection Strategy on Cavitation Development in Diesel Injector Nozzle Holes*. SAE 05P-330, 2005.
  42. Scholz, J., K. Roetmann and V. Beushausen, *Influence of the internal flow conditions of slit nozzles on the stability of liquid sheets: Experimental results*. ICLASS 2003, 2003.
  43. Roth, H., M. Gavaises and C. Arcoumanis, *Cavitation Initiation, Its Development and Link with Flow Turbulence in Diesel Injector Nozzles*. SAE Paper 2002-01-0214, 2002.
  44. Arcoumanis, C., M. Gavaises, H. Flora and H. Roth, *Visualisation of Cavitation in Diesel Engine Injectors*. *Mecanique & Industries*, 2001. 2(5): p. 375-381.
  45. Soteriou, C., R. Andrews, M. Smith, N. Torres and S. Sankhalpara, *The Flow Patterns and Sprays of Variable Orifice Nozzle Geometries for Diesel Injection*. SAE Paper 2000-01-0943, 2000.
  46. Afzal, H., C. Arcoumanis, M. Gavaises and N. Kampanis, *Internal Flow in Diesel Injector Nozzles: Modelling and Experiments*. IMechE Paper S492/S2/99, 1999.
  47. Arcoumanis, C., M. Gavaises, J.M. Nouri, E. Abdul-Wahab and R.W. Horrocks, *Analysis of the Flow in the Nozzle of a Vertical Multi Hole Diesel Engine Injector*. SAE Paper 980811, 1998.
  48. Yule, A.J., A.M. Dalli and K.B. Yeong, *Transient Cavitation and Separation in a Scaled-Up Model of a VCO Orifice*. Proc. ILASS-EUROPE, 1998.
  49. Arcoumanis, C. and M. Gavaises, *Cavitation in Diesel Injectors: Modelling and Experiments*. Proc. ILASS-EUROPE, 1998.
  50. Soteriou, C.C.E., M. Smith and R.J. Andrews, *Cavitation Hydraulic Flip and Aton:ization in Direct Injection Diesel Sprays*. IMechE Paper C465/051/93, 1993.
  51. Arcoumanis, C., J.M. Nouri and R.J. Andrews, *Application of Refractive Index Matching to a Diesel Nozzle Internal Flow*. Proc. IMechE Seminar on Diesel Fuel Injection Systems, 1992.

52. Nauwerck, A., J. Pfeil, A. Velji, U. Spicher and B. Richter, *A Basic Experimental Study of Gasoline Direct Injection at Significantly High Injection Pressures*. SAE 2005-01-0098, 2005.
53. Pontoppidan, M., G. Gaviani, G. Bella and A. De Maio, *Optimisation by CFD Simulation of Spray Formation Parameters to Adapt Direct Injection High-Pressure Fuel Injectors to High-Speed SI-Engines*. SAE 2004-01-0539, 2004.
54. Abe, M., Y. Okamoto, Y. Kadomukai, Y. Tanabe and T. Ishikawa, *Fuel Spray Pattern Control Using L-Step Nozzle for Swirl-Type Injector*. SAE 2004-01-0540, 2004.
55. Wigley, G., M. Goodwin, G. Pitcher and D. Blondel, *Imaging and PDA analysis of a GDI spray in the near-nozzle region*. *Experiments in Fluids*, 2004. **36**: p. 565-574.
56. Choi, J., S. Lee and C. Bae, *Spray and Flow-Field Interaction of gasoline Direct Injection*. *Atomization and Sprays*, 2004. **Vol 14**: p. pp159-174.
57. Abo-Serie, E., M. Gavaises and C. Arcoumanis, *Spray/Wall Interaction in Direct-Injection Spark Ignition Engines Equipped with Multi-Hole Injectors*. ILASS Europe, 2003.
58. Duewel, I., T. Kunzelmann, J. Schorr, C. Schulz and J. Wolfrum, *Application of fuel tracers with different volatilities for planar LIF/Mie dropsizing in evaporating systems*. ICLASS 2003, 2003.
59. Ineichen, B., *Recent Findings of Simultaneous Droplet Size, Shape and Velocity Detection of Injection Sprays in a High Pressure - High Temperature Cell*. ICLASS 2003, 2003.
60. Goodwin, M. and G. Wigley, *A Fundamental Study of Liquid Sheet Breakup and its Relationship to GDI Sprays*. ICLASS 2003, 2003.
61. Hung, D.L.S., D.M. Chmiel and L.E. Markle, *Application of an Imaging-based Diagnostic Technique to Quantify the Fuel Spray Variations in a Direct-Injection Spark-Ignition Engine*. SAE 2003-01-0062, 2003.
62. Stegemann, J., J. Seebode, J. Baltes, C. Baumgarten and G.P. Merker, *Influence of throttle effects at the needle seat on the spray characteristics of a multihole injection nozzle*. ILASS Europe, 2002.
63. Wigley, G., J. Heath, G. Pitcher and A. Whybrew, *Experimental Analysis of the Response of a Laser/Phase Doppler Anemometer System to a Partially Atomised Spray*. *Part. Part. Syst. Charact.*, 2001. **18**: p. 169-178.
64. Arndt, S., K. Gartung, T. Pauer, M. Staudt and U. Renz, *Analysis of high pressure sprays for diesel and SI engines with direct fuel injection: Evaluation of evaporation and spray induced turbulence. PART I: Influence of spray induced air flow on spray structure and mixture preparation*. ILASS Europe, 2000.

65. Arndt, S., K. Gartung, T. Pauer, D. Zeh, D. Brueggemann, J. Egermann, W. Ipp, V. Wagner and A. Leipertz, *Analysis of high-pressure sprays for diesel and SI engines with direct fuel injection: Evaluation of evaporation and spray induced turbulence. PART II: Spray evaporation and quantification of the local fuel air ratio inside the spray*. ILASS Europe, 2000.
66. Boyaval, S. and C. Dumouchel, *Experimental investigation on the drop size distribution of sprays produced by GDI injectors*. ILASS Europe, 2000.
67. Allen, J. and G. Hargrave, *Fundamental Study of In-nozzle fluid flow and its effect on liquid jet break-up in Gasoline Direct Injectors*. ILASS Europe, 2000.
68. Lee, C.H. and R.D. Reitz, *An experimental study of the effect of gas density on the distortion and breakup mechanism of drops in high speed gas stream*. International Journal of Multiphase Flow, 2000. **26**: p. 229-244.
69. Jeong, K.S., M.C. Jermy and D.A. Greenhalgh, *Laser Sheet Dropsizing in Evaporating Sprays using Laser Induced Exciplex Fluorescence*. 9th International Symposium on Flow Visualisation, 2000, 2000.
70. Araneo, L., A. Coghe, G. Brunello and R. Donde, *Effects of Fuel Temperature and Ambient Pressure on a GDI Swirled Injector Spray*. SAE 2000-01-1901, 2000.
71. Fansler, T. and M. Drake, *Designer diagnostics for developing direct-injection gasoline engines*. International Conference on Optical and Laser Diagnostics, 2005.
72. Fajardo, C.M., J.D. Smith and V. Sick, *PIV, high-speed PLIF and chemiluminescence imaging for near-spark-plug investigations in IC engines*. International Conference on Optical and Laser Diagnostics, 2005.
73. Wiles, M.A., D.M. Probst and J.B. Ghandhi, *Bulk Cylinder Flowfield Effects on Mixing in DISI Engines*. SAE 2005-01-0096, 2005.
74. Wang, Y.-J., J.-X. Wang, S.-J. Shuai, X.-H. Lei and X.-L. An, *Study of Injection Strategies of Two-Stage Gasoline Direct Injection (TSGDI) Combustion System*. SAE 2005-01-0107, 2005.
75. McGee, J., T. Alger, E. Blobaum and S. Wooldridge, *Evaluation of a Direct-Injected Stratified Charge Combustion System Using Tracer PLIF*. SAE 2004-01-0548, 2004.
76. Frieden, D. and V. Sick, *Investigation of the Fuel Injection, Mixing and Combustion Processes in an SIDI Engine using Quasi-3D LIF Imaging*. SAE 2003-01-0068, 2003.
77. Stan, C., A. Stanciu, R. Troeger, L. Martorano, C. Tarantino, M. Antonelli and R. Lenzi, *Direct Injection Concept as a Support of Engine Down-Sizing*. SAE 2003-01-0541, 2003.

78. Samson, E., B. Renou and A. Boukhalifa, *Coupling Laser Sheet Tomography and P.L.I.F. for the Study of Atmospheric Stratified Charge Combustion*. SAE 2003-01-0065, 2003.
79. Moreau, J., J. Boree, R. Bazile and G. Charnay, *Modification of an Experimental Model GDI Tumbling Flow by Direct Injection*. SAE 2003-01-0064, 2003.
80. Alger, T., M. Hall and R. Matthews, *Effects of In-cylinder Flow on Fuel Concentration at the Spark Plug, Engine Performance and Emissions in a DISI Engine*. SAE 2002-01-0831, 2002.
81. Gold, M., G. Li, S. Sapsford and J. Stokes, *Application of Optical Techniques to the Study of Mixture Preparation in Direct Injection Gasoline Engines and Validation of a CFD Model*. SAE 2000-01-0538, 2000.
82. Lee, S., K. Tong, B.D. Quay, J.V. Zello and D.A. Santavicca, *Effects of Swirl and Tumble on Mixture Preparation During Cold Start of a Gasoline Direct-Injection Engine*. SAE 2000-01-1900, 2000.
83. Ekenberg, M. and B. Johansson, *Fuel Distribution in an Air Assist Direct Injected Spark Ignition Engine with Central Injection and Spark Plug measured with Laser Induced Fluorescence*. SAE 2000-01-1898, 2000.
84. Alger, T., M. Hall and R.D. Matthews, *Effects of Swirl and Tumble on In-Cylinder Fuel Distribution in a Central Injected DISI Engine*. SAE 2000-01-0533, 2000.
85. Pontoppidan, M., G. Gaviani, G. Bella, M. Schilardi and V. Rocco, *Enhanced Mixture Preparation Approach for Lean Stratified SI-Combustion by a Combined Use of GDI and Electronically Controlled Valve-Timing*. SAE 2000-01-0532, 2000.
86. Kakuhou, A., T. Urushihara, T. Itoh and Y. Takagi, *Characteristics of Mixture Formation in a Direct Injection SI Engine with Optimised In-Cylinder Swirl Air Motion*. SAE 1999-01-0505, 1999.
87. Choi, K.H., J.H. Park, N.H. Lee, C.H. Yu and S.H. Noh, *A Research on Fuel Spray and Air Flow Fields for Spark-Ignited Direct Injection using Laser Measurement Technology*. SAE 1999-01-0503, 1999.
88. Alger, T., M. Hall and R. Matthews, *Fuel Spray Dynamics and Fuel Vapor Concentration Near the Spark Plug in a Direct-Injected 4-Valve SI Engine*. SAE 1998-01-0497, 1998.
89. Ohsuga, M., T. Shiraishi, T. Nogi, Y. Nakayama and Y.-H.L. Sukegawa, *Mixture Preparation for Direct-Injection SI Engines*. SAE 970542, 1997.
90. Ghandhi, J.B. and F.V. Bracco, *Mixture Preparation Effects on Ignition and Combustion in a Direct-Injection Spark-Ignition Engine*. SAE 962013, 1996.

91. Kume, T., Y. Iwamoto, K. Lida, M. Murakami, K. Akishino and H. Ando, *Combustion Control Technologies for Direct Injection SI Engines*. SAE 960600, 1996.
92. Lang, O., J. Geiger, K. Habermann and M. Wittler, *Boosting and Direct Injection-Synergies for Future Gasoline Engines*. SAE 2005-01-1144, 2005.
93. Kawamoto, M., T. Honda, H. Katashiba, M. Sumida, N. Fukutomi and K. Kawajiri, *A Study of Centre and Side Injection in Spray Guided DISI Concept*. SAE 2005-01-0106, 2005.
94. Szekely, G.A.J., A.S. Solomon and P.-H. Tsai, *Optimisation of the Stratified-Charge Regime of the Reverse-Tumble Wall-Controlled Gasoline Direct-Injection Engine*. SAE 2004-01-0037, 2004.
95. Lake, T., J. Stokes, R. Murphy, R. Osborne and A. Schamel, *Turbocharging Concepts for Downsized DI Gasoline Engines*. SAE 2004-01-0036, 2004.
96. Solomon, A.S. and G.A.J. Szekely, *Combustion Characteristics of a Reverse-Tumble Wall-Controlled Direct-Injection Stratified-Charge Engine*. SAE 2003-01-0543, 2003.
97. Eichlseder, H., E. Baumann, P. Mueller and S. Rubbert, *Gasoline Direct Injection - A Promising Engine Concept for Future Demands*. SAE 2000-01-0248, 2000.
98. Fry, M., J. King and C. White, *A Comparison of Gasoline Direct Injection Systems and Discussion of Development Techniques*. SAE 1999-01-0171, 1999.
99. Pontoppidan, M., G. Gaviani, G. Bella, A. DeMaio and V. Rocco, *Experimental and numerical Approach to Injection and Ignition Optimisation of Lean GDI-Combustion Behaviour*. SAE 1999-01-0173, 1999.
100. Whitaker, P.A., J. Stokes and T.H. Lake, *Comparison of Top-Entry and Side-Entry Direct Injection Gasoline Combustion Systems*. IMechE International Conference "Combustion Engines and Hybrid Vehicles", 28-30 April 1998, 1998.
101. Harada, J., T. Tomita, H. Mizuno, Z. Mashiki and Y. Ito, *Development of Direct Injection Gasoline Engine*. SAE 970540, 1997.
102. Roth, H., *Experimental and Computational Investigation of Cavitation in Diesel Injector Nozzles*. Imperial College, 2004. **PhD Thesis**.
103. Tonini, S., *Fuel Spray Modelling in Direct-Injection Diesel and Gasoline Engines*. City University, London., 2006. **PhD Thesis**.
104. Soteriou, C., R. Andrews and M. Smith, *Further Studies of Cavitation and Atomisation in Diesel Injection*. SAE 1999-01-1486, 1999.

105. Fujikawa, T., Y. Hattori and K.-T.C.R.a.D.L. Akihama, Inc., *Quantitative 2-D Fuel Distribution Measurements in an SI Engine Using Laser-Induced Fluorescence with Suitable Combination of Fluorescence Tracer and Excitation Wavelength*. SAE 972944, 1997.
106. Zhao, H. and N. Ladommatos, *Optical diagnostics for in-cylinder mixture formation measurements in IC engines*. Progress in Energy and Combustion Science, 1998. **24**: p. 297-336.
107. Weimar, H.-J., G. Toepfer and U. Spicher, *Optical Investigations on a Mitsubishi GDI-Engine in the Driving Mode*. SAE 1999-01-0504, 1999.
108. Beushausen, V., T. Mueller, O. Thiele, T. Wesker, R. Grzeszik, J. Raimann and S. Arndt, *Spatially Resolved Determination of Fuel/Air Ratio Inside a Direct Injection SI-Engine Under Real Fuel Conditions*. 2000.
109. Sakadura, J.C., L. Robin, F.-C.-R. Dionnet, D. Gervais, P. Gastaldi and A.-R.-R.M. Ahmed, *Experimental Investigation of an Optical Direct Injection SI Engine Using Fuel-Air Ratio Laser Induced Fluorescence*. SAE 2000-01-1794, 2000.
110. Schulz, C. and V. Sick, *Tracer-LIF diagnostics: quantitative measurement of fuel concentration, temperature and fuel/air ratio in practical combustion systems*. Progress in Energy and Combustion Science, 2005. **31**: p. 75-121.
111. Schmidt, D.P., C.J. Rutland and M.L. Corradini, *A Numerical Study of Cavitating Flow Through Various Nozzle Shapes*. SAE 971597, 1997.
112. Giannadakis, E., M. Gavaises, H. Roth and C. Arcoumanis, *Cavitation Modelling in Single-Hole Diesel Injectors Based on Eulerian-Lagrangian Approach*. Proc. THIESEL 2004, 2004.
113. Papoulias, D., E. Giannadakis, M. Gavaises and A. Theodorakakos, *Modelling and Experimental Validation of Cavitation in Fuel Injection Systems for Direct-Injection Gasoline Engines*. to be published in SAE 2007, 2007.
114. [www.ni.com](http://www.ni.com).
115. Kampanis, N., *Flow, Mixture Distribution and Combustion in Five-Valve Gasoline Engines*. Imperial College, 2003. **PhD Thesis**.
116. [www.pco.de](http://www.pco.de).
117. Tait, N.P., *Development of Planar Laser Diagnostic Techniques for Fuel and Soot Imaging in Combustion Applications, in Mechanical Engineering Department*. Cranfield University, Bedfordshire, 1994.
118. Le Gal, P., N. Farrugia and D.A. Greenhalgh, *Laser Sheet Dropletsizing (LSD) Development for Dense Spray Characterisation*. ILASS Europe 98, 1998.
119. Guibert, P., M. Durget and M. Murat, *Concentration Fields in a Confined*

- Two-Gas Mixture and Engine In-Cylinder Flow: Laser Tomography Measurement by Mie Scattering*. Experiments in Fluids, 2001. **31**: p. 630-642.
120. Mitschke, M., G. Schulte, J. Koeser, M. Zorn and T. Wriedt, *Reconstruction of velocity-diameter relations obtained from PDA measurements during atomisation of inhomogeneous liquids*. ILASS Europe, 1999.
121. Tropea, C. and N. Damaschke, *Phase Doppler Measurements in Ultra-Dense Sprays*. Short Course - TU Darmstadt, 2005.
122. Kashdan, J.T., J.S. Shrimpton and C. Arcoumanis, *Dynamic Structure of Direct-Injection Gasoline Engine Sprays: Airflow and Density Effects*. Imperial College, 1999.
123. Berckmueller, M., *A Study of Mixture Formation in a Lean Burn Research Engine Using Laser Fluorescence Imaging*, in *Mechanical Engineering Department*. Cranfield University, Bedfordshire, 1999.
124. Fujikawa, T., Y. Hattori and K. Akihama, *Quantitative 2-D Fuel Distribution Measurements in an SI Engine Using Laser-Induced Fluorescence with Suitable Combination of Fluorescence Tracer and Excitation Wavelength*. SAE 972944, 1997.
125. Thurber, M.C. and R.K. Hanson, *Simultaneous Imaging of Temperature and Mole Fraction Using Acetone Planar Laser-Induced Fluorescence*. Experiments in Fluids, 2001. **30**: p. 93-101.
126. Koban, W., J. Schorr and C. Schulz, *Oxygen-Distribution Imaging with a Novel Two-Tracer Laser-Induced Fluorescence Technique*. Applied Physics, 2002. **B 74**: p. 111-114.
127. Sick, V., *Exhaust-Gas Imaging Via Planar Laser Induced Fluorescence of Sulfur Dioxide*. Applied Physics, 2002. **B 74**: p. 461-463.
128. Nygren, J., *Temporally Resolved Single-Cycle*. Proceedings of The Fifth International Symposium on Diagnostics and Modeling of Combustion in Internal Combustion Engines, 2001: p. 572-580.
129. Thurber, M.C., *Measurements and Modeling of Acetone Laser-Induced Fluorescence with Implications for Temperature-Imaging Diagnostics*. Applied Optics, 1998. **37**(21): p. 4963-4978.
130. Hentschel, W., A. Grote and O. Langer, *Measurement of Wall Film Thickness in the Intake Manifold of a Standard Production SI Engine by a Spectroscopic Technique*. SAE 972832, 1997.
131. Almkvist, G., *Measurements of Fuel Film Thickness in the Inlet Port of an S.I. Engine by Laser Induced Fluorescence*. SAE 952483, 1995.
132. Stevens, E. and R. Steeper, *Piston Wetting in an Optical DISI Engine: Fuel Films, Pool Fires and Soot Generation*. SAE 2001-01-1203, 2001.

133. Gold, M., J. Stokes and R. Morgan, *Air-Fuel Mixing in a Homogeneous Charge DI Gasoline Engine*. SAE 2001-01-0968, 2001.
134. Gold, M.R., *Mixture Preparation Strategies in an Optical Four-Valve Port-Injected Gasoline Engine*. International Journal of Engine Research, 2000. **1**(1).
135. Berckmueller, M., N.P. Tait, R.D. Lockett, D.A.-C.U. Greenhalgh, K. Ishii, Y. Urata, H. Umiyama and K.-H.R.D.C.L. Yoshida, *In-Cylinder Crank-Angle-Resolved Imaging of Fuel Concentration in a Firing Spark-Ignition Engine Using Planar Laser-Induced Fluorescence*. The Combustion Institute, 25th International Symposium on Combustion, 1994, 1994: p. 151-156.
136. Han, D. and R. Steeper, *Examination of Iso-Octane/Ketone Mixtures for Quantitative LIF Measurements in a DISI Engine*. SAE 2002-01-0837, 2002.
137. Arcoumanis, C., P. Cutter and J.H. Whitelaw, *Heat Transfer Processes in Diesel Engines*. Trans. IChemE., 1998. **76 Part A**.
138. Kampanis, N., C. Arcoumanis, S. Kometani, R. Kato and H. Kinoshita, *Flow and mixture distribution in a high-speed five-valve direct injected gasoline engine*. International Journal of Engine Research, 2006. **7**(No.2): p. 143-166.